

Expression of a gene-encoded FtsZ-based minimal machinery to drive synthetic cell division

Godino, E.

DOI

[10.4233/uuid:c43c9b99-585a-4929-9bee-2c6d87a3b2c1](https://doi.org/10.4233/uuid:c43c9b99-585a-4929-9bee-2c6d87a3b2c1)

Publication date

2022

Document Version

Final published version

Citation (APA)

Godino, E. (2022). *Expression of a gene-encoded FtsZ-based minimal machinery to drive synthetic cell division*. [Dissertation (TU Delft), Delft University of Technology]. <https://doi.org/10.4233/uuid:c43c9b99-585a-4929-9bee-2c6d87a3b2c1>

Important note

To cite this publication, please use the final published version (if applicable).
Please check the document version above.

Copyright

Other than for strictly personal use, it is not permitted to download, forward or distribute the text or part of it, without the consent of the author(s) and/or copyright holder(s), unless the work is under an open content license such as Creative Commons.

Takedown policy

Please contact us and provide details if you believe this document breaches copyrights.
We will remove access to the work immediately and investigate your claim.

Expression of a gene-encoded FtsZ-based minimal machinery to drive synthetic cell division

Dissertation

for the purpose of obtaining the degree of doctor

at Delft University of Technology

by the authority of the Rector Magnificus Prof.dr.ir. T.H.J.J. van der Hagen

Chair of the Board for Doctorates

to be defended publicly on

Wednesday 6th April 2022 at 10:00 o'clock

by

Elisa GODINO

Master of Science in Cellular and Molecular Biotechnology

University of Trento, Italy

born in Cles, Italy

This dissertation has been approved by the promotor.

Table of content

Composition of the doctoral committee:

Rector Magnificus	Chairperson
Dr. C.J.A. Danelon	Delft University of Technology, promotor
Dr. M.E. Aubin-Tam	Delft University of Technology, copromotor

Independent members:

Prof. dr. G.H. Koenderink	Delft University of Technology
Prof. dr. G. Rivas Caballero	Spanish National Research Council
Dr. J. Bonnet	Centre de Biologie Structurale de Montpellier
Dr. K.A. Ganzinger	AMOLF
Dr. T-Y.D. Tang	Max Planck Institute
Prof. dr. A.M. Dogterom	Delft University of Technology, reserve member



Keywords:	Synthetic biology, liposomes, synthetic cell, cell-free gene expression, cell division, FtsZ, Min system.
Printed by:	Ridderprint https://www.ridderprint.nl/
Cover:	Elisa Godino

Copyrights © 2022 Elisa Godino
Casimir PhD-series, Delft-Leiden 2022-07
ISBN 978.90.8593.518.6

An electronic copy of this dissertation is available at <https://repository.tudelft.nl/>

CHAPTER 1:

Introduction	5
--------------------	---

CHAPTER 2:

De novo synthesized Min proteins drive oscillatory liposome deformation and regulate FtsA-FtsZ cytoskeletal patterns	27
--	----

CHAPTER 3:

Cell-free biogenesis of bacterial division proto-rings that can constrict liposomes	69
---	----

CHAPTER 4:

Min waves without MinC can pattern FtsA-FtsZ filaments on model membranes	113
---	-----

CHAPTER 5:

FtsA-FtsZ in liposomes: constricting necks and budding vesicles, yet a step away from division	147
--	-----

CHAPTER 6:

Imaging flow cytometry for high-throughput phenotypic characterization of synthetic cells	171
---	-----

CHAPTER 7:

FtsZ and Min systems: concluding remarks and future perspectives	199
--	-----

SUMMARY	219
---------------	-----

SAMENVATTING	223
--------------------	-----

ACKNOWLEDGMENTS	227
-----------------------	-----

CURRICULUM VITAE	233
------------------------	-----

LIST OF PUBLICATIONS	235
----------------------------	-----

Chapter 1

Introduction

Comprehending the complexity of cells

The cell is extraordinarily complex. Billions of years of evolution brought to the gathering of an extreme diversity of highly interconnected functional parts. The sophistication of even the simplest organism known so far is such that it makes one wonder if life actually requires such complexity. Is it possible to sustain cellular life with much fewer components? The investigation of whether life might be conceivable in a less complex form, led to the formation of a rapidly expanding branch of synthetic biology in which the simplest living system, the minimal cell¹⁻⁵, will be built on the basis of fundamental principles. The goal is to gain insights into the core concepts embedded in the intertwined nature of the cell by using a 'understanding by building' approach.

There are two strategies to build a minimal cell: a top-down and a bottom-up approach⁶. In the top-down approach, the genetic complexity of the living cell is sequentially stripped to preserve only the information that are purely required to maintain it alive. In the bottom-up approach essential cellular components are assembled from scratch to build a synthetic cell. The bottom-up approach consists of two sub-approaches: the synthetic and the semi-synthetic approach. The former attempts to create protocells using elements that plausibly have been present in a prebiotic environment, while the latter focuses on semi-synthetic cells relying on extant biomolecules.

While defining life is a tough prospect, there is a general agreed-upon definition of a living synthetic cell. Synthetic cells must be able to self-maintain, self-replicate and evolve to be considered alive. Those functions must be implemented in an entity that has a compartment, to identify a boundary, and genetic information, to encode for all the core biomolecules that will autonomously sustain the cell (Fig. 1). The genetic information must be replicated, and in doing so mutations may be introduced providing selective advantages to the synthetic unit. Self-replication implies compartment growth and division, the latter being an essential operation for self-maintenance and evolution.

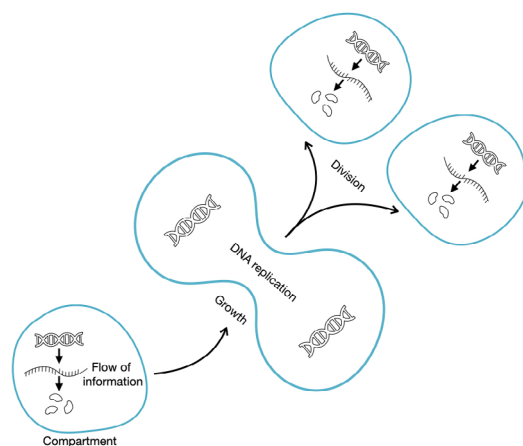


Figure 1: The characteristics of the synthetic cell. A synthetic cell is composed of a compartment that carries genetic information which, in nature, is typically stored in the form of DNA that is then transcribed and translated inside the self-contained unit. The information transfer directs the synthetic cell cycle, which includes compartment growth, genomic replication, and compartment division.

Gene expressing liposomes

All living organisms store hereditary information in semipermeable compartments. This information is encoded in nucleic acid sequences and must be expressed into proteins to sustain the cell. The information is transmitted by the two-step process formulated in the central dogma of molecular biology: transcription and translation⁷. During transcription, the replicated DNA is converted into RNA and, during translation, RNA is decoded to produce one or more proteins. DNA is a chemically and mechanically stable information carrier that has been vastly exploited in molecular biology encouraging the development of a plethora of standard techniques. An effective DNA-based technology is in vitro transcription-translation (IVTT), which consists in the expression of DNA in a cell-free assay by mixing essential components obtained from different organisms. IVTT represents a platform that allows to recreate the flow of information in vitro allowing the synthetic cell to guide its essential processes in autonomy starting from its own genetic material.

The flow of information, as the full content of the cell, is selectively isolated from the external environment by a semipermeable compartment. Compartmentalization is crucial as it outlines the cell as a unit in space, provides an energy storage mechanism and enables evolutionary processes⁸. All living systems are based on compartments defined by the cell membrane, a thin and flexible layer of lipids and proteins. The amphipathic nature of lipids renders them particularly adapted to delimitate polar environments: the hydrophilic heads and hydrophobic tails of the lipids spontaneously assemble into nano-sized bilayers that fold into spherical structures known as liposomes. These biomimetic compartments, with a size ranging from 0.1 to 10 μm , closely resemble living cells with regard to semi-permeability, size, containment, and biocompatibility^{9,10}. Apart from liposomes, a broad range of other synthetic compartments have been established¹¹, including polymersomes^{12,13}, fatty acid vesicles^{8,14,15}, water-in-oil droplets^{16,17}, colloidosomes^{18,19}, and coacervates^{20,21}. Each methodology, however, has its own limitations, such as incompatibility with protein interacting with specific lipids, lack of stability or short lifetime, high surface tension, no deformability, oil phase surroundings preventing the exchange of materials, and lack of permeability. All these approaches to the assembly of synthetic cell compartments are of considerable importance, but liposomes remain the most biologically compatible form of synthetic cell compartment.

Integrating in-liposome protein production from DNA template might be the most suited approach to introduce hereditary information and semipermeable compartment into the experimental design of a self-replicating synthetic cell. Early works²²⁻²⁴ have laid the foundation for current studies on gene expression inside compartments. Oberholzer et al., showed functional activity of ribosomes encapsulated within liposomes²⁵. Yu et al., focused on the synthesis of folded and functional protein products²⁶. The *Escherichia coli* cell extract enabled the first demonstration of cell-free protein synthesis inside liposomes^{10,26,27}. In their work Nomura et al., encapsulated the cell-extract via the natural swelling method to produce

rsGFP (red-shifted green fluorescent protein) expressing liposome¹⁰. Noireaux and Libchaber cell-free expressed the α -hemolysin pore, showing that, by allowing for selective permeability of nutrients, the expression reactions can be extended over several days²⁷. Ishikawa et al., expanded the potential of in-liposome gene expression, reconstituting a two-step cascade genetic network by co-encapsulating two genes and cell-extract²⁸. Because of the low price, the high yield of protein expression, and the opportunity to employ endogenous RNA polymerases, the *Escherichia coli* cell extract has become the most popular formulation for in vitro gene expression^{29–33}. However, due to the undefined and uncharacterized nature of cell lysates, it is impossible to know or control the composition of the expression reaction, and the possible presence of proteases and/or nucleases may have a negative impact on experiments. Unlike whole cell extracts, the protein synthesis using recombinant elements (PURE) system^{34,35}, developed by the group of Takuya Ueda, is free of endogenous proteins that may interfere with the cellular function to be reconstituted. The PURE system is a minimal gene expression system with a well-defined mixture of purified proteins, substrates and cofactors that recapitulates transcription, translation, tRNA aminoacylation and energy regeneration (Fig. 2). Although combining all the necessary functions of a cell is still a major challenge^{2,36}, several milestones in the cell-free expression of individual modules inside liposomes have been achieved: from the characterization of gene expression itself^{37–40}, to DNA replication^{41,42}, membrane synthesis^{43–46}, division machineries^{47–50}, evolution⁵¹ and communication^{52–54}. Hence, we picture the self-replicating synthetic cell as a liposome compartment producing its own constituents from a purified cell-free gene expression system. It should be noted that synthetic cell research is not restricted to gene expression in liposomes but incorporates a wide range of extremely relevant methodologies not covered in this dissertation.

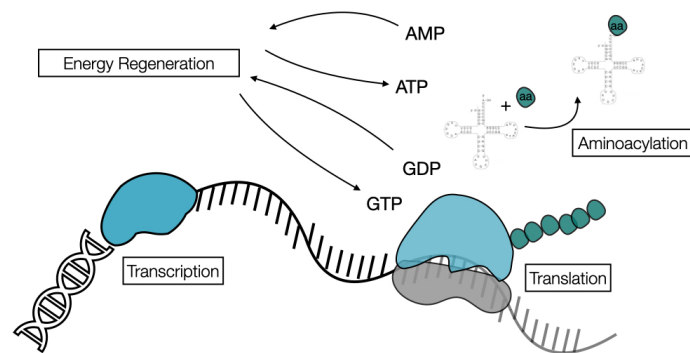


Figure 2: The PURE system as a tool for gene expression inside liposomes. The PURE system^{34,35}, is a reconstituted cell-free transcription-translation system that enables the production of recombinant proteins starting from DNA. Transcription, translation, tRNA aminoacylation, and energy regeneration are all modules of the PURE system. AMP/ATP stands for adenosine mono/triphosphate; GDP/GTP refers to guanosine di/triphosphate; and aa stands for amino acid.

Our approach to semi synthetic cells and division

The Danelon lab aims to reconstitute an autonomous semi-synthetic cell with a bottom-up approach. We postulate that in-liposome protein production from DNA template is an effective route to build such a minimal cell. Within our framework, semipermeable phospholipid vesicles, DNA, and the PURE system are employed to reconstitute the three essential functions of living cells: self-maintenance, self-reproduction, and evolution (Fig. 3). To achieve autonomy a DNA-based minimal genome eventually must encode all the necessary genetic information, including the program for its own replication, the regeneration of the PURE system, and the growth and division of the compartment. Our lab has developed a method based on swelling from lipid-coated glass beads, which allows functional encapsulation of the IVTT machinery in liposome. Various aspects of the PURE system activity have been explored, such as the effects of confinement in liposome compartments^{37,38}, the modeling of the gene expression dynamics and ribosomal processivity^{39,55,56}. Our strategy for DNA replication is inspired by the mechanism of the ϕ 29 bacteriophage. We designed a self-replicating linear DNA template by encoding genes of the ϕ 29 virus⁴¹. Compartment growth is approached via in-liposome phospholipid synthesis directed by a multi-cistronic DNA construct^{43,46}. Two different lines are explored in the lab to achieve autonomous, DNA-based division⁵⁷. One involves spontaneous division driven by lipid synthesis and the energetically unfavorable excess of membrane. The other comprises the synthesis of division or membrane-remodeling proteins to exert a mechanical force and eventually split the liposome.

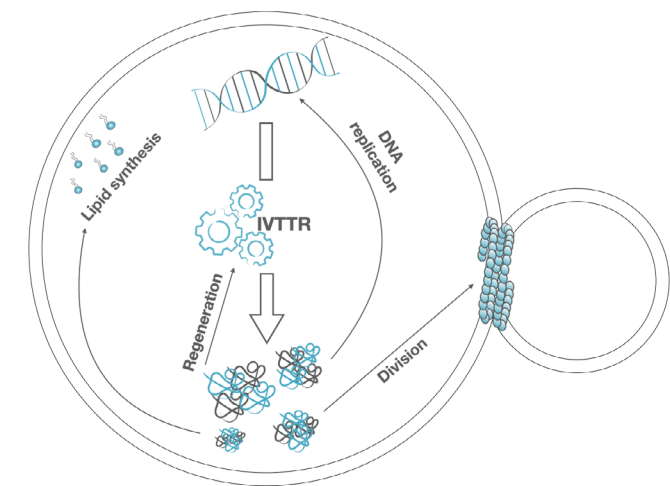


Figure 3: In-liposome protein synthesis from a DNA template to construct an autonomous semi-synthetic cell capable of self-maintenance, self-replication, and evolution. The Danelon lab's design strategy to build a replicating synthetic cell comprises the encapsulation of PURE system and DNA into semipermeable phospholipid liposomes. The minimal genome encodes all the necessary components to sustain in vitro transcription-translation, DNA replication, phospholipid biosynthesis, and cell division.

The work described in this dissertation is part of the group's mission to build a module for autonomous division. As already mentioned, self-replication entails compartment division. Division is an essential step as it protects the cells from the threats posed by the environment and side product accumulation that would otherwise lead to the collapse of the cells. In addition, the information transfer alongside division provides a stage at which functional evolution can take place. In this context the assembly of the division module is tackled by de novo synthesizing a minimal version of the *Escherichia coli* division mechanism. Using liposomes as compartments and the PURE system as a gene expression machinery, we aim to reconstitute a minimal divisome in vitro, towards the goal of achieving DNA-encoded spatial localization of membrane constriction and symmetrical division.

Technical note: gene expression and liposome production

Given the aforementioned synthetic cell design, the method for liposomes production should not interfere with the PURE system. Therefore, strong ionic solutions or solvent and oil residues should be avoided. In this context, the lipid film swelling method represents a valid option to obtain high-yielding gene expressing liposomes. Vesicles are formed by hydrating a lipid film composed of several phospholipid bilayers. As the water molecules are drawn in between the bilayers, the film swells and liposomes spontaneously form¹⁰. The Danelon lab modified the classic protocol by hydrating lipid-coated glass beads with PURE system (Fig. 4). The changes were introduced to enhance the active lipid film surface area, thereby allowing for high yield liposome production in low-volume PURE system solutions. Since the protocol generates multilamellar vesicles, a step of freeze-thaw cycles was included to increase the number of unilamellar liposomes. The protocol yields liposomes with a high heterogeneity in size and encapsulation efficiency^{37,40}. When the PURE system and DNA are introduced to the hydration solution, expression may begin. To ensure that gene expression occurs exclusively within the liposomes, activity must be suppressed during liposome preparation (by conducting the swelling on ice or in a cold room) and avoided on the outside of the liposomes (using Proteinase K and/or DNase).

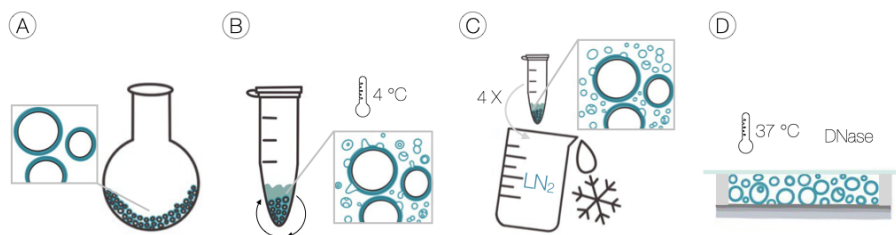


Figure 4: Schematic representation of gene expressing liposome formation. a, In a round-bottom glass flask, 212–300 µm glass beads are coated with a lipid film at a mass ratio lipids/beads

of 0.002:1. b, A PURE system reaction mixture is then assembled in a test tube, together with the DNA template, to form the swelling solution. The lipid coated beads are rehydrated in the swelling solution. Natural swelling of the lipid film is performed at low temperatures to prevent the start of gene expression. The tube is gently rotated throughout incubation. c, After swelling, to alleviate the presence of multilamellar structures, four freeze–thaw cycles are applied by dipping the sample in liquid nitrogen and thawing on ice. d, The liposome solution is pipetted with a cut tip into the imaging chamber. To inhibit gene expression outside liposomes, the sample is supplemented with DNase or Proteinase K. The chamber is covered, and expression is performed at 37 °C.

To perform cell-free expression, the commercially available PURE^{frex}® (GeneFrontier; PURE^{frex}) was employed in this study. Specifically, we used PURE^{frex}®2.0, an enhanced version that was developed by adjusting the purification of the expression elements and improving the co-factors mixture. The upgraded kit has higher protein yields and has an extended lifespan. Moreover, the kit composition is known by us through a confidential agreement with GeneFrontier, making gene expression more predictable and manageable. The system comprises 36 purified proteins, ribosomes, and nutrients (i.e., amino acids, nucleotides, transfer-RNAs and ions) that are required to ensure in vitro transcription, translation, tRNA aminoacylation, and energy regeneration³⁴. Except for a couple of proteins (e.g. the RNA polymerase from the T7 bacteriophage), all constituents of the PURE^{frex}® system are purified from *E. coli*. Once assembled, PURE^{frex}®, along with the DNA template, is sufficient for in vitro protein synthesis. Expression reactions are typically carried at 37 °C.

Both linear and circular DNA can be used as template. The DNA that will be supplied to the expression reaction must meet certain requirements and should include a T7 promoter and an *E. coli* consensus ribosome binding site (RBS) at the upstream of the coding sequence, and a transcription terminator at the downstream of the coding sequence.

The DNA constructs were often synthesized de novo (GenScript) by optimizing DNA sequences from start to stop codon for codon usage in *E. coli*, from which the PURE^{frex}® translation machinery is derived. Optimization includes lowering, in the first 30 base pairs, the GC content and intramolecular base pairing without altering the amino acid composition. This step supposedly reduces the occurrence of inhibitory mRNA structures resulting in a higher expression yield.

Before we concentrate on synthetic cell division powered by the *Escherichia coli* divisome, it is important to state that we recognize that autonomous and robust synthetic cell division could also be reproduced starting from different molecular assemblies like actomyosin-based machines^{58,59}, the ESRCT system^{60,61}, Cdv system^{62,63} and different viral proteins^{64,65}. In addition, innovative division mechanisms may be created, for example using DNA

origami⁶⁶ or engineered proteins^{67,68}. Lastly, in the absence of a dedicated division machinery, autonomous division of the compartment could also be achieved through lipid-based biophysical processes⁶⁹.

The master player in bacterial division: The Z-ring

We know that bacterial division is performed by a large macromolecular complex whose assembly and disassembly are finely orchestrated in time and space. This complex is referred to as the divisome and it consists of more than two dozen proteins^{70,71}. Although most of the divisome players (essential and nonessential) have been identified, their exact roles and dynamic organization are still unclear.

At the core of the divisome is FtsZ (filamentous temperature sensitive Z), a bacterial homologue of tubulin⁷²⁻⁷⁴. Upon binding with GTP, FtsZ polymerizes into protofilaments which can further self-interact to form filaments or bundles⁷⁵⁻⁷⁸. The filaments display treadmilling dynamics, in which one end of the polymer grows and the other shrinks^{79,80}. Early in the cell cycle, these filaments form a ring-like structure at midcell, where it marks the future division site. This structure is called the Z-ring⁸¹ and it guides the recruitment of structural and signaling proteins that eventually mature into a functional divisome. At the onset of cytokinesis, the Z-ring (or protoring) comprises FtsZ, FtsA and ZipA⁸².

FtsZ is a highly conserved protein composed of three domains. The N-terminus globular domain is a GTPase domain involved in GTP binding, FtsZ self-interaction and linear polymerization^{83,84}. The intrinsically disordered flexible linker connects the N-terminus with the C-terminus⁸⁵. The C-terminus comprises two parts: a short highly conserved sequence responsible for the binding of FtsZ with accessory proteins and a variable region that plays a role in the reorganization of FtsZ polymers into bundles⁸⁵⁻⁸⁹.

FtsZ does not have a membrane targeting domain, and it is anchored to the cytoplasmic membrane by the two essential division proteins FtsA and ZipA. Both membrane anchoring proteins bind the C-terminus of FtsZ and influence its dynamics. Either FtsA or ZipA is sufficient for Z-ring assembly, however the presence of both proteins is required to recruit the other division players and achieve division⁹⁰. In the absence of both membrane proteins the Z-ring does not form⁹⁰.

FtsA (Filamentous thermosensitive mutant A) is highly conserved and binds to the membrane via a C-terminal amphipathic helix⁹¹. FtsA requires a conformational change that is driven by ATP binding^{92,93} to interact with FtsZ and the membrane. ZipA (FtsZ interacting protein A) is exclusively found in gammaproteobacteria, and integrates into the membrane by its hydrophobic N-terminal single-transmembrane domain⁸³. ZipA is the only essential cell division protein that can be depleted when its absence is compensated by the FtsA polymorphic FtsA^{*94}.

Along with FtsA and ZipA, a few other binding proteins are responsible for promoting Z-ring

formation and dynamics stabilization, one example are the FtsZ-cross linking Zaps proteins (FtsZ associated protein, ZapA, ZapC and ZapD)⁹⁵⁻⁹⁷.

Z-ring localization: The Min system

Escherichia coli duplicates by splitting the mother cell into two identical daughter cells. To ensure symmetrical division, the cell employs different mechanisms that secure the Z-ring at the future division site. The most studied Z-ring localization mechanism is the Min system. This mechanism consists of three proteins: MinC, MinD, and MinE⁹⁸. MinD and MinE self-organize and dynamically oscillate between the two cell poles⁹⁹⁻¹⁰². MinC is a passenger of the oscillating system which, when in complex with MinD, inhibits FtsZ polymerization. As a result of the oscillations, the highest concentration of the MinD-MinC complex is at the cell poles, confining Z-ring formation to the middle of the cell¹⁰³⁻¹⁰⁵.

The *E. coli* MinCDE system is encoded in the *minB* operon¹⁰⁶. The molecular mechanism behind Min oscillations is based on nonlinear reaction-diffusion dynamics between MinD and MinE. MinD is a cytosolic ATPase¹⁰⁷ which, upon ATP binding, homodimerizes with ATP¹⁰⁸ and is recruited on the membrane via its C-terminal amphipathic helix^{109,110}. Membrane bound MinD-ATP forms clusters that recruit MinC, a cytosolic protein responsible of inhibiting FtsZ polymerization. MinC and MinD act synergistically to inhibit FtsZ. Upon interaction with MinD, MinC C-terminal domain interacts with FtsZ C-terminal domain and prevents its lateral interactions¹¹¹. In the next stage, MinE, a small soluble protein that works as a restricting factor against the MinCD complex, dimerizes and competes with MinC to interact with the membrane-bound MinD-ATP. MinE dimers displace MinC which is then released in the cytoplasm¹¹². Once bound to MinD, MinE triggers ATP hydrolysis by MinD-ATP, MinD dimers disassemble, and MinD-ADP monomers are released from the membrane into the cytosol¹¹³. MinE remains temporarily in the membrane-bound state and targets more membrane-bound MinD-ATP dimers or diffuses back to the cytoplasm^{112,114}. Cytosolic MinD-ADP can exchange ADP for ATP, MinD-ATP re-binds to the membrane on the opposite site, where MinE is not present. This interplay between MinD and MinE proteins leads to sustained oscillatory gradients along the long axis of the cell. The pole-to-pole MinD-MinE oscillations results in MinC concentrations that are high at the cell poles and low at midcell, where FtsZ can polymerize and assemble into a ring.

In vivo, if the Min system is completely depleted, the Z-ring is misplaced near the cell poles. This leads to asymmetric division and a phenotype called minicell (from which the “min” system gets its name)^{106,115}. Depletion of MinD or MinC also leads to the same phenotype¹⁰⁶. Instead, in the absence of MinE, MinD-MinC are distributed homogeneously on the membrane, thus impairing Z-ring assembly and therefore division^{102,105,116,117}.

In vitro reconstitution of *E. coli* division elements

The in vitro reconstitution of cell division is a necessary, yet ambitious, objective to realize a self-replicating synthetic cell. Because of the incredible sophistication of the macromolecular complexes involved, the strong regulations and interconnections between the various players, and the highly dynamic nature of the protein-protein and protein-membrane interactions, recreating a fully functional dividing apparatus in vitro represents a daunting challenge. Detailed mechanistic insights have been collected while reconstituting parts of this complex machine, and it is clear that integration of other elements of the divisome will help identify the minimal requirements to mimic bacterial division.

In vitro investigations of FtsZ assembly and structures found that FtsZ rearranges into protofilaments that may emerge as either single protofilaments (minirings) or as small sheets or bundles^{77,118,119}. When imaging protein self-organization on supported lipid bilayers, Loose and Mitchison¹²⁰ observed that FtsA-bound FtsZ assembled in dynamic bundles (Fig. 5a), while ZipA-bound FtsZ formed static filaments (Fig. 5b), demonstrating that different membrane proteins lead to different FtsZ phenotypes¹²⁰. In this work, the authors showed that FtsA-FtsZ co-filaments undergo treadmilling in the presence of GTP and a sufficiently high local concentration of FtsZ. Moreover, sZipA-bound FtsZ polymers can form higher order structures with GTP on top of supported lipid membranes, as observed by atomic force microscopy¹²¹. These structures adopted linear or curved shapes depending on the lipid composition of the underlying membrane.

Another study reported that a chimeric version of FtsZ fused to a membrane targeting sequence (MTS) underwent treadmilling only for a narrow range of free Mg^{2+} concentrations establishing a link between the local concentration of FtsZ and GTP hydrolysis¹²².

The core components of the *E. coli* divisome have also been encapsulated inside vesicles, providing information about ring-like structures formation in confined volumes and about membrane deformation. Purified FtsZ fused to an MTS was encapsulated within liposomes and led to membrane deformation in the presence of GTP¹²³ (Fig. 5c). This result was interpreted as evidence that FtsZ acts as the force generator for membrane constriction. Vesicles shrinkage was also reported when FtsZ and a soluble version of ZipA (sZipA) were provided within liposomes in the presence of GTP¹²⁴ (Fig. 5d). In the same year, Osawa and Erickson claimed they observed division events of liposomes using FtsA* (a self-interaction impaired FtsA) to recruit FtsZ to the membrane¹²⁵ (Fig. 5e). Such a phenotype was not reproduced in the presence of wildtype FtsA.

More recently, cell-free synthesis of key division proteins inside liposomes was described⁴⁷. The co-expression of full length ZipA and FtsZ led to the formation of clusters that prompted local deformations of the lipid membrane. When FtsA and FtsZ were co-expressed inside liposomes, the proteins were homogeneously recruited on the membrane and no deformation was observed.

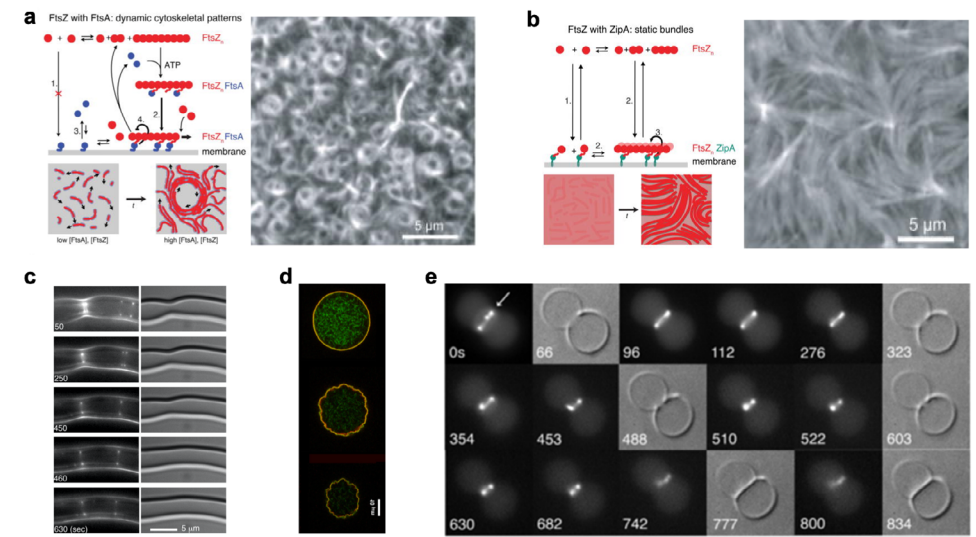


Figure 5: In vitro reconstitution of *E. coli* Z-ring elements. **a**, and **b**, The molecular mechanisms of Z-ring assembly in the presence of FtsA and ZipA, adapted from Loose and Mitchison¹²⁰. **a**, Model for FtsZ–FtsA co-assembly on supported lipid bilayers. Monomeric FtsZ is not recruited by FtsA. Following FtsZ polymerization, an FtsA–FtsZ filament complex forms and binds to the membrane. As protein concentration increases, the dynamic filaments rearrange into streams and vortices. A microscope view of the typical FtsA–FtsZ cytoskeletal patterns that arise on the bilayer is shown. **b**, Model for FtsZ–ZipA co-assembly on supported lipid bilayers. ZipA recruits polymerized and non-polymerized FtsZ to the membrane. Membrane-bound FtsZ polymerizes, and lateral interactions allow the assembly of thick static bundles. A fluorescence microscopy image of FtsZ long thick filament bundles is shown. **c**, Osawa's¹²³ images of tubular liposomes show modestly constricting rings composed of purified FtsZ linked to a membrane targeting sequence. Fluorescence captures on the left, bright field images on the right. **d**, Cabré's¹²⁴ equatorial cross-sectional images show vesicle membrane invagination during shrinkage induced by the interaction of membrane-bound ZipA (red) and FtsZ (green) polymers upon GTP hydrolysis. **e**, Osawa & Erickson reported¹²⁵ time series images of constricting liposomes driven by FtsA* and FtsZ structures (arrow). Scale bar: 10 μ m. Time in seconds.

The min system has also been the center of multiple studies to achieve symmetrical synthetic cell division in vitro, leading to several fruitful outcomes. The commonly named 'Min waves' were reconstituted in vitro for the first time in 2008¹²⁶. Loose and colleagues¹²⁶ reported directional spatiotemporal pattern of moving proteins on top of a supported lipid bilayer (Fig. 6a). MinD and MinE were found to be indispensable and sufficient to form the oscillations. The same group further expanded their original study by following the three MinCDE proteins¹¹⁴ and characterizing the intensity profile of the Min proteins on the membrane. MinE was found to accumulate at the back of the MinDE dynamic pattern, resembling the in vivo MinE-ring.

This fascinating protein interaction network inspired many others to characterize the dynamics of the Min waves in different settings, such as changing membrane lipid

compositions^{127,128}, buffer salt concentrations¹²⁷, temperature¹²⁹, crowding^{129,130} and different involved players^{128,131,132}.

Min proteins dynamics have been further investigated employing a range of different geometries and compartments. Protein patterns were studied on photolithographically patterned membranes¹³³, showing that the Min waves respond to two-dimensional geometrical obstacles. Oscillations were also reconstituted in open cell-shape compartments¹²⁸ and fully confined chambers¹³⁴, where pole-to-pole oscillations were observed. Recently, the Min oscillations have been studied also inside liposomes (Fig. 6b), where three dynamic behaviors were observed: circular, pole-to-pole and pulsing¹³⁵. Under hypertonic conditions GUVs displayed Min-driven shape deformation¹³⁵. Only very recently MinDE has been synthesized under an inducible promoter inside lipid microdroplets⁴⁹, demonstrating that gene expression of Min proteins can be triggered in a controlled manner. Furthermore, MinD and MinE have been reported to operate as a propagating diffusion barrier exerting steric pressure (Fig. 6c), which results in membrane protein and lipid redistribution^{136,137}.

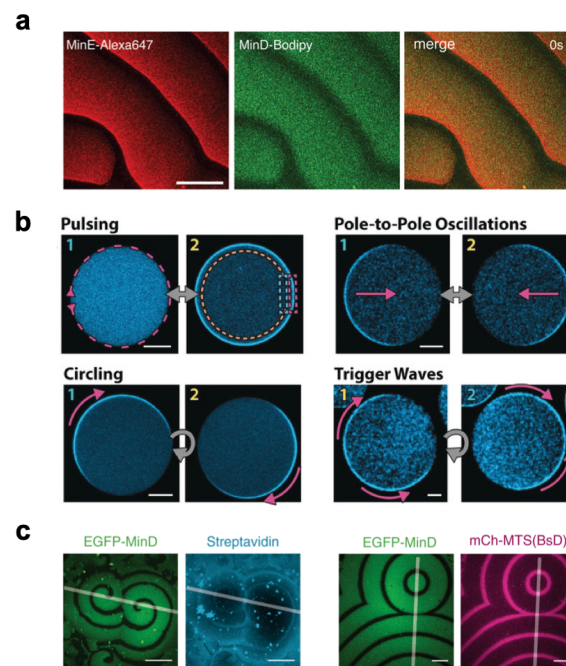


Figure 6: In vitro reconstitution of the *E. coli* Min system. **a**, Confocal images from Loose and colleagues¹²⁶ showing MinD and MinE proteins self-organizing in surface waves on a supported lipid membrane. MinD (green), and MinE (red). Scale bar: 50 μ m. **b**, Min oscillations inside liposomes as reported in Litschel et al.¹³⁵. Each Min oscillation mode in GUVs is represented by two frames from a confocal time series. MinD is depicted in cyan. The wave directions are shown by magenta arrows. Scale bars: 10 μ m. **c**, Images as reported in¹³⁶, showing that MinDE (green) modulates the spatial and temporal dynamics of membrane-bound mCh-MTS (cyan) and streptavidin (magenta) in vitro. Scale bars: 50 μ m.

The FtsZ-ring and force generation during bacteria cytokinesis

FtsZ has traditionally been described as the primary source of constrictive force in vivo¹³⁸. The reconstruction of Z-rings provided some evidence that FtsZ filaments could also act as a force generator in vitro and deform liposomes. According to the FtsZ filament bending model^{139,140}, the force needed to constrict the membrane is entirely supplied by the Z-ring pulling inwards. In the FtsZ condensation model, the Z-ring exerts a constriction force on the membrane as it transitions into high-density structures^{141,142}. *E. coli* has a turgor pressures around ~ 0.3 MPa¹⁴³, not considering the resistance posed by the cell wall. To help counter this tension, a force of about 50 nN would be necessary¹⁴⁴. FtsZ-generated force is estimated to be around a few pN^{141,145}, making it insufficient to drive cell division. Throughout the years there has been significant debate over the involvement of FtsZ in cell constriction. It was found that the pace of septum closure in *E. coli* cytokinesis is resistant to several Z-ring disturbances¹⁴⁶, including changes in FtsZ GTPase activity, Z-ring density, and time of ring assembling. In their work, Coltharp et al., demonstrated that the pace of constriction is instead regulated by peptidoglycan metabolism¹⁴⁶. A single molecule fluorescence microscopy study tracked the proteins at the *E. coli* division septum and reported that FtsZ assemblies were dismantled before cell constriction¹⁴⁷. Further research also found that FtsZ leaves the septum before the compartment is split, indicating that FtsZ is not engaged in the late stage of division¹⁴⁸.

Nowadays, the peptidoglycan biosynthesis machinery is the most plausible contender as main force generator. The most recent acknowledged hypothesis contemplates the combined involvement of peptidoglycan and FtsZ^{149,150}. The Z-ring could exert initial forces that may provide a spatiotemporal cue that directs the regulation of peptidoglycan synthesis. In support of this, it was recently shown that FtsZ dynamic treadmilling coordinates both the position and activity of peptidoglycan synthesizing enzymes⁷⁹. Cell wall synthesis is predicted to have a significant role in advancing constriction and is currently under study. Together, it appears that in vivo the Z-ring can be reinterpreted as a director for septum formation rather than the main constrictive player. Whether the reconstituted Z-ring can robustly constrict and physically divide liposomes and, ultimately, a synthetic cell, remains an open question.

Thesis outline

In this work we aim at synthesizing de novo a minimal version of the *Escherichia coli* division mechanism, including the Z-ring and the MinCDE positioning system, in order to achieve DNA-driven symmetrical liposome division.

- In **chapter 2**, the Min system is synthesized from its genes on supported lipid bilayers and inside liposomes. Cell-free expressed MinD and MinE lead to dynamic protein patterns that accompany liposome deformation. When coupled with FtsA and FtsZ, the Min system is able to dynamically regulate FtsZ patterns.
- In **chapter 3**, we demonstrate that FtsA-FtsZ ring-like structures driven by cell-free gene expression can be reconstituted on planar membranes and inside liposome compartments. These cytoskeletal structures constrict liposomes, resulting in extended membrane necks and budding vesicles. ZapA expression causes stiff FtsZ bundles to attach to the membrane, but it hampers the formation of budding liposomes. ZipA is also investigated as a membrane anchor for FtsZ cytoskeletal structures. In these assays, a crowding agent or ZapA is necessary to induce bundle formation.
- In **chapter 4**, we use cell-free gene expression from a polycistronic DNA template to examine the spatiotemporal control of FtsA-FtsZ cytoskeletal structures by the Min proteins. We find that MinDE oscillations are sufficient to generate dynamic, antiphase FtsA-FtsZ patterns.
- In **chapter 5**, we further characterize the structure and dynamics of the membrane necks and budding vesicles produced by FtsA-FtsZ ring-like structures. We report on the co-existing mechanisms of membrane deformations and elaborate on the unlikely event of division in such conditions.
- In **chapter 6**, we introduce imaging flow cytometry as a high-content and rapid liposome screening platform that combines the advantages of fluorescence imaging and flow cytometry. Liposome populations with reconstituted biological processes are used as a demonstration of the instrument's potential.
- In **chapter 7**, we offer a critical conclusion on the current status of autonomous synthetic cell division exploiting the *E. coli* division mechanism and propose several paths to pursue in the near future to achieve this objective.

References

1. Noireaux, V., Maeda, Y. T. & Libchaber, A. Development of an artificial cell, from self-organization to computation and self-reproduction. *Proc. Natl. Acad. Sci.* **108**, 3473–3480 (2011).
2. Forster, A. C. & Church, G. M. Towards synthesis of a minimal cell. *Molecular Systems Biology* vol. **2** (2006).
3. Murtagh, G. Artificial assembly of a minimal cell. *Molecular BioSystems* vol. **5** 1292–1297 (2009).
4. Schwille, P. *et al.* MaxSynBio: Avenues towards creating cells from the bottom up. *Angew. Chemie Int. Ed.* **57**, 13382–13392 (2018).
5. Powell, K. Biology from scratch: Built from the bottom up, synthetic cells could reveal the boundaries of life. *Nature* **563**, 72–175 (2018).
6. Luisi, P. L., Walde, P. & Oberholzer, T. Lipid vesicles as possible intermediates in the origin of life. *Curr. Opin. Colloid Interface Sci.* **4**, 33–39 (1999).
7. Crick, F. Central dogma of molecular biology. *Nature* **227**, 561–563 (1970).
8. Chen, I. A., Roberts, R. W. & Szostak, J. W. The emergence of competition between model protocells. *Science*. **305**, 1474–1476 (2004).
9. Szostak, J. W., Bartel, D. P. & Luisi, P. L. Synthesizing life. *Nature* **409**, 387–390 (2001).
10. Nomura, S. I. M. *et al.* Gene expression within cell-sized lipid vesicles. *ChemBioChem* **4**, 1172–1175 (2003).
11. Schoonen, L. & Hest, J. C. M. van. Compartmentalization approaches in soft matter science: from nanoreactor development to organelle mimics. *Adv. Mater.* **28**, 1109–1128 (2016).
12. Martino, C. *et al.* Protein expression, aggregation, and triggered release from polymersomes as artificial cell-like structures. *Angew. Chemie Int. Ed.* **51**, 6416–6420 (2012).
13. Meng, F. & Zhong, Z. Polymersomes spanning from nano- to microscale: advanced vehicles for controlled drug delivery and robust vesicles for virus and cell mimicking. *J. Phys. Chem. Lett.* **2**, 1533–1539 (2011).
14. Chen, I. A. & Walde, P. From self-assembled vesicles to protocells. *Cold Spring Harb. Perspect. Biol.* **2**, a002170 (2010).
15. SS, M. Membrane transport in primitive cells. *Cold Spring Harb. Perspect. Biol.* **2**, (2010).
16. Torre, P., Keating, C. D. & Mansy, S. S. Multiphase water-in-oil emulsion droplets for cell-free transcription–translation. *Langmuir* **30**, 5695–5699 (2014).
17. Fanalista, F. *et al.* Shape and size control of artificial cells for bottom-up biology. *ACS Nano* **13**, 5439–5450 (2019).
18. Li, M., Huang, X. & Mann, S. Spontaneous growth and division in self-reproducing inorganic colloidosomes. *Small* **10**, 3291–3298 (2014).
19. Tamate, R., Ueki, T. & Yoshida, R. Evolved colloidosomes undergoing cell-like autonomous shape oscillations with buckling. *Angew. Chemie Int. Ed.* **55**, 5179–5183 (2016).
20. Brangwynne, C. P., Tompa, P. & Pappu, R. V. Polymer physics of intracellular phase transitions. *Nat. Phys.* **11**, 899–904 (2015).
21. Deshpande, S. *et al.* Spatiotemporal control of coacervate formation within liposomes. *Nat. Commun.* **10**, 1–11 (2019).
22. Morowitz, H. J., Heinz, B. & Deamer, D. W. The chemical logic of a minimum protocell. *Orig. Life Evol. Biosph.* **18**, 281–287 (1988).
23. Luisi, P. L. & Varela, F. J. Self-replicating micelles - A chemical version of a minimal autopoietic system. *Orig. Life Evol. Biosph.* **19**, 633–643 (1989).
24. Luisi, P. L. Toward the engineering of minimal living cells. *Anat. Rec.* **268**, 208–214 (2002).
25. Oberholzer, T., Nierhaus, K. H. & Luisi, P. L. Protein expression in liposomes. *Biochem. Biophys. Res. Commun.* **261**, 238–241 (1999).
26. W, Y. *et al.* Synthesis of functional protein in liposome. *J. Biosci. Bioeng.* **92**, 590–593 (2001).
27. Noireaux, V. & Libchaber, A. A vesicle bioreactor as a step toward an artificial cell assembly. *Proc. Natl. Acad. Sci. U. S. A.* **101**, 17669–17674 (2004).
28. Ishikawa, K., Sato, K., Shima, Y., Urabe, I. & Yomo, T. Expression of a cascading genetic network within liposomes. *FEBS Lett.* **576**, 387–390 (2004).
29. Caschera, F. & Noireaux, V. Synthesis of 2.3 mg/ml of protein with an all *Escherichia coli* cell-free transcription-translation

- system. *Biochimie* **99**, 162–168 (2014).
30. Jewett, M. C. & Forster, A. C. Update on designing and building minimal cells. *Current Opinion in Biotechnology* vol. **21** 697–703 (2010).
 31. Shin, J. & Noireaux, V. Efficient cell-free expression with the endogenous *E. Coli* RNA polymerase and sigma factor 70. *J. Biol. Eng.* **4**, 8 (2010).
 32. Garamella, J., Marshall, R., Rustad, M. & Noireaux, V. The all *E. coli* TX-TL toolbox 2.0: A platform for cell-free synthetic biology. *ACS Synth. Biol.* **5**, 344–355 (2016).
 33. Karim, A. S. & Jewett, M. C. Cell-free synthetic biology for pathway prototyping. in *Methods in Enzymology* vol. 608 31–57 (2018).
 34. Shimizu, Y. *et al.* Cell-free translation reconstituted with purified components. *Nat. Biotechnol.* **19**, 751–755 (2001).
 35. Shimizu, Y., Kanamori, T. & Ueda, T. Protein synthesis by pure translation systems. *Methods* **36**, 299–304 (2005).
 36. Jia, H., Heymann, M., Bernhard, F., Schwill, P. & Kai, L. Cell-free protein synthesis in micro compartments: building a minimal cell from biobricks. *New Biotechnology* vol. **39** 199–205 (2017).
 37. Nourian, Z., Roelofsen, W. & Danelon, C. Triggered gene expression in fed-vesicle microreactors with a multifunctional membrane. *Angew. Chemie Int. Ed.* **51**, 3114–3118 (2012).
 38. Nourian, Z. & Danelon, C. Linking genotype and phenotype in protein synthesizing liposomes with external supply of resources. *ACS Synth. Biol.* **2**, 186–193 (2013).
 39. van Nies, P. *et al.* Unbiased tracking of the progression of mRNA and protein synthesis in bulk and in liposome-confined reactions. *ChemBioChem* **14**, 1963–1966 (2013).
 40. Blanken, D., van Nies, P. & Danelon, C. Quantitative imaging of gene-expressing liposomes reveals rare favorable phenotypes. *Phys. Biol.* **16**, 045002 (2019).
 41. van Nies, P. *et al.* Self-replication of DNA by its encoded proteins in liposome-based synthetic cells. *Nat. Commun.* **9**, 1583 (2018).
 42. Libicher, K., Hornberger, R., Heymann, M. & Mutschler, H. In vitro self-replication and multicistronic expression of large synthetic genomes. *Nat. Commun.* **11**, 1–8 (2020).
 43. Scott, A. *et al.* Cell-free phospholipid biosynthesis by gene-encoded enzymes reconstituted in liposomes. *PLoS One* **11**, e0163058 (2016).
 44. Voegelé, K. *et al.* Towards synthetic cells using peptide-based reaction compartments. *Nat. Commun.* **9**, 1–7 (2018).
 45. Bhattacharya, A., Brea, R. J., Niederholtmeyer, H. & Devaraj, N. K. A minimal biochemical route towards de novo formation of synthetic phospholipid membranes. *Nat. Commun.* **10**, 300 (2019).
 46. Blanken, D., Foschepoth, D., Serrão, A. C. & Danelon, C. Genetically controlled membrane synthesis in liposomes. *Nat. Commun.* **11**, (2020).
 47. Furusato, T. *et al.* De novo synthesis of basal bacterial cell division proteins FtsZ, FtsA, and ZipA inside giant vesicles. *ACS Synth. Biol.* **7**, 953–961 (2018).
 48. Godino, E. *et al.* De novo synthesized Min proteins drive oscillatory liposome deformation and regulate FtsA-FtsZ cytoskeletal patterns. *Nat. Commun.* **10**, 4969 (2019).
 49. Yoshida, A., Kohyama, S., Fujiwara, K., Nishikawa, S. & Doi, N. Regulation of spatiotemporal patterning in artificial cells by a defined protein expression system. *Chem. Sci.* **10**, 11064–11072 (2019).
 50. Godino, E. *et al.* Cell-free biogenesis of bacterial division proto-rings that can constrict liposomes. *Commun. Biol.* **3**, (2020).
 51. Fujii, S., Matsuura, T., Sunami, T., Kazuta, Y. & Yomo, T. In vitro evolution of α -hemolysin using a liposome display. *Proc. Natl. Acad. Sci. U. S. A.* **110**, 16796–16801 (2013).
 52. Lentini, R. *et al.* Integrating artificial with natural cells to translate chemical messages that direct *E. coli* behaviour. *Nat. Commun.* **5**, 4012 (2014).
 53. Booth, M. J., Schild, V. R., Graham, A. D., Olof, S. N. & Bayley, H. Light-activated communication in synthetic tissues. *Sci. Adv.* **2**, e1600056 (2016).
 54. Rampioni, G. *et al.* Synthetic cells produce a quorum sensing chemical signal perceived by: *Pseudomonas aeruginosa*. *Chem. Commun.* **54**, 2090–2093 (2018).
 55. P, van N., AS, C., Z, N. & C, D. Monitoring mRNA and protein levels in bulk and in model vesicle-based artificial cells. *Methods Enzymol.* **550**, 187–214 (2015).
 56. Doerr, A. *et al.* Modelling cell-free RNA and protein synthesis with minimal systems. *Phys. Biol.* **16**, 025001 (2019).
 57. Nourian, Z., Scott, A. & Danelon, C. Toward the assembly of a minimal divisome. *Syst. Synth. Biol.* **8**, 237 (2014).
 58. M, M. *et al.* In vitro contraction of cytokinetic ring depends on myosin II but not on actin dynamics. *Nat. Cell Biol.* **15**, 853–859 (2013).
 59. Litschel, T. & Schwill, P. Reconstitution of contractile actomyosin rings in vesicles. *Nat. Commun.* **2021** **12**, 1–10 (2021).
 60. J, S., IH, L., JH, I. & JH, H. Reverse-topology membrane scission by the ESCRT proteins. *Nat. Rev. Mol. Cell Biol.* **18**, 5–17 (2017).
 61. Booth, A., Marklew, C. J., Ciani, B. & Beales, P. A. In vitro membrane remodeling by ESCRT is regulated by negative feedback from membrane tension. *iScience* **15**, 173 (2019).
 62. Härtel, T. & Schwill, P. ESCRT-III mediated cell division in *Sulfolobus acidocaldarius* – a reconstitution perspective. *Front. Microbiol.* **0**, 257 (2014).
 63. G, T. R. *et al.* The proteasome controls ESCRT-III-mediated cell division in an archaeon. *Science* **369**, (2020).
 64. JS, R., X, J., GP, L. & RA, L. Influenza virus M2 protein mediates ESCRT-independent membrane scission. *Cell* **142**, 902–913 (2010).
 65. Soni, S. P. & Stahelin, R. V. The Ebola virus matrix protein VP40 selectively induces vesiculation from phosphatidylserine-enriched membranes. *J. Biol. Chem.* **289**, 33590 (2014).
 66. Akbari, E. *et al.* Engineering cell surface function with DNA origami. *Adv. Mater.* **29**, (2017).
 67. PS, H., SE, B. & D, B. The coming of age of de novo protein design. *Nature* **537**, 320–327 (2016).
 68. Ulijn, R. V. & Jerala, R. Peptide and protein nanotechnology into the 2020s: beyond biology. *Chem. Soc. Rev.* **47**, 3391–3394 (2018).
 69. R, M., Y, K. & J, E. Excess membrane synthesis drives a primitive mode of cell proliferation. *Cell* **152**, 997–1007 (2013).
 70. Errington, J., Daniel, R. A. & Scheffers, D.-J. Cytokinesis in bacteria. *Microbiol. Mol. Biol. Rev.* **67**, 52–65, table of contents (2003).
 71. Trip, E. N. & Scheffers, D.J. A 1 MDa protein complex containing critical components of the *Escherichia coli* divisome. *Sci. Rep.* **5**, 1–10 (2015).
 72. de Boer, P., Crossley, R. & Rothfield, L. The essential bacterial cell-division protein FtsZ is a GTPase. *Nature* **359**, 254–256 (1992).
 73. RayChaudhuri, D. & Park, J. T. *Escherichia coli* cell-division gene ftsZ encodes a novel GTP-binding protein. *Nature* **359**, 251–254 (1992).
 74. Mukherjee, A., Dai, K. & Lutkenhaus, J. *Escherichia coli* cell division protein FtsZ is a guanine nucleotide binding protein. *Proc. Natl. Acad. Sci. U. S. A.* **90**, 1053–1057 (1993).
 75. Huang, K. H., Durand-Heredia, J. & Janakiraman, A. FtsZ ring stability: Of bundles, tubules, crosslinks, and curves. *Journal of Bacteriology* vol. **195** 1859–1868 (2013).
 76. Bramhill, D. & Thompson, C. M. GTP-dependent polymerization of *Escherichia coli* FtsZ protein to form tubules. *Proc. Natl. Acad. Sci. U. S. A.* **91**, 5813–5817 (1994).
 77. Erickson, H. P., Taylor, D. W., Taylor, K. A. & Bramhill, D. Bacterial cell division protein FtsZ assembles into protofilament sheets and minirings, structural homologs of tubulin polymers. *Proc. Natl. Acad. Sci. U. S. A.* **93**, 519–523 (1996).
 78. Oliva, M. A. *et al.* Assembly of archaeal cell division protein FtsZ and a GTPase-inactive mutant into double-stranded filaments. *J. Biol. Chem.* **278**, 33562–33570 (2003).
 79. Bisson-Filho, A. W. *et al.* Treadmilling by FtsZ filaments drives peptidoglycan synthesis and bacterial cell division. *Science* **355**, 739–743 (2017).
 80. Yang, X. *et al.* GTPase activity-coupled treadmilling of the bacterial tubulin FtsZ organizes septal cell wall synthesis. *Science* **355**, 744–747 (2017).
 81. Peters, P. C., Migocki, M. D., Thoni, C. & Harry, E. J. A new assembly pathway for the cytokinetic Z ring from a dynamic helical structure in vegetatively growing cells of *Bacillus subtilis*. *Mol. Microbiol.* **64**, 487–499 (2007).
 82. Jiménez, M., Martos, A., Vicente, M. & Rivas, G. Reconstitution and organization of *Escherichia coli* proto-ring elements (FtsZ and FtsA) inside giant unilamellar vesicles obtained from bacterial inner membranes. *J. Biol. Chem.* **286**, 11236–11241 (2011).
 83. Vaughan, S., Wickstead, B., Gull, K. & Addinall, S. G. Molecular evolution of FtsZ protein sequences encoded within the genomes of archaea, bacteria, and eukaryota. *J. Mol. Evol.* **58**, 19–39 (2004).

84. Redick, S. D., Stricker, J., Briscoe, G. & Erickson, H. P. Mutants of FtsZ targeting the protofilament interface: Effects on cell division and GTPase activity. *J. Bacteriol.* **187**, 2727–2736 (2005).
85. Gardner, K. A. J. A., Moore, D. A. & Erickson, H. P. The C-terminal linker of *Escherichia coli* FtsZ functions as an intrinsically disordered peptide. *Mol. Microbiol.* **89**, 264–275 (2013).
86. Ma, X. & Margolin, W. Genetic and functional analyses of the conserved C-terminal core domain of *Escherichia coli* FtsZ. *J. Bacteriol.* **181**, 7531–7544 (1999).
87. Mosyak, L. *et al.* The bacterial cell-division protein ZipA and its interaction with an FtsZ fragment revealed by X-ray crystallography. *EMBO J.* **19**, 3179–3191 (2000).
88. Buske, P. J. & Levin, P. A. Extreme C terminus of bacterial cytoskeletal protein FtsZ plays fundamental role in assembly independent of modulatory proteins. *J. Biol. Chem.* **287**, 10945–10957 (2012).
89. Rueda, S., Vicente, M. & Mingorance, J. Concentration and assembly of the division ring proteins FtsZ, FtsA, and ZipA during the *Escherichia coli* cell cycle. *J. Bacteriol.* **185**, 3344–51 (2003).
90. Pichoff, S. & Lutkenhaus, J. Unique and overlapping roles for ZipA and FtsA in septal ring assembly in *Escherichia coli*. *EMBO J.* **21**, 685–93 (2002).
91. Szwedziak, P., Wang, Q., Freund, S. M. & Löwe, J. FtsA forms actin-like protofilaments. *EMBO J.* **31**, 2249–2260 (2012).
92. Krupka, M. *et al.* Role of the FtsA C terminus as a switch for polymerization and membrane association. *MBio* **5**, (2014).
93. Pichoff, S. & Lutkenhaus, J. Identification of a region of FtsA required for interaction with FtsZ. *Mol. Microbiol.* **64**, 1129–1138 (2007).
94. Geissler, B., Elraheb, D. & Margolin, W. A gain-of-function mutation in *ftsA* bypasses the requirement for the essential cell division gene *zipA* in *Escherichia coli*. *Proc. Natl. Acad. Sci.* **100**, 4197–4202 (2003).
95. Gueiros-Filho, F. J. & Losick, R. A widely conserved bacterial cell division protein that promotes assembly of the tubulin-like protein FtsZ. *Genes Dev.* **16**, 2544–2556 (2002).
96. Durand-Heredia, J. M., Yu, H. H., De Carlo, S., Lesser, C. F. & Janakiraman, A. Identification and characterization of ZapC, a stabilizer of the FtsZ ring in *Escherichia coli*. *J. Bacteriol.* **193**, 1405–1413 (2011).
97. Hale, C. A. *et al.* Identification of *Escherichia coli* ZapC (YcbW) as a component of the division apparatus that binds and bundles FtsZ polymers. *J. Bacteriol.* **193**, 1393–1404 (2011).
98. Rowlett, V. W. & Margolin, W. The Min system and other nucleoid-independent regulators of Z ring positioning. *Front. Microbiol.* **6**, 478 (2015).
99. De Boer, P. A. J., Crossley, R. E. & Rothfield, L. I. A division inhibitor and a topological specificity factor coded for by the minicell locus determine proper placement of the division septum in *E. coli*. *Cell* vol. **56** (1989).
100. Hu, Z., Mukherjee, A., Pichoff, S. & Lutkenhaus, J. The MinC component of the division site selection system in *Escherichia coli* interacts with FtsZ to prevent polymerization. *Proc. Natl. Acad. Sci. U. S. A.* **96**, 14819–24 (1999).
101. Hu, Z., Saez, C. & Lutkenhaus, J. Recruitment of MinC, an inhibitor of Z-ring formation, to the membrane in *Escherichia coli*: role of MinD and MinE. *J. Bacteriol.* **185**, 196–203 (2003).
102. Raskin, D. M. & de Boer, P. A. MinDE-dependent pole-to-pole oscillation of division inhibitor MinC in *Escherichia coli*. *J. Bacteriol.* **181**, 6419–24 (1999).
103. Hale, C. A., Meinhardt, H. & de Boer, P. A. Dynamic localization cycle of the cell division regulator MinE in *Escherichia coli*. *EMBO J.* **20**, 1563–72 (2001).
104. Kruse, K. A dynamic model for determining the middle of *Escherichia coli*. *Biophys. J.* **82**, 618–27 (2002).
105. Raskin, D. M. & de Boer, P. A. Rapid pole-to-pole oscillation of a protein required for directing division to the middle of *Escherichia coli*. *Proc. Natl. Acad. Sci. U. S. A.* **96**, 4971–6 (1999).
106. de Boer, P. A. J., Crossley, R. E. & Rothfield, L. I. A division inhibitor and a topological specificity factor coded for by the minicell locus determine proper placement of the division septum in *E. coli*. *Cell* **56**, 641–649 (1989).
107. de Boer, P. A., Crossley, R. E., Hand, A. R. & Rothfield, L. I. The MinD protein is a membrane ATPase required for the correct placement of the *Escherichia coli* division site. *EMBO J.* **10**, 4371–80 (1991).
108. Wu, W., Park, K. T., Holyoak, T. & Lutkenhaus, J. Determination of the structure of the MinD-ATP complex reveals the orientation of MinD on the membrane and the relative location of the binding sites for MinE and MinC. *Mol. Microbiol.* **79**, 1515–1528 (2011).
109. Mileykovskaya, E. *et al.* Effects of phospholipid composition on MinD-membrane interactions in vitro and in vivo. *J. Biol. Chem.* **278**, 22193–8 (2003).
110. Lackner, L. L., Raskin, D. M. & de Boer, P. A. J. ATP-dependent interactions between *Escherichia coli* Min proteins and the phospholipid membrane in vitro. *J. Bacteriol.* **185**, 735–49 (2003).
111. Shiomi, D. & Margolin, W. The C-terminal domain of MinC inhibits assembly of the Z ring in *Escherichia coli*. *J. Bacteriol.* **189**, 236–243 (2007).
112. Park, K. T. *et al.* The min oscillator uses MinD-dependent conformational changes in MinE to spatially regulate cytokinesis. *Cell* **146**, 396–407 (2011).
113. Park, K. T., Wu, W., Lovell, S. & Lutkenhaus, J. Mechanism of the asymmetric activation of the MinD ATPase by MinE. *Mol. Microbiol.* **85**, 271–281 (2012).
114. Loose, M., Fischer-Friedrich, E., Herold, C., Kruse, K. & Schwille, P. Min protein patterns emerge from rapid rebinding and membrane interaction of MinE. *Nat. Struct. Mol. Biol.* **18**, 577–583 (2011).
115. Marston, A. L. & Errington, J. Selection of the midcell division site in *Bacillus subtilis* through MinD-dependent polar localization and activation of MinC. *Mol. Microbiol.* **33**, 84–96 (1999).
116. Hu, Z. & Lutkenhaus, J. Topological regulation of cell division in *E. coli*. Spatiotemporal oscillation of MinD requires stimulation of its ATPase by MinE and phospholipid. *Mol. Cell* **7**, 1337–43 (2001).
117. Rowland, S. L. *et al.* Membrane redistribution of the *Escherichia coli* MinD protein induced by MinE. *J. Bacteriol.* **182**, 613–619 (2000).
118. Mukherjee, A. & Lutkenhaus, J. Analysis of FtsZ assembly by light scattering and determination of the role of divalent metal cations. *J. Bacteriol.* **181**, 823–832 (1999).
119. Mukherjee, A. & Lutkenhaus, J. Guanine nucleotide-dependent assembly of FtsZ into filaments. *J. Bacteriol.* **176**, 2754–8 (1994).
120. Loose, M. & Mitchison, T. J. The bacterial cell division proteins FtsA and FtsZ self-organize into dynamic cytoskeletal patterns. *Nat. Cell Biol.* **16**, 38–46 (2014).
121. Mateos-Gil, P. *et al.* FtsZ polymers bound to lipid bilayers through ZipA form dynamic two dimensional networks. *Biochim. Biophys. Acta - Biomembr.* **1818**, 806–813 (2012).
122. Ramirez-Diaz, D. A. *et al.* Treadmilling analysis reveals new insights into dynamic FtsZ ring architecture. *PLOS Biol.* **16**, e2004845 (2018).
123. Osawa, M., Anderson, D. E. & Erickson, H. P. Reconstitution of contractile FtsZ rings in liposomes. *Science*. **320**, 792–794 (2008).
124. Cabré, E. J. *et al.* Bacterial division proteins FtsZ and ZipA induce vesicle shrinkage and cell membrane invagination. *J. Biol. Chem.* **288**, 26625–34 (2013).
125. Osawa, M. & Erickson, H. P. Liposome division by a simple bacterial division machinery. *Proc. Natl. Acad. Sci. U. S. A.* **110**, 11000–4 (2013).
126. Loose, M., Fischer-Friedrich, E., Ries, J., Kruse, K. & Schwille, P. Spatial regulators for bacterial cell division self-organize into surface waves in vitro. *Science*. **320**, 789–792 (2008).
127. Vecchiarelli, A. G., Li, M., Mizuuchi, M. & Mizuuchi, K. Differential affinities of MinD and MinE to anionic phospholipid influence Min patterning dynamics in vitro. *Mol. Microbiol.* **93**, 453–463 (2014).
128. Zieske, K. & Schwille, P. Reconstitution of self-organizing protein gradients as spatial cues in cell-free systems. *Elife* **3**, (2014).
129. Caspi, Y. & Dekker, C. Mapping out Min protein patterns in fully confined fluidic chambers. *Elife* **5**, (2016).
130. Martos, A., Petrasek, Z. & Schwille, P. Propagation of MinCDE waves on free-standing membranes. *Environ. Microbiol.* **15**, 3319–3326 (2013).
131. Martos, A. *et al.* FtsZ polymers tethered to the membrane by ZipA are susceptible to spatial regulation by min waves. *Biophys. J.* **108**, 2371–2383 (2015).
132. Ramm, B. *et al.* The MinDE system is a generic spatial cue for membrane protein distribution in vitro. *Nat. Commun.* **9**, 3942 (2018).
133. Schweizer, J. *et al.* Geometry sensing by self-organized protein patterns. *Proc. Natl. Acad. Sci. U. S. A.* **109**, 15283–15288 (2012).
134. Zieske, K., Chwastek, G. & Schwille, P. Protein patterns and oscillations on lipid monolayers and in microdroplets. *Angew. Chemie* **128**, 13653–13657 (2016).

135. Litschel, T., Ramm, B., Maas, R., Heymann, M. & Schwille, P. Beating vesicles: Encapsulated protein oscillations cause dynamic membrane deformations. *Angew. Chemie Int. Ed.* **57**, 16286-16290 (2018).
136. Ramm, B. *et al.* The MinDE system is a generic spatial cue for membrane protein distribution in vitro. *Nat. Commun.* **9**, 1–16 (2018).
137. Shih, Y. L. *et al.* Active transport of membrane components by self-organization of the Min proteins. *Biophys. J.* **116**, 1469–1482 (2019).
138. Rico, A. I., Krupka, M. & Vicente, M. In the beginning, *Escherichia coli* assembled the proto-ring: an initial phase of division. *J. Biol. Chem.* **288**, 20830–20836 (2013).
139. Li, Z., Trimble, M. J., Brun, Y. V & Jensen, G. J. The structure of FtsZ filaments in vivo suggests a force-generating role in cell division. *EMBO J.* **26**, 4694 (2007).
140. Lan, G., Wolgemuth, C. W. & Sun, S. X. Z-ring force and cell shape during division in rod-like bacteria. *Proc. Natl. Acad. Sci. U. S. A.* **104**, 16110 (2007).
141. G, L., BR, D., TM, D., D, W. & SX, S. Condensation of FtsZ filaments can drive bacterial cell division. *Proc. Natl. Acad. Sci. U. S. A.* **106**, 121–126 (2009).
142. Whitley, K. D. *et al.* FtsZ treadmilling is essential for Z-ring condensation and septal constriction initiation in *Bacillus subtilis* cell division. *Nat. Commun.* **2021 121 12**, 1–13 (2021).
143. Deng, Y., Sun, M. & Shaevitz, J. W. Direct measurement of cell wall stress stiffening and turgor pressure in live bacterial cells. *Phys. Rev. Lett.* **107**, 158101 (2011).
144. Xiao, J. & Goley, E. D. Redefining the roles of the FtsZ-ring in bacterial cytokinesis. *Curr. Opin. Microbiol.* **34**, 90 (2016).
145. Osawa, M. & Erickson, H. P. Turgor pressure and possible constriction mechanisms in bacterial division. *Front. Microbiol.* **0**, 111 (2018).
146. Coltharp, C., Buss, J., Plumer, T. M. & Xiao, J. Defining the rate-limiting processes of bacterial cytokinesis. *Proc. Natl. Acad. Sci.* **113**, E1044–E1053 (2016).
147. B, S. *et al.* Coordinated disassembly of the divisome complex in *Escherichia coli*. *Mol. Microbiol.* **101**, 425–438 (2016).
148. Söderström, B. *et al.* Disassembly of the divisome in *Escherichia coli*: Evidence that FtsZ dissociates before compartmentalization. *Mol. Microbiol.* **92**, 1 (2014).
149. B, G. & A, S. Origin of contractile force during cell division of bacteria. *Phys. Rev. Lett.* **101**, (2008).
150. Surovtsev, I. V., Morgan, J. J. & Lindahl, P. A. Kinetic modeling of the assembly, dynamic steady state, and contraction of the ftsz ring in prokaryotic cytokinesis. *PLOS Comput. Biol.* **4**, e1000102 (2008).

De novo synthesized Min proteins drive oscillatory liposome deformation and regulate FtsA-FtsZ cytoskeletal patterns

Elisa Godino, Jonás Noguera López, David Foschepoth, Céline Cleij, Anne Doerr, Clara Ferrer Castellà & Christophe Danelon

The Min biochemical network regulates bacterial cell division and is a prototypical example of self-organizing molecular systems. Cell-free assays relying on purified proteins have shown that MinE and MinD self-organize into surface waves and oscillatory patterns. In the context of developing a synthetic cell from elementary biological modules, harnessing Min oscillations might allow us to implement higher-order cellular functions. To convey hereditary information, the Min system must be encoded in a DNA molecule that can be copied, transcribed, and translated. Here, the MinD and MinE proteins are de novo synthesized from their genes inside liposomes. Dynamic protein patterns and accompanying liposome shape deformation are observed. When integrated with the cytoskeletal proteins FtsA and FtsZ, the synthetic Min system is able to dynamically regulate FtsZ patterns. By enabling genetic control over Min protein self-organization and membrane remodeling, our methodology offers unique opportunities towards directed evolution of bacterial division processes in vitro.

Essentially as published: Godino, E. *et al.* De novo synthesized Min proteins drive oscillatory liposome deformation and regulate FtsA-FtsZ cytoskeletal patterns. *Nat. Commun.* **10**, 4969 (2019).

Introduction

The construction of a synthetic cell from basic molecular components has become an engaging frontier in bottom-up synthetic biology¹⁻⁴. Creating a synthetic system endowed with life-like features will arguably help us understand the fundamental principles of biological cells, while providing a test bed for the engineering of biotechnologically or medically relevant functionalities. Such a constructive approach towards an elementary cell entails the collaborative operation of essential cellular subsystems based on the extant molecular hardware comprising DNA, RNAs, proteins and lipids. Like its natural counterpart, synthetic cells must be able to self-reproduce to propagate information and develop new functionalities, a process that implies replication of the genetic material, biosynthesis of the basal constituents and division of the compartment.

One possible strategy to divide synthetic cell models is to consider the canonical division mechanism of prokaryotes. In rod-shaped bacteria like *Escherichia coli*, division is carried out by a multiprotein complex, the divisome, and is tightly regulated in time and space by associated mechanisms⁵. FtsZ, the core component of the divisome, polymerizes and assembles into a contractile ring-like structure, called the Z-ring⁶. Symmetrical cell division is ensured by restricting the formation of the Z-ring at mid-cell through different inhibitory mechanisms of FtsZ polymerization. In *E. coli* this spatial organization is primarily achieved by the Min system, which consists of three proteins encoded by the *minB* operon: MinC, MinD and MinE⁷. The Min proteins self-organize at the inner surface of the cytoplasmic membrane and dynamically oscillate between the two cell poles⁸⁻¹¹. These oscillations are driven by a reaction-diffusion mechanism involving MinD and MinE, nucleotide exchange and transitions between cytoplasmic and membrane-bound states¹². MinC, an inhibitor of FtsZ polymerization, passively travels along the dynamic MinDE protein pattern. The oscillations impose a time-averaged intracellular gradient of MinC concentration that is minimal in the middle of the cell, where FtsZ polymerizes as an early stage of divisome maturation¹³⁻¹⁵.

The in vitro reconstitution of *E. coli* Min protein oscillations has been the focus of many studies since the first report by Loose et al.¹⁶. Using supported lipid bilayers (SLBs) as a model membrane system, planar waves and rotating spirals of purified Min proteins were observed^{16,17}. Key factors influencing the wave parameters were identified, such as the ratio between MinD and MinE levels¹⁶, the flow of the solution¹⁷, the phospholipid composition and the buffer composition¹⁷. Going beyond planar membranes, various oscillating patterns have been observed in 3D cell-shaped polydimethylsiloxane containers^{18,19}, as well as in fully enclosed biological compartments like microdroplets²⁰ and giant liposomes²¹. Noteworthy, attempts to encapsulate an active Min system inside liposomes have long faced technical challenges and successful experiments have only been reported recently²¹. A variety of dynamical behaviors has been evidenced, which includes pulsing, circling and pole-to-pole oscillations^{20,21}. Remarkably, in some liposomes and under hypertonic conditions, Min protein

oscillations were accompanied by large scale membrane deformation²¹.

While these experiments unveiled some of the critical parameters governing Min oscillations and, in the latter study, beautifully demonstrated the interplay between membrane-assisted protein self-organization and the mechanical properties of the liposome compartment, it remains unknown whether Min oscillations can functionally be encoded in a DNA-based synthetic cell. Unlike earlier efforts that exclusively relied on purified Min proteins, the present work is motivated by the *de novo* synthesis and functional self-organization of the Min system inside liposomes. In analogy with information storage and transfer in biology, we believe that in-liposome protein production from a DNA template is a viable route to build an autonomous, self-replicating synthetic cell.

Herein, we reconstitute oscillatory patterns of cell-free expressed *E. coli* MinD and MinE proteins. The PURE (for Protein synthesis Using Recombinant Elements) system²² was chosen for its low protease and nuclease activity, and for the well-defined nature of its constituents. Unlike whole cell extracts, the PURE system is devoted to gene expression and is devoid of endogenous proteins (here Min and Min-interacting partners) that may interfere with the cellular function to be reconstituted. After optimizing the conditions for in vitro gene expression with the PURE system²² and for Min protein activity on SLBs, encapsulation inside cell-sized liposomes is successfully realized. Distinct modes of oscillations are reproduced, and extensive membrane deformation coupled to internal Min system dynamics is demonstrated. Cytoskeletal patterns of FtsZ and its natural membrane-anchoring protein FtsA which is also synthesized in the PURE system are reconstituted on SLBs, and their spatial regulation by cell-free expressed MinDE(C) is investigated.

Results

Cell-free expression of Min proteins with the PURE system

We first verified that cell-free expression of the *E. coli minC*, *minD* and *minE* genes leads to full-length proteins. PURE_{flex}2.0 was chosen among the different variants of the commercially available PURE system for its relatively high yield and prolonged expression lifetime in bulk²³ and inside liposomes²⁴. The MinC/D/E proteins were synthesized from their respective DNA template and the translation products were first analyzed by SDS-PAGE. Visualization of synthesized proteins was achieved by co-translational incorporation of fluorescently labelled lysine residues and fluorescence gel imaging (Fig. 1a). Expression of MinC (~25 kDa), MinD (~29 kDa) and MinE (~10 kDa) proteins was confirmed and a main band of expected molecular weight was detected in each case, as well as in MinD/E co-expression reactions (Fig. 1b). To obtain quantitative insights about the amount of synthesized proteins, pre-ran PURE system samples were trypsin-digested (Supplementary Fig. 1) and analyzed by liquid chromatography-coupled mass spectrometry (LC-MS). Specific proteolytic peptides covering different locations from the N- to C-terminal parts were identified in both MinD

and MinE proteins, whereas only two MinC-specific peptides were found (Supplementary Table 1 and Supplementary Fig. 2). Their abundance was quantified using purified proteins of known concentrations (Supplementary Table 2 and Supplementary Fig. 3) and plotted as a function of their position along the protein primary sequence (Fig. 1c and Supplementary Fig. 4). Protein concentration was assessed by considering the most C-terminal peptide. Values of $19 \pm 7 \mu\text{M}$ and $5 \pm 4 \mu\text{M}$ (mean \pm standard deviation, five biological replicates) were obtained for MinD and MinE, respectively, when the two genes are co-expressed for 3 h. Such concentrations are sufficient to generate dynamic patterns onto a lipid membrane¹⁶. An estimation of MinC concentration is $\sim 2.5 \mu\text{M}$ after 3 h, but no peptide localized close to the C-terminal part could clearly be identified. Kinetics of MinD/E production reveals that most proteins are synthesized within ~ 4 h co-expression (Fig. 1d). Estimations of the apparent translation rate are $0.09 \pm 0.05 \mu\text{M min}^{-1}$ (MinD) and $0.03 \pm 0.02 \mu\text{M min}^{-1}$ (MinE) (mean \pm standard deviation of fitted parameter values, three biological replicates), and the expression lifespans, defined as the time points at which protein production stops, are 307 ± 63 min (MinD) and 194 ± 38 min (MinE). These values are consistent with previous gene expression kinetics using the PURE system²³. The concentration ratio of synthesized MinE and MinD proteins decreases during the first hour of expression and stabilizes to values $[\text{MinE}]/[\text{MinD}] \sim 0.3$ between 1 h and 5 h reaction (Supplementary Fig. 5).

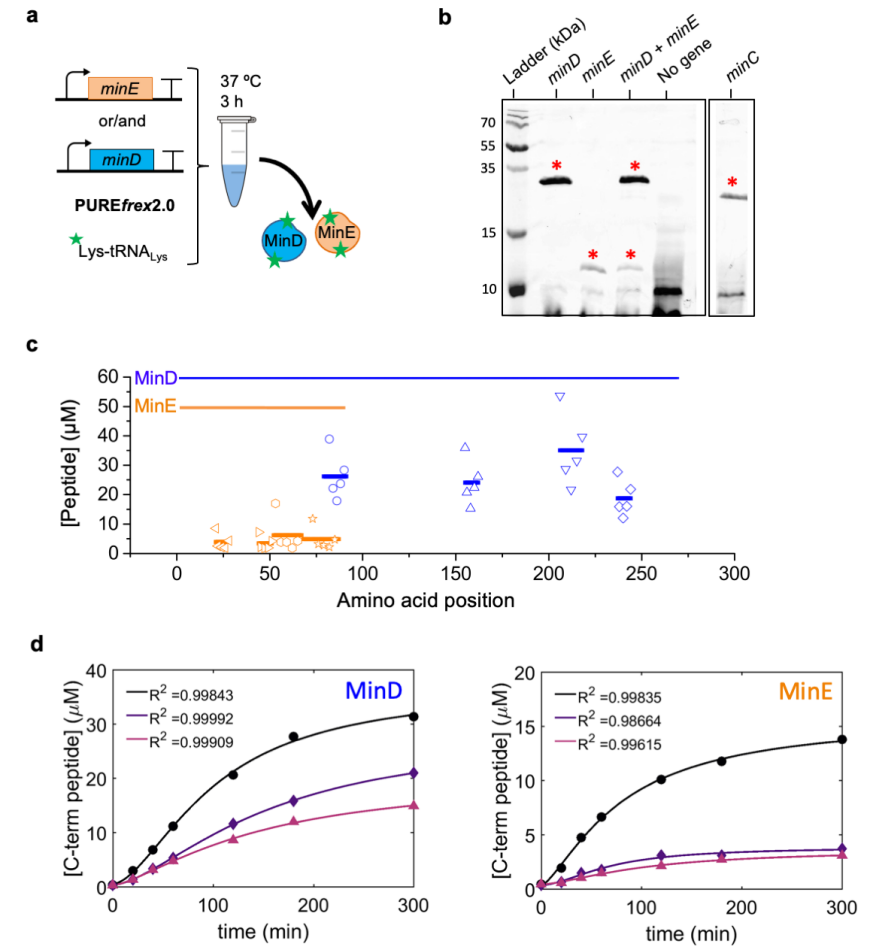


Figure 1: Quantification of cell-free gene-expressed MinE and MinD proteins. **a**, Schematic of co-translational labeling of MinD and MinE proteins in the PURE system. tRNA_{Lys} preloaded with a BODIPY-conjugated lysine (GreenLys) is supplemented in a PUREfrex2.0 reaction. Same strategy was applied with MinC. **b**, Translation products were analyzed by fluorescence imaging of a 18% polyacrylamide gel. The bands depicted with an upper red star correspond to the full-length protein with expected molecular weight. In a control experiment with no genes added, a smear background of GreenLys is visible that is distinct from the gene-specific bands. **c**, Quantitative LC-MS analysis of MinD and MinE proteolytic peptides and their position along the primary sequence of the proteins. The MinD- and MinE-annotated lines depict the full-length sequences. The amino acid sequence of the different peptides is reported in Supplementary Table 2. Peptide concentrations represent averaged values (displayed as segments whose length matches with the length of the corresponding peptide) over five biological repeats (markers represent individual measurements), of which two included three technical replicates. **d**, Concentration of the most C-terminal peptide of MinD (AYADTVER) and of MinE (DGDISILEL-NVTLPAAEELK) as a function of the expression time course. Symbols represent data from three independent experiments. The solid lines are fits to a mathematical model for gene expression (Equation (1)).

Synthetic MinDE self-organize into dynamic patterns

In the course of our investigations to optimize activity assays on SLBs with cell-free expressed MinDE proteins, we empirically discovered three critical conditions to reconstitute surface waves. First, PURE_{flex}2.0 must be supplemented with adenosine triphosphate (ATP, additional 2.5 mM). Presumably, the ATP-dependent MinD dimerization²⁵ competes with other ATP-consuming processes, e.g. transcription and amino acylation, which reduce the amount of ATP despite the energy recycling enzymatic set present in the PURE system. Second, although the *minE* gene is directly amplified from the *E. coli* genome, we found that sequence optimization for averaged codon usage in *E. coli* genes, GC content and avoidance of 5' RNA secondary structure was necessary. This result may account for the different conditions and limiting reaction steps between cell-free and in vivo gene expression²³. Third, addition of a DnaK mix (a cocktail of highly purified chaperone proteins) during expression enhances protein activity. Under these optimized conditions (Fig. 2a), incubation of co-synthesized MinD and MinE proteins onto an SLB led to the formation of planar waves, rotating spirals and standing waves (Fig. 2b, Supplementary Movie 1), three typical behaviors of the Min system¹⁶. Trace amount of purified eGFP-MinD (100 nM) was employed to visualize Min dynamics by spinning disc fluorescence microscopy without directly contributing to wave generation.

Next, we asked whether Min dynamic patterns could be monitored concurrently to protein production directly on top of the membrane (Fig. 2c). Our gene expression-based approach allowed us to observe in real-time the evolution of the surface waves as a function of MinD/E protein concentrations, providing a decisive advantage over SLB assays conducted exclusively with purified Min proteins. After 1 h expression, the fluorescence intensity was high enough to detect planar waves. As time progresses, the waves become more discernable but their dynamic properties remain constant up to 4 h measurements (Fig. 2d) despite an increase of both MinD and MinE concentrations during this time interval (Fig. 1d). Calculated wavelength is $43 \pm 7 \mu\text{m}$ and wave velocity is $0.49 \pm 0.06 \mu\text{m s}^{-1}$ (mean \pm standard deviation, 26 data points from two biological replicates) (Supplementary Fig. 6). The robustness of Min dynamics over absolute protein concentrations may be explained by the relatively steady ratio of MinE and MinD proteins after 1 h expression (Supplementary Fig. 5). Interestingly, changes between two types of dynamic patterns – from traveling to standing waves – could be tracked (Fig. 2d, Supplementary Movie 2). Standing waves of expressed MinD/E have a characteristic oscillation time of $47 \pm 4 \text{ s}$ (mean \pm standard deviation, 30 data points from two biological replicates). Because such transitions were only observed at long time points ($>3 \text{ h}$), we hypothesize that a possible cause could be a decrease of ATP concentration. In addition, we performed SLB assays using $1 \mu\text{M}$ of purified MinD and MinE proteins mixed in a PURE system background. Regular standing and traveling waves with similar properties as synthetic Min patterns were observed (Supplementary Fig. 7 and Supplementary Movie 3). This result indicates that the PURE system itself does not significantly influence Min dynamic

properties. Reconstituted surface waves with purified Min proteins in minimal buffers display a wavelength between 25 and 90 μm and a velocity between 0.1 and 0.4 $\mu\text{m s}^{-1}$ ^{16,17}.

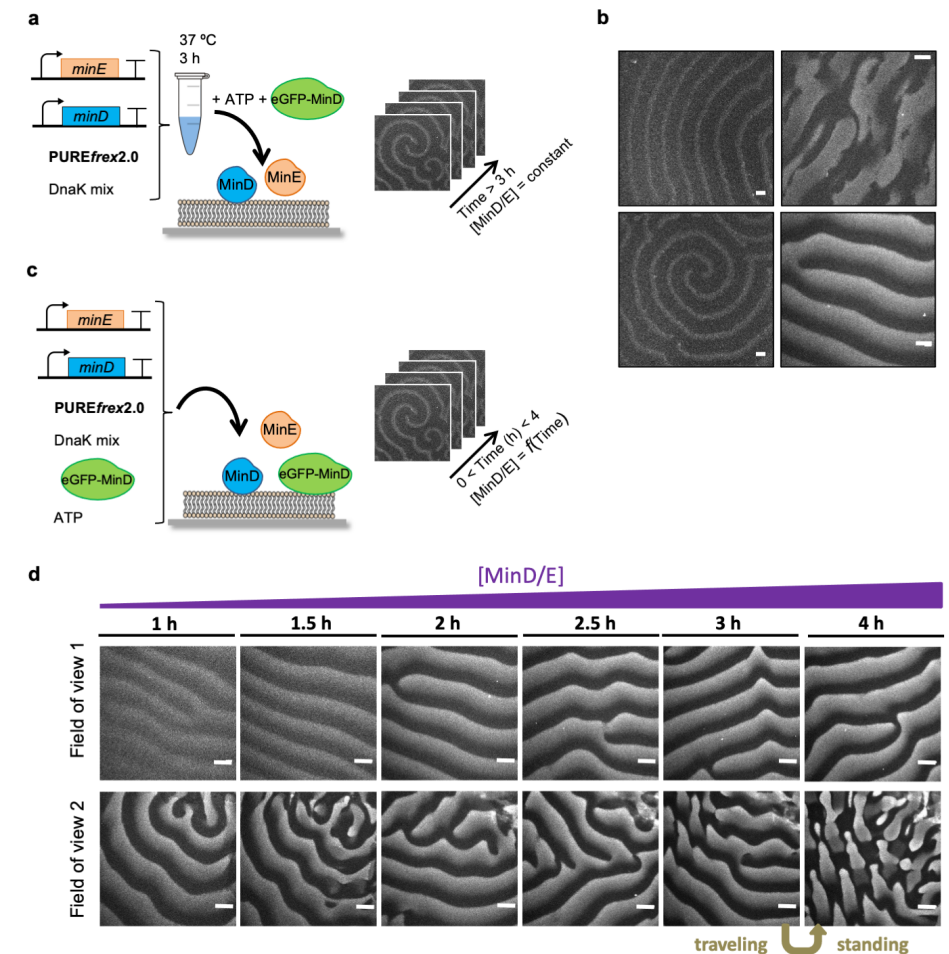


Figure 2: Supported membrane assays with *de novo* synthesized MinD and MinE proteins. **a**, Schematic of the experimental workflow for end-point expression assays. Both *minD* and *minE* genes are expressed in a PURE system reaction in the presence of DnaK chaperone mix for 3 h. The solution is then supplemented with 2.5 mM ATP and a trace amount of purified eGFP-MinD (100 nM) before transfer on top of a supported lipid bilayer. **b**, Fluorescence microscopy images of representative types of MinDE dynamic patterns. Videos can be found in Supplementary Movie 1. Scale bars are 20 μm . **c**, Schematic illustration of the in situ MinDE co-expression and self-organization on an SLB. **d**, Several SLB fields of view were imaged at different points during in situ co-expression of MinD and MinE proteins. Corresponding videos are shown in Supplementary Movie 2. Scale bars are 20 μm .

In-liposome synthesized MinDE proteins oscillate

After having established a working protocol to produce an active MinDE system in SLB assays, we sought to recapitulate gene expression and Min oscillations within liposomes. Liposomes were prepared using glass bead-assisted lipid film hydration^{24,26}. Compared to microfluidic- and droplet-transfer-based approaches, our method presents the advantage of not containing organic solvent. Moreover, the produced liposomes are smaller (diameter ranging from 1 to 20 μm with an average size around 4 μm), which mimics more closely the size of a bacterial cell than conventional $>20 \mu\text{m}$ giant vesicles. Two lipid compositions were used: a binary lipid mixture with DOPC and DOPG ($\sim 3:1$ molar ratio) called PC/PG that is commonly used in liposome research and Min reconstitution assays, or a more complex mixture of DOPC, DOPG, DOPE and C18:1 cardiolipin ($\sim 5:3.6:1.2:0.2$ molar ratio) called PC/PG/PE/CL which emulates more closely the *E. coli* lipid composition. Both types of membranes were doped with biotin-PEG- and TexasRed-conjugated lipids. Liposomes enclose PURE_{flex}2.0 along with the *minD* and *minE* genes (or one of them in negative controls), DnaK mix, extra ATP and 1 μM purified eGFP-MinC as a fluorescent reporter of the Min oscillations (Fig. 3a). We initially opted for eGFP-MinC in place of eGFP-MinD to avoid interference with lipid film swelling and staining of the outer surface of the liposome membrane. Time-lapse imaging of liposomes at (or close to) their equatorial plane revealed dynamic re-localization of eGFP-MinC between the membrane and the lumen, giving rise to different types of oscillations about 1.5 h after triggering gene expression (earlier time points have not been considered) (Fig. 3b,c). Consistent with previous observations with purified MinDE proteins²¹, in situ synthesized Min proteins undergo three prevalent behaviors: pulsing, pole-to-pole and circling oscillations, with pulsing being the most frequently observed one (Fig. 3, Supplementary Movies 4 and 5). Liposomes exhibiting Min waving patterns have a diameter spanning the range of 3.5 to 20 μm and no clear correlation between liposome size and Min pulsing frequency was measured (Fig. 3e).

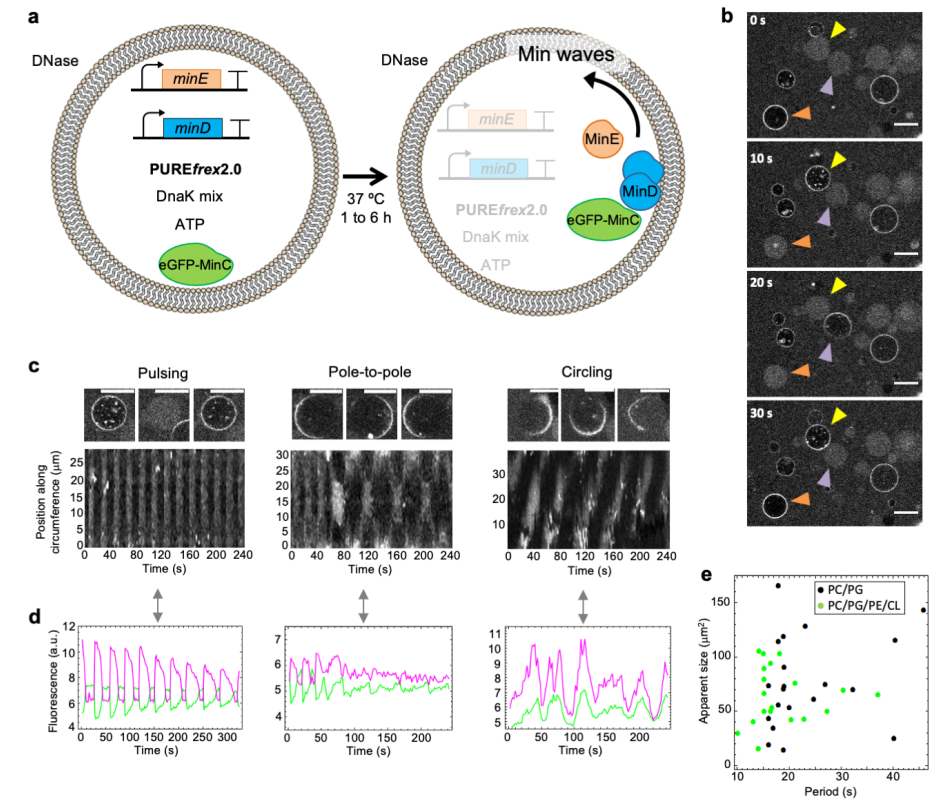


Figure 3: In-liposome production and self-organization of MinDE proteins. **a**, Schematic illustration of liposome reconstitution assays. The *minD* and *minE* genes are co-expressed within phospholipid vesicles in the presence of DnaK chaperones, extra ATP and 1 μM of purified eGFP-MinC to report for MinDE dynamics. **b**, Time series images showing liposomes (PC/PG composition) exhibiting periodic redistribution of eGFP-MinC between the membrane and the lumen (Supplementary Movie 4). Colored arrowheads point to Min-active liposomes. Other liposomes show stable fluorescence signal at the membrane or in the lumen throughout the image sequence. Scale bars are 10 μm . **c**, Zoomed-in images taken at three different time points (from left to right) of liposomes (PC/PG composition) exhibiting the pulsing, pole-to-pole or circling modes of oscillations (Supplementary Movie 5). The corresponding kymographs are displayed below. Scale bars are 10 μm . **d**, Time traces of the fluorescence intensity of eGFP-MinC at the membrane (magenta) and in the lumen (green) for the three liposomes shown in (c). a.u., arbitrary unit. **e**, The effects of lipid composition and vesicle size have been analyzed for liposomes with a Min-pulsing behavior. Both PC/PG (black dots) and PC/PG/PE/CL (green dots) liposomes show a cross-section area (averaged over the different time point images) that is not obviously correlated with the period of oscillations. Twenty liposomes of each composition have been analyzed.

Some liposomes exhibit more complex phenotypes, such as Min waves switching from one oscillation mode to another or to an uncategorized type, halted oscillations and circling waves that change directionality (Fig. 4a,b and Supplementary Movie 6). The oscillation features can also change over time (Fig. 4c,d), or the membrane signal attenuates while the lumen signal correspondingly increases (Supplementary Fig. 8). All dynamic behaviors described above are unambiguously attributed to successful expression of both functional MinD and MinE, since production of only one of the two proteins fails to reproduce oscillations (Supplementary Movie 7). Sole expression of the *MinD* gene leads to stable recruitment of eGFP-MinC to the membrane up to at least 5 h incubation. In contrast, individual expression of MinE results in exclusive localization of eGFP-MinC in the lumen, as expected given that the two proteins do not directly interact.

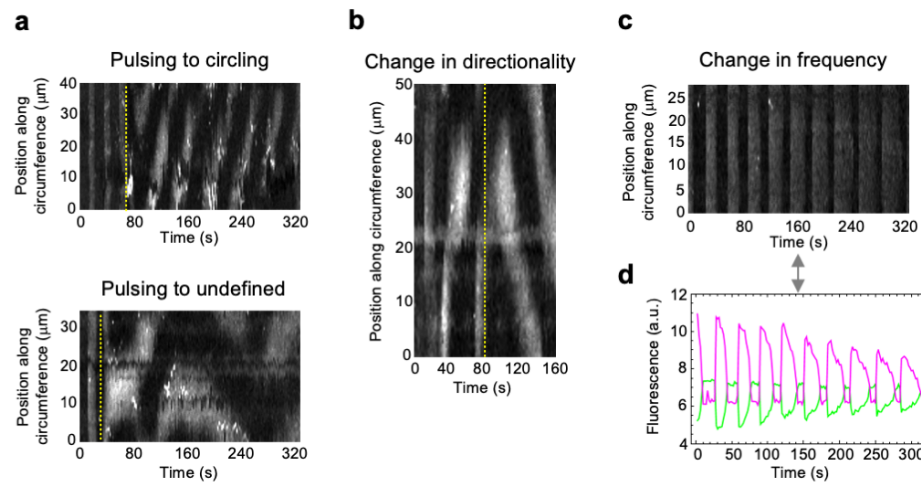


Figure 4: Transitions of Min oscillating patterns in liposomes. **a**, Kymographs of liposomes exhibiting transitions from the pulsing oscillation mode to a different behavior. **b**, Kymograph of a liposome showing circling Min dynamics that changes directionality. In **a** and **b**, the vertical dotted lines depict the transition between two types of oscillations. **c**, Kymograph of a liposome with pulsing Min waves whose peak sharpness, frequency and amplitude decrease over time. **d**, Fluorescence time traces of the eGFP-MinC signal localized at the membrane (magenta) or in the lumen (green). The same liposome as in **c** was analyzed. All corresponding videos are shown in Supplementary Movie 6.

Moreover, no major differences were observed between the two lipid compositions, both in terms of the oscillation modes and period of Min pulsing (Fig. 3e). It is known that MinD has a higher affinity for anionic lipids²⁷. In vitro, it was found that changing the fraction of anionic lipids affects the retention time of MinD and MinE, leading to spatiotemporal modifications in Min patterning¹⁷. Our results indicate that Min self-organization is robust to the difference in surface charge density between the PC/PG and PC/PG/PE/CL membranes.

In some liposomes, Min oscillations could be monitored for up to 6 h. The time-dependent loss of eGFP-MinC signal at the membrane, or more generally the damping of Min oscillations may indicate the release of MinD as ATP is being consumed, among other possible scenarios. Indeed, ATP depletion would weaken the ability of MinD to dimerize and bind to the membrane. The fact that not all liposomes exhibit dynamic waves, and potentially also the fact that different types of oscillations are observed, may be explained by different absolute or stoichiometric amounts of synthesized MinD and MinE proteins. Such a functional heterogeneity has been reported for other expressed proteins and is intrinsic to the stochastic partitioning of the many reactants during liposome formation^{24,28}. Moreover, we noticed that the success rate of these experiments critically depends on the purity of the DNA template. Although PCR products from the same parental plasmid are prepared with the same reagents according to the same protocol, the number of liposomes displaying Min waves can significantly vary between experiments.

Notably, reconstitution of the complete MinCDE system inside liposomes had not been realized so far. The absolute amount of purified eGFP-MinC (1 μM) is relatively high compared to the concentration used in other studies²⁹. Yet, if one assumes similar amounts of synthesized MinD and MinE in liposomes and in bulk reactions, the ratios of [MinC]/[MinE] and [MinC]/[MinD] are ~0.3 and ~0.1, respectively, which is comparable to previous reports³⁰. We performed control experiments with a lower concentration of purified eGFP-MinC (0.4 μM), or with 0.2 μM of eGFP-MinD (no MinC). In both conditions, we were able to observe pulsing Min behaviors (Supplementary Fig. 9). However, long time-lapse imaging was challenging due to the low signal intensity.

Autonomously deforming liposomes by synthetic MinDE proteins

In a subset of liposomes exhibiting waves, MinDE oscillations are accompanied by membrane remodeling and liposome shape transformation (Fig. 5a and Supplementary Movie 8). When MinD (as deduced from the eGFP-MinC signal) is recruited to the membrane, initially spherical liposomes can elongate and subsequently resume to a sphere as MinD redistributes into the lumen. A similar behavior has recently been reported for deflated vesicles in hypertonic stress conditions²¹. In contrast, no osmotic pressure was externally imposed in the present assay. Although we cannot rule out an osmolarity mismatch between the interior and exterior of some liposomes due to anomalous encapsulation efficiency, it is clear from the apparent sphericity in the non-membrane-bound state of Min proteins that shape deformation is also possible in (near-)isotonic conditions. Of note, when only MinD is expressed, its binding to the membrane (as probed with eGFP-MinC) does not change liposome morphology (Supplementary Movie 7). This observation suggests that transient recruitment of MinE to the membrane actually contributes to liposome deformation.

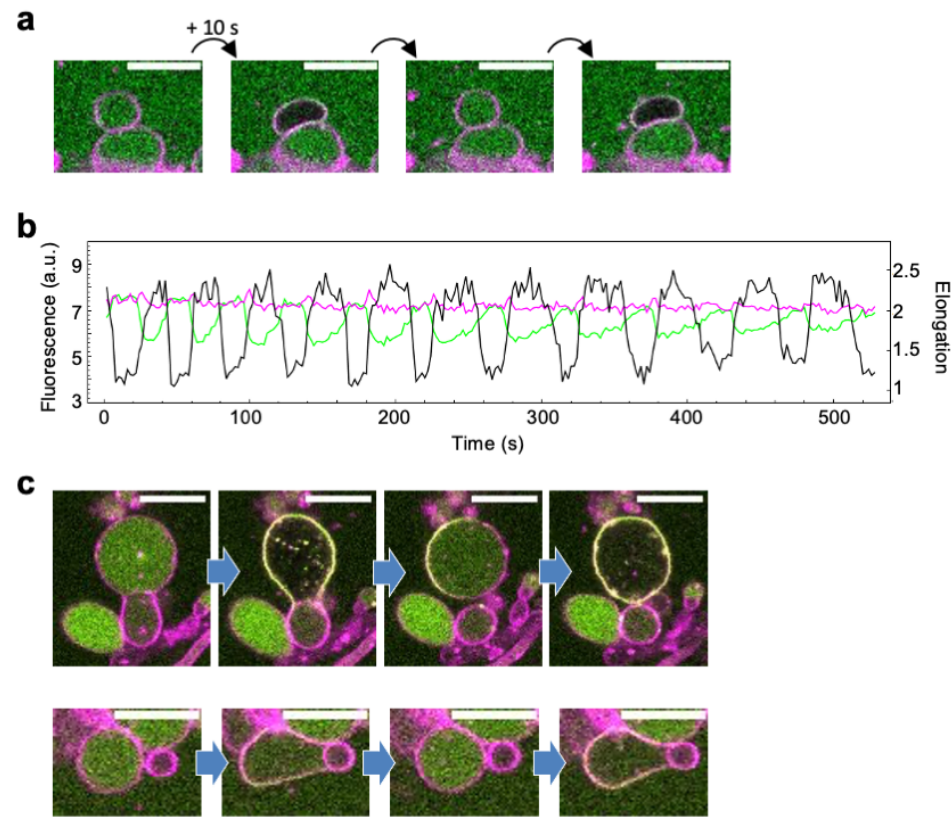


Figure 5: Autonomous liposome deformation induced by synthetic Min oscillations. **a**, Time series images of a liposome that changes morphology in response to Min oscillations. The membrane dye signal is colored in magenta and the eGFP-MinC reporting the waves is in green. The corresponding movie is shown in Supplementary Movie 8. Scale bars are 10 μm . **b**, Fluorescence time traces of the eGFP-MinC intensity localized at the membrane (magenta) and in the lumen (green) of the liposome displayed in (a). The time profile of the liposome elongation is overlaid in black and is phase shifted with respect to the amount of eGFP-MinC in the lumen. **c**, Timelapse fluorescence images of two liposomes exposed to a hypertonic external medium (100 mM sucrose). Liposomes undergo dramatic shape deformation upon recruitment of Min proteins to the inner surface of the lipid bilayer. The force generated by the redistribution of the Min proteins is sufficient to push a membrane septum and remodel adjacent vesicles. The corresponding videos are shown in Supplementary Movie 9. Scale bars are 10 μm .

We further examined membrane deformation in hypertonic conditions by adding 100 mM sucrose to the external medium of the liposomes. Spherical liposomes became deflated exhibiting membrane fluctuations as the Min proteins reorganize (Fig. 5c, Supplementary Fig. 10 and Supplementary Movie 9). When Min oscillations do not take place, liposomes do not periodically change shape (Supplementary Fig. 11). After a few pulsing events the liposomes relax into a stable sphere even in the presence of a polarized Min protein distribution at

the membrane. Remarkably, the force exerted by the Min waves on the inner surface of the liposome membrane, combined with increased membrane flexibility, is sometimes high enough to displace, even to expel an adjacent vesicle attached to the waving liposome (Fig. 5c and Supplementary Movie 9).

Association of MinD to a lipid bilayer through the formation of an amphipathic helix upon ATP binding is a well-established mechanism^{27,31}. The insertion of this helix into the cell membrane can influence the local curvature and lead to changes in membrane topology. Moreover, it has been reported that MinE can directly interact with the membrane and induce membrane deformation in vitro in the presence of PG or cardiolipin lipids^{31,32}. The interplay between the binding dynamics of MinD and MinE to the membrane and the local variations of membrane curvature remains to be elucidated, in particular, the degree to which MinE-induced membrane deformation contributes to the dissociation of MinD from the bilayer. Moreover, the state of membrane permeability to solvent and small solutes, and the effect of an osmolarity differential across the membrane to establish sustained Min oscillations and liposome deformation cycles require further investigation.

Integration of the synthetic Min and FtsZ systems on SLBs

Our next goal was to co-reconstitute Min protein patterns and membrane-tethered FtsZ filaments. The third element of the Min system, MinC, interacts with the oscillating MinDE by binding to MinD and it inhibits polymerization of the division protein FtsZ. We first reconstituted membrane-associated FtsZ filaments by anchoring purified FtsZ-Alexa647 to an SLB through the membrane binding protein FtsA synthesized in the PURE system. Large areas of the SLB were covered with ring-like structures of FtsA-FtsZ copolymers, consistent with previous observations using purified FtsA³³. MinC and MinD were separately expressed in a test tube and the pre-ran PURE_{flex}2.0 solutions were either mixed together or individually mixed with a PURE_{flex}2.0 sample containing a mock expressed protein (the phi29 terminal protein) to account for volume dilution. With both samples containing solely MinC or MinD, FtsA-FtsZ bundles and rings were clearly visible, although the SLB coverage was much less with MinC (Fig. 6a and Supplementary Fig. 12 and 13). In contrast, addition of MinC plus MinD impaired formation of rings, and only unresolved FtsZ structures, presumably monomers or short oligomers, remained recruited to the membrane (Fig. 6a and Supplementary Fig. 14). These results confirm that MinD, by increasing the local concentration of MinC at the membrane, reduces the effective MinC concentration to inhibit FtsZ polymerization.

The complete synthetic MinCDE system was co-reconstituted with the expressed FtsA and purified FtsZ-Alexa647, the latter acting as the fluorescence readout in this assay (Fig. 6b). Large-scale dynamic FtsZ patterns with calculated wavelength and velocity values of $34 \pm 8 \mu\text{m}$ and $1.1 \pm 0.3 \mu\text{m s}^{-1}$ (mean \pm standard deviation, three different fields of view from one sample) (Fig. 6b, pattern 1), or $115 \pm 42 \mu\text{m}$ and $2.9 \pm 0.8 \mu\text{m s}^{-1}$ (mean \pm standard deviation,

twelve kymographs from two biological replicates) (Fig. 6b, pattern 2), were observed, confirming the full activity spectrum of the *in vitro* synthesized MinC (Fig. 6c). In the absence of MinC, two types of FtsZ-Alexa647 patterns coexist: dim propagating waves with wavelength $152 \pm 53 \mu\text{m}$ and velocity $2.8 \pm 0.9 \mu\text{m s}^{-1}$ (mean \pm standard deviation, twelve kymographs from one sample) that presumably anticorrelate with MinDE waves³⁴, and a globally stable cytoskeletal network of FtsA-FtsZ ring-like structures (Fig. 6d, e, Supplementary Movie 11).

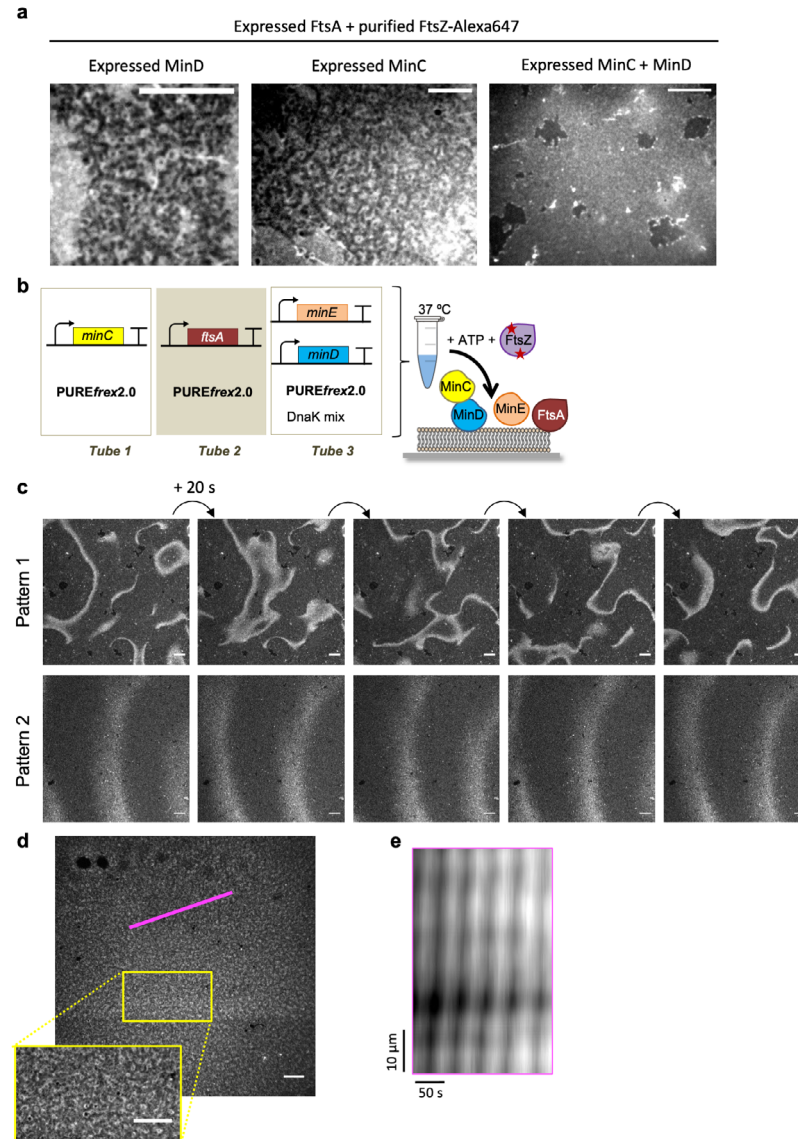


Figure 6: Cell-free expressed MinDE(C) regulates FtsZ spatial organization. **a**, Ring-like structures composed of purified FtsZ-Alexa647 and expressed FtsA can assemble on an SLB. The ability of sep-

arately expressed MinC and MinD, or co-expressed MinC/D to inhibit formation of FtsA-FtsZ rings was investigated. A representative fluorescence image is shown for each condition. 8x8 fields of view montages are shown in Supplementary Fig. 12-14. Scale bars are $10 \mu\text{m}$. **b**, Schematic of the MinCDE and FtsA-FtsZ coupled SLB assay. **c**, Two time series images of FtsZ-Alexa647 dynamic patterns. Scale bars are $10 \mu\text{m}$. The corresponding videos are shown in Supplementary Movie 10. An 8x8 fields of view montage of pattern 1 is shown in Supplementary Fig. 15. **d**, Cytoskeletal pattern of expressed FtsA and purified FtsZ-Alexa647 combined with MinDE. In the absence of MinC, the FtsZ bundle network is maintained but traveling waves of FtsZ-Alexa647 are also visible (see Supplementary Movie 11). Scale bars are $10 \mu\text{m}$. **e**, Kymograph of the FtsZ-Alexa647 signal along the magenta line shown in (d). The images were preprocessed to filter out small-scale features (Methods).

This observation suggests that bundles of FtsA-FtsZ are less affected by MinDE waves than short filaments that are more transiently anchored to the bilayer, hence more susceptible to be outcompeted by the membrane-binding MinD. Moreover, our data indicate that FtsA-FtsZ cytoskeletal patterns might influence MinDE waves properties by increasing both the wavelength and velocity. Interestingly, FtsZ bundles comprising the FtsZ-YFP-membrane-targeting sequence protein for membrane binding were unaffected by purified MinDE³⁰, suggesting that FtsA-FtsZ co-filaments are more responsive to the Min system. The role of FtsA as an FtsZ-depolymerizing factor in regulating the composite behavior observed here (Fig. 6d, Supplementary Movie 11) remains to be elucidated.

These results demonstrate for the first time that coupling Min system dynamics with FtsZ and the membrane-associated FtsA is possible. A future challenge will consist in co-expressing all five proteins inside liposomes. This will require the concatenation of multiple genes on a single DNA template to avoid heterogeneous encapsulation of the different DNA molecules. Moreover, the productivity of the PURE system and ribosome processivity will have to be improved to synthesize sufficient amounts of all full-length proteins.

Discussion

Assembly of a synthetic biological cell from elementary building blocks is arguably one of the biggest and most exciting challenges facing science today. Recent methodological advances in liposome preparation and high-throughput analysis²⁴, and in reconstitution of functional modules, such as transcription-translation²², DNA replication²⁸, phospholipid synthesis^{35,36}, light-activated energy production³⁷, represent encouraging steps towards the construction of a fully autonomous artificial cell. Yet, the implementation of a DNA-encoded liposome division machinery remains a major milestone.

In summary, we showed in the present study that MinD and MinE proteins expressed from their genes can self-organize into planar waves on SLBs or oscillate between the membrane and lumen when enclosed inside liposomes. Global shape transformations and local membrane undulations can result from dynamic redistribution of the *in vesiculo*-synthesized Min proteins. This reversible and autonomous Min-assisted membrane deformability represents one of the

few examples of active vesicles³⁸. Conceptually, a DNA-centered approach to build cellular functions is less pragmatic than merely relying on purified proteins. Yet, it adheres with our framework to create a synthetic cell from a minimal genome^{24,28,39}. Three pillars of cellular life were reconstituted in the present study: (i) a lipid compartment as the evolutionary unit, (ii) information storage in the form of DNA and its decoding with the PURE system to produce proteins, (iii) protein self-organization mediated by nucleotide exchange, ATP hydrolysis and transient membrane binding, a hallmark in biological systems. Moreover, the observed membrane remodeling ability of the synthesized Min proteins imposes less constraints in terms of lipid composition and temperature than alternative mechanisms reported earlier^{40–44}. Therefore, one could envision to exploit Min waves to stimulate division by budding in a liposome-based synthetic cell.

Endowing the Min biochemical network with genetic control is uniquely suited to investigate the evolution of pattern dynamics and membrane deformation as a function of protein concentration and synthesis rate, in real-time. In general, our methodology is instrumental to further apprehend the interplay between genetic and nongenetic factors involved in the bacterial division processes. Furthermore, the PURE system should be harnessed to co-express MinDEC with FtsZ and its membrane-anchoring proteins. Min oscillations would then drive both liposome elongation and FtsZ-ring positioning. Tuning the absolute and relative protein abundance to ensure proper functioning of the two sub-systems could be achieved by modulating the strength of transcription and translation of the individual genes. Additional temporal control over protein production could be realized by implementing transcriptional delay or feedback loops^{45,46}. Such a rational engineering approach to endow liposomes with a division mechanism might be complemented with an evolutionary route, whereby a liposome population randomly encloses mutagenized *min* genes from a library. Those liposomes exhibiting a desirable phenotype, for instance pole-to-pole oscillations or membrane constriction, would be selected and their DNA variants amplified for further rounds of directed evolution.

Methods

Purified proteins

Proteins eGFP-MinD and eGFP-MinC were purified according to published protocols²⁹. Protein concentrations were determined in a Bradford assay and by measuring eGFP absorbance. Purified MinE used for mass spectrometry was a kind gift from the Cees Dekker lab¹⁹. Purified FtsZ-Alexa647 (kindly provided by Germán Rivas lab) was stored in a buffer containing 50 mM Tris, 500 mM KCl, 5 mM MgCl₂ and 5% glycerol at pH 7 as previously described⁴⁷.

Preparation of DNA constructs

minD and *minE* gene fragments were amplified by standard PCR with Phusion High Fidelity DNA polymerase (ThermoFisher Scientific) from chromosomal *E. coli* MG1655 (K12) DNA with primers ChD511 and ChD382 (*minD*), and ChD512 and ChD384 (*minE*) (Supplementary Table 3). These primers contain overhangs for the pET11-a backbone plasmid. The PCR products and linearized backbone pET11-a DNA were checked on a 1% agarose gel stained with SYBR safe, imaged with a ChemiDoc™ Imaging System (BioRad Laboratories) and purified with Wizard SV Gel kit (Promega). The purified DNA was incubated with DpnI (New England BioLabs® Inc.) to remove residual plasmid and the linear DNA was purified again with Wizard SV Gel kit. DNA concentration and purity were measured using a ND-1000 UV-Vis Spectrophotometer (Nanodrop Technologies). Gibson assembly (Gibson Assembly® Master Mix of New England BioLabs® Inc) was performed at equimolar concentrations of linearized plasmid (pET11-a) and DNA fragments for 1 h at 50 °C. Transformation of the Gibson assembly products into *E. coli* TOP10 competent cells was done by heat shock, after which cells were resuspended in 200 µL of fresh prechilled liquid LB medium and incubated for 1 h at 37 °C and 250 rpm. Then, the cultures were plated in solid LB medium with ampicillin and grew overnight at 37 °C. Colonies were picked up and cultured in 1 mL of liquid LB medium with 100 µg/mL of ampicillin for 16 h at 37 °C and 250 rpm. Plasmid purification was performed using the PureYield™ Plasmid Miniprep System (Promega). The phi29 terminal protein (TP) coding DNA construct was prepared by PCR as previously described²⁸. Concentration and purity of DNA were checked on NanoDrop. All sequences were confirmed by sequencing. MinE-, MinC- and FtsA-coding DNA fragments (starting with a T7 promoter and ending with a T7 terminator) with optimized sequence for codon usage, CG content and 5' mRNA secondary structures were inserted in a pUC57, pCC1 and pJET1 plasmid (GeneScript), respectively. Plasmids were amplified and purified as described above.

Linear DNA constructs were prepared by polymerase chain reaction (PCR) from a parental plasmid using the forward and reverse primers ChD709 and ChD757, respectively annealing

to the T7 promoter and T7 terminator sequences (Supplementary Table 3). Amplification products were checked on a 1% agarose gel and were further purified using Wizard SV gel (standard column protocol). Concentration and purity were measured by NanoDrop. Sequences of the linearized constructs can be found in the Supplementary Methods.

Cell-free gene expression in bulk

PUREfrex2.0 (GeneFrontier Corporation, Chiba) was utilized following storage and handling instructions provided by the supplier. Linear DNA constructs were added at a concentration of 5 nM for gel analysis. In co-expression reactions, *minD* and *minE* DNA templates were included at 4 nM and 8 nM, respectively, and the solution was supplemented with 1 µL of DnaK Mix (GeneFrontier Corporation). DnaK Mix consists of highly purified *E. coli* DnaK, DnaJ and GrpE chaperone proteins. In single-gene expression reactions of *minC*, *ftsA* and *TP*, the DNA template was included at 5 nM. Gene expression reactions were carried out in 20-µL volume in PCR tubes for 3 h at 37 °C.

Labeling of in vitro synthesized proteins and gel analysis

PUREfrex2.0 reaction mixture was supplemented with 0.5 µL of GreenLys reagent (FluoroTect™ GreenLys, Promega) and gene expression was performed in a test tube as described above. Sample was treated with RNAase (RNaseA Solution, Promega) for 30 min and proteins denatured for 10 min at 90 °C in 2 SDS loading buffer with 10 mM dithiotreitol (DTT). Samples were loaded on a 18% SDS-PAGE (polyacrylamide gel electrophoresis) gel. Visualization of the fluorescently labeled protein was performed on a fluorescence gel imager (Typhoon, Amersham Biosciences) using a 488-nm laser and a band pass emission filter of 520 nm.

Quantitative proteomics

A targeted proteomics approach was used to determine the concentration of cell-free synthesized MinC, and co-synthesized MinD and MinE proteins. For the MinD/E co-expression, a kinetic experiment (three independent repeats) was performed to determine protein concentrations at 0, 20, 40, 60, 120, 180 and 300 min. Additionally, end-point measurements (two independent repeats) were performed by taking the samples after 180 min. Samples of 5 µL of pre-ran PUREfrex2.0 were incubated at 90 °C for 10 min in 22.6 µL of 27.56 mM Tris-HCl pH 7.6, 4.5 mM DTT and 1.1 mM CaCl₂. Another 2.5 µL and 1.25 µL of the pre-incubated PUREfrex2.0 solution were diluted to a final volume of 5 µL giving a 2 and 4 dilution of the expressed proteins. Then, 15.52 mM final concentration of iodoacetamide was added and the solution was incubated for 30 min in the dark. The iodoacetamide reaction was quenched by addition of 4.2 mM final concentration of DTT. Finally, 0.625 µg of Trypsin was added and the solution was incubated overnight at 37 °C. The following day, 2.52 µL of

10% trifluoroacetic acid was added, the sample was incubated at room temperature for 5 min, the solution was centrifuged at 16,200 rcf for 30 min and the supernatant was transferred to an HPLC-vial for mass spectrometry analysis.

Mass spectrometry analysis of tryptic peptides was conducted on a 6460 Triple Quad LC/MS system (Agilent Technologies, USA). From the samples prepared as described above, 10 µL were injected to an ACQUITY UPLC® Peptide CSH™ C18 Column (Waters Corporation, USA). The peptides were separated in a gradient of buffer A (25 mM formic acid in milliQ water) and buffer B (50 mM formic acid in acetonitrile) at a flow rate of 500 µL per minute and at a column temperature of 40 °C. The column was equilibrated with 98:2 ratio of buffer A to B. After injection over 20 min the ratio was changed to 75:25 of buffer A to B after which, within 30 s, the ratio went to 20:80 of buffer A to B and was held for another 30 s. Finally, the column was flushed for 5 min with 98:2 of buffer A to B.

Supplementary Table 1 shows the transitions of the MS/MS measurements that were observed in every experiment. EF-Tu is a constant component of the PURE system and we used its proteolytic peptide TTLTAAITTVLAK as an internal standard for variations during sample handling. All proteomics data were analysed in Skyline-daily 4.1.1.18179 (MacCoss lab, University of Washington, USA). Retention time was predicted after standard runs with the method described above using the Pierce™ Peptide Retention Time Calibration Mixture (Catalog number 88320, Thermo Scientific, USA).

Purified proteins eGFP-MinD and MinE with stock concentrations of 64 µM and 89 µM, respectively, and purified eGFP-MinC with a stock concentration of 127 µM were used as standards for quantitative LC-MS. The MinD and MinE proteins were mixed and a serial dilution was prepared in a buffer containing 20 mM HEPES pH 7.6, 180 mM potassium glutamate and 14 mM magnesium glutamate. Three dilution series of 10 µM, 5 µM, 2.5 µM, 1.25 µM and 0.625 µM were prepared independently of each other and treated according to the same digestion protocol as described above for the PUREfrex2.0 samples. Samples of 10 µL from two dilution rows were injected from the lowest concentration to the highest with blank measurements between every standard row. Then, the three dilutions of two biological replicates of PUREfrex2.0 reactions were injected with the lowest concentration first. The third standard row was injected last. Three MinC standard rows were prepared in a similar manner but with the highest concentration being 30 µM of purified protein, which was pipetted individually. A 20 µM standard was prepared independently and used for the serial dilution giving concentrations of 20 µM, 10 µM, 5 µM, 2.5 µM, 1.25 µM and 0.625 µM. MinC expression reactions in PURE system were prepared and treated the same way as the MinD and MinE samples. Expression reactions with MinC (four independent experiments) were run for 3 h at 37 °C. Mass spectrometry data were analyzed in Skyline-daily as mentioned above and integrated peak intensities were plotted in OriginPro 2015 (b9.2.257, OriginLab Corporation, USA). The plotted concentrations of each peptide were fitted with Instrumental

variance weighting using the formula $w_i = 1/\sigma_i^2$, where σ_i is the error bar size (standard deviation from the average) of each value. The scatter plots with linear regression are shown in Supplementary Fig. 3. and the extracted parameters are listed in Supplementary Table 2.

Phenomenological fitting of MinD/E production kinetics

Measured concentrations of MinD/E most C-terminal peptides were fit with a phenomenological model to estimate the main kinetic parameters, such as the final yield, production rate and translation lifespan (or time to plateau). The following sigmoid equation was used²⁴:

$$y = k' + k \frac{t^n}{t^n + K^n} \quad (\text{Eq. 1})$$

where t is the time in minutes, y the MinD/E peptide concentration at a given time point, and k' , k , K and n are fit parameters. Using this expression, the final yield corresponds to k and the plateau time, or expression lifespan, is expressed as:

$$T_{\text{plateau}} = \frac{2K}{n} + K \quad (\text{Eq. 2})$$

The apparent translation rate, which is defined as the steepness at time $t = K$, is:

$$v_{\text{translation}} = \frac{kn}{4K} \quad (\text{Eq. 3})$$

Kinetics obtained from three independent experiments were fit (Fig. 1d) and the parameter values are reported as the average and standard deviation.

Fabrication and cleaning of the imaging chamber

Home-made glass chambers were used in both SLB and liposome experiments. Three microscopy glass slides were glued on top of each other with NOA 61 glue (Norland Products). Holes with a diameter of 2.5 mm were drilled across the slides and then covered on one side by gluing a 150- μm -thick coverslip (Menzel-Gläser) with NOA 61, creating the bottom of the glass chamber. Cleaning was performed by successive washing steps of 10 min each in a bath sonicator (Sonorex digitec, Bandelin), as follows: chloroform and methanol (volume 1:1), 2% Hellmanex, 1M KOH, 100% ethanol and milliQ water. For SLB experiments the glass chambers were further treated every 1-2 experiments with Acid Piranha cleaning.

Lipids

1,2-dioleoyl-sn-glycero-3-phosphocholine (DOPC), 1,2-dioleoyl-sn-glycero-3-phosphoethanolamine (DOPE), 1,2-dioleoyl-sn-glycero-3-phosphoglycerol (DOPG), 1,3'-bis[1,2-dioleoyl-sn-glycero-3-phospho]-glycerol (18:1 CL) and 1,2-distearoyl-snglycero-3-phosphoethanolamine-N-[biotinyl(polyethylene glycol)-2000 (DSPE-PEG-biotin) were from Avanti Polar Lipids. Texas Red 1,2-dihexadecanoyl-sn-glycero-3-phosphoethanolamine

(DHPE-TexasRed) was from Invitrogen.

Preparation of small unilamellar vesicles

Small unilamellar vesicles (SUV) were used as precursors for SLB formation. Lipids DOPC (4 μmol) and DOPG (1 μmol) dissolved in chloroform, were mixed in a small glass vial. A lipid film was deposited on the wall of the vial upon solvent evaporation through a gentle flow of argon and was further desiccated for 30 min at room temperature. The lipid film was resuspended with 400 μL of SLB buffer (50 mM Tris, 300 mM KCl, 5 mM MgCl_2 , pH 7.5) and the solution was vortexed for a few minutes. The final lipid concentration was 1.25 mg mL^{-1} . A two-step extrusion (each of 11 passages) was carried out using the Avanti mini extruder (Avanti Polar Lipids) equipped with 250 μL Hamilton syringes (Avant Polar Lipids), filters (drain disc 10 mm diameter, Whatman) and a polycarbonate membrane with pore size 0.2 μm (step 1) or 0.03 μm (step 2) (Nuclepore track-etched membrane, Whatman).

Formation of supported lipid bilayers

The imaging chamber was treated with oxygen plasma (Harrick Plasma basic plasma cleaner) for 30 min to activate the glass surface. Immediately after plasma cleaning the SUV solution was added to the sample reservoir at a final lipid concentration of 0.94 mg mL^{-1} and CaCl_2 was added at a final concentration of 3 mM. The chamber was closed by sticking a coverslip using a double-sided adhesive silicone sheet (Life Technologies) and the SLB was formed during 30 min incubation at 37 °C. Next, the chamber was opened and the SLB was carefully washed six times with SLB buffer.

Activity assays on supported membranes

A PUREflex2.0 reaction mixture was assembled as described above to express the *minD* and *minE* (optimized or non-optimized sequences) genes. Unless specified otherwise, the sequence-optimized *minE* construct was used in SLB and liposome experiments. The *minE* and *minD* DNA constructs were added at a final concentration of 4 nM and 8 nM, respectively, in both single-gene and double-gene expression reactions. In single-gene expression reactions with the sequence-optimized *minC* and sequence-optimized *ftsA* genes, the constructs were added at a final concentration of 5 nM. The solution was supplemented with (final concentrations indicated): 2.5 mM ATP, 100 nM purified eGFP-MinD, DnaK (GeneFrontier Corporation) and MilliQ water to adjust the final volume to 20 μL . Following 3 h incubation at 37 °C, the solution was added on top of an SLB and the chamber was sealed by sticking a 2020 mm coverslip with a double-sided adhesive silicone sheet.

For in situ expression of MinD/E proteins, the *minE* and *minD* DNA templates were added at a final concentration of 4 nM and 8 nM, respectively. A 20- μL PUREflex2.0 mixture was supplemented with 2.5 mM ATP, 100 nM purified eGFP-MinD and DnaK mix, and the

solution was incubated on top of an SLB. The chamber was sealed as described above and the sample was immediately visualized on a laser scanning confocal microscope up to 4 h of expression. Several fields of view were imaged at different time points throughout the incubation period.

For assays involving FtsZ, the *ftsA*, *minC* and *TP* genes were individually expressed in a test tube, while *minE* and *minD* were co-expressed. After 3 h incubation at 37 °C, 5.5 µL aliquots of the appropriate reaction samples were mixed together with 2 µM GTP, 2.5 mM ATP and 3 µM purified FtsZ-A647 (all final concentrations) in a total volume of 20 µL. The mixture was added on top of an SLB and the chamber was sealed before imaging.

Planar membrane assays with purified proteins were performed by adding on an SLB a reaction mixture containing 1 µM eGFP-MinD, 1 µM MinE, 2.5 mM ATP and, as a background medium, a pre-ran PURE_{flex}2.0 solution with the expressed TP protein.

Spinning disk microscopy

Min activity assays on SLB were performed using spinning disk imaging with an Olympus iX81 inverted fluorescence microscope equipped with a 100 oil immersion objective (Olympus), an iXon3 EMCCD camera (Andor Technology) and a Nipkow spinning disk (CSU-XI, Yokogawa). Fluorescence of eGFP-MinD was measured using a 491-nm laser line and appropriate emission filters (525/50 nm). The software Andor IQ3 (Andor Technology Ltd.) was used for image acquisition and identical settings were used for all experiments. Experiments were conducted at 37 °C using an OKO lab incubator box.

Preparation of lipid-coated beads

Two different lipid mixtures were utilized. Composition 1 contains DOPC (50 mol%), DOPE (36 mol%), DOPG (12 mol%), 18:1 CL (2 mol%), DSPE-PEG-biotin (1 mass%) and DHPE-TexasRed (0.5 mass%) for a total mass of 2 mg. Composition 2 contains DOPC (75 mol%), DOPG (25 mol%), DSPE-PEG-biotin (1 mass%) and DHPE-TexasRed (0.5 mass%) for a total mass of 5 mg. Lipids dissolved in chloroform were mixed in a round-bottom glass flask. Methanol containing 100 mM rhamnose was added to the lipid solution in a chloroform-to-methanol volume ratio of 2.5:1. Then, 1.5 g of 212-300-µm glass beads (acid washed, Sigma Aldrich) was poured to the lipid-rhamnose solution and the organic solvent was removed by rotary evaporation at 200 mbar for 2 h at room temperature, followed by overnight desiccation. Lipid-coated beads were stored under argon at -20 °C until use.

Production and immobilization of gene-expressing liposomes

A PURE_{flex}2.0 reaction mixture was assembled in a test tube as described above. Either or both *minD* and *minE* DNA constructs were added at a final concentration of 4 nM and 8 nM, respectively. The solution was supplemented with (final concentrations indicated): 2.5

mM ATP, 1 µM purified eGFP-MinC, DnaK mix and MilliQ water to reach a final volume of 30 µL. Whenever specified, 1 µM purified eGFP-MinC was substituted with 0.4 µM of eGFP-MinC or 0.2 µM eGFP-MinD. About 25 mg of lipid-coated beads was transferred to the PURE_{flex}2.0 solution and liposomes were formed by natural swelling of the lipid film for 2 h on ice, protected from light. During incubation, the tube was gently rotated manually a few times. Four freeze-thaw cycles were then applied by dipping the sample in liquid nitrogen and thawing on ice. The sample reservoir of the imaging chamber was functionalized with 1:1 molar ratio of BSA and BSA-biotin (1 mg/mL, Thermo Fisher Scientific), and then with Neutravidin (1 mg/mL, Sigma Aldrich) in order to tether the biotinylated liposomes. About 7 µL of the liposome solution was carefully pipetted (with a cut tip) into the imaging chamber and supplemented with RQ1 DNase (0.07 U/µL) to preclude gene expression outside liposomes. The chamber was sealed by sticking a 2020 mm coverslip with a double-sided adhesive silicone sheet. Expression was performed directly on the confocal microscope at 37 °C for 1.5 h to 6 h.

Confocal microscopy

A Nikon A1R Laser scanning confocal microscope equipped with an SR Apo TIRF 100 oil immersion objective was used to image liposomes and SLB in Min-FtsZ combined experiments and in situ MinD/E expression kinetics. The 561-nm and 488-nm laser lines were used in combination with appropriate emission filters to image the Texas Red membrane dye and eGFP-MinC, respectively. The software NIS (Nikon) was used for image acquisition and identical settings were used for all experiments. Samples were mounted on a temperature-controlled stage maintained at 37 °C during imaging.

Image analysis

Image analysis was performed using custom scripts in MatLab version 2018a. Liposome images in the Texas-Red channel were background corrected by morphological opening with a disk radius of 4 pixels. To enhance coherence of the liposome membrane signal a series of rotated elongated Laplacian of Gaussian filters of size 10 pixels with standard deviations of 3 and 0.1 pixels was applied. The maximum projection of these filtered images was used as input for a seeded watershed segmentation, where the seed was derived from the segmentation of the previous image by image erosion with a disk radius dependent on the liposome size. For the first frame of the time-lapse images a user-supplied seed was used. A Gaussian filter of size 10 pixels with a sigma of 1.2 pixels was applied to all GFP images and the pixel intensities corresponding to the segmentation result were extracted to generate kymographs. As the length of the circumference changes during the time series images when liposomes undergo shape changes, the individual lines of the kymograph were all adjusted to the number of pixels of the longest circumference using linear interpolation. Liposome elongation was calculated as the

ratio of major to minor axis length of the ellipse that has the same normalized second central moments as the segmented liposome. The normalized perimeter length is the circumference of a circle with the same area, A , as the liposome and was calculated as $\pi \times \sqrt{4A/\pi}$.

The frequency of oscillations of the standing wave patterns on SLB was determined by calculating the autocorrelation function over time for each pixel and extracting the first peak of the function if existing. The median of those values for one image is reported. The wavelength and velocity of the traveling waves on SLB were analyzed by generating a kymograph along a line in the direction of the traveling wave. For the experiments combining MinDE with FtsA and FtsZ-Alexa647, images were pre-processed with an 8-pixel radius Gaussian blur filter before generating the kymographs. After binarization of the kymograph by Sobel edge detection, lines were detected using a linear Hough transform. The slope of the lines corresponds to the wave velocity, the spacing between the lines to the wavelength.

References

1. Powell, K. Biology from scratch: Built from the bottom up, synthetic cells could reveal the boundaries of life. *Nature* **563**, 172–175 (2018).
2. Schwille, P. *et al.* MaxSynBio: Avenues towards creating cells from the bottom up. *Angew. Chemie Int. Ed.* **57**, 13382–13392 (2018).
3. Noireaux, V., Maeda, Y. T. & Libchaber, A. Development of an artificial cell, from self-organization to computation and self-reproduction. *Proc. Natl. Acad. Sci.* **108**, 3473–3480 (2011).
4. Khalil, A. S. & Collins, J. J. Synthetic biology: applications come of age. *Nat. Rev. Genet.* **11**, 367–379 (2010).
5. Errington, J., Daniel, R. A. & Scheffers, D.-J. Cytokinesis in bacteria. *Microbiol. Mol. Biol. Rev.* **67**, 52–65 (2003).
6. Rico, A. I., Krupka, M. & Vicente, M. In the beginning, *Escherichia coli* assembled the proto-ring: An initial phase of division. *J. Biol. Chem.* **288**, 20830–20836 (2013).
7. Rowlett, V. W. & Margolin, W. The Min system and other nucleoid-independent regulators of Z ring positioning. *Front. Microbiol.* **6**, 478 (2015).
8. De Boer, P. A. J., Crossley, R. E. & Rothfield, L. I. A division inhibitor and a topological specificity factor coded for by the Minicell locus determine proper placement of the division septum in *E. Coli*. *Cell* **56**, 641–9 (1989).
9. Hu, Z., Mukherjee, A., Pichoff, S. & Lutkenhaus, J. The MinC component of the division site selection system in *Escherichia coli* interacts with FtsZ to prevent polymerization. *Proc. Natl. Acad. Sci. U. S. A.* **96**, 14819–24 (1999).
10. Hu, Z., Saez, C. & Lutkenhaus, J. Recruitment of MinC, an inhibitor of Z-ring formation, to the membrane in *Escherichia coli*: role of MinD and MinE. *J. Bacteriol.* **185**, 196–203 (2003).
11. Raskin, D. M. & de Boer, P. A. MinDE-dependent pole-to-pole oscillation of division inhibitor MinC in *Escherichia coli*. *J. Bacteriol.* **181**, 6419–24 (1999).
12. Halatek, J., Brauns, F. & Frey, E. Self-organization principles of intracellular pattern formation. *Philos Trans R Soc Lond Biol Sci.* **373**, 1747 (2018).
13. Hale, C. A., Meinhardt, H. & de Boer, P. A. Dynamic localization cycle of the cell division regulator MinE in *Escherichia coli*. *EMBO J.* **20**, 1563–72 (2001).
14. Kruse, K. A dynamic model for determining the middle of *Escherichia coli*. *Biophys. J.* **82**, 618–27 (2002).
15. Raskin, D. M. & de Boer, P. A. Rapid pole-to-pole oscillation of a protein required for directing division to the middle of *Escherichia coli*. *Proc. Natl. Acad. Sci. U. S. A.* **96**, 4971–6 (1999).
16. Loose, M., Fischer-Friedrich, E., Ries, J., Kruse, K. & Schwille, P. Spatial regulators for bacterial cell division self-organize into surface waves in vitro. *Science* **320**, 789–92 (2008).
17. Vecchiarelli, A. G., Li, M., Mizuuchi, M. & Mizuuchi, K. Differential affinities of MinD and MinE to anionic phospholipid influence Min patterning dynamics in vitro. *Mol. Microbiol.* **93**, 453–463 (2014).
18. Zieske, K. & Schwille, P. Reconstitution of pole-to-pole oscillations of Min proteins in microengineered polydimethylsiloxane compartments. *Angew. Chemie Int. Ed.* **52**, 459–462 (2013).
19. Caspi, Y. & Dekker, C. Mapping out Min protein patterns in fully confined fluidic chambers. *Elife* **5**, (2016).
20. Zieske, K., Chwastek, G. & Schwille, P. Protein patterns and oscillations on lipid monolayers and in microdroplets. *Angew. Chemie Int. Ed.* **55**, 13455–13459 (2016).
21. Litschel, T., Ramm, B., Maas, R., Heymann, M. & Schwille, P. Beating vesicles: Encapsulated protein oscillations cause dynamic membrane deformations. *Angew. Chemie Int. Ed.* **57**, 16286–16290 (2018).
22. Shimizu, Y. *et al.* Cell-free translation reconstituted with purified components. *Nat. Biotechnol.* **19**, 751–755 (2001).
23. Doerr, A. *et al.* Modelling cell-free RNA and protein synthesis with minimal systems. *Phys. Biol.* **16**, 025001 (2019).
24. Blanken, D., van Nies, P. & Danelon, C. Quantitative imaging of gene-expressing liposomes reveals rare favorable phenotypes. *Phys. Biol.* **16**, 045002 (2019).
25. de Boer, P. A., Crossley, R. E., Hand, A. R. & Rothfield, L. I. The MinD protein is a membrane ATPase required for the correct placement of the *Escherichia coli* division site. *EMBO J.* **10**, 4371–80 (1991).
26. Nourian, Z., Roelofsen, W. & Danelon, C. Triggered gene expression in fed-vesicle microreactors with a multifunctional membrane. *Angew. Chemie Int. Ed.* **51**, 3114–3118 (2012).
27. Zhou, H. & Lutkenhaus, J. Membrane binding by MinD involves insertion of hydrophobic residues within the C-terminal

amphipathic helix into the bilayer. *J. Bacteriol.* **185**, 4326–35 (2003).

28. van Nies, P. *et al.* Self-replication of DNA by its encoded proteins in liposome-based synthetic cells. *Nat. Commun.* **9**, 1583 (2018).

29. Loose, M., Fischer-Friedrich, E., Herold, C., Kruse, K. & Schwille, P. Min protein patterns emerge from rapid rebinding and membrane interaction of MinE. *Nat. Struct. Mol. Biol.* **18**, 577–583 (2011).

30. Arumugam, S., Petrašek, Z. & Schwille, P. MinCDE exploits the dynamic nature of FtsZ filaments for its spatial regulation. *Proc. Natl. Acad. Sci. U. S. A.* **111**, E1192–200 (2014).

31. Mazor, S. *et al.* Mutual effects of MinD-membrane interaction: I. Changes in the membrane properties induced by MinD binding. *Biochim. Biophys. Acta* **1778**, 2496–504 (2008).

32. Hsieh, C.-W. *et al.* Direct MinE-membrane interaction contributes to the proper localization of MinDE in *E. coli*. *Mol. Microbiol.* **75**, 499–512 (2010).

33. Loose, M. & Mitchison, T. J. The bacterial cell division proteins FtsA and FtsZ self-organize into dynamic cytoskeletal patterns. *Nat. Cell Biol.* **16**, 38–46 (2014).

34. Ramm, B. *et al.* The MinDE system is a generic spatial cue for membrane protein distribution in vitro. *Nat. Commun.* **9**, 3942 (2018).

35. Scott, A. *et al.* Cell-free phospholipid biosynthesis by gene-encoded enzymes reconstituted in liposomes. *PLoS One* **11**, e0163058 (2016).

36. Bhattacharya, A., Brea, R. J., Niederholtmeyer, H. & Devaraj, N. K. A minimal biochemical route towards de novo formation of synthetic phospholipid membranes. *Nat. Commun.* **10**, 300 (2019).

37. Berhanu, S., Ueda, T. & Kuruma, Y. Artificial photosynthetic cell producing energy for protein synthesis. *Nat. Commun* **10**, 1325 (2019)

38. Keber, F. C. *et al.* Topology and dynamics of active nematic vesicles. *Science* **345**, 1135–1139 (2014).

39. Nourian, Z., Scott, A. & Danelon, C. Toward the assembly of a minimal divisome. *Syst. Synth. Biol.* **8**, 237 (2014).

40. Döbereiner, H. G., Käs, J., Noppl, D., Sprenger, I. & Sackmann, E. Budding and fission of vesicles. *Biophys. J.* **65**, 1396–403 (1993).

41. Leirer, C., Wunderlich, B., Myles, V. M. & Schneider, M. F. Phase transition induced fission in lipid vesicles. *Biophys. Chem.* **143**, 106–109 (2009).

42. Sakuma, Y. & Imai, M. Model system of self-reproducing vesicles. *Phys. Rev. Lett.* **107**, 198101 (2011).

43. Hardy, M. D. *et al.* Self-reproducing catalyst drives repeated phospholipid synthesis and membrane growth. *Proc. Natl. Acad. Sci.* **112**, 8187–8192 (2015).

44. Kurihara, K. *et al.* Self-reproduction of supramolecular giant vesicles combined with the amplification of encapsulated DNA. *Nat. Chem.* **3**, 775–781 (2011).

45. Noireaux, V., Bar-Ziv, R. & Libchaber, A. Principles of cell-free genetic circuit assembly. *Proc. Natl. Acad. Sci.* **100**, 12672–12677 (2003).

46. Shin, J. & Noireaux, V. An *E. coli* cell-free expression toolbox: Application to synthetic gene circuits and artificial cells. *ACS Synth. Biol.* **1**, 29–41 (2012).

47. Rivas, G. *et al.* Magnesium-induced linear self-association of the FtsZ bacterial cell division protein monomer. The primary steps for FtsZ assembly. *J. Biol. Chem.* **275**, 11740–9 (2000).

Supplementary information

Sequence of *MinD* construct

TAATACGACTCACTATAGGGGAATTGTGAGCGGATAACAATTCCCCTCTAGAAATAATTTTGTTTAACTTTAAGAAG-GAGATATACATATGGCACGCATTATTGTTGTTACTTCGGGCAAAGGGGGTGTTGGTAAGACAACCTCCAGCGCGC-CATCGCCACTGGTTTGGCCCAGAAAGGAAAGAAAAGTGTCTGATAGATTTTGATATCGGCCTGCGTAATCTCGACCT-GATTATGGGTTGTGAACGCCGGTTCGTTTACGATTTTCGTCAACGTCATTACAGGGCGATGCAACGCTAAATCAGGCGT-TAATTAAGATAAGCGTACTGAAAATCTCTATATTCTGCCGGCATCGCAAACACGCGATAAAGATGCCCTACCCGT-GAAGGGGTCGCCAAAGTTCTTGATGATCTGAAAGCGATGGATTTTGAATTTATCGTTTGTGACTCCCGGCAGG-GATTGAAACCGGTGCGTTAATGGCACTCTATTTGCAGACGAAGCCATTATTACCACCAACCCGGAAGTCTCCTCAG-TACGCGACTCTGACCGTATTTTAGGCATTCTGGCGTCGAAATCACGCCGCGCAGAAAATGGCGAAGAGCCTATTAAA-GAGCACCTGCTGTTAACGCGCTATAACCCAGGCCGCGTAAGCAGAGGTGACATGCTGAGCATGGAAAGATGTGCTG-GAGATCCTGCGCATCAAACCTCGTCGGCGTGATCCCAGAGGATCAATCAGTATTGCGCGCCTCTAACAGGGTGAAACCG-GTCAATTCCTGCACATTAACGCCGATGCGGGTAAAGCCTACGCAGATACCGTAGAACGCTGTTGGGAGAGAAGACGTCCT-TTCCGCTTCATTGAAGAAGAGAAGAAAGGCTTCCTCAAACGCTTGTTTCGGAGGATAAGGATCCGGCTGCTAA-CAAAGCCGAAAGGAAGTGAGTTGGCTGCTGCCACCGCTGAGCAATAACTAGCATAACCCCTTGGGGCCTCTAAACG-GGCTTGAGGGGTTTTTTG

Sequence of optimized *MinE* construct

TAATACGACTCACTATAGGGGAATTGTGAGCGGATAACAATTCCCCTCTAGAAATAATTTTGTTTAACTTTAAGAAG-GAGATATACATATGGCGCTGCTGGATTCTTTCTGAGCCGTAAGAAAAACACCGGAACATCGCGAAAGAGCGTCTG-CAAATCATTGTTGCGGAGCGTCGTCGTAGCGATGCGGAACCGCACTACCTGCCGCAGCTGCGTAAAGATATCCTG-GAAGTGATTTGCAAGTATGTTCAAATTGACCCGGAGATGGTGACCGTTACGTGGAACAAAAGGACGGTGATATCAG-CATTCTGGAGCTGAACGTTACCCTGCCGGAAGCGGAGGAAGTGAAGTAAGGATCCGGCTGCTAACAAGCCCGAAAG-GAAGCTGAGTTGGCTGCTGCCACCGCTGAGCAATAACTAGCATAACCCCTTGGGGCCTCTAAACGGGTCTTGAGGGGT-TTTTTG

Sequence of optimized *MinC* construct

TAATACGACTCACTATAGGGGAATTGTGAGCGGATAACAATTCCCCTCTAGAAATAATTTTGTTTAACTTTAAGAAG-GAGATATACATATGAGCAATACCCCGATTGAACTGAAAGGCAGCAGCTTTACCTGAGCGTTGTGCATCTGCATGAAG-CGGAGCCGAAGGTGATCCATCAGCGCGCTGGAGGACAAAATCGCGCAAGCGCCGGCGTTCTCTGAAGCATGCGCCGGT-GGTTCTGAACGTGAGCGCGCTGGAAGATCCGGTTAACTGGAGCGGATGCACAAAGCGGTGAGCGCGACCGGTCTG-CGTGTGATTGGTGTTAGCGGCTGCAAGGACGCGCAGCTGAAAGCGGAGATCGAAAAGATGGGTCTGCCGATTCTGAC-CGAAGGCAAGGAAAAAGCGCCGCTCCGGCGCGACCCCGCAGGCGCCGGCGCAAAACACCACCCCGGTGACCAA-GACCCGTCTGATCGACACCCCGGTTCTGAGCGGCCAGCGTATCTACGCGCCGCAATGCGATCTGATTGTGACCAGC-CACGTTAGCGCGGGTGCGGAGCTGATTGCGGATGGTAACATTACGTGTATGGTATGATGCGTGGCCGTGCGCTGGCG-GGTGCGAGCGCGATCGTGAAACCCAGATTTTCTGCACCAACCTGATGGCGGAGCTGGTTAGCATCGCGGTGAAT-ACTGGCTGAGCGATCAAATTCCGGCGGAGTTTATGTTAAGGCGGCGCTCTGCAACTGGTGGAGAATGCGCTGAC-CGTGCAACCGCTGAACTAAGGATCCGGCTGCTAACAAGCCCGAAAGGAAGCTGAGTTGGCTGCTGCCACCGCTGAG-CAATAACTAGCATAACCCCTTGGGGCCTCTAAACGGGTCTTGAGGGGTTTTTTG

Sequence of optimized *FtsA* construct

TAATACGACTCACTATAGGGGAATTGTGAGCGGATAACAATTCCCCTCTAGAAATAATTTTGTTTAACTTTAAGAAG-GAGATATACATATGATCAAGGCGACCGACCGTAAGCTGGTTGTGGGCCTGGAGATTGGCACCGCGAAGGTTGCGG-CGCTGGTTGGCGAGGTTCTGCCGGATGGTATGGTTAACATATCGGCGTTGGTAGCTGCCGAGCCGTGGCATGGA-CAAAGTGGTGTGAACGACCTGGAAGCGTGGTTAAGTGCGTGCAGCGTGCGATTGACCAGGCGGAGCTGATGGCG-GACTGCCAAATCAGCAGCGTTTACCTGGCGCTGAGCGGCAAGCACATCAGCTGCCAAAACGAGATTGGTATGGTGC-CGATTAGCGAAGAGGAAGTTACCCAGGAAGATGTGGAGAACGTGGTTACACCGCGAAAAGCGTTTCGTGTGCGTGAT-GAACACCGTGTGCTGCACGTTATCCCGCAAGAATACGCGATCGATTACCAGGAAGGTATCAAAAACCCGGTTGGTCT-GAGCGGTGTTTCGTATGCAGGCGAAAGTGCACCTGATTACCTGCCACAACGATATGGCGAAGAACATTGTGAAAGCG-GTTGAACGTTGCGGTCTGAAGGTTGACCAGCTGATCTTCGCGGGTCTGGCGAGCAGCTACAGCGTTCTGACCGGAA-

GATGAGCGTGAACTGGGTGTTTGCCTTGTGGATATCGGCGGTGGCACGATGGATATCGCGGTGTATACCGGTGGCG-
CGCTGCGTCACACCAAAGTGATTCCGTATGCGGGTAACGTGGTTACCAGCGACATCGCGTACGCGTTTGGCACCCCGC-
CGAGCGATGCGGAGGCGGATCAAAGTGCGTCACGGTTGCGCGCTGGGTAGCATTGTGGGTAAAGATGAGAGCGTG-
GAAGTTCCGAGCGTTGGTGGCCGTCCGCGCGTAGCCTGCAACGTCAGACCCTGGCGGAAGTTATCGAGCCGCGT-
TACACCGAACTGCTGAACCTGGTGAACGAAGAGATCCTGCAACTGCAAGAGAAACTGCGTCAGCAAGGTGTTAAG-
CACCACCTGGCGGCGGGCATTGTTCTGACCGGCGGTGCGGCGCAGATCGAAGGTCTGCGGCGGTGCGCGCAACGT-
GTTTTCCACACCCAAGTTCGTATCGGTGCGCGCTGAACATCACCGGTCTGACCGATTACGCGCAAGAGCCGTACTAT-
AGCACCGCGGTGGTCTGCTGCACTATGGCAAAGAGAGCCACCTGAACGGCGAGGCGGAAGTGAGAAAGCGTGT-
GACCGCGAGCGTTGGTAGCTGGATTAAGCGTCTGAATAGCTGGCTGCGTAAGGAGTTCTAAGGATCCGGCTGCTAA-
CAAAGCCCGAAAGGAAGCTGAGTTGGCTGCTGCCACCGCTGAGCAATAACTAGCATAACCCCTTGGGGCCTCTAAACG-
GGTCTTGAGGGGTTTTTG

Supplementary Table 1: Transitions of the MS/MS measurements used in this study.

Protein	Peptide	Precursor Ion	MS1 Res	Product Ion	MS2 Res	Fragmentor (V)	Energy (eV)	Cell Accelerator Voltage (V)	Ret Time (min)	Delta Ret Time	Ion Name
MinD	IIVVTS GK	408.763103	Unit	590.350802	Unit	130	13.7	4	5.07	1.5	y6
MinD	IIVVTS GK	408.763103	Unit	491.282388	Unit	130	13.7	4	5.07	1.5	y5
MinD	IIVVTS GK	408.763103	Unit	392.213974	Unit	130	13.7	4	5.07	1.5	y4
MinD	IIVVTS GK	408.763103	Unit	227.175404	Unit	130	13.7	4	5.07	1.5	b2
MinD	TENLYLPASQTR	753.401555	Unit	1048.578571	Unit	130	24.4	4	11.62	1.5	y9
MinD	TENLYLPASQTR	753.401555	Unit	885.515242	Unit	130	24.4	4	11.62	1.5	y8
MinD	TENLYLPASQTR	753.401555	Unit	772.431178	Unit	130	24.4	4	11.62	1.5	y7
MinD	TENLYLPASQTR	753.401555	Unit	659.347114	Unit	130	24.4	4	11.62	1.5	y6
MinD	TENLYLPASQTR	753.401555	Unit	345.140475	Unit	130	24.4	4	11.62	1.5	b3
MinD	ILGILASK	407.773471	Unit	701.455602	Unit	130	13.6	4	10.32	1.5	y7
MinD	ILGILASK	407.773471	Unit	588.371538	Unit	130	13.6	4	10.32	1.5	y6
MinD	ILGILASK	407.773471	Unit	418.26601	Unit	130	13.6	4	10.32	1.5	y4
MinD	ILGILASK	407.773471	Unit	227.175404	Unit	130	13.6	4	10.32	1.5	b2
MinD	LVGVIPEDQSVLR	712.909016	Unit	943.484336	Unit	130	23.1	4	13.19	1.5	y8
MinD	LVGVIPEDQSVLR	712.909016	Unit	270.181218	Unit	130	23.1	4	13.19	1.5	b3
MinD	LVGVIPEDQSVLR	712.909016	Unit	369.249632	Unit	130	23.1	4	13.19	1.5	b4
MinD	LVGVIPEDQSVLR	712.909016	Unit	482.333696	Unit	130	23.1	4	13.19	1.5	b5
MinD	AYADTVR	462.724706	Unit	690.341694	Unit	130	15.3	4	3.76	1.5	y6
MinD	AYADTVR	462.724706	Unit	619.30458	Unit	130	15.3	4	3.76	1.5	y5
MinD	AYADTVR	462.724706	Unit	504.277637	Unit	130	15.3	4	3.76	1.5	y4
MinD	AYADTVR	462.724706	Unit	235.107718	Unit	130	15.3	4	3.76	1.5	b2
MinE	LQIIVAE R	471.292559	Unit	700.435201	Unit	130	15.6	4	9.18	1.5	y6
MinE	LQIIVAE R	471.292559	Unit	587.351137	Unit	130	15.6	4	9.18	1.5	y5
MinE	LQIIVAE R	471.292559	Unit	474.267073	Unit	130	15.6	4	9.18	1.5	y4
MinE	LQIIVAE R	471.292559	Unit	242.149918	Unit	130	15.6	4	9.18	1.5	b2
MinE	LQIIVAE R	471.292559	Unit	355.233982	Unit	130	15.6	4	9.18	1.5	b3
MinE	DILEVICI(+57.021464)K	495.270435	Unit	761.422587	Unit	130	16.4	4	13.24	1.5	y6
MinE	DILEVICI(+57.021464)K	495.270435	Unit	648.338523	Unit	130	16.4	4	13.24	1.5	y5
MinE	DILEVICI(+57.021464)K	495.270435	Unit	519.29593	Unit	130	16.4	4	13.24	1.5	y4

Conitintuation from the previous page.

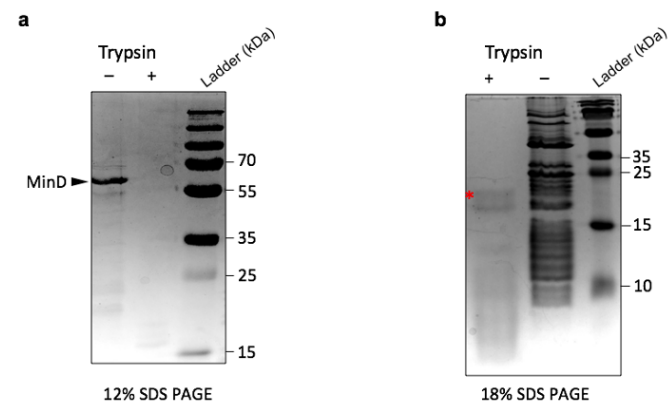
MinE	DILEVIC[+57,021464]K	495.270435	Unit	307.143452	Unit	130	16.4	4	13.24	1.5	y2
MinE	DILEVIC[+57,021464]K	495.270435	Unit	229.118283	Unit	130	16.4	4	13.24	1.5	b2
MinE	YVQIDPEMVTVQLEQK	960.492784	Unit	1416.703907	Unit	130	30.8	4	16.3	1.5	y12
MinE	YVQIDPEMVTVQLEQK	960.492784	Unit	1301.676964	Unit	130	30.8	4	16.3	1.5	y11
MinE	YVQIDPEMVTVQLEQK	960.492784	Unit	845.472708	Unit	130	30.8	4	16.3	1.5	y7
MinE	YVQIDPEMVTVQLEQK	960.492784	Unit	263.139019	Unit	130	30.8	4	16.3	1.5	b2
MinE	YVQIDPEMVTVQLEQK	960.492784	Unit	391.197596	Unit	130	30.8	4	16.3	1.5	b3
MinE	DGDISILELNVTLPEAEELK	1099.575556	Unit	1242.657609	Unit	130	35.1	4	21.53	1.5	y11
MinE	DGDISILELNVTLPEAEELK	1099.575556	Unit	1029.546267	Unit	130	35.1	4	21.53	1.5	y9
MinE	DGDISILELNVTLPEAEELK	1099.575556	Unit	928.498589	Unit	130	35.1	4	21.53	1.5	y8
MinE	DGDISILELNVTLPEAEELK	1099.575556	Unit	815.414525	Unit	130	35.1	4	21.53	1.5	y7
MinC	IAQAPAFLK	479.789652	Unit	774.450851	Unit	130	8.9	4	8.81	3	y7
MinC	IAQAPAFLK	479.789652	Unit	646.392273	Unit	130	8.9	4	8.81	3	y6
MinC	IAQAPAFLK	479.789652	Unit	575.355159	Unit	130	8.9	4	8.81	3	y5
MinC	IAQAPAFLK	479.789652	Unit	185.128454	Unit	130	8.9	4	8.81	3	b2
MinC	IAQAPAFLK	479.789652	Unit	384.224145	Unit	130	8.9	4	8.81	3	b4
MinC	MGLPILTEGK	529.79936	Unit	927.550959	Unit	130	11.5	4	12.53	3	y9
MinC	MGLPILTEGK	529.79936	Unit	870.529495	Unit	130	11.5	4	12.53	3	y8
MinC	MGLPILTEGK	529.79936	Unit	302.153288	Unit	130	11.5	4	12.53	3	b3
MinC	MGLPILTEGK	529.79936	Unit	625.37418	Unit	130	11.5	4	12.53	3	b6
EF-Tu	TTLTAAITTVLAK	652.39521	Unit	887.556044	Unit	130	21.2	4	16.34	1.5	y9
EF-Tu	TTLTAAITTVLAK	652.39521	Unit	816.51893	Unit	130	21.2	4	16.34	1.5	y8
EF-Tu	TTLTAAITTVLAK	652.39521	Unit	745.481817	Unit	130	21.2	4	16.34	1.5	y7
EF-Tu	TTLTAAITTVLAK	652.39521	Unit	632.397753	Unit	130	21.2	4	16.34	1.5	y6
EF-Tu	GITINTSHVEYDTPTR	601.96724	Unit	752.357344	Unit	130	16.9	4	9.26	1.5	y6
EF-Tu	GITINTSHVEYDTPTR	601.96724	Unit	474.267073	Unit	130	16.9	4	9.26	1.5	y4
EF-Tu	GITINTSHVEYDTPTR	601.96724	Unit	710.328587	Unit	130	16.9	4	9.26	1.5	y12
EF-Tu	GITINTSHVEYDTPTR	601.96724	Unit	187.113335	Unit	130	16.9	4	9.26	1.5	y3

Supplementary Table 2: Fit parameter values for the LC-MS calibration curves shown in Supplementary Fig. 3. The peptide IIVVTSGK of MinD was disregarded for further quantitation because the integrated peak intensity value of the peptide originating from the cell-free synthesized protein was higher than the value obtained with the most concentrated standard. The proteolytic peptides are listed according to their position along the amino acid sequence, i.e. from the most N-terminal (top) to the most C-terminal (bottom) as graphically represented in Fig. 1c for MinD/E and in Supplementary Fig. 4 for MinC. The standard rows for MinD and MinE were repeated on one day for two biological replicates for quantification after 180 min and a second time for a kinetic measurement. On both days, independent standard rows were measured and calculated peak areas were compared only to same-day standards.

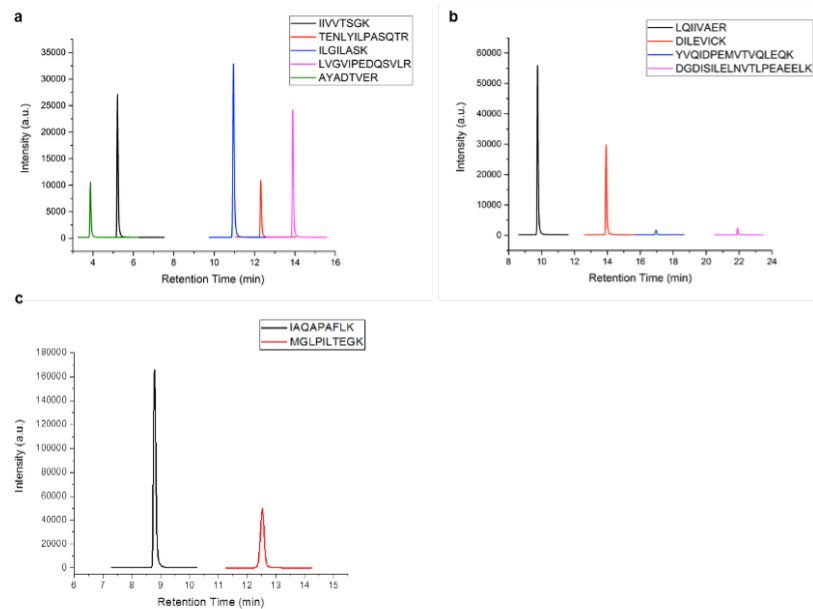
	Intercept value	Intercept standard error	Slope value	Slope standard error	R ² value
MinD (end-point assay)					
IIVVTSGK	-1422	894	6773	879	0.935
TENLYILPASQTR	-663	386	5522	217	0.993
ILGILASK	-2337	1878	19090	1235	0.983
LVGVIPEDQSVLR	-1350	717	9949	468	0.991
AYADTVER	-1019	456	4552	333	0.978
MinD (kinetic assay)					
IIVVTSGK	-1876	567	7859	329	0.993
TENLYILPASQTR	-4175	1157	11705	593	0.99
ILGILASK	-6153	1794	22846	686	0.996
LVGVIPEDQSVLR	-4883	1479	16642	688	0.993
AYADTVER	-2256	601	7091	329	0.991
MinE (end-point assay)					
LQIIVAER	-16171	3717	40112	3533	0.969
DILEVIC[+57]K	-11759	1405	21821	1743	0.974
YVQIDPEMVTVQLEQK	-1235	204	2152	237	0.953
DGDISILELNVTLPEAEELK	-1046	125	1887	173	0.967
MinE (kinetic assay)					
LQIIVAER	-13769	7191	36750	4990	0.930
DILEVIC[+57]K	-7882	2820	18262	2406	0.934
YVQIDPEMVTVQLEQK	-620	195	1627	252	0.910
DGDISILELNVTLPEAEELK	-660	353	2080	367	0.886
MinC (end-point assay)					
IAQAPAFLK	-501	2080	29228	2236	0.966
MGLPILTEGK	-1820	225	14575	333	0.997

Supplementary Table 3: List of primers used in this study

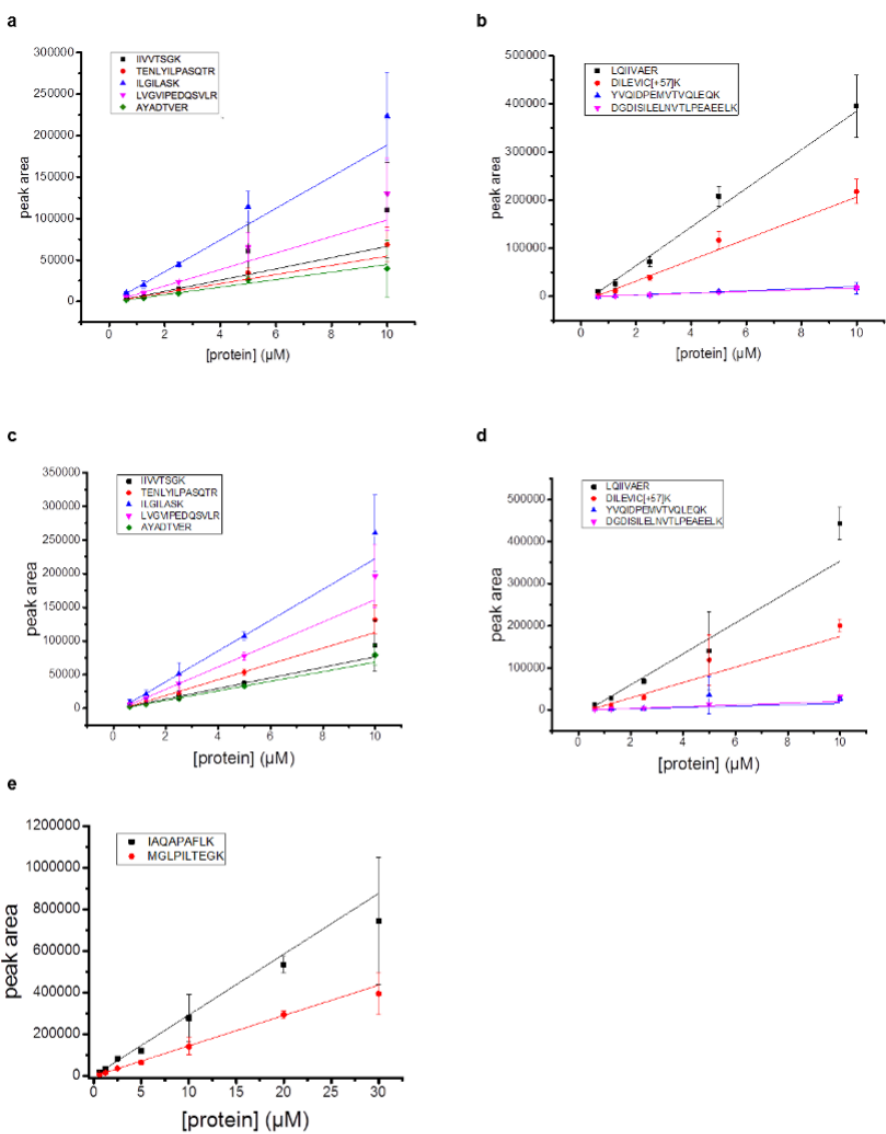
Name	Sequence (5' 3')
ChD382	TCCTTTCGGGCTTTGTAGCAGCCGGATCCTTATCCTCCGAACAAGCGTTTG
ChD384	TCCTTTCGGGCTTTGTAGCAGCCGGATCCTTATTCAGCTCTTCTGCTTCC
ChD511	TTAACTTTAAGAAGGAGATATACATATGGCAGCATTATTGTTG
ChD512	TTAACTTTAAGAAGGAGATATACATATGGCATTACTCGATTTCTTTCTC
ChD709	CAAAAAACCCCTCAAGACCCGTTTAGAGG
ChD757	TAATACGACTCACTATAGGG



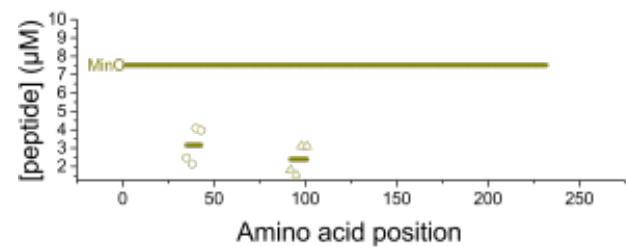
Supplementary Fig. 1: Validation of protein digestion for quantification by LC-MS. **a**, Coomassie stained SDS PAGE loaded with 1.48 μg of purified MinD and 0.5 μg MinE (equivalent to 10 μM) which were used as a standard for mass spectrometry measurements. The first lane contains the undigested protein sample. The second lane was loaded with a similar sample digested with trypsin (See Methods section). The MinE band is not visible on this gel (below the 15 kDa marker). 5 μl of Pageruler plus ladder was loaded. **b**, Coomassie stained SDS PAGE loaded with PURE $_{\text{frex2.0}}$ after 3 h co-expression of the *minD* and *minE* genes. The sample was either loaded directly or after treatment with Trypsin. The star indicates the Trypsin band. 5 μl of Pageruler plus ladder was loaded. Complete protein digestion with both purified MinDE and PURE $_{\text{frex2.0}}$ samples was confirmed. Source data are provided as a Source Data file.



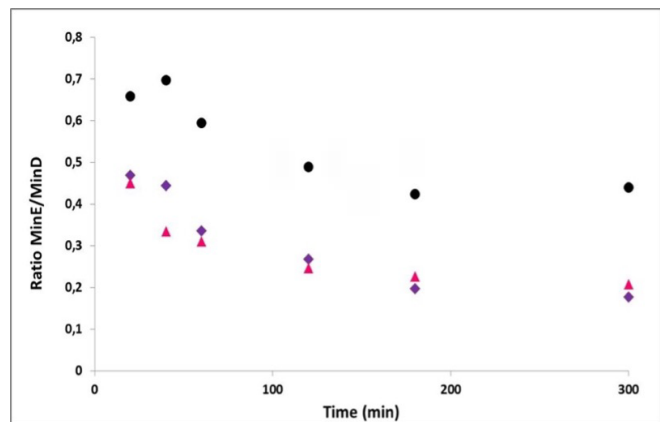
Supplementary Fig. 2: Peptide chromatograms of the LC-MS method. **a**, MinD proteolytic peptides. **b**, MinE proteolytic peptides. **c**, MinC proteolytic peptides.



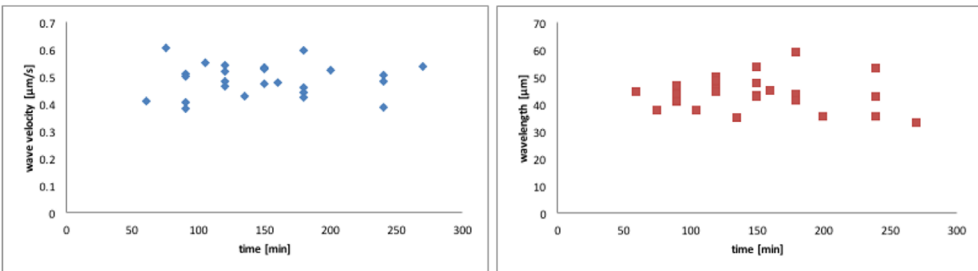
Supplementary Fig. 3: LC-MS calibration curves with MinD and MinE protein standards. The peak area of various proteolytic peptides is plotted versus different concentrations of purified MinD (**a**) and MinE (**b**) for two PURE system reactions incubated for 180 min. Panels (**c**) and (**d**) show a similar calibration for three additional reactions in order to provide kinetic data about MinD and MinE co-expression. **e**, Calibration for the two peptides of MinC. Linear fits through the measurement points are appended for each peptide. Each point represents the average of three independent measurements and the error bars indicate standard deviation. The amino acid sequences of the considered MinD-, MinE- and MinC-specific peptides are displayed in the legend boxes. The extracted fit parameters are reported in Supplementary Table 2. Source data are provided as a Source Data file.



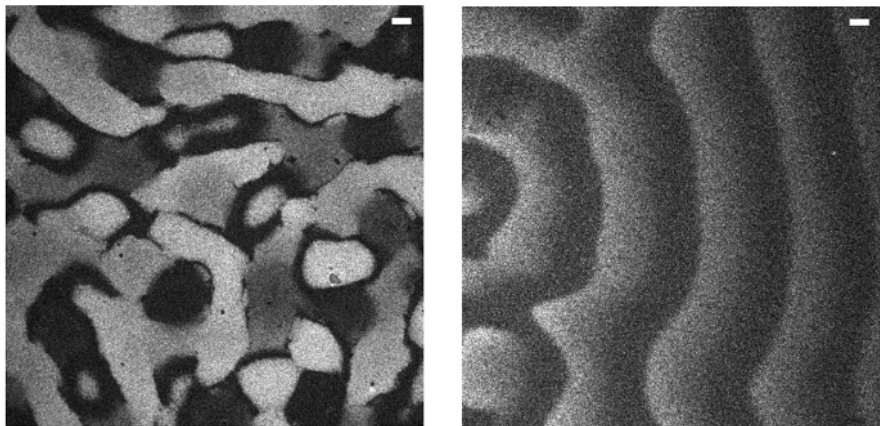
Supplementary Fig. 4: Concentration of MinC proteolytic peptides plotted as a function of their position in the protein primary sequence. The markers represent measurements from four different experiments and the average values are displayed as short segments whose length corresponds to the peptide length. The MinC-annotated line depicts the full length sequence. Source data are provided as a Source Data file.



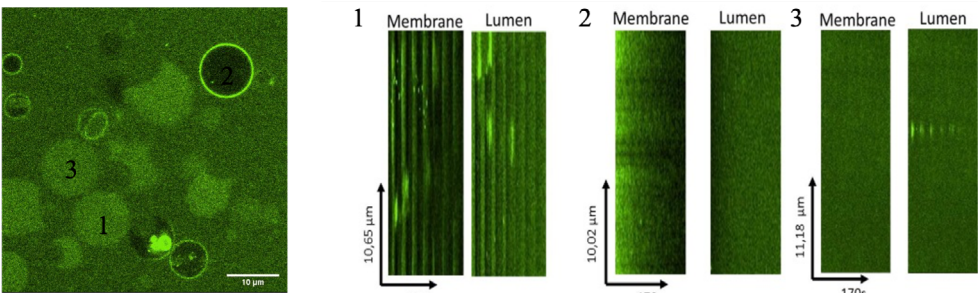
Supplementary Fig. 5: Concentration ratio of MinE and MinD C-terminal peptides in the course of a co-expression reaction. The different markers correspond to data from three independent experiments shown in Fig. 1d.



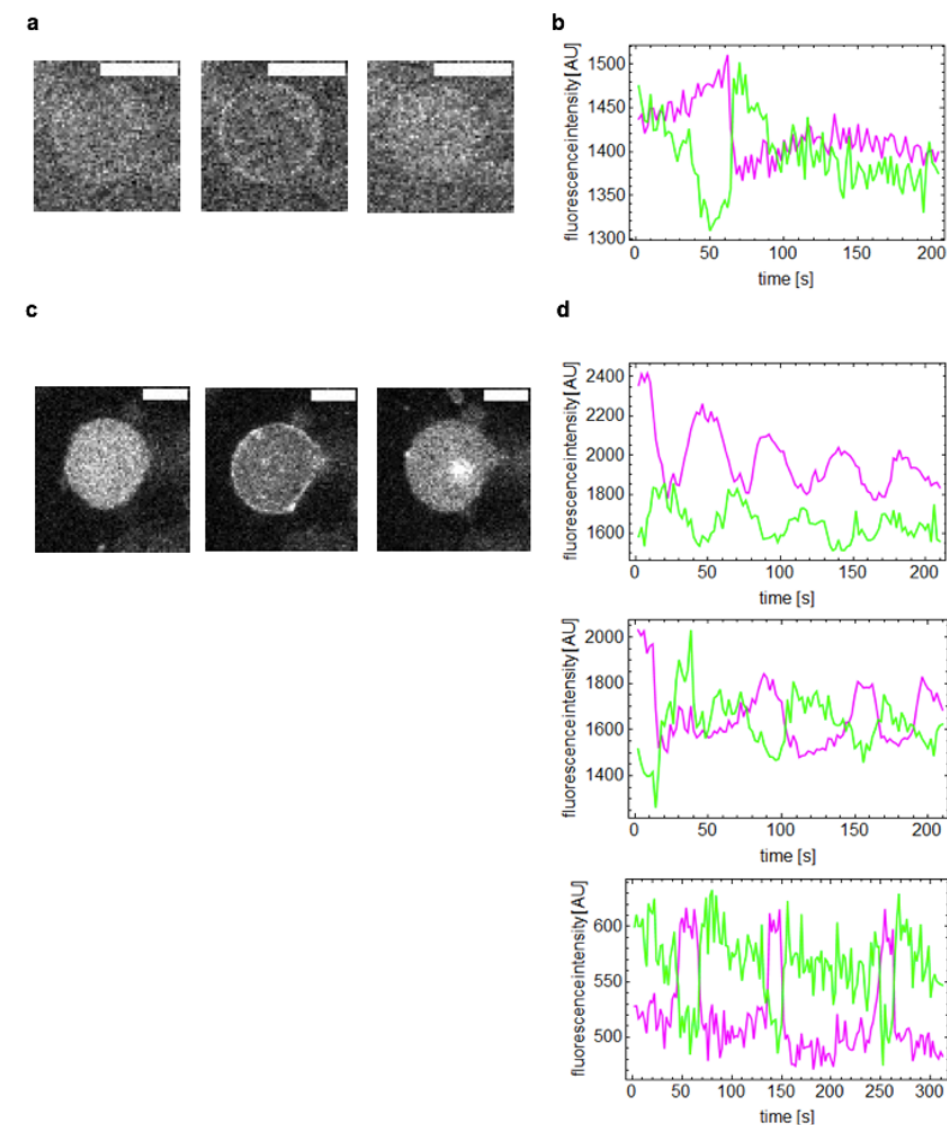
Supplementary Fig. 6: Quantification of Min pattern dynamics from SLB assays with in situ co-expressed MinD/E proteins. Data points are from five different fields of view imaged at different time points, and they have been collected from two independent kinetic experiments.



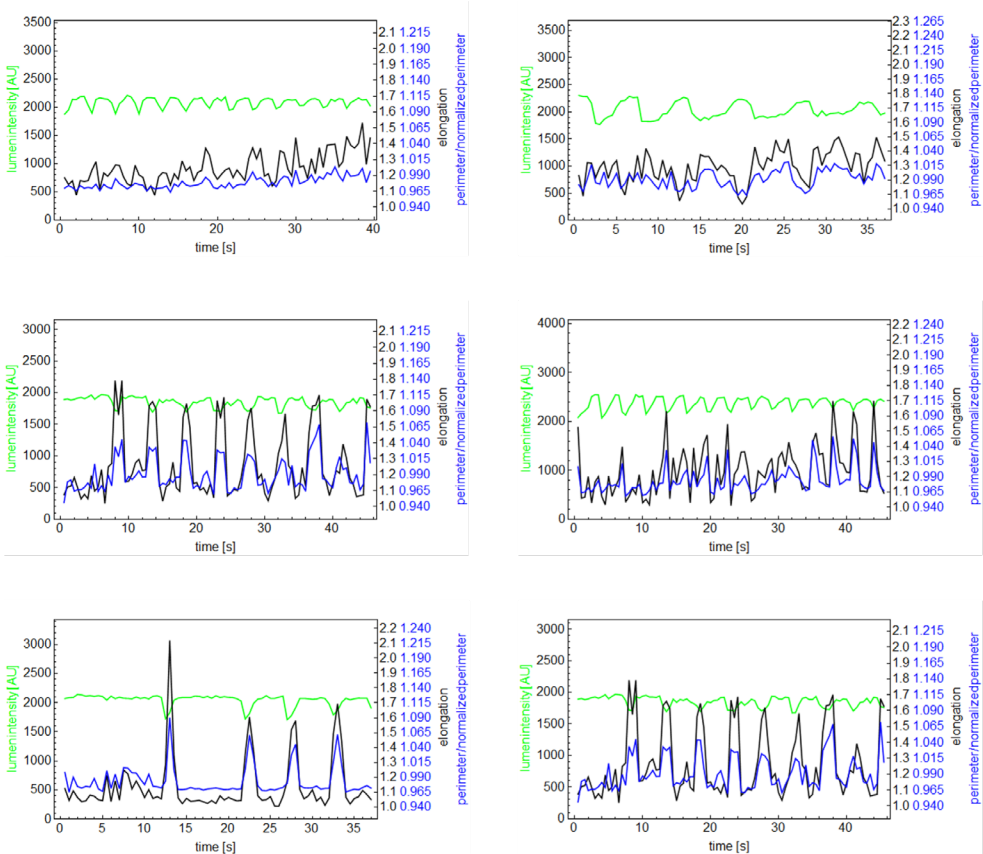
Supplementary Fig. 7: Representative patterns of purified MinD/E proteins mixed in a pre-ran PUREflex2.0 solution containing the TP-coding DNA and added on top of an SLB. Standing waves (left panel) and traveling waves (right panel) are observed. MinD and MinE were used at 1 μM each. Traveling waves have a wavelength of ~ 61 μm and a velocity of ~ 0.47 μm s⁻¹. Corresponding videos are shown in Supplementary Movie 3. Scale bars are 10 μm.



Supplementary Fig. 8: Image analysis of liposomes whose membrane signal attenuates over time while the lumen signal correspondingly increases. Fluorescence microscopy image acquired in the eGFP-MinC channel under similar conditions as shown in Fig. 3 and Fig. 4. The three liposomes analyzed are numbered and their corresponding kymographs are displayed. Liposome 1 exhibits a Min pulsing behavior. The amplitude of the membrane signal decreases over time, while the fluorescence in the lumen proportionally increases. Liposome 2 does not undergo oscillations, but eGFP-MinC is initially recruited to the membrane. The kymograph shows that the membrane signal continuously attenuates over time, while the lumen fluorescence intensity increases. This observation suggests that the ability of MinD to bind to the membrane decreases over time, perhaps a consequence of ATP depletion in this liposome. In Liposome 3, eGFP-MinC is only localized in the lumen and the intensity remains constant during the measurement period. This observation indicates that photobleaching is negligible.

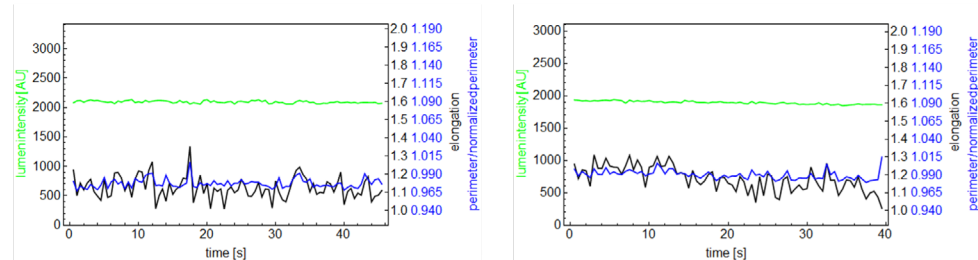


Supplementary Fig. 9: Min oscillations in liposomes using eGFP-MinD or low concentration of eGFP-MinC as a reporter. **a**, Time sequence images of a liposome expressing MinD/E in the presence of 0.4 μ M of eGFP-MinC. **b**, Corresponding time traces of the fluorescence intensity at the membrane (magenta) and in the lumen (green). **c**, Time sequence images of a liposome expressing MinD/E in the presence of 0.2 μ M of eGFP-MinD. **d**, Time traces of the fluorescence intensity at the membrane (magenta) and in the lumen (green) for three liposomes. The upper most panel corresponds to the liposome shown in (c). Scale bars are 5 μ m.

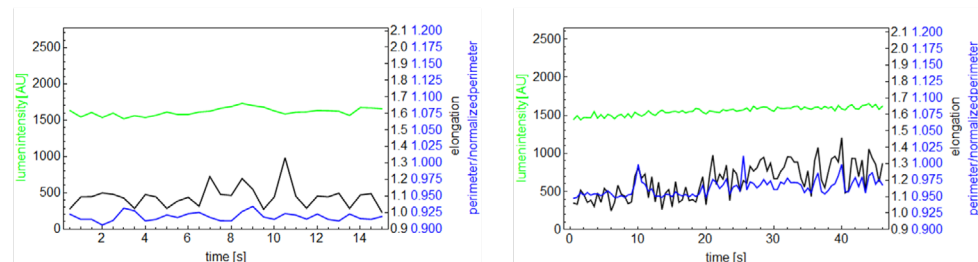


Supplementary Fig. 10: Boundary signature plots of six waving liposomes in hypertonic conditions. Lumen fluorescence intensity is colored in green, liposome elongation in black and perimeter in blue. See the Methods section for the definition of the parameters. The experimental conditions are identical as in Fig. 5. The results show that periodic MinDE-induced relocation of eGFP-MinC from the lumen to the membrane is accompanied with an increase of liposome elongation and perimeter.

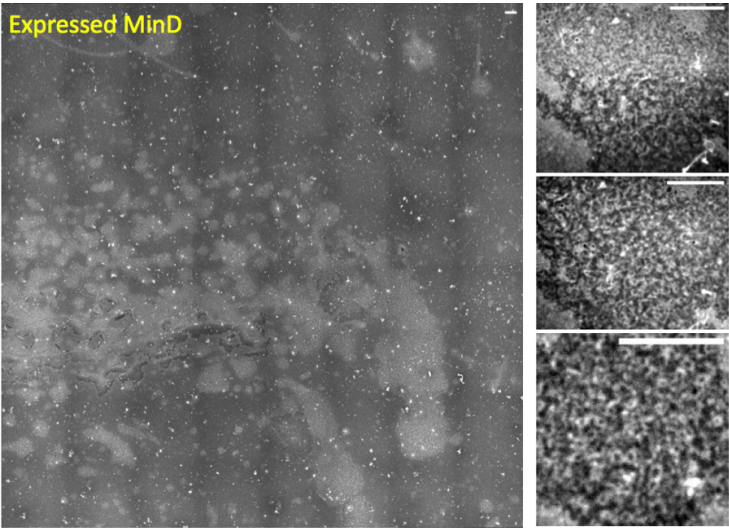
No oscillations, no membrane recruitment



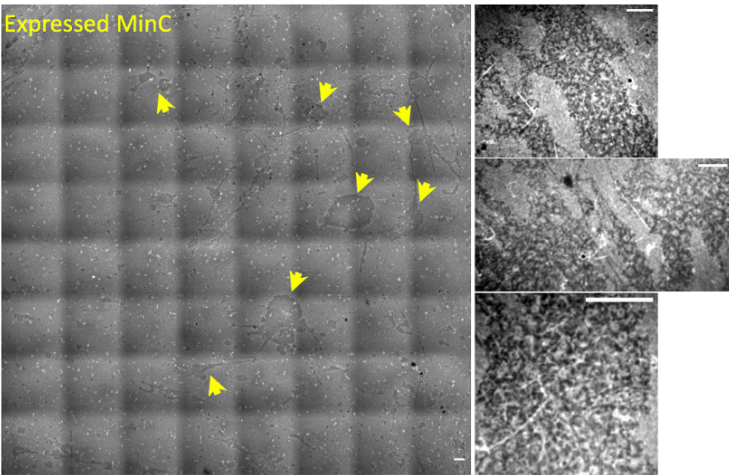
No oscillations, but membrane recruitment



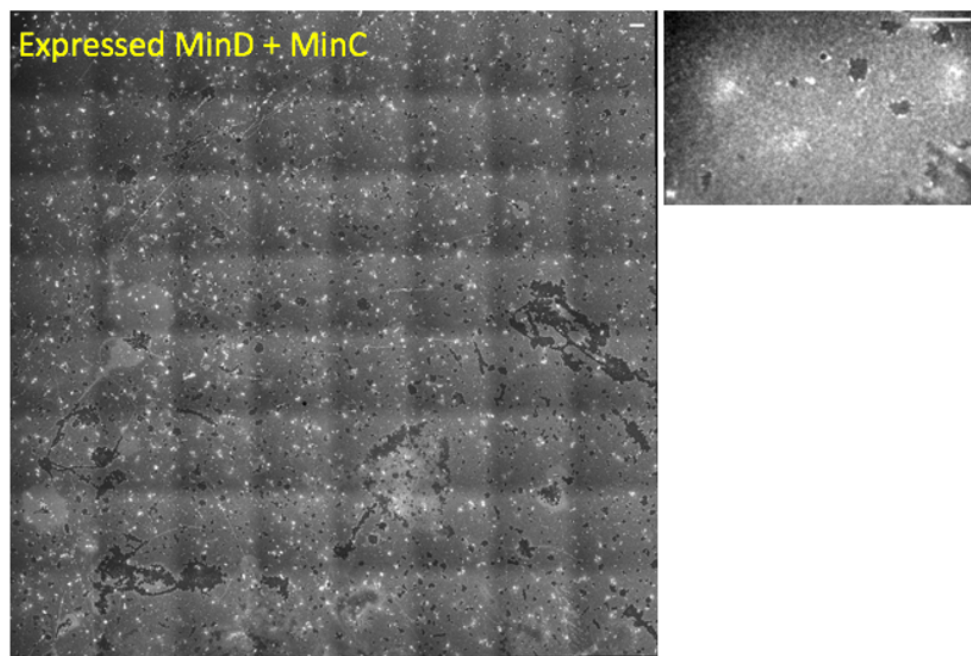
Supplementary Fig. 11. Boundary signature plots of four non-waving liposomes in hypertonic conditions. Lumen fluorescence intensity is colored in green, liposome elongation in black and perimeter in blue. See the Methods section for the definition of the parameters. The experimental conditions are identical as in Fig. 5. A clear difference in the time-course of the parameters is observed compared to Min oscillating liposomes (Supplementary Fig. 10).



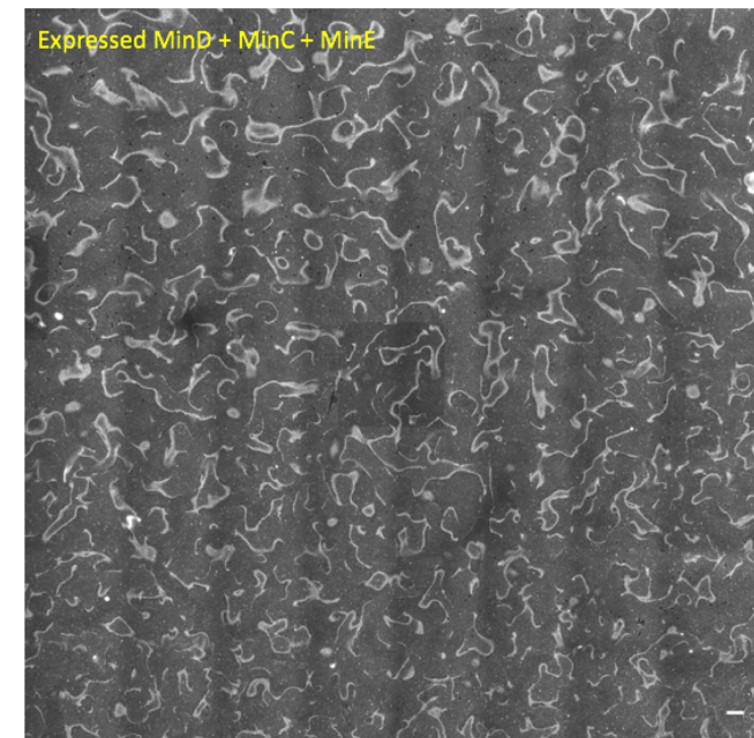
Supplementary Fig. 12: Expressed MinD was mixed with expressed FtsA, expressed TP and purified FtsZ-Alexa647, and added on top of an SLB. The conditions are as described in Fig. 6a. The large panel is a montage of 8 x 8 fields of view acquired by laser scanning confocal microscopy. The lighter areas of the SLB contain FtsZ ring-like structures. Scale bar is 20 μm. The smaller panels are zoom-in images of the SLB displaying FtsZ bundles and rings. Those images were acquired by spinning disc microscopy. Scale bars are 10 μm.



Supplementary Fig. 13: Expressed MinC was mixed with expressed FtsA, expressed TP and purified FtsZ-Alexa647, and added on top of an SLB. The conditions are as described in Fig. 6a. The large panel is a montage of 8 x 8 fields of view acquired by laser scanning confocal microscopy. The arrowheads point to areas of the SLB containing FtsZ ring-like structures. Scale bar is 20 μm. The smaller panels are zoom-in images of the SLB displaying FtsZ bundles and rings. Those images were acquired by spinning disc microscopy. Scale bars are 10 μm.



Supplementary Fig. 14: Expressed MinC and MinD were mixed with expressed FtsA and purified FtsZ-Alexa647, and added on top of an SLB. The conditions are as described in Fig. 6a. The large panel is a montage of 8 x 8 fields of view acquired by laser scanning confocal microscopy. FtsZ is recruited to the membrane but no ring-like structures appear. Scale bar is 20 μm . The smaller panel is a zoom-in image of the SLB. This image was acquired by spinning disc microscopy. Scale bar is 10 μm .



Supplementary Fig. 15: Expressed MinC and MinD/E were mixed with expressed FtsA and purified FtsZ-Alexa647, and added on top of an SLB. The conditions are as described in Fig. 6c (pattern 1). The image is a montage of 8 x 8 fields of view acquired by laser scanning confocal microscopy. FtsZ is recruited to the membrane and forms dynamic patterns. Scale bar is 20 μm .

Supplementary files

The Supplementary Movies and Source Data file are provided here <https://www.nature.com/articles/s41467-019-12932-w#Sec27>

Cell-free biogenesis of bacterial division proto-rings that can constrict liposomes

Elisa Godino, Jonás Noguera López, Ilias Zarguit, Anne Doerr, Mercedes Jimenez, Germán Rivas, Christophe Danelon

A major challenge towards the realization of an autonomous synthetic cell resides in the encoding of a division machinery in a genetic programme. In the bacterial cell cycle, the assembly of cytoskeletal proteins into a ring defines the division site. At the onset of the formation of the *Escherichia coli* divisome, a proto-ring consisting of FtsZ and its membrane-recruiting proteins takes place. Here, we show that FtsA-FtsZ ring-like structures driven by cell-free gene expression can be reconstituted on planar membranes and inside liposome compartments. Such cytoskeletal structures are found to constrict the liposome, generating elongated membrane necks and budding vesicles. Additional expression of the FtsZ cross-linker protein ZapA yields more rigid FtsZ bundles that attach to the membrane but fail to produce budding spots or necks in liposomes. These results demonstrate that gene-directed protein synthesis and assembly of membrane-constricting FtsZ-rings can be combined in a liposome-based artificial cell.

Essentially as published: Godino, E. *et al.* Cell-free biogenesis of bacterial division proto-rings that can constrict liposomes. *Commun. Biol.* **3**, (2020).

Introduction

Cell-free biology aims at understanding cellular processes by reconstituting biological functions from their isolated elementary components in in vitro model systems. Owing to their openness and easy manipulation, cytoplasmic extracts and systems reconstituted from purified elements are more amenable to customized experimental design and quantitative description compared to living cells. Therefore, the minimal requirements to achieve a particular function can be assessed more reliably. Many complex biological structures and processes taking place in bacterial or eukaryotic cells have already been reconstituted in vitro. Notable achievements include the reconstitution of the minimal translation machinery from *Escherichia coli*¹, the yeast DNA replication apparatus², filopodial structures³, cytoskeleton self-organization and centrosome positioning⁴, egg cytokinesis signaling⁵, DNA segregation with Par⁶, and clathrin-coated buds⁷. Encouraged by the many cellular pieces that have already been reconstituted in vitro, synthetic biologists have now engaged in the construction of an entire cell^{8–12}.

One of the hallmarks of living systems is their ability to divide. An obvious starting point to conceiving a biology-inspired division mechanism in artificial cells is to consider the canonical pathways taking place in prokaryotes. In most bacteria, symmetrical cell division proceeds by forming a constriction ring that eventually splits the mother cell into equally sized daughter cells¹³. At an earlier stage of cytokinesis, a proto-ring composed of the FtsZ, FtsA and ZipA proteins, assembles on the inner leaflet of the cytoplasmic membrane at the future division site^{14–16}. The tubulin-related FtsZ is the core constituent of the proto-ring. FtsZ is a GTPase that can polymerize into protofilaments^{17,18}. Anchoring of FtsZ protofilaments to the cytoplasmic membrane is mediated by ZipA and the actin homologue FtsA^{19–21}. This process is regulated by accessory proteins belonging to the Zap family²².

Earlier attempts to divide cell-like liposomal compartments have focused on the reconstitution of the Z-ring from purified proteins^{23,24}. These studies have shown that FtsZ aided by one of its anchoring protein partners - or a chimeric FtsZ bearing a membrane targeting segment²⁵ - can self-organize into filament patterns on supported lipid membranes^{25–28}. When encapsulated inside vesicles, the elementary cytoskeletal proteins form ring-like structures that can deform the liposome membrane^{24,29,30}. Whether FtsZ filaments alone exert a contractile force and contribute to the final stage of division remains a subject of debate^{31,32} and evidence for complete liposome division is still lacking.

A conceptual issue which is inherent to reconstitution assays solely relying on purified proteins, is the impossibility to maintain steady amounts of cytoskeletal proteins from internal mechanisms as the compartment undergoes division. Another problem raised by conventional cell-free assays is the use of oversimplified buffer compositions that have been tailored for a particular set of enzymatic reactions but fail to reproduce the cytoplasmic environment.

Herein, we address these issues by encoding *E. coli* division proteins on DNA templates. Genetic control over protein production offers a general solution to achieve self-replication, as well as self-regulation by establishing feedback loops. In this context, the PURE system, a minimal gene expression system reconstituted primarily from *E. coli* constituents¹ was employed. Different types of proteins and biological functions have already been synthesized de novo with the PURE system, including membrane-associated proteins^{10–12,33}. Moreover, by containing all relevant factors for gene expression, the PURE system emulates more closely the molecular composition of the bacterial cytoplasm than simple buffers. In the present study we utilized PUREflex2.0 which provides the best combination of protein yield and expression lifespan^{34,35}.

We show that cell-free expressed FtsA is able to recruit FtsZ polymers, forming large-scale two-dimensional networks of curved and ring-like structures in the absence of bundling factors. When the entire set of reactions is encapsulated inside liposomes, proto-rings of FtsA-FtsZ filaments are found to constrict the vesicle, generating extended membrane necks and budding vesicles, a phenotype that has not been reported before. Co-expression of ZapA, a native stabilizer of FtsZ filaments, yields stiffer FtsZ bundles attached to the membrane that fail to constrict into bud necks. FtsZ cytoskeletal structures are also investigated with ZipA membrane-anchor protein. We find that in our low-volume supported lipid bilayers (SLBs) assays with ZipA and $\leq 3 \mu\text{M}$ FtsZ, the generic crowding agent Ficoll70 is necessary to elicit bundle formation. Cell-free expressed ZapA obviates the need of Ficoll70 and promotes formation of cytoskeletal networks with different, likely more physiological, morphology and protein monomer dynamics. The prospects of further improvement suggest that the DNA-programmed hierarchical assembly of the Z-ring in liposomes is a promising strategy for dividing synthetic cells. In addition, our approach to reconstituting cellular processes in PURE system provides a generic platform that fills the gap between classical in vitro and in cellulo experiments.

Results

Cell-free synthesized FtsA drives the formation of curved FtsZ filaments

An essential component of the *E. coli* division proto-ring is FtsA, a homologue of actin that anchors FtsZ filaments to the cytoplasmic membrane. To bypass the difficult purification of FtsA²⁸, we directly expressed a sequence optimized *ftsA_{opt}* gene on a supported lipid bilayer (SLB) (Fig. 1a). In the presence of $3 \mu\text{M}$ purified FtsZ-A647, curved filaments and dynamic ring-like structures formed on the membrane (Fig. 1b, Supplementary Fig. 1, Supplementary Note 1, Movie 1), concurring with previous reports^{12,28}.

To obtain quantitative insights about the concentration of cell-free synthesized FtsA, pre-ran PURE system samples were analysed by liquid chromatography-coupled mass spectrometry (LC-MS) (Supplementary Fig. 2, Supplementary Table 1). Protein abundance was quantified

using an internal standard (QconCAT) for the most C-terminal peptide detected. We deduced that, after 3 h of expression, FtsA concentration on the SLB was $2.2 \pm 0.2 \mu\text{M}$ (mean \pm SD, three biological repeats) (Fig. 1a-d, Supplementary Tables 2, 3), corresponding to a protein ratio [FtsZ]:[FtsA] 1.5:1. In vivo, FtsA concentration is about $0.5 \mu\text{M}$ and the protein ratio [FtsZ]:[FtsA]=3:1 to 5:1³⁶. However, overlapping rings and dynamic filaments on lipid membrane have also been observed at protein ratios similar as in our cell-free assay^{26,28}. Note that LC-MS data do not report the concentration of active protein, which may differ from the measured concentration of proteolytic peptides.

Promoting lateral interactions of FtsZ protofilaments stimulates the formation of higher-order cytoskeletal structures in vitro³⁷. However, little is known about how the nature of these lateral interactions influences the morphology of the FtsZ network. Therefore, we decided to investigate the architecture and dynamics of FtsZ protofilaments in a molecular environment that favours lateral interactions. First, we employed Ficoll70, a generic crowding agent known to elicit FtsZ bundle formation (Fig. 1c). Large SLB areas were covered with curved filaments, rings of different sizes (most having a diameter of 1 – 2 μm , phenotype 1) and large circular patterns (phenotype 2) (Fig. 1d).

Although Ficoll70 is commonly used as a macromolecular crowder to mimic cytoplasmic conditions^{24,33,38,39}, we reasoned that ZapA, an in vivo regulator of FtsZ polymerization, would provide a more targeted and native mechanism to elicit lateral interaction, thus conferring physiologically relevant properties of cytoskeletal patterns. For this reason, ZapA was produced in PUREfrex2.0 starting from its native gene sequence. Substitution of Ficoll70 with cell-free synthesized ZapA produced curved bundles but also long and straight filaments of FtsZ-A647 recruited to the membrane by cell-free synthesized FtsA (Fig. 1e,f). The concentration of cell-free synthesized ZapA in the SLB assay was estimated by LC-MS to be $0.2 \pm 0.1 \mu\text{M}$ (mean \pm SD, three biological repeats, Supplementary Table 3), which is significantly lower than in *E. coli* ($1.5 \mu\text{M}$)⁴⁰. Remarkably, even at such a low concentration, ZapA is able to reshape FtsZ protofilaments (Fig. 1f).

Quantitative image analysis revealed that both the curvature and occurrence of branching points of the filament network were reduced in the presence of either Ficoll70 or ZapA (Supplementary Fig. 3b). Differences between the two phenotypes observed in each condition were also quantified (Supplementary Fig. 3c). We speculate that local changes, such as protein concentration (e.g., due to edge effects in the chamber) and possible defects in the membrane, may play a role in the nucleation, morphology or dynamics of the cytoskeletal network, therefore driving formation of one versus the other phenotype on the same SLB.

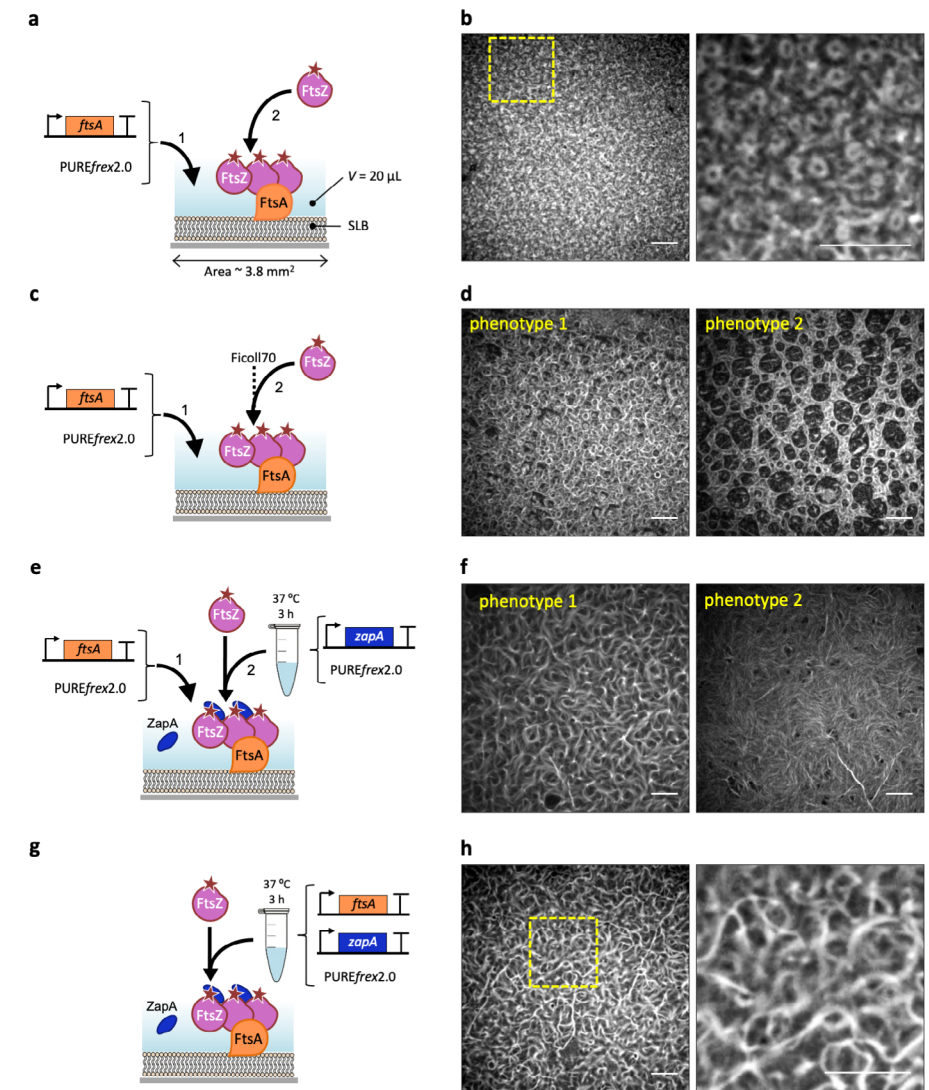


Figure 1: Cell-free expressed FtsA recruits FtsZ to an SLB and drives the formation of ring-like structures. **a**, Schematic representation of the SLB assays with FtsA directly expressed on the membrane. Purified FtsZ-A647 ($3 \mu\text{M}$) was added. The sequence-optimized construct *ftsA_{opt}* was used. **b**, Fluorescence image of FtsZ-A647 forming curved filaments and rings in the presence of in situ synthesized FtsA. The zoom-in image (right) corresponds to the framed region in the left image. **c**, As in **a**, but the solution was supplemented with Ficoll70. **d**, Fluorescence image of FtsZ-A647 forming curved filaments and rings in the presence of in situ synthesized FtsA and Ficoll70. Two representative filament network morphologies observed on the same SLB are shown, phenotype 1 being the most prominent. **e**, Schematic illustration of the SLB assays with separately expressed FtsA and ZapA. The constructs *ftsA_{opt}* and *zapA* were used. Purified FtsZ-A647 ($3 \mu\text{M}$) was included. **f**, Fluorescence images of FtsZ-A647 displaying two representative phenotypes from different regions of the same SLB, phenotype 1 being the

most prominent. **g**, Schematic illustration of the SLB assays with co-expressed FtsA and ZapA from *ftsA_{opt}* and *zapA_{opt}* constructs. Purified FtsZ-A647 (3 μ M) was added. **h**, Fluorescence images of FtsZ-A647. The zoom-in image (right) corresponds to the framed area in the left image. Scale bars indicate 10 μ m.

We challenged the PURE system to co-express both FtsA and ZapA in a single reaction. Given the low amount of ZapA produced in a single-gene reaction and the extra burden imposed on the biosynthesis machinery when expressing an additional gene, we attempted to boost ZapA concentration by substituting the native gene with a sequence optimized *zapA_{opt}* DNA construct (Supplementary Fig. 4). Co-expression of the *ftsA_{opt}* and *zapA_{opt}* genes in a one-pot PURE system reaction led also to the formation of bended and straight bundles (Fig. 1g,h, Supplementary Fig. 5) that qualitatively resemble phenotype 1 obtained in separate expression (Fig. 1e,f). Protein quantification was performed by LC-MS, and concentrations values of 2.4 ± 0.3 μ M FtsA and 0.4 ± 0.2 μ M ZapA in the SLB assay were determined (mean \pm SD, three biological repeats, Supplementary Table 3). Quantitative inspection of the protein patterns in co-expression experiments shows a lower curvature and branch point density than in single-gene expression assays (Supplementary Fig. 3b), which may be attributed to higher protein concentrations on the SLB when FtsA and ZapA are co-expressed (Supplementary Table 3). Note again that LC-MS data do not provide an accurate measure of the concentration of active protein. Furthermore, usage of PURE system substrates and cofactors, such as the tRNAs and NTPs, is different in a single-gene or double-gene expression (e.g. nucleotide and codon abundance), which may influence reactions not directly involved in transcription/translation. Despite morphological differences observed in the protein patterns between the Ficoll70- and ZapA-containing samples, quantitative analysis of FtsZ subunit dynamics by fluorescence recovery after photobleaching (FRAP) revealed similar recovery halftime values under the tested conditions (Supplementary Fig. 6).

Formation of long sZipA-FtsZ cytoskeletal structures

We then examined the self-organization of FtsZ with the membrane anchor soluble ZipA (sZipA) using purified proteins supplied in a minimal buffer or in PURE_{frex2.0} background. The soluble variant sZipA does not contain the transmembrane region by elimination of the hydrophobic N-terminal domain (amino acids 1-25) of the full-length protein. This domain was substituted by a His₆-tag for binding NTA-conjugated lipids. The FtsZ-binding properties of sZipA are essentially the same as those of the native protein when incorporated in nanodiscs^{41,42}. We found that in our low-volume SLB assays with ≤ 3 μ M FtsZ, filament bundling with either Ficoll70 or ZapA was required to trigger large-scale cytoskeletal networks (Fig. 2a,b, Supplementary Note 2). This result contrasts with previous observations^{20,28}, highlighting the role of the total reaction volume as a control parameter in the formation of cytoskeletal patterns. The network morphology, as well as the sZipA and FtsZ monomer dynamics differ whether lateral interactions are promoted by the artificial molecular crowder

Ficoll70 or by cell-free synthesized ZapA (Fig. 2c-f, Supplementary Fig. 7-11). Moreover, we found that increasing the expression level of ZapA (Supplementary Fig. 4) results in more stable filaments that can even extend above the SLB (Supplementary Fig. 8,9). Taken together, our results show that ZapA encourages the formation of membrane-bound sZipA-FtsZ filament network having a different - presumably more physiological - morphology and subunit turnover compared to Ficoll70.

We conclude from these SLB experiments that short, curved filaments and rings that resemble physiological structures are more prominent with FtsA compared to sZipA, and can develop in the absence of a bundling agent.

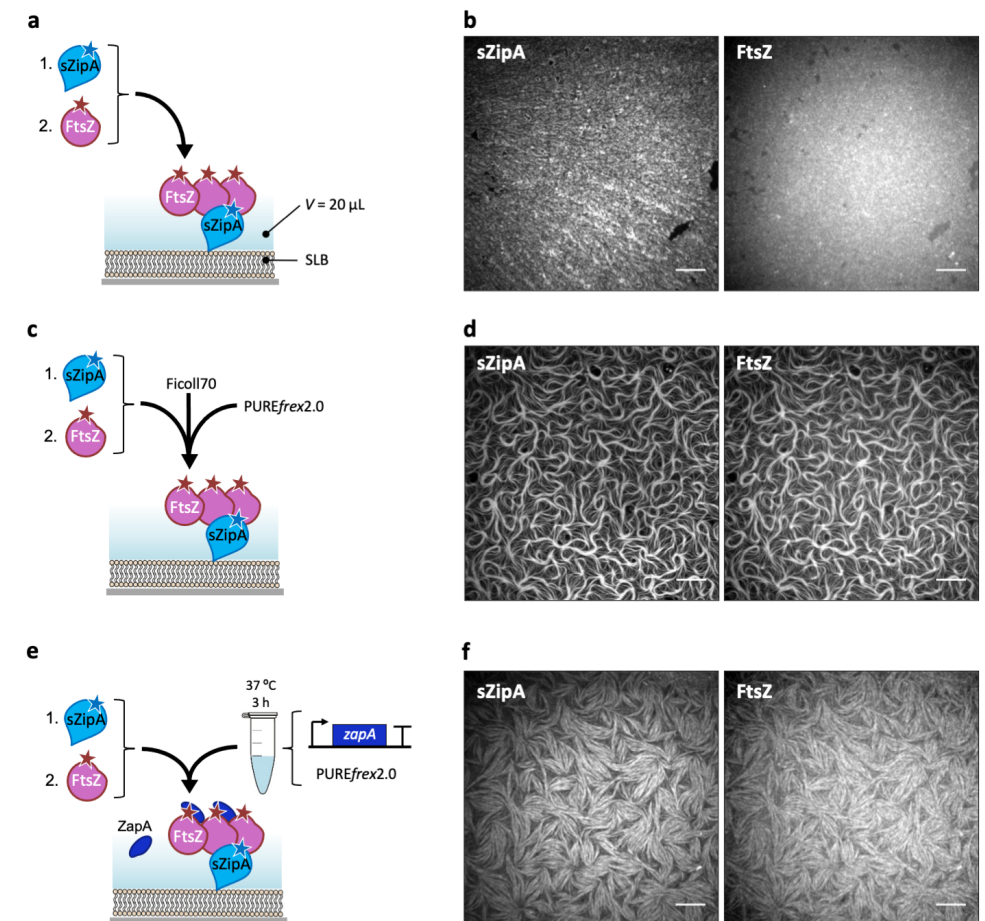


Figure 2: Purified sZipA and FtsZ form co-filament networks in the PURE system. **a**, Schematic representation of the SLB assays. Purified sZipA-A488 was first incubated on an SLB. The solution on top of the SLB was replaced by a minimal reaction buffer containing 3 μ M purified FtsZ-A647 and 2 mM GTP. **b**, Fluorescence images of sZipA-A488 (left) and FtsZ-A647 (right) in the minimal reaction buffer

without Ficoll70. **c**, Schematic representation of the SLB assays. Purified sZipA-A488 was first incubated on an SLB. The solution on top of the SLB was replaced by PURE_{flex}2.0 supplemented with 3 μ M purified FtsZ-A647, 2 mM GTP and 50 g L⁻¹ Ficoll70. **d**, Fluorescence images of sZipA-A488 (left) and FtsZ-A647 (right) in PURE_{flex}2.0 with Ficoll70. Large-scale filaments with co-localizing FtsZ-A647 and sZipA-A488 are exclusively observed in the presence of Ficoll70. This conclusion is valid in both the minimal reaction buffer and in PURE_{flex}2.0 background. More fields of view are displayed in Supplementary Fig. 7. **e**, Schematic illustration of the SLB assays with purified FtsZ-A647 (3 μ M) and cell-free synthesized ZapA incubated on top of an sZipA-A488-bound SLB. ZapA was expressed from the native gene *zapA*. **f**, Fluorescence images of sZipA-A488 (left) and FtsZ-A647 (right) in a sample containing cell-free synthesized ZapA and additional 2 mM GTP. Different cytoskeletal network phenotypes were observed when ZapA concentration was increased upon expression of the optimized *zapA*_{opt} construct (Supplementary Fig. 9). Scale bars indicate 10 μ m.

The identification of FtsZ and FtsA as the minimal molecular set to obtain membrane-anchored curved filaments and rings in the PURE system prompted us to reconstitute FtsA-FtsZ cytoskeletal networks inside liposomes (Fig. 3a). The cell-free gene expression solution was supplemented with adenosine triphosphate (ATP, additional 2 mM), guanosine triphosphate (GTP, additional 2 mM) and a mixture of highly purified chaperones (DnaK mix). Although energy regeneration components are present in the PURE system, extra ATP and GTP were provided to compensate for the extra demand from FtsA and FtsZ. Purified FtsZ-A647 was used to visualize protein localization by laser scanning confocal microscopy. FtsZ-A647 was employed at 3 μ M concentration which is similar to that measured in vivo (\sim 3.5 μ M)³⁶. Liposomes were formed by natural swelling, with a composition of zwitterionic PC and PE phospholipids, anionic PG and cardiolipin, and a small fraction of TexasRed-conjugated lipid for membrane imaging³⁵. Such a lipid mixture and liposome preparation method have proved compatible with the cell-free synthesis of membrane-associated enzymes¹⁰, DNA replication proteins¹¹ and division proteins¹². Liposome size distribution ranges from \sim 1 μ m up to over 15 μ m in diameter, which provides a more relevant bacterial cell-size compartment than >20 μ m liposomes produced with other methods^{23,33}. In contrast with previous studies³³, no crowding agent was included during liposome formation. In fact, we found that Ficoll70 impairs formation of gene-expressing liposomes with our methodology (Supplementary Fig. 12).

In control experiments where the *ftsA*_{opt} gene was omitted, FtsZ was exclusively located in the liposome lumen (Supplementary Fig. 13). De novo synthesized FtsA successfully recruited FtsZ on the membrane as shown by the co-localization of the FtsZ-A647 and membrane dye signals (Fig. 3, Supplementary Fig. 14). Although homogeneous recruitment of FtsZ to the membrane was commonly found within the liposome population, the majority of the liposomes displayed regions with patches of FtsZ on the inner surface of the membrane (Fig. 3b). Noticeably, the membrane spots with clustered FtsZ coincide with different types of membrane remodelling. In some cases, the recruited FtsZ localizes with outward membrane deformation or short protrusions (Fig. 3c, Supplementary Fig. 15). In other instances, the

protrusions developed into vesicles or blebs tethered to the parental liposome through a membrane neck coated with FtsZ (Fig. 3d, Supplementary Fig. 15). Sometimes, the budding neck extends over a few microns in the form of a tubular structure containing one or a few FtsA-FtsZ rings (Fig. 3d,e). Interestingly, these blebbing structures are dynamic. Events, such as appearance of new constriction sites, growing vesicles and diffusion of protein rings along the tube axis were observed (Fig. 3e, Movie 2). Although membrane recruitment of FtsZ in the form of patches was visible already within 2 h of expression, major liposome remodelling events, such as budding spots and elongated blebs were observed only after 3 to 4 h. Moreover, after 6 h expression, small vesicles were found to agglutinate to larger liposomes (Supplementary Fig. 13). FtsA concentration does not significantly increase beyond the first 3 h of expression (Supplementary Fig. 2), in agreement with the kinetic profiles of protein production with the PURE system³⁴. Concentration of synthesized FtsA was compared after 3 and 6 h expression, yielding 4.5 ± 0.5 M and 5.8 ± 1.1 M, respectively. Therefore, we do not expect that the differences observed at incubation times longer than 3 h can be attributed to an increase in protein concentration. Instead, the time-dependent changes could be due to some delaying factors, such as recruitment of proteins to the membrane, assembly of filaments and bundles, protein clustering into patches and remodeling of the membrane. It is unclear whether the FtsZ-coated membrane necks can close to release mature vesicles. Therefore, we cannot ascertain that the small vesicles observed after 6 h are reminiscent to division events. Yet, these aggregated vesicles were not observed when the *ftsA*_{opt} gene was omitted (Supplementary Fig. 13), indicating that this global remodelling is dependent on the expression of FtsA.

We then decided to investigate how the presence of cell-free expressed ZapA would modulate the properties of the cytoskeletal patterns in liposomes (Fig. 4a). Co-expression of *ftsA*_{opt} and *zapA*_{opt} DNA constructs induced formation of FtsZ-A647 clusters on the inner surface of the membrane (Fig. 4b). Liposomes with different cytoskeletal protein phenotypes were observed, such as homogeneous coating to the membrane, patches or filaments, and large ring-like structures. Bundles of FtsZ polymers adopting apparent ring-like structures predominantly localize at the interface of two liposomes (Fig. 4b), coinciding with a membrane septum (i.e. a membrane separating two adjacent vesicles; it could be a single bilayer or two bilayers). However, ZapA abolishes the formation of membrane protrusions, vesicle budding and clustering of FtsZ on tubular membrane structures (Fig. 4b). We have seen that, in the presence of ZapA, the small ring-like structures do not form on SLB, where longer, curved filaments dominate (Fig. 1). We observed a decrease of the filament curvature in the presence of ZapA, especially during co-expression of FtsA and ZapA (Supplementary Fig. 3b), which correlates with a higher concentration of ZapA in the assay (Supplementary Table 3). The straighter cytoskeletal filaments are likely not able to develop into contractile rings.

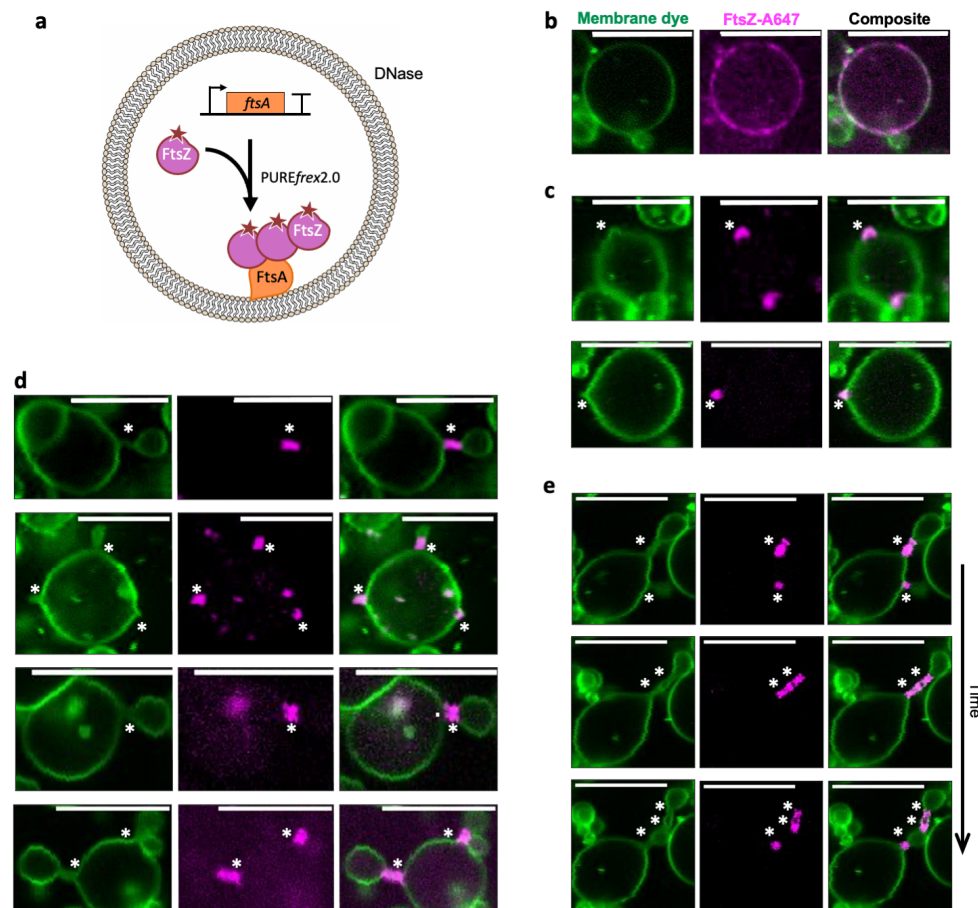


Figure 3: In-liposome synthesized FtsA assembles with FtsZ into ring-like structures that drive vesicle budding. **a**, Schematic illustration of liposome reconstitution assays. The *ftsA_{opt}* DNA template was expressed within phospholipid vesicles in the presence of 3 μ M purified FtsZ-A647. **b-d**, Confocal fluorescence images of liposomes exhibiting different morphologies of FtsZ-FtsA cytoskeletal structures and membrane remodelling: recruitment of proteins to the membrane in the form of clusters with no visible membrane deformation (**b**), budding spots induced by local accumulation of FtsZ-FtsA (**c**), and budding vesicles from a parental liposome with a clear FtsA-FtsZ-coated membrane neck (**d**). **e**, Time series images showing that a ring-forming protein cluster localized at a constriction site can split, which induces multiple necks separated by blebbing vesicles (see Movie 2). Timespan is 120 s between the first and second row of images, and 96 s between the second and third row. Fluorescence from the membrane dye is coloured in green and FtsZ-A647 signal is in magenta. The composite image is the overlay of the two channels. Asterisks indicate budding spots or constriction sites. Scale bars represent 10 μ m. More examples of liposomes are shown in Supplementary Fig. 14 and 15.

Instead, they accommodate to the large compartment and are unable to deform the membrane into narrow necks (Fig. 4b). These results indicate that the mechanical properties of FtsZ-ZapA bundles impede the formation of membrane-constricting, high-curvature cytoskeletal filaments, which suggests that temporal regulation of the local concentration of ZapA might play a role in the constriction of the FtsZ ring.

Collectively, the results demonstrate that gene-based reconstitution of membrane-constricting cytoskeletal protein filaments within liposomes is feasible. Moreover, FtsA and FtsZ form the minimal architecture to establish *E. coli* cell division proto-rings from native constituents in vitro.

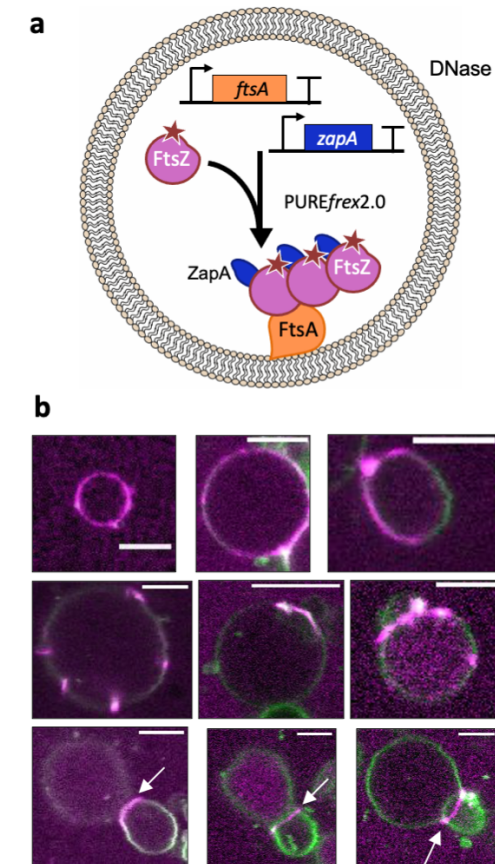


Figure 4: Co-expressed FtsA and ZapA organize FtsZ into long membrane-tethered bundles within liposomes. **a**, Schematic illustration of liposome reconstitution assays with 3 μ M purified FtsZ-A647 and co-expression of the *ftsA_{opt}* and *zapA_{opt}* DNA constructs. **b**, Confocal fluorescence images of liposomes exhibiting membrane recruitment of FtsZ-A647 after 3 h incubation. Fluorescence from the membrane dye is coloured in green and FtsZ-A647 signal is in magenta. Only the composite images are displayed. Arrows indicate membrane septa with co-localised FtsZ. Scale bars represent 5 μ m.

Discussion

Compartmentalization of PURE system and of the Z-ring constituents inside liposomes provides a realistic cellular environment. Purified FtsZ and FtsA proteins have already been enclosed within small (diameter < 200 nm) liposomes³⁰ or giant vesicles⁴³. In these earlier studies, membrane-tethered protofilaments of FtsZ could assemble with FtsA*, a mutant of FtsA that cannot polymerize^{44,45}. In another report, the FtsZ-sfGFP fusion protein was recruited to the membrane of giant liposomes (diameter 15 – 100 µm) by FtsA in the presence of Ficoll70³³. In their work, Furusato et al. reported a homogenous recruitment of FtsZ to the membrane in the presence of FtsA but no membrane deformation³³. Local reshaping of liposomes was exclusively observed with ZipA as the FtsZ membrane anchor, but no constriction sites nor protein ring-like structures were observed³³. Here, we show that wild-type FtsA and FtsZ are capable to deform the membrane in PURE system-loaded liposomes with a size <15 µm. The FtsA-dependent recruitment of FtsZ on the membrane frequently induces the formation of FtsZ clusters that constrict the liposome membrane into bud necks. It is clear from our data that FtsZ, assisted by FtsA, does not preferentially accommodate to pre-existing membrane areas with a high curvature. Conversely, membrane constriction and extended neck-like regions connecting the mother and budding vesicles are the product of localised FtsZ-FtsA pattern assembly. Noteworthy, these types of membrane remodelling, cytoskeletal protein organization, and dynamic blebbing structures were not observed in previous reports^{23,24,33,46}.

Not every liposome exhibits the same phenotype with regard to FtsZ recruitment and membrane deformation. This disparity is presumably the manifestation of the probabilistic encapsulation of all PURE system components and DNA, which leads to a large heterogeneity in FtsA expression levels, as recently quantified with a fluorescence reporter gene³⁵. It is therefore difficult to know the precise concentration of synthesized FtsA in individual liposomes and to correlate it with a particular phenotype. Further investigations will be necessary for directing the assembly of an all-gene based contractile FtsZ proto-ring that can divide liposomes. Although we do not exclude that assisting proteins, such as the Min system¹² and the FtsZ-interacting partners SlmA⁴⁷ and ZapB⁴⁸, might have to be introduced to complete membrane scission and release budding vesicles, the present results suggest that expression of FtsA and FtsZ might suffice to generate daughter vesicles of a few microns in size. The precise timing of protein interaction is essential for the hierarchical assembly of the proto-ring. This represents a major issue that is inherent to in-liposome compartmentalization of purified cytoskeletal proteins or with temporally unregulated expression of multiple genes. An additional level of temporal control that might be decisive for sequential assembly of the Z-ring constituents could be provided by regulating the expression of individual genes through transcriptional circuits, such as cascade or feedback motifs⁴⁹. Mindful of the limitations to apprehend the PURE system³⁴ and to rationally design liposomes harbouring desirable properties encoded

in genes, we believe that in vitro evolutionary optimization, by exploring a wide genetic diversity, provides additional opportunities to build cellular functions, and FtsZ proto-rings in particular.

Methods

DNA constructs

ftsZ and *ftsA* gene fragments were amplified by standard polymerase chain reaction (PCR) from the chromosomal *E. coli* BL21 DNA with primers 509 and 374 (*ftsZ*), and 508 and 376 (*ftsA*) (Supplementary Table 4). These primers contain overhangs for Gibson assembly with the pET11-a plasmid. PCR products were checked on a 1% agarose gel stained with EtBr or SYBR safe, imaged with a ChemiDoc™ Imaging System (BioRad Laboratories), and purified with the Wizard SV Gel kit (Promega). The purified DNA was incubated with DpnI (New England BioLabs®, Inc.) to remove residual plasmid and the linear DNA was purified again with Wizard SV Gel kit. DNA concentration and purity were measured using a ND-1000 UV-Vis Spectrophotometer (Nanodrop Technologies). Gibson assembly (Gibson Assembly® Master Mix of New England BioLabs®, Inc.) was performed at equimolar concentrations of linearized plasmid (pET11-a) and DNA fragments for 1 h at 50 °C. *E. coli* TOP10 competent cells (ThermoFisher Scientific, USA, catalogue number C4040-10) were transformed with the Gibson assembly products by heat shock. Cells were centrifuged, resuspended in 50 µL of fresh prechilled liquid lysogen broth (LB) medium and incubated for 1 h at 37 °C and 250 rpm. The cultures were plated on solid LB medium with ampicillin and grew overnight at 37 °C. Colonies were picked up and cultured in 1 mL of liquid LB medium with 50 µg µL⁻¹ of ampicillin in 1.5-mL Eppendorf tubes for 6 h at 37 °C and 250 rpm. Plasmid purification was performed using the PureYield™ Plasmid Miniprep System (column method, Promega). Plasmid concentration and purity were checked on a Nanodrop. Linear templates for PURE system reactions were prepared by PCR using the plasmids as substrates with primers 194 and 709 (Supplementary Table 4). Amplification products were checked on a 1% agarose gel and were purified using the Wizard SV Gel kit. DNA concentration and purity were measured using a ND-1000 UV-Vis Spectrophotometer (Nanodrop Technologies).

The DNA fragment containing the *zapA* gene (original sequence from *E. coli* K12 strain) was inserted in a pIDTSMART-AMP plasmid (Integrated DNA Technologies). The plasmid was transformed into *E. coli* TOP10 cells. Transformation, plasmid purification and production of linear DNA templates were performed as described above.

The *ftsA*_{opt} and *zapA*_{opt} constructs (starting with a T7 promoter and ending with the T7 terminator) were sequence-optimized for codon usage, GC content and 5' mRNA secondary structures, and were inserted in a pJET1 and pUC57 plasmid, respectively (GeneScript). Plasmids were amplified and purified as described above. All sequences of the linearized constructs can be found in the Supplementary Methods.

Purified proteins

Purified FtsZ and sZipA were prepared and labelled with Alexa Fluor probes according to published protocols^{24,50,51}. The degree of labelling was 0.9 ± 0.2 mol of fluorophore per mol of protein in both cases. FtsZ (150 M) was dialyzed against 20 mM Hepes/HCl, pH 8.0, with 50 mM KCl, 5 mM MgCl₂, and 1 mM EDTA. To minimize perturbations on FtsZ assembly properties due to labelling, the protein was first polymerized at 30 °C upon addition of 20 mM CaCl₂ and 2 mM GTP. A 20-fold excess of Alexa Fluor 647 (A647) was added, and the mixture was incubated for 15 min at 30 °C. The precipitate was resuspended on ice in 50 mM Tris/HCl, pH 7.4, with 100 mM KCl, and the free fluorescent probe was removed by gel filtration. ZipA (50 M) was labelled by adding 10-fold excess of Alexa Fluor 488 (A488) during 15 min at room temperature in 20 mM Hepes/HCl, pH 8.0, with 50 mM KCl. Labelling reaction was stopped by the addition of a 1:100 dilution of 1 M Tris buffer. The unreacted probe was removed by gel filtration. FtsZ-A647 (45 µM stock) was stored in a buffer containing 50 mM Tris, 500 mM KCl, 5 mM MgCl₂ and 5% glycerol at pH 7.4. sZipA-A488 (14.33 µM stock) was stored in a buffer containing 50 mM Tris, 50 mM KCl, and 1 mM EDTA at pH 7.4.

Cell-free gene expression

PUREfrex2.0 (GeneFrontier Corporation, Japan) was utilized following storing and handling instructions provided by the supplier. Linear DNA templates were used in single-gene expression assays at a final concentration of 5 nM. In co-expression experiments, both *ftsA*_{opt} and *zapA*_{opt} constructs were included at 5 nM and 10 nM, respectively, along with 1 µL of DnaK Mix (GeneFrontier Corporation). DnaK Mix consists of highly purified *E. coli* DnaK, DnaJ and GrpE chaperone proteins. Reactions of 20 µL volume were carried out in test tubes for 3 h at 37 °C. When indicated, samples were supplemented with purified proteins (FtsZ-A647, sZipA-A488) and added either on top of an SLB or used for lipid film swelling.

QconCAT purification

QconCAT was designed to contain two specific peptides for FtsA and two for ZapA (Supplementary Table 1, Supplementary Fig. 2). QconCAT was expressed in BL21(DE3) cells in M9 medium with ¹⁵NH₄Cl and ampicillin. A pre-culture was diluted 1:100 to a 50-mL expression culture. Protein expression was induced at OD₆₀₀=0.5 with 1 mM IPTG and cells were grown for 3 h at 37 °C. Cells were harvested by centrifugation and the pellet was dissolved in 1 mL B-PER. 10 µL of 10 mg mL⁻¹ lysozyme and 10 µL of DNaseI (ThermoScientific, 1 U µL⁻¹) were added and the sample was incubated for 10 min at room temperature. The lysate was centrifuged for 20 min at 16,000 g and the pellet resuspended in 2 mL of a 1:10 dilution of B-PER in MilliQ water. The sample was twice again centrifuged, and the pellet was resuspended in 2 mL 1:10 diluted B-PER and centrifuged again. The pellet was resuspended 600 µL 10 mM Tris-HCl pH 8.0, 6 M guanidinium chloride and incubated at room temperature for 30 min.

After spinning down unsolubilised protein the supernatant was loaded onto an equilibrated mini NiNTA spin column and the flow-through was reloaded twice to maximize protein binding. The column was washed twice with 600 µL of 10 mM Tris-HCl pH 6.3, 8 M urea and the QconCAT was eluted with 3 200 µL of 10 mM Tris-HCl pH 4.5, 8 M urea, 400 mM imidazole. The eluate was dialysed overnight and for additional 4 h against 10 mM Tris-HCl pH 8.0, 100 mM KCl with a 10-kDa cut-off slide-a-lyzer device/cassette (ThermoScientific).

Trypsin digest

Per LC-MS injection, 1.5 µL of PURE system reaction was mixed with 3 µL of 100 mM Tris-HCl pH8.0, 0.3 µL of 20 mM CaCl₂, and 0.8 µL MilliQ water. Samples were incubated at 90 °C for 10 min to stop the reaction. Then, 0.6 µL of QconCAT (0.3 mg mL⁻¹) was added, the sample was incubated again at 90 °C for 10 min and after cooling to room temperature 0.3 µL of 1 mg mL⁻¹ trypsin (trypsin-ultra, MS-grade, New England Biolabs) was added. Samples were then incubated at 37 °C overnight. After addition of 0.7 µL 10% trifluoroacetic acid, samples were centrifuged in a table-top centrifuge (5415R, Eppendorf) for 10 min at maximum speed. The supernatant was transferred to a glass vial with small-volume insert for LC-MS/MS analysis.

LC-MS/MS analysis

LC-MS/MS analysis was performed on a 6460 Triple Quad LCMS system (Agilent Technologies, USA) using Skyline software⁵². 7 µL of sample was injected per run to an ACQUITY UPLC® Peptide CSH™ C18 Column (Waters Corporation, USA). The peptides were separated in a gradient of buffer A (25 mM formic acid in MilliQ water) and buffer B (50 mM formic acid in acetonitrile) at a flow rate of 500 µL per minute and at a column temperature of 40 °C. The column was equilibrated with 98% buffer A. After injection, the gradient was changed linearly over 20 min to 70% buffer A, over the next 4 min to 60% buffer A, and over the next 30 s to 20% buffer A. This ratio was held for another 30 s and the column was finally flushed with 98% buffer A to equilibrate for the next run. Selected peptides were measured by multiple reaction monitoring (MRM). For both ZapA and FtsA, two peptides were present in the QconCAT. In addition, two peptides from ribosomal proteins were also measured as control.

Labelling of *in vitro* synthesized proteins and gel analysis

PUREfrex2.0 reaction mixtures were supplemented with 0.5 µL of GreenLys (FluoroTect™ GreenLys, Promega) and gene expression was performed in a test tube as described above. Samples were treated with RNase (RNaseA Solution, Promega) for 30 min and proteins were denatured for 10 min at 90 °C in 2 SDS loading buffer with 10 mM DTT. Samples were loaded on a 18% SDS-PAGE (polyacrylamide gel electrophoresis) gel. Visualization of the fluorescently labelled translation products was performed on a fluorescence gel imager (Typhoon, Amersham Biosciences) using a 488-nm laser and a band pass emission filter of

520 nm.

Fabrication and cleaning of the imaging chambers

Home-made glass chambers were used in both SLB and liposome experiments¹². Three microscopy glass slides (1-mm thick) were glued on top of each other with NOA 61 glue (Norland Products) and holes with a diameter of 2.5 mm were drilled. A 150 µm-thick coverslip (Menzel-Gläser, Germany) was glued with NOA 61 to cover the apertures, creating the bottom of glass chambers. Cleaning was performed by successive washing steps of 10 min each in a bath sonicator (Sonorex digitec, Bandelin), as follows: chloroform and methanol (1:1 volume ratio), 2% Hellmanex, 1 M KOH, 100% ethanol and finally MilliQ water. For SLB experiments the glass chambers were further treated every two to three experiments with Acid Piranha.

Lipids

1,2-dioleoyl-sn-glycero-3-phosphocholine (DOPC), 1,2-dioleoyl-sn-glycero-3-phosphoethanolamine (DOPE), 1,2-dioleoyl-sn-glycero-3-phosphoglycerol (DOPG), 1',3'-bis[1,2-dioleoyl-sn-glycero-3-phospho]-glycerol (18:1 CL), 1,2-distearoyl-sn-glycero-3-phosphoethanolamine-N-[biotinyl(polyethylene glycol)-2000 (DSPE-PEG-biotin), and 1,2-dioleoyl-sn-glycero-3-[(N-(5-amino-1-carboxypentyl)iminodiacetic acid)succinyl] (DGS-NTA) were from Avanti Polar Lipids. Texas Red 1,2-dihexadecanoyl-sn-glycero-3-phosphoethanolamine (DHPE-TexasRed) was from Invitrogen.

Preparation of small unilamellar vesicles

Small unilamellar vesicles (SUVs) were used as precursors for the formation of SLBs¹². Lipids DOPC (4 µmol), DOPG (1 µmol) and DGS-NTA (0.25 µmol), all dissolved in chloroform (Avanti Polar Lipids), were mixed in a glass vial. A lipid film was deposited on the wall of the vial upon solvent evaporation by applying a gentle flow of argon and was further desiccated for 30 min at room temperature. The lipid film was resuspended with 400 µL of SLB buffer (50 mM Tris, 300 mM KCl, 5 mM MgCl₂, pH 7.5) and the solution was vortexed for a few minutes. The final lipid concentration was 1.25 mg mL⁻¹. A two-step extrusion (each of 11 passages) was carried out using the Avanti mini extruder (Avanti Polar Lipids) equipped with 250 µL Hamilton syringes (Avant Polar Lipids), filters (drain disc 10 mm diameter, Whatman) and a polycarbonate membrane with a pore size of 0.2 µm (step 1) or 0.03 µm (step 2) (Nuclepore track-etched membrane, Whatman).

Formation of supported lipid bilayers

The imaging chamber was treated with oxygen plasma (Harrick Plasma basic plasma cleaner) for 30 min to activate the glass surface. Immediately after plasma cleaning the SUV solution

was added to the sample reservoir at a final lipid concentration of 0.94 mg mL⁻¹ together with 3 mM CaCl₂. The chamber was closed by sticking a coverslip using a double-sided adhesive silicone sheet (Life Technologies) and the sample was incubated for 30 min at 37 °C. Next, the chamber was opened and the SLB was carefully washed six times with SLB buffer. Under these conditions, the SLB contains 4.8 molar % of 18:1 DGS-NTA (Ni²⁺) lipids, which is within the range studied by ref.²⁷ (0.5 – 10 mol%), similar as in ref.²⁸ (1-8 mol%) but higher than in ref.³⁸ (0.02 – 0.08 mol% of full length ZipA, DGS-NTA lipid was not used in this study) and lower than in ref.⁵⁰ (10 mol%).

Activity assays on supported membranes

In the experiments involving sZipA-Alexa488, 1 µM of the purified protein was first incubated on top of an SLB for 10 min at room temperature. The SLB was washed with 10 µL reaction buffer (50 mM Tris-HCl, 150 mM KCl, 5 mM MgCl₂, pH 7.5). Then, 20 µL of sample (composition is specified where relevant) was added on top of the SLB and the chamber was sealed by sticking a 2020 mm coverslip with a double-sided adhesive silicone sheet. In the experiments with FtsA, the *ftsA* or *ftsA_{opt}* gene was either directly expressed on top of the SLB, or in a test tube and subsequently added onto an SLB as part of the sample. In the earlier configuration, a 20 µL PURE_{flex}2.0 reaction was carried out on top of an SLB and 10 µL were removed and replaced by the activity assay mixture. The exact composition of the sample varies for the different experiments and is specified where appropriate. In all cases, samples contained 2 mM GTP, supplemented with 2 mM ATP in FtsA experiments. In all assays without ZapA, Ficoll70 was added to a final concentration of 50 g L⁻¹. No oxygen-scavenging system was used, unlike in ref.²⁸ but like in ref.³⁸.

Spinning disk microscopy

Supported lipid bilayers were imaged with an Olympus iX81 inverted fluorescence microscope equipped with a 100 oil immersion objective (Olympus), an iXon3 EMCCD camera (Andor Technology) and a Nipkow spinning disk (CSU-XI, Yokogawa). FtsZ-A647 and sZipA-A488 were imaged using a 640 nm and 491 nm laser line, respectively, and appropriate emission filters (685/40 nm or 525/50 nm). The software Andor IQ3 (Andor Technology Ltd.) was used for image acquisition and identical settings were used for all experiments. Experiments were conducted at room temperature.

Preparation of lipid-coated beads

Lipid-coated beads were prepared according to our published protocol³⁵ with the following lipid composition: DOPC (50 mol%), DOPE (36 mol%), DOPG (12 mol%), 18:1 CL (2 mol%), DSPE-PEG-biotin (1 mass%) and DHPE-TexasRed (0.5 mass%) for a total mass of 2 mg. Lipids dissolved in chloroform were mixed in a round-bottom glass flask. Methanol

containing 100 mM rhamnose (Sigma-Aldrich) was added to the solution in a chloroform-to-methanol volume ratio of 2.5:1. Then, 1.5 g of 212-300 μm glass beads (acid washed, Sigma Aldrich) were poured to the lipid-rhamnose mixture and the organic solvent was removed by rotary evaporation at 200 mbar for 2 h at room temperature, followed by overnight desiccation. Lipid-coated beads were stored under argon at -20°C until use.

Production and immobilization of gene-expressing liposomes

A PUREflex2.0 reaction mixture was assembled as described above. Either or both $ftsA_{\text{opt}}$ and $zapA_{\text{opt}}$ DNA constructs were added at a final concentration of 5 nM and 10 nM, respectively. The solution was supplemented with (final concentrations indicated): 2 mM GTP, 2 mM ATP, 3 μM FtsZ-A647 and MilliQ to reach a final volume of 20 μL . About 20 mg of lipid-coated beads was added to the solution and liposomes were formed by natural swelling of the lipid film for 2 h on ice, protected from light. During incubation, the tube was gently rotated manually a few times. Four freeze-thaw cycles were then applied by dipping the sample in liquid nitrogen and thawing on ice. The sample reservoir of the imaging chamber was functionalized with 1:1 molar ratio of bovine serum albumin (BSA) and BSA-biotin (1 mg mL^{-1} , Thermo Fisher Scientific), and then with Neutravidin (1 mg mL^{-1} , Sigma Aldrich), to tether the biotinylated liposomes. About 7 μL of the liposome solution was carefully pipetted (with a cut tip) into the imaging chamber and supplemented with RQ1 DNase ($0.07\text{ U } \mu\text{L}^{-1}$) to preclude gene expression outside liposomes. The chamber was sealed by sticking a 20 \times 20 mm coverslip with a double-sided adhesive silicone sheet. Expression was performed directly on the confocal microscope at 37°C for 1.5 to 6 h.

Confocal microscopy

A Nikon A1R Laser scanning confocal microscope equipped with an SR Apo TIRF 100 oil immersion objective was used to image liposomes. The 561 nm and 640 nm laser lines were used in combination with appropriate emission filters to image the Texas Red membrane dye and FtsZ-A647, respectively. The software NIS (Nikon) was used for image acquisition and identical settings were used for all experiments. Samples were mounted on a temperature-controlled stage maintained at 37°C during imaging.

Fluorescence recovery after photobleaching (FRAP)

FRAP experiments were performed on an Olympus iX81 spinning disk microscope. Images were acquired using the following protocol: 10 frames every s, 10 frames every 250 ms, 10 frames every 2 s, 10 frames every 4 s. Analysis of the FRAP images was performed with ImageJ^{53,54} using the *FRAP profiler* plug-in. The intensity of a bleached region of interest (ROI, 2929 pixels) was measured over time and normalized to the intensity of the surrounding (250250 pixels area centred on the ROI) to correct for the bleaching that occurs during image

acquisition. Fitting of the FRAP curves was generated in GraphPad Software Inc. using a one-phase exponential model. At least three FRAP measurements were performed in each sample analysed.

Structured illumination microscopy (SIM)

3D SIM images have been acquired with a Nikon SIM microscope equipped with a Nikon 100 and 1.49 NA Apo TIRF SR objective and a 640 nm laser line. The acquisition and reconstruction of the SIM images have been performed using the Nikon NIS element software. SIM RAW data and their corresponding reconstructed images were quality-checked using the Fiji plug-in *SIMcheck*⁵⁵.

Total internal reflection fluorescence microscopy

FtsA-FtsZ ring dynamic was investigated using a Nikon TiE inverted fluorescence microscope equipped with an iLAS2 illumination system, a Plan Apo 100 oil immersion objective and a 2 Photometrics EMCCD Evolve Camera. The 640 nm laser line was used in combination with appropriate emission filters to image FtsZ-A647. MetaMorph® Microscopy Automation Software was used for image acquisition.

Quantitative image analysis

Image analysis was performed using Mathematica (Wolfram Research, version 11.3). All images were corrected for uneven illumination by applying a Gaussian filter with radius 70 pixels to each image, fitting a third-degree polynomial to the filtered image, and dividing the original image pixel-by-pixel with the fitted polynomial. To segment the filaments a ridge filter with sigma=1 was applied and the resulting image binarized using morphological binarization with the default parameters. When needed this image was convolved with a Laplacian-of-Gaussian filter with radius 2 pixels and inversed (necessary for images with thin filaments). Filament thicknesses were calculated from this image as the distance of the centerline of filaments to the edge using the distance transform function. Branch point density and filament curvature were calculated after the thinning operation was applied to the segmented image. Curvatures were approximated at each pixel along the thinned filament with a distance larger than 2 pixels to the next branch point using Gaussian smoothing on the derivative functions. The image processing steps are illustrated in Supplementary Fig. 3. Filament dynamic was analysed by computing kymographs in MatLab version 2018a. A user-defined ellipse was overlaid on the ring-like structures of interest based on the first image of the movie and the boundary pixel intensities of all frames were extracted.

Statistics and reproducibility

All experiments reported in this study have been reproduced and similar results have

been obtained. Microscopy images displayed in the main text figures are representative of the sample properties as analysed from larger fields of view in at least three independent biological repeats.

References

1. Shimizu, Y. *et al.* Cell-free translation reconstituted with purified components. *Nat. Biotechnol.* **19**, 751–755 (2001).
2. Gros, J., Devbhandari, S. & Remus, D. Origin plasticity during budding yeast DNA replication in vitro. *EMBO J.* **33**, 621–636 (2014).
3. Lee, K., Gallop, J. L., Rambani, K. & Kirschner, M. W. Self-Assembly of filopodia-like structures on supported lipid bilayers. *Science*. **329**, 1341–1345 (2010).
4. Vignaud, T., Blanchoin, L. & Théry, M. Directed cytoskeleton self-organization. *Trends in Cell Biology* vol. 22 671–682 (2012).
5. Nguyen, P. A. *et al.* Spatial organization of cytokinesis signaling reconstituted in a cell-free system. *Science*. **346**, 244–247 (2014).
6. Garner, E. C., Campbell, C. S., Weibel, D. B. & Mullins, R. D. Reconstitution of DNA segregation driven by assembly of a prokaryotic actin homolog. *Science*. **315**, 1270–1274 (2007).
7. Dannhauser, P. N. & Ungewickell, E. J. Reconstitution of clathrin-coated bud and vesicle formation with minimal components. *Nat. Cell Biol.* **14**, 634–639 (2012).
8. Focus on the benefits of building life's systems from scratch. *Nature* **563**, 155–155 (2018).
9. Nourian, Z., Scott, A. & Danelon, C. Toward the assembly of a minimal divisome. *Syst. Synth. Biol.* **8**, 237 (2014).
10. Scott, A. *et al.* Cell-free phospholipid biosynthesis by gene-encoded enzymes reconstituted in liposomes. *PLoS One* **11**, e0163058 (2016).
11. van Nies, P. *et al.* Self-replication of DNA by its encoded proteins in liposome-based synthetic cells. *Nat. Commun.* **9**, 1583 (2018).
12. Godino, E. *et al.* De novo synthesized Min proteins drive oscillatory liposome deformation and regulate FtsA-FtsZ cytoskeletal patterns. *Nat. Commun.* **10**, 4969 (2019).
13. Bi, E. & Lutkenhaus, J. FtsZ ring structure associated with division in *Escherichia coli*. *Nature* **354**, 161–164 (1991).
14. Ma, X., Ehrhardt, D. W. & Margolin, W. Colocalization of cell division proteins FtsZ and FtsA to cytoskeletal structures in living *Escherichia coli* cells by using green fluorescent protein. *Proc. Natl. Acad. Sci.* **93**, 12998–13003 (1996).
15. Hale, C. A. & de Boer, P. A. Recruitment of ZipA to the septal ring of *Escherichia coli* is dependent on FtsZ and independent of FtsA. *J. Bacteriol.* **181**, 167–76 (1999).
16. Walker, B. E., Männik, J. & Mannik, J. Transient membrane-linked FtsZ assemblies precede Z-ring formation in *Escherichia coli*. *Current Biology* **30**, 499–508 (2019).
17. de Boer, P., Crossley, R. & Rothfield, L. The essential bacterial cell-division protein FtsZ is a GTPase. *Nature* **359**, 254–256 (1992).
18. Mukherjee, A. & Lutkenhaus, J. Guanine nucleotide-dependent assembly of FtsZ into filaments. *J. Bacteriol.* **176**, 2754–8 (1994).
19. Pichoff, S. & Lutkenhaus, J. Unique and overlapping roles for ZipA and FtsA in septal ring assembly in *Escherichia coli*. *EMBO J.* **21**, 685–93 (2002).
20. Pichoff, S. & Lutkenhaus, J. Tethering the Z ring to the membrane through a conserved membrane targeting sequence in FtsA. *Mol. Microbiol.* **55**, 1722–1734 (2005).
21. Hale, C. A. & de Boer, P. A. Direct binding of FtsZ to ZipA, an essential component of the septal ring structure that mediates cell division in *E. coli*. *Cell* **88**, 175–85 (1997).
22. Ortiz, C., Natale, P., Cueto, L. & Vicente, M. The keepers of the ring: regulators of FtsZ assembly. *FEMS Microbiol. Rev.* **40**, 57–67 (2016).
23. Osawa, M. & Erickson, H. P. Liposome division by a simple bacterial division machinery. *Proc. Natl. Acad. Sci. U. S. A.* **110**, 11000–4 (2013).
24. Cabré, E. J. *et al.* Bacterial division proteins FtsZ and ZipA induce vesicle shrinkage and cell membrane invagination. *J. Biol. Chem.* **288**, 26625–34 (2013).
25. Ramirez-Diaz, D. A. *et al.* Treadmilling analysis reveals new insights into dynamic FtsZ ring architecture. *PLOS Biol.* **16**, e2004845 (2018).
26. Krupka, M. *et al.* *Escherichia coli* FtsA forms lipid-bound minirings that antagonize lateral interactions between FtsZ proto-filaments. *Nat. Commun.* **8**, 15957 (2017).

27. Krupka, M., Sobrinos-Sanguino, M., Jiménez, M., Rivas, G. & Margolin, W. *Escherichia coli* ZipA organizes FtsZ Polymers into dynamic ring-like protofilament structures. *MBio* **9**, e01008-18 (2018).

28. Loose, M. & Mitchison, T. J. The bacterial cell division proteins FtsA and FtsZ self-organize into dynamic cytoskeletal patterns. *Nat. Cell Biol.* **16**, 38–46 (2014).

29. Osawa, M., Anderson, D. E. & Erickson, H. P. Curved FtsZ protofilaments generate bending forces on liposome membranes. *EMBO J.* **28**, 3476–84 (2009).

30. Szwedziak, P., Wang, Q., Bharat, T. A. M., Tsim, M. & Löwe, J. Architecture of the ring formed by the tubulin homologue FtsZ in bacterial cell division. *Elife* **3**, e04601 (2014).

31. Söderström, B. *et al.* Disassembly of the divisome in *Escherichia coli*: evidence that FtsZ dissociates before compartmentalization. *Mol. Microbiol.* **92**, 1–9 (2014).

32. Daley, D. O., Skoglund, U. & Söderström, B. FtsZ does not initiate membrane constriction at the onset of division. *Sci. Rep.* **6**, 33138 (2016).

33. Furusato, T. *et al.* *De novo* synthesis of basal bacterial cell division proteins FtsZ, FtsA, and ZipA inside giant vesicles. *ACS Synth. Biol.* **7**, 953–961 (2018).

34. Doerr, A. *et al.* Modelling cell-free RNA and protein synthesis with minimal systems. *Phys. Biol.* **16**, 025001 (2019).

35. Blanken, D., van Nies, P. & Danelon, C. Quantitative imaging of gene-expressing liposomes reveals rare favorable phenotypes. *Phys. Biol.* **16**, 045002 (2019).

36. Rueda, S., Vicente, M. & Mingorance, J. Concentration and assembly of the division ring proteins FtsZ, FtsA, and ZipA during the *Escherichia coli* cell cycle. *J. Bacteriol.* **185**, 3344–51 (2003).

37. Caldas, P., López-Pelegrín, M., Pearce, D.J.G. *et al.* Cooperative ordering of treadmilling filaments in cytoskeletal networks of FtsZ and its crosslinker ZapA. *Nat. Commun.* **10**, 5744 (2019).

38. Martos, A. *et al.* FtsZ polymers tethered to the membrane by ZipA are susceptible to spatial regulation by Min waves. *Biophys. J.* **108**, 2371–2383 (2015).

39. Rivas, G., Alfonso, C., Jiménez, M., Monterroso, B. & Zorrilla, S. Macromolecular interactions of the bacterial division FtsZ protein: from quantitative biochemistry and crowding to reconstructing minimal divisomes in the test tube. *Biophys. Rev.* **5**, 63–77 (2013).

40. Small, E. *et al.* FtsZ Polymer-bundling by the *Escherichia coli* ZapA orthologue, YgfE, involves a conformational change in bound GTP. *J. Mol. Biol.* **369**, 210–221 (2007).

41. Martos, A. *et al.* Characterization of self-association and heteroassociation of bacterial cell division proteins FtsZ and ZipA in solution by composition gradient-static light scattering. *Biochemistry* **49**, 10780–10787 (2010).

42. Hernández-Rocamora, V. M. *et al.* Dynamic interaction of the *Escherichia coli* cell division ZipA and FtsZ proteins evidenced in nanodiscs. *J. Biol. Chem.* **287**, 30097–30104 (2012).

43. Osawa, M. & Erickson, H. P. Inside-out Z rings - constriction with and without GTP hydrolysis. *Mol. Microbiol.* **81**, 571–579 (2011).

44. Geissler, B., Elraheb, D. & Margolin, W. A gain-of-function mutation in ftsA bypasses the requirement for the essential cell division gene zipA in *Escherichia coli*. *Proc. Natl. Acad. Sci.* **100**, 4197–4202 (2003).

45. Pichoff, S., Shen, B., Sullivan, B. & Lutkenhaus, J. FtsA mutants impaired for self-interaction bypass ZipA suggesting a model in which FtsA's self-interaction competes with its ability to recruit downstream division proteins. *Mol. Microbiol.* **83**, 151–167 (2012).

46. Osawa, M., Anderson, D. E. & Erickson, H. P. Reconstitution of contractile FtsZ rings in liposomes. *Science.* **320**, 792–794 (2008).

47. Cabré, E. J. *et al.* The nucleoid occlusion SlmA protein accelerates the disassembly of the FtsZ protein polymers without affecting their GTPase activity. *PLoS One* **10**, e0126434 (2015).

48. Monterroso, B. *et al.* The bacterial DNA binding protein MatP involved in linking the nucleoid terminal domain to the divisome at midcell interacts with lipid membranes. *MBio* **10**, e00376-19 (2019).

49. Noireaux, V., Bar-Ziv, R. & Libchaber, A. Principles of cell-free genetic circuit assembly. *Proc. Natl. Acad. Sci.* **100**, 12672–12677 (2003).

50. Mateos-Gil, P. *et al.* FtsZ polymers bound to lipid bilayers through ZipA form dynamic two dimensional networks. *Biochim. Biophys. Acta - Biomembr.* **1818**, 806–813 (2012).

51. González, J. M. *et al.* Essential cell division protein FtsZ assembles into one monomer-thick ribbons under conditions resembling the crowded intracellular environment. *J. Biol. Chem.* **278**, 37664–71 (2003).

52. MacLean, B. *et al.* Skyline: An open source document editor for creating and analyzing targeted proteomics experiments. *Bioinformatics.* **26**, 966–968 (2010)

53. Schneider, C. A., Rasband, W. S., & Eliceiri, K. W. NIH Image to ImageJ: 25 years of image analysis. *Nat. Methods.* **9**, 671–675 (2012).

54. Rueden, C. T. *et al.* ImageJ2: ImageJ for the next generation of scientific image data. *BMC Bioinformatics.* **18**, 529 (2017).

55. Ball, G. *et al.* SIMcheck: a toolbox for successful super-resolution structured illumination microscopy. *Sci. Rep.* **5**, 15915 (2015).

Supplementary Information

Sequence of the *ftsA* construct

TAATACGACTCACTATAGGGGAATTGTGAGCGGATAACAATTCCCCTCTAGAAATAATTTTGTTTAACTTTAAGAAG-GAGATATACATATGATCAAGGCGACGGACAGAAAAGCTGGTAGTAGGACTGGAGATTGGTACCGCGAAGGTTGCCGCT-TTAGTAGGGGAAGTTCTGCCCGACGGTATGGTCAATATCATTGGCGTGGGCAGCTGCCGCTCGCGTGGTATGGA-TAAAGGCGGGGTGAACGACCTCGAATCCGTGGTCAAGTGCCTGACGCGCCATTGACCAGGCAGAATTGATGG-CAGATTGTGAGATCTCTTCGGTATATCTGGCGCTTTCTGGTAAGCACATCAGCTGCCAGAATGAAATTGGTATG-GTGCTATTCTGAAGAAGAAGTGACGCAAGAAGATGTGAAAACGTCGTCCATACCGCGAAATCGGTGCGTGTGCG-CGATGAGCATCGTGTGCTGCATGTGATCCCGCAAGAGTATGCGATTGACTATCAGGAAGGGATCAAGAATCCGGTAG-GACTTTCGGGCGTGCAGATGCAGGCAAAAGTGCACCTGATCATGTGCACACGATATGGCGAAAAACATCGTCAAAG-CGGTTGAACGTTGTGGGCTGAAAGTTGACCAACTGATATTTGCCGACTGGCATCAAGTTATTTCGGTATTGACGGAA-GATGAACGTGAACTGGGTGCTGCGTCGTGATATCGGTGGTGGTACAATGGATATCGCCGTTTATACCGGTGGGG-CATTGCGCCACACTAAGGTAATTCCTTATGCTGGCAATGTCGTGACCAGTGATATCGCTTACGCCCTTTGGCACGCCG-CGAAGCGACGCCGAAGCGATTAAAGTTTCGCCACGGTTGTGCGCTGGGTTCATCGTTGGAAAAGATGAGAGCGTG-GAAGTGCCGAGCGTAGGTGGTCCGCCACGGAGTCTGCAACGTCAGACACTGGCAGAGGTGATCGAGCCGCGC-TATACCGAGCTGCTCAACCTGGTCAACGAAAGAGATATTGCAGTTGCAGGAAAAGCTTCGCCAACAAGGGGTTAAA-CATCACCTGGCGGCAGGCATTGTATTAACCGGTGGCGCAGCGCAGATCGAAGGTTTGCAGCCTGTGCTCAGCG-CGTGTTTCATACGCAAGTGCATCGGCGCGCCGCTGAACATTACCGGTTTAAACGATTATGCTCAGGAGCCGTAT-TATTCGACGGCGGTGGGATTGCTTCACTATGGGAAAGAGTCACATCTTAACGGTGAAGCTGAAGTAGAAAAACGTGT-TACAGCATCAGTTGGCTCGTGATCAAGCGACTCAATAGTTGGTGCGAAAAGAGTTTAAAGATCCGGCTGCTAA-CAAAGCCCGAAAGGAAGCTGAGTTGGCTGCTGCCACCGCTGAGCAATAACTAGCATAACCCCTTGGGGCTCTAAACG-GGTCTTGAGGGGTTTTTTG

Sequence of the optimized *ftsA_{opt}* construct

TAATACGACTCACTATAGGGGAATTGTGAGCGGATAACAATTCCCCTCTAGAAATAATTTTGTTTAACTTTAAGAAG-GAGATATACATATGATCAAGGCGACCGACCGTAAGCTGGTTGTGGGCTGGAGATTGGCACCGCGAAGGTTGCCG-GCGTGGTTGGCGAGGTTCTGCCGGATGGTATGGTTAACATTATCGGCGTTGGTAGCTGCCGAGCCGTGGCATGGA-CAAAGTGGTGTGAACGACCTGGAAGCGTGGTTAAGTGCCTGCAGCGTGCATTGACCAGGCGGAGCTGATGGCG-GACTGCCAAATCAGCAGCGTTTACCTGGCGCTGAGCGGCAAGCACATCAGCTGCCAAAACGAGATTGGTATGGTGC-CGATTAGCGAAGAGGAAGTTACCCAGGAAGATGTGGAGAACGTGGTTACACCGCGAAAAGCGTTTCGTGTGCGTGAT-GAACACCGTGTGCTGCACGTTATCCCGCAAGAATACGCGATCGATTACCAGGAAGGTATCAAAAACCCGTTTGGTCT-GAGCGGTGTTTCGTATGCAGGCGAAAGTGCACCTGATTACCTGCCACAACGATATGGCGAAGAACATTGTGAAAGCG-GTTGAACGTTGCGGTCTGAAGGTTGACCAGCTGATCTTCGCGGGTCTGGCGAGCAGCTACAGCGTTCTGACCGAA-GATGAGCGTGAACTGGGTGTTTGCCTGTGGATATCGGCGGTGGCACGATGGATATCGCGGTGTATACCGGTGGCG-CGCTGCGTCACACCAAAGTGATTCCGTATCGGGTAACGTGGTTACCAGCGACATCGCGTACGCGTTTGGCACCCGCG-CGAGCGATGCGGAGGCGATCAAAGTGCCTGACGCTGCGCGCTGGGTAGCATTTGTGGGTAAAGATGAGAGCGTG-GAAGTTCGAGCGTTGGTGGCGCTCCGCCGCTAGCCTGCAACGTCAGACCCTGGCGGAAGTTATCGAGCCGCGT-

TACACCGAACTGCTGAACCTGGTGAACGAAGAGATCCTGCAACTGCAAGAGAACTGCGTCAGCAAGGTGTTAAG-
CACCACCTGGCGGCGGGCATTTGTTCTGACCGGCGGTGCGGCGCAGATCGAAGGTCTGGCGGCGTGCGCGCAACGT-
GTTTTCCACACCCAAGTTGCTATCGGTGCGCGCTGAACATCACCGGTCTGACCGATTACGCGCAAGAGCCGTACTAT-
AGCACCGCGGTGGTCTGCTGCACTATGGCAAAGAGAGCCACCTGAACGGCGAGGCGGAAGTGGAGAAGCGTGT-
GACCGCGAGCGTTGGTAGCTGGATTAAGCGTCTGAATAGCTGGCTGCGTAAGGAGTTCTAAGGATCCGGCTGCTAA-
CAAAGCCCGAAAGGAAGCTGAGTTGGCTGCTGCCACCGCTGAGCAATAACTAGCATAACCCCTTGGGGCCTCTAAACG-
GGTCTTAGGGGTTTTTG

Sequence of the *zapa* construct

TAATACGACTCACTATAGGGGAATTGTGAGCGGATAACAATCCCCTCTAGAAATAATTTGTTTAACTTTAAGAAG-
GAGATATACATATGTCTGCACAACCGTCGATATCCAAATTTTGGCCGTTCACTGCGTGTGAAGTCCCGCTGAC-
CAAAGGGATGCGTTGAATCAGGCAGCGGACGATCTGAACCAACGGTTGCAAGATCTGAAAGAAGCACTAGAGTCA-
CAAATACTGAACAGTTGGTCTTCAATGGCGCATGAATATCAGTATGAGTTAGCGCAAGAAAAAGCAAGACTCGT-
GACTACGCGGCAAGTATGGAACAGCGTATTCGGATGCTGCAGCAGACCATAGAACAAGCGTTACTTGAACAAG-
GTCGCATCACCGAAAAAACTAACCAAACTTTGAATGAGGATCCGGCTGCTAACAAAGCCCGAAAGGAAGCT-
GAGTTGGCTGCTGCCACCGCTGAGCAATAACTAGCATAACCCCTTGGGGCCTCTAACGGGTCTTGAGGGGTTTTTG

Sequence of the optimized *zapa_{opt}* construct

TAATACGACTCACTATAGGGGAATTGTGAGCGGATAACAATCCCCTCTAGAAATAATTTGTTTAACTTTAAGAAG-
GAGATATACATATGAGCGCGCAACCGGTGGACATCCAGATTTTGGCCGTAGCCTGCGTGTGAAGTCCCGCGGAC-
CAACGTGATGCGCTGAACCAGGCGGCGGACGATCTGAACCAGCGTCTGCAAGACCTGAAGGAGCGTACCCGT-
GTGACCAACACCGAACAGCTGGTTTTTCATCGCGGCGTGAACATTAGCTACGAGCTGGCGCAGGAAAAGCGGAA-
AACCCGTGATTATGCGGCGAGCATGGAGCAACGTATCCGTATGCTGCAACAAACCATGAACAGGCGCTGCTGGAA-
CAGGGTCGCATCACCGAGAAGACCAATCAGAATTTGAATAAGGATCCGGCTGCTAACAAAGCCCGAAAGGAAGCT-
GAGTTGGCTGCTGCCACCGCTGAGCAATAACTAGCATAACCCCTTGGGGCCTCTAACGGGTCTTGAGGGGTTTTTG

DNA sequence *QconCAT*

TAATACGACTCACTATAGGGAGACCACAACGGTTTCCCTCTAGAAATAATTTGTTTAACTTTAAGAAGGAGATATA-
CATATGCGGGTTCTCATCATCATCATCATGTTATGGCTAGCATGACTGGTGGACAGCAAATGGGTGCGGACCT-
GTACGACGACGACGATAAGAGCCTGTTTCCGAAAAGCAGCGTGGCGGTTAGCTGGATTGGTAAAGCGGCGGCGG-
CGGGTGTGAGCGATGATGCGCGTATGGACCTGGCGAGCCAGTTTACGAGAAGGCGGTGCTGGTTGATCTGGAAC-
CGGGTGTATTGCGCGTGCGACCAACCCGCTGGTGGTGGCGGAGCCTGCTGGTTGACAACTGGGCGAGAG-
CAGCAGCGGTAGCTATGTTCCGCGTAACATCATGGGTATTGAGGTGCGGAAACCCTGGTTCACAAGACCATCTTCT-
TTAAACAGGCGAGCGAACAACAACTGGGCGAACTACAGCGCGGAGCAGAACCCGTTTCAAGGCGATACCCCTGGTGAAC-
CGTACCTACATCATCAGCATCCTGTTCAAGAACCAGATTGCGACCCTGGCGCAAAGCTATCGTGGTCTGGGTGCGG-
GTGCGAACCCGGAAGTGGGTGCTGAATATCAAGACATTATCCGTATGCTGCAGCAAACCATCGAGCAGGCGCTGCT-
GGAACAAGGTCGTCTGATTGTGCTGCTGCTGCTGGGCTTCGGCGAGCGTGCTACGCGGATACCGTTGAACGT-
GGCAGCAGCTTTACCTGAGCGTGGTTACCTGCACGAGGCGGAACCGAAGCTGCAGTGGCAAGAGAGCGACGG-
TACCATCAAATACCGTCCGACCGACGATTTTCGATGCGCGTTATACCGAACTGCTGAACCTGGTGAACGAGGAAAT-
TCTGCAGCTGCAAGAGAAGGACATCCTGGAAGTTATTTGCAAGATGCGCTGAACAGGCGGCGGACGATCTGAAC-
CAACGTGTGGTTAACGACAACGCGCGGAGACCGGAAAGATGCGCTGAGCCTGGCGCGTGGCGGTGTAACGACCT-
GGAGAGCGTGGTTAAGATTATCGTGGTTACAGCGGTAAGCGCTGGCGGGTGGAGCGGTGACCGTGATACCATCGG-
CGACATTATCATCTGCGCGCTGAGCGATTACGGTGTCAACTGCGTGCGCCGGTGGTTGTTCCGGCGGGTGTG-
GACGTGAAAGCGATTAGCCTGAGCGTGCGTTAACTAGCATAACCCCTTGGGGCCTCTAACGGGTCTTGAGGGGT-
TTTTTG

Supplementary notes

Supplementary Note 1: FtsA-FtsZ bundles are dynamic

FtsA directly expressed on a supported lipid bilayer (SLB) in the presence of 3 μM purified FtsZ-A647 led to curved filaments and ring-like structures (see main text Fig. 1a,b). We investigated the dynamics of the ring-like structures using total internal reflection fluorescence (TIRF) and structure illumination microscopy (SIM). We confirmed that FtsA-FtsZ bundles are dynamic (Movie 1), in agreement with previous observations with purified proteins¹. However, the generated kymographs do not display features characteristic of treadmilling (Movie 1), as previously demonstrated¹. We attribute this to the suboptimal quality of the movies and not necessarily to the fact that treadmilling does not occur. We attempted to improve the fluorophore stability by using different oxygen scavengers. We tested a solution including 200 mM DTT, 10 mg mL⁻¹ catalase, 20 mg mL⁻¹ glucose oxidase, with or without 1 mM Trolox and lastly a solution made of 10 nM protocatechuate-dioxygenase and 2 mM 3,4-protocatechuic acid. Unfortunately, the cytoskeletal structures became unstable in the presence of any of these oxygen scavenging solutions tested and, in some cases, ring formation was inhibited.

Supplementary Note 2: Bundling of FtsZ filaments is required for the formation of long ZipA-FtsZ cytoskeletal structures in low-volume SLB assays

We examined the ability of purified FtsZ and the cytoplasmic domain of ZipA, sZipA², to assemble into membrane-tethered protofilaments in a PURE system background. Specifically, we attempted to reproduce previous results using purified FtsZ and sZipA in SLB assays¹. To simultaneously visualize both proteins, FtsZ and sZipA were labelled with Alexa Fluor-647 and 488, respectively. Membrane recruitment and spatial organization of the proteins were imaged using spinning disk fluorescence microscopy. We used 3 μM FtsZ-A647, which is above the critical concentration for in vitro polymerization^{3,4}, and about 1 μM sZipA-A488 in the presence of GTP. The 4.8 mol% of DOGS lipid results in a regime of high-density of sZipA. While sZipA-conditional recruitment of FtsZ to the membrane was confirmed, no visible large-scale filaments could develop under these conditions, in contrast with previous observations². To our surprise, repeating the experiment in the same minimal buffer as in Loose et al.² in place of PURE_{flex}2.0 failed to reproduce filament networks (Fig. 2a,b). Given our unconventional setup for SLB assays which is designed for low-volume PURE system solutions, we asked whether the chamber dimension and geometry could cause this different behaviour. In both PURE_{flex}2.0 background and minimal buffer, supplementing the solution with 12.5% Ficoll70, an artificial crowding agent known to promote FtsZ filament condensation⁵, triggered the formation of a dense network of sZipA-FtsZ co-filaments (Fig. 2c,d, Supplementary Fig. 7) having a similar morphology as previously reported². The presence

of long (>10 μm) bundles is typical to high membrane coverage with sZipA. At low-density sZipA and identical concentration of Ficoll70, only short bundles and three-dimensional networks of FtsZ were observed⁶. Although different areas of an SLB can show various protein network phenotypes, more condensed bundles were observed in PURE_{flex}2.0 compared to the minimal buffer (Fig. 2d, Supplementary Fig. 7). Once formed, these structures are stable in time (at least up to 3 hours) with no large-scale reorganization within minutes. Fluorescence recovery after photobleaching (FRAP) experiments revealed that membrane-bound sZipA is immobile within the cytoskeletal network (Supplementary Fig. 11).

Collectively, these results indicate that the Ficoll70-induced sZipA-FtsZ filament networks have a different morphology in the physiological PURE_{flex}2.0 background compared to the minimal buffer. Moreover, the total reaction volume acts as a control parameter in the formation of cytoskeletal patterns in SLB assays.

The above experiments involved Ficoll70 to promote lateral interaction of FtsZ filaments⁶⁻⁹. Alternatively, ZapA was produced in PURE_{flex}2.0 starting from its native gene sequence and its ability to crosslink FtsZ filaments was examined using purified FtsZ on sZipA-membranes (Fig. 2e,f). Protein networks of typical flower-like morphology with less condensed filaments than in the presence of Ficoll70 were observed after 3 h expression (Fig. 2f). We noticed that these filament structures are not stable in time and vanished after a few seconds imaging (Supplementary Fig. 8). Because gene sequence optimization resulted in a higher yield of synthesized ZapA (Supplementary Fig. 4), this engineered construct was also tested in the activity assay. Expression of the *zapA*_{opt} DNA template triggered the formation of a dense network of sZipA-FtsZ co-filaments that are stable in time (Supplementary Fig. 9). We attribute these new properties to the higher concentration of ZapA when expressed from the *zapA*_{opt} gene (Supplementary Fig. 4). Different areas of the SLB show various protein network phenotypes ranging from flower-like morphology to long condensed bundles (Supplementary Fig. 9). Although many filaments were localizing on the membrane, sZipA-FtsZ co-filaments were abundantly found to extend in the bulk phase (Supplementary Fig. 9). This suggests that the pre-assembly of ZapA-FtsZ bundles compromises the ability of sZipA-FtsZ to stably bind the membrane. We verified that cell-free synthesized ZapA is unable to produce membrane-bound FtsZ filaments in the absence of ZipA (Supplementary Fig. 10).

The exchange dynamics of FtsZ and sZipA subunits within polymers were quantified by FRAP. With Ficoll70, no recovery of sZipA signal was observed indicating poor lateral diffusion and turnover of the membrane-bound sZipA (Supplementary Fig. 11). In contrast, ZapA-mediated bundling of FtsZ filaments does not impair recovery of sZipA signal (Supplementary Fig. 11). Furthermore, FRAP experiments show that FtsZ-A647 monomers undergo twice faster exchange rate between filaments and bulk with expressed ZapA than with Ficoll70 (Supplementary Fig. 11). All together these results underline the importance of using ZapA to drive physiological filament network morphology and subunit turnover in membrane-

bound sZipA-FtsZ cytoskeletal structures. Furthermore, the experiments highlight that ZapA concentration is important for long-term stability of filaments.

Supplementary tables

Supplementary Table 1: Transitions of the MS/MS measurements for the proteolytic peptides of the indicated proteins.

Protein	Compound Name	Precursor Ion [m/z]	Product Ion [m/z]	Collision Energy [eV]	Accelerator Voltage [eV]	Ion Name
ZapA	MLQQTIEQALLEQGR.light	879.464	1043.548	28.3	4	y9
ZapA	MLQQTIEQALLEQGR.light	879.464	786.447	28.3	4	y7
ZapA	MLQQTIEQALLEQGR.light	879.464	715.410	28.3	4	y6
ZapA	MLQQTIEQALLEQGR.light	879.464	602.326	28.3	4	y5
ZapA	MLQQTIEQALLEQGR.light	879.464	489.242	28.3	4	y4
ZapA	MLQQTIEQALLEQGR.light	879.464	360.199	28.3	4	y3
QconCAT	MLQQTIEQALLEQGR.heavy	890.432	1057.506	28.3	4	y9
QconCAT	MLQQTIEQALLEQGR.heavy	890.432	797.414	28.3	4	y7
QconCAT	MLQQTIEQALLEQGR.heavy	890.432	725.380	28.3	4	y6
QconCAT	MLQQTIEQALLEQGR.heavy	890.432	611.299	28.3	4	y5
QconCAT	MLQQTIEQALLEQGR.heavy	890.432	497.218	28.3	4	y4
QconCAT	MLQQTIEQALLEQGR.heavy	890.432	367.178	28.3	4	y3
FtsA	YTELLNLVNEEILQLQEK.light	1095.089	1243.653	34.9	4	y10
FtsA	YTELLNLVNEEILQLQEK.light	1095.089	871.525	34.9	4	y7
FtsA	YTELLNLVNEEILQLQEK.light	1095.089	758.441	34.9	4	y6
FtsA	YTELLNLVNEEILQLQEK.light	1095.089	645.357	34.9	4	y5
FtsA	YTELLNLVNEEILQLQEK.light	1095.089	517.298	34.9	4	y4
FtsA	YTELLNLVNEEILQLQEK.light	1095.089	847.456	34.9	4	b7
QconCAT	YTELLNLVNEEILQLQEK.heavy	1106.555	1257.611	34.9	4	y10
QconCAT	YTELLNLVNEEILQLQEK.heavy	1106.555	881.495	34.9	4	y7
QconCAT	YTELLNLVNEEILQLQEK.heavy	1106.555	767.414	34.9	4	y6
QconCAT	YTELLNLVNEEILQLQEK.heavy	1106.555	653.333	34.9	4	y5
QconCAT	YTELLNLVNEEILQLQEK.heavy	1106.555	523.280	34.9	4	y4
QconCAT	YTELLNLVNEEILQLQEK.heavy	1106.555	855.432	34.9	4	b7
ZapA	DALNQAADDLNQR.light	722.345	902.433	23.4	4	y8
ZapA	DALNQAADDLNQR.light	722.345	831.396	23.4	4	y7
ZapA	DALNQAADDLNQR.light	722.345	760.358	23.4	4	y6
ZapA	DALNQAADDLNQR.light	722.345	645.331	23.4	4	y5
ZapA	DALNQAADDLNQR.light	722.345	417.220	23.4	4	y3
ZapA	DALNQAADDLNQR.light	722.345	542.257	23.4	4	b5
QconCAT	DALNQAADDLNQR.heavy	732.315	915.394	23.4	4	y8
QconCAT	DALNQAADDLNQR.heavy	732.315	843.360	23.4	4	y7
QconCAT	DALNQAADDLNQR.heavy	732.315	771.326	23.4	4	y6
QconCAT	DALNQAADDLNQR.heavy	732.315	655.302	23.4	4	y5
QconCAT	DALNQAADDLNQR.heavy	732.315	425.197	23.4	4	y3
QconCAT	DALNQAADDLNQR.heavy	732.315	549.236	23.4	4	b5
FtsA	GGVNDLESVVK.light	558.798	903.478	18.3	4	y8

FtsA	GGVNDLESVVK.light	558.798	789.435	18.3	4	y7
FtsA	GGVNDLESVVK.light	558.798	674.408	18.3	4	y6
FtsA	GGVNDLESVVK.light	558.798	561.324	18.3	4	y5
FtsA	GGVNDLESVVK.light	558.798	432.282	18.3	4	y4
FtsA	GGVNDLESVVK.light	558.798	214.119	18.3	4	b3
QconCAT	GGVNDLESVVK.heavy	565.279	913.449	18.3	4	y8
QconCAT	GGVNDLESVVK.heavy	565.279	797.412	18.3	4	y7
QconCAT	GGVNDLESVVK.heavy	565.279	681.388	18.3	4	y6
QconCAT	GGVNDLESVVK.heavy	565.279	567.306	18.3	4	y5
QconCAT	GGVNDLESVVK.heavy	565.279	437.267	18.3	4	y4
QconCAT	GGVNDLESVVK.heavy	565.279	217.110	18.3	4	b3
ribosomal protein S4	LSDYGVQLR.light	525.783	850.442	17.3	4	y7
ribosomal protein S4	LSDYGVQLR.light	525.783	735.415	17.3	4	y6
ribosomal protein S4	LSDYGVQLR.light	525.783	572.351	17.3	4	y5
ribosomal protein S4	LSDYGVQLR.light	525.783	635.304	17.3	4	b6
QconCAT	LSDYGVQLR.heavy	532.263	949.438	17.3	4	y8
QconCAT	LSDYGVQLR.heavy	532.263	861.409	17.3	4	y7
QconCAT	LSDYGVQLR.heavy	532.263	745.385	17.3	4	y6
QconCAT	LSDYGVQLR.heavy	532.263	581.325	17.3	4	y5
QconCAT	LSDYGVQLR.heavy	532.263	541.220	17.3	4	b5
QconCAT	LSDYGVQLR.heavy	532.263	641.286	17.3	4	b6
ribosomal protein L6	APVVVPAGVDVK.light	575.845	883.525	18.9	4	y9
ribosomal protein L6	APVVVPAGVDVK.light	575.845	784.456	18.9	4	y8
ribosomal protein L6	APVVVPAGVDVK.light	575.845	685.388	18.9	4	y7
ribosomal protein L6	APVVVPAGVDVK.light	575.845	268.166	18.9	4	b3
ribosomal protein L6	APVVVPAGVDVK.light	575.845	367.234	18.9	4	b4
ribosomal protein L6	APVVVPAGVDVK.light	575.845	466.302	18.9	4	b5
QconCAT	APVVVPAGVDVK.heavy	582.326	893.495	18.9	4	y9
QconCAT	APVVVPAGVDVK.heavy	582.326	793.430	18.9	4	y8
QconCAT	APVVVPAGVDVK.heavy	582.326	693.364	18.9	4	y7
QconCAT	APVVVPAGVDVK.heavy	582.326	271.157	18.9	4	b3
QconCAT	APVVVPAGVDVK.heavy	582.326	371.222	18.9	4	b4
QconCAT	APVVVPAGVDVK.heavy	582.326	471.288	18.9	4	b5

Supplementary Table 2: Bulk concentrations of cell-free expressed proteins measured by LC-MS.

Protein	Concentration single expression	Concentration co-expression	Concentration in <i>E. coli</i>
FtsA	4.5 ± 0.5 µM	2.9 ± 0.5 µM	0.5 µM
ZapA	0.54 ± 0.02 µM	0.5 ± 0.3 µM	1.5 µM

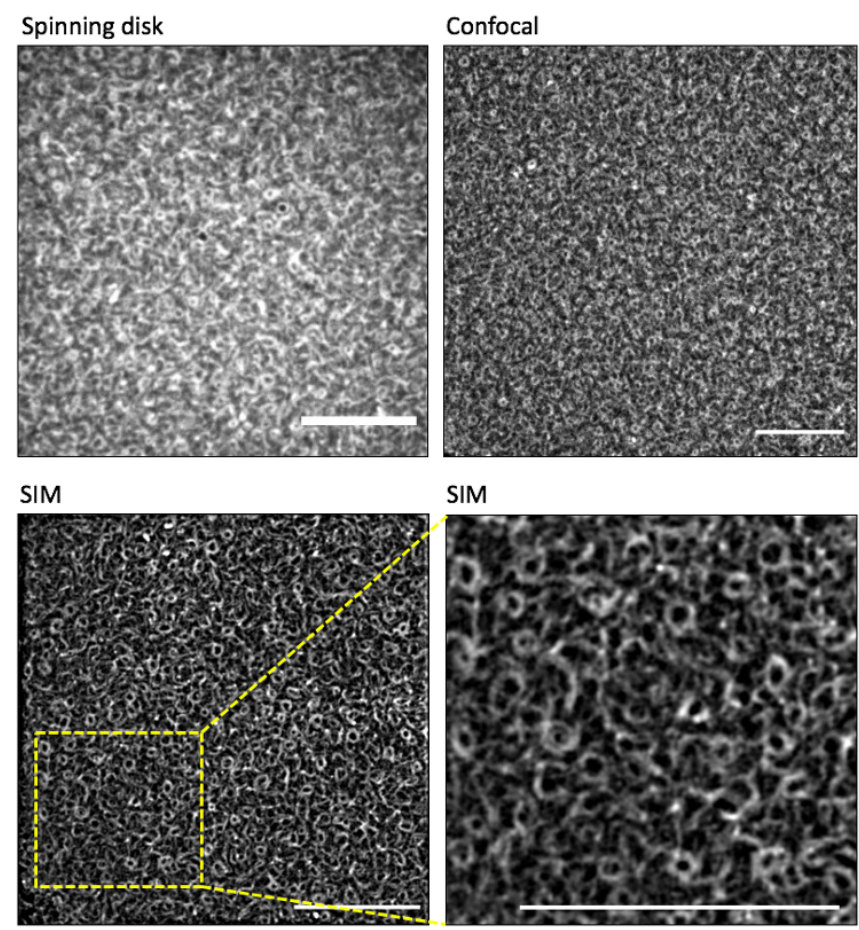
Supplementary Table 3: Concentrations of FtsA and ZapA in the SLB assays shown in main text Fig. 1. Concentration values have been corrected for dilution effect when assembling the SLB reaction solution.

Panel	Protein	Working concentration
a-b, c-d	FtsA	2.2 ± 0.2 µM
	ZapA	-
e-f	FtsA	1.6 ± 0.2 µM
	ZapA	0.2 ± 0.1 µM
g- h	FtsA	2.4 ± 0.3 µM
	ZapA	0.4 ± 0.2 µM
All	FtsZ	3 µM

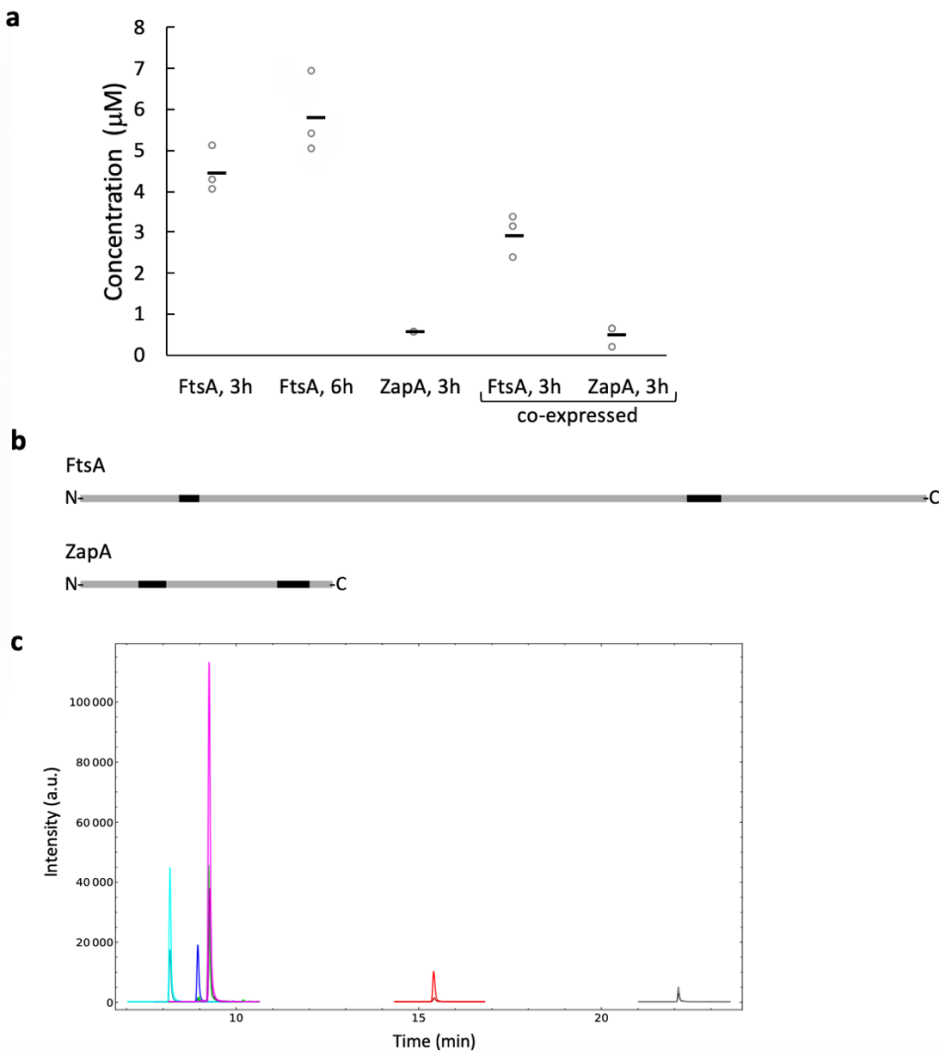
Supplementary Table 4: List of primers used in this study.

Name	Sequence (5' 3')	Comment
709	CAAAAAACCCCTCAAGACCCGTTTAGAGG	Anneals at the T7 terminator
757	TAATACGACTCACTATAGGG	Anneals at the T7 promoter
376	CTTTCTGGGCTTTGTTAGCAGCCGGATCCTTA- AAACTCTTTTCGCAGCCAAC	<i>ftsA</i> (with overhang for pET11-a)
508	TTTGTTAACTTTAAGAAGGAGATATACATATGATCAAG- GCGACGGACAG	<i>ftsA</i> (with overhang for pET11-a)
194	TAATACGACTCACTATAGGGGAATTGTGAGCGGATAA- CAATTCCT	Anneals at the T7 promoter

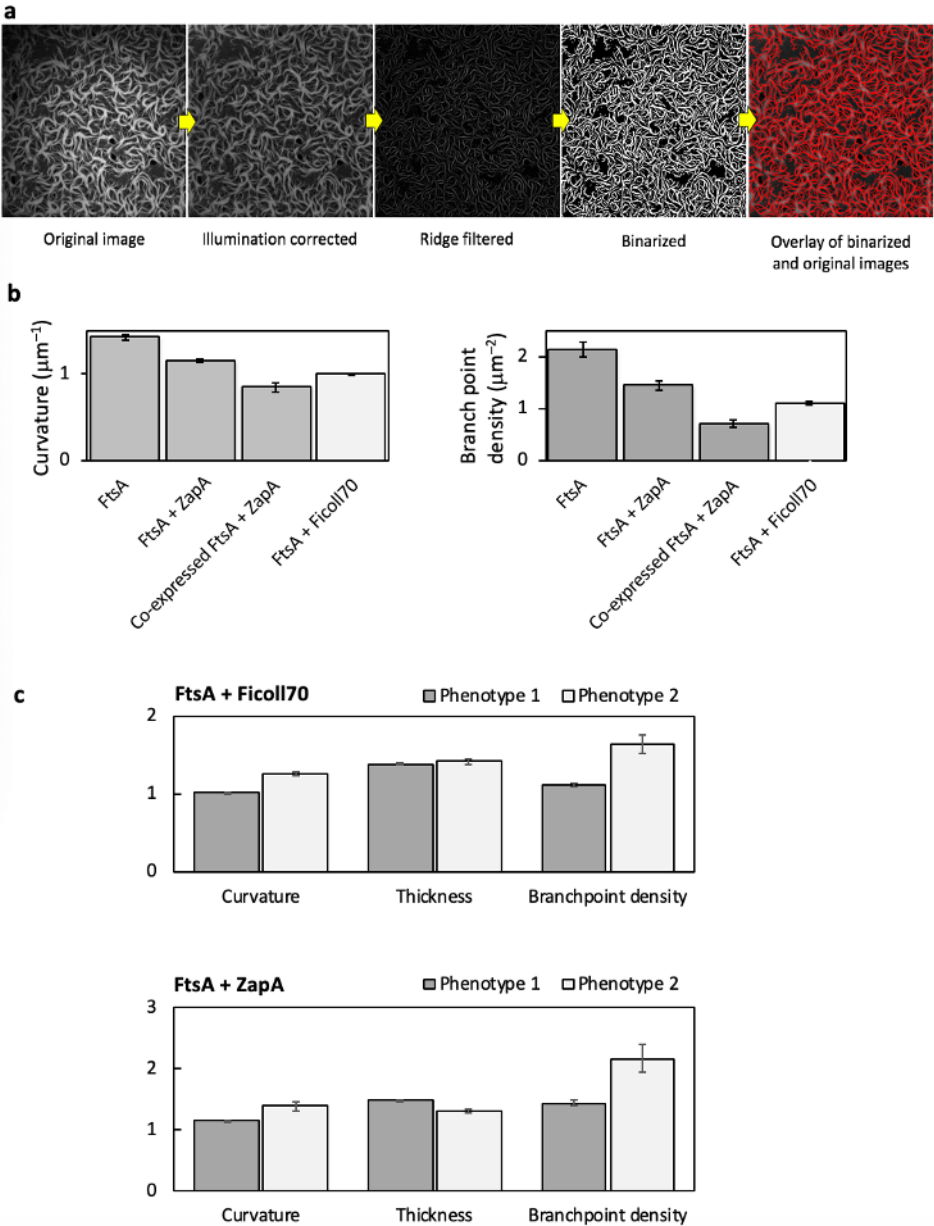
Supplementary figures



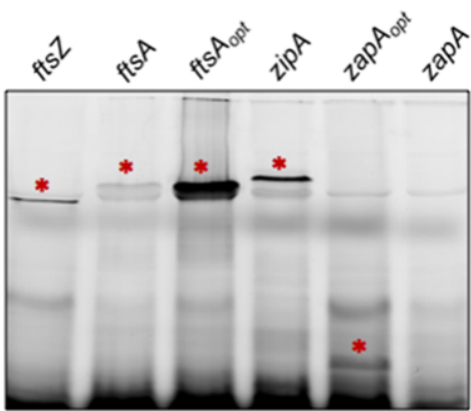
Supplementary Fig. 1: Cell-free synthesized FtsA shapes FtsZ filaments into characteristic ring-like structures. In situ expressed FtsA is sufficient to promote assembly of short and curved filaments of FtsZ (3 μM of purified FtsZ-A647) in the absence of Ficoll70. The sequence-optimized *ftsA_{opt}* gene was used. Sample preparation was the same as in the main text Fig. 1a,b. Different fluorescence imaging modes have been employed: spinning disk, laser scanning confocal and structured illumination microscopy (SIM). Scale bars indicate 10 μm. SIM provides a higher spatial resolution, while spinning disk offers faster image acquisition.



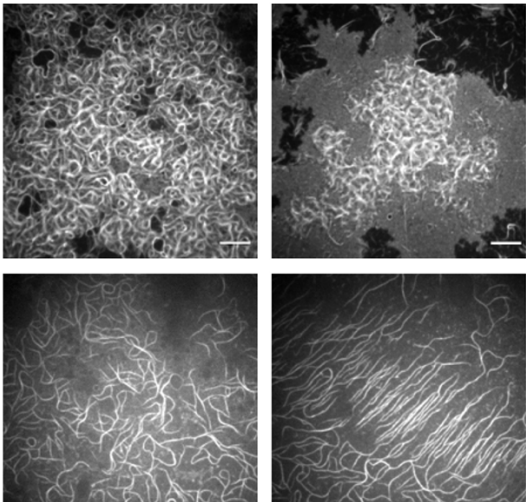
Supplementary Fig. 2: Quantitative LC-MS analysis of cell-free synthesized FtsA and ZapA in bulk reactions. **a**, Proteins were expressed individually or together (co-expressed) during a period of 3 h or 6 h. Abundance of the most C-terminal proteolytic peptide was quantified using an internal standard (QconCAT). Data represent mean values (displayed as segments) over three biological repeats (data points from individual measurements are shown), each analysed in three technical replicates. **b**, Cartoon depicting the position of the two specific proteolytic peptides along the primary sequence of FtsA and ZapA. **c**, LC-MS chromatogram of the investigated peptides. Color coding: red, MLQQTIEQAL-LEQGR (ZapA); black, YTELLNLVNEEILQLQEK (FtsA); blue, DALNQAADDLNQR (ZapA); green, GGVNDLESVVK (FtsA); cyan, LSDYGVQLR (ribosomal protein L6); magenta, APVVVPAGVDVK (ribosomal protein S1). The lighter colors are ¹⁵N labelled peptides (QconCAT), the darker colors ¹⁴N peptides (expressed proteins or PURE_{flex}2.0 ribosomal components). The two peptides for ribosomal proteins are used for quality control.



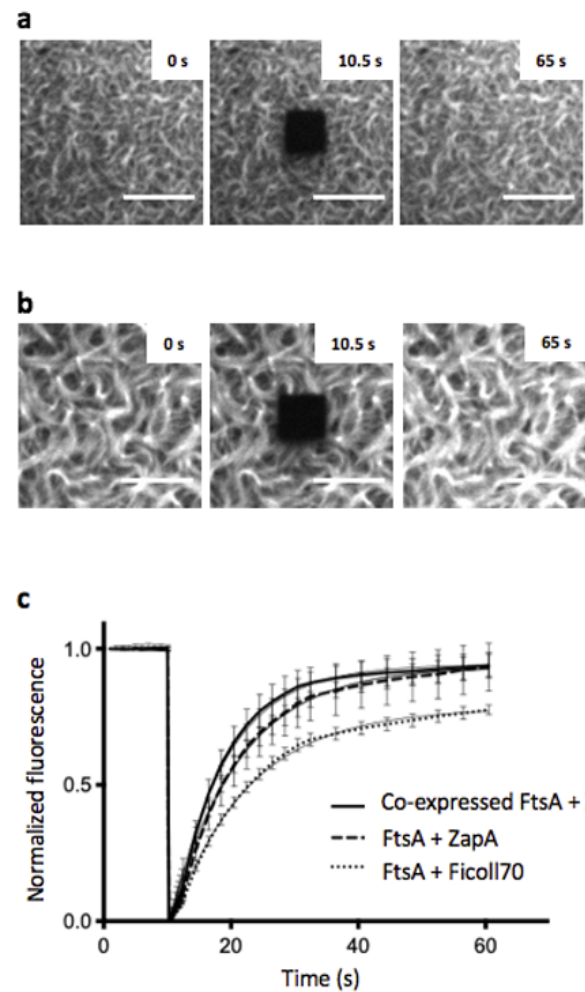
Supplementary Fig. 3: Quantitative image analysis of cytoskeletal network properties on SLB. a, Image processing workflow. **b,c,** Extracted parameters from the binarized images include filament curvature, thickness and branch point density. Four different fields of view (Fig. 1) have been analysed per experimental condition. Mean \pm standard deviation values are reported. **b,** Images from the most prominent phenotype were included in the analysis. **c,** Comparison between phenotypes 1 and 2 shown in the main text Fig. 1d (top) and Fig. 1f (bottom). Units: thickness (μm), curvature (μm^{-1}) and branch point density (μm^{-2}).



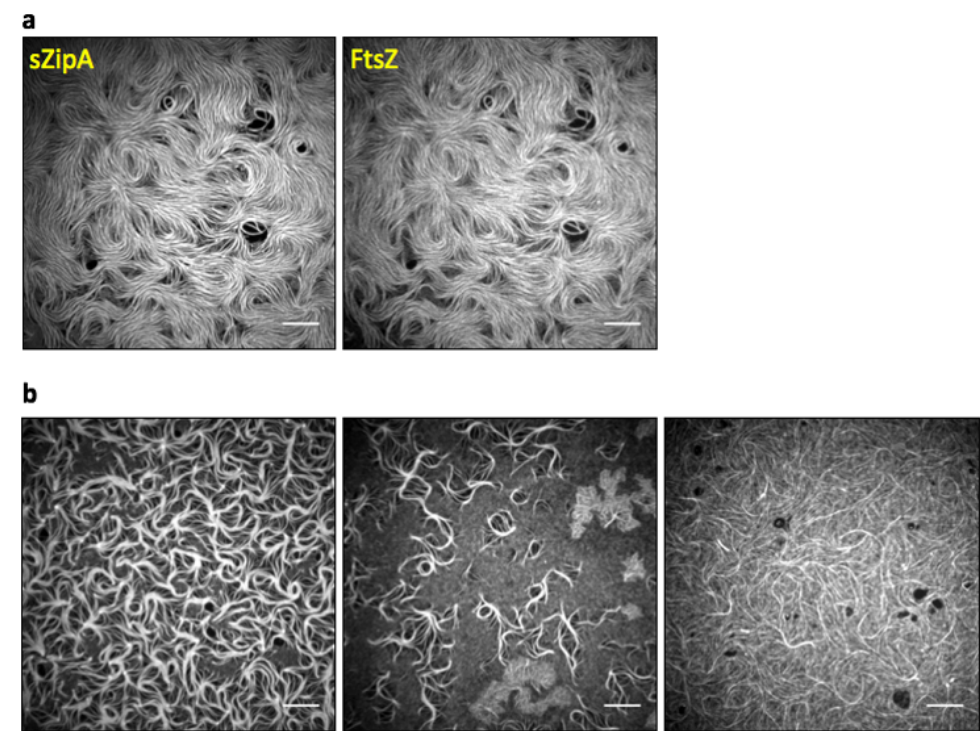
Supplementary Fig. 4: Visualization of cell-free expressed proteins by SDS-PAGE imaging. Single genes were expressed in PURE system reactions in the presence of the GreenLys reagent for co-translational labelling with a BODIPY-conjugated lysine residue. Translation products were analysed by fluorescence imaging of a 18% polyacrylamide gel. The bands depicted with an upper red star correspond to the full-length protein with expected molecular weight. The sequence-optimized constructs encoding FtsA and ZapA are named *ftsA_{opt}* and *zapA_{opt}*, respectively. No specific band was clearly visible when the native sequence of the *zapA* gene was expressed, denoting a low protein yield.



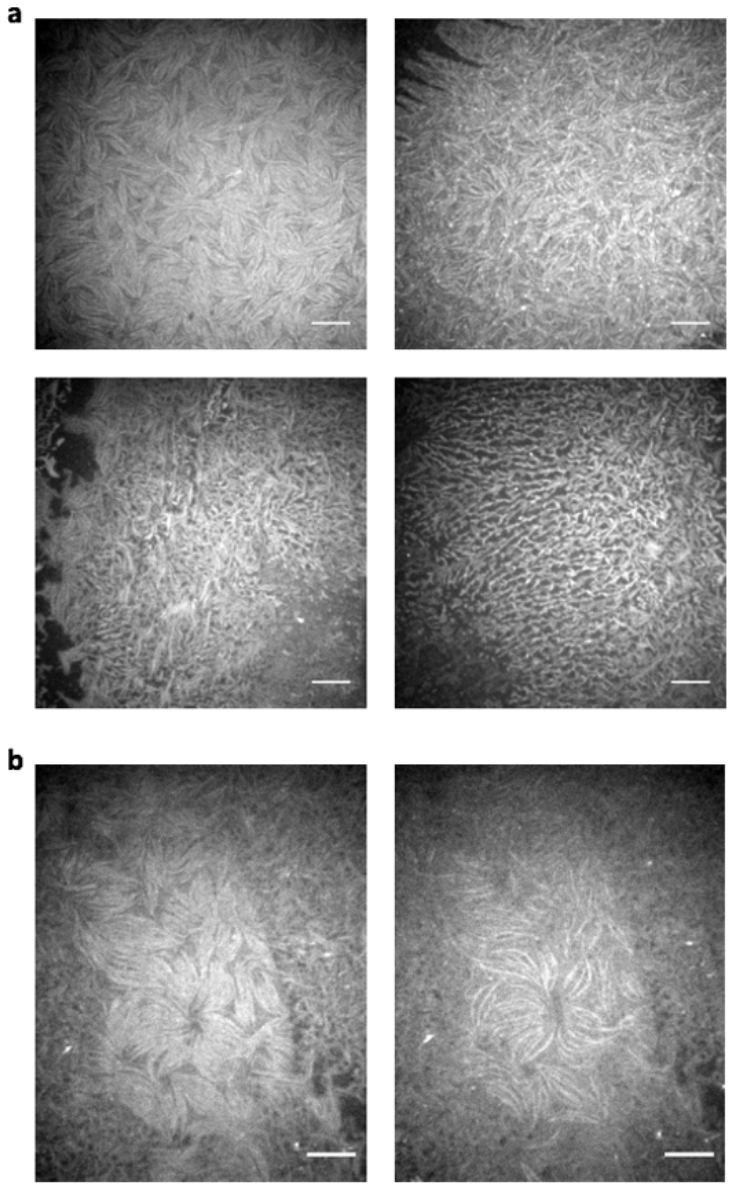
Supplementary Fig. 5: Cytoskeletal filaments of FtsZ in the presence of co-expressed FtsA and ZapA proteins on an SLB. FtsA and ZapA were directly expressed from their sequence-optimized constructs on an SLB, which drives the formation of thick FtsZ ($3 \mu\text{M}$ of purified FtsZ-A647) filaments developing in large-scale networks with various morphologies. Four different fields of view are shown. Images were acquired in the FtsZ-A647 channel. Experimental conditions are similar as in the main text Fig. 1g,h. Scale bars indicate $10 \mu\text{m}$.



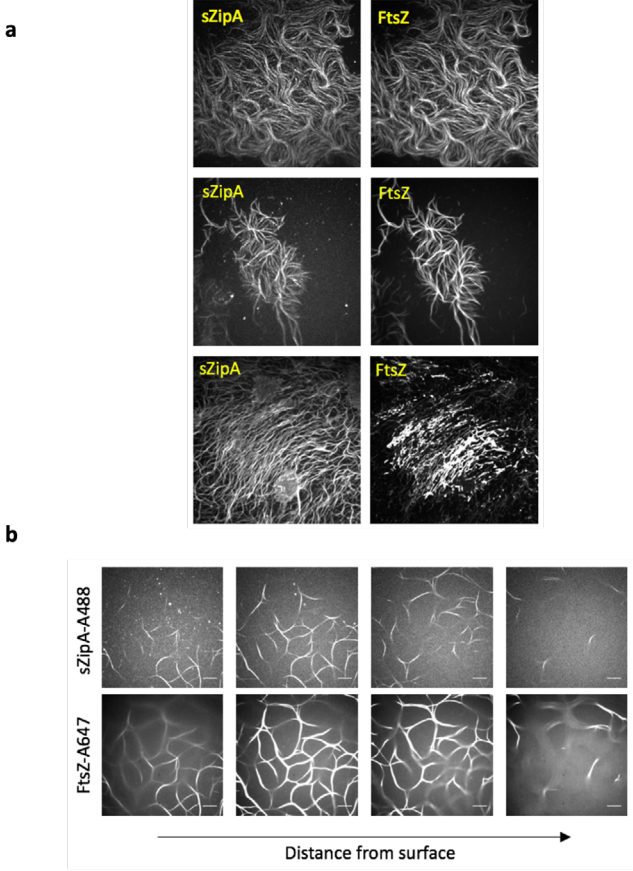
Supplementary Fig. 6: FRAP experiments with purified FtsZ-A647 and cell-free expressed FtsA. **a**, Time-lapsed fluorescence images of 3 μM FtsZ-A647 and cell-free expressed FtsA on an SLB in the presence of Ficoll70. The optimized *ftsA_{opt}* construct was used. Scale bars represent 10 μm. **b**, Time-lapsed fluorescence images of 3 μM FtsZ-A647 and separately expressed FtsA and ZapA on an SLB. The optimized *ftsA_{opt}* and native *zapA* constructs were used. Scale bars represent 10 μm. **c**, FRAP curves showing FtsZ monomer turnover under different experimental conditions, as annotated. Data are mean ± standard deviation values from four FRAP measurements per condition. Mono-exponential fits are appended. When bundling of FtsZ filaments was promoted by ZapA, a recovery halftime value of 7 ± 2 s was found with both separately and co-expressed FtsA. With Ficoll70, the recovery halftime value is 8.4 ± 1.9 s, which is markedly lower than with sZipA (17.6 ± 1.3 s, Supplementary Fig. 11). These values are also similar (7.5 ± 2.4 s) for FtsZ turnover in protofilaments seeded on sZipA membranes with ZapA (Supplementary Fig. 11).



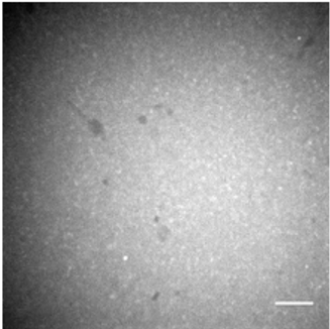
Supplementary Fig. 7: Heterogeneity of FtsZ polymer network morphologies on sZipA-bound membranes. **a**, Fluorescence images of sZipA-A488 (left) and FtsZ-A647 (right) in the minimal reaction buffer with Ficoll70. In the absence of Ficoll70, no large-scale filament networks develop (see main text Fig. 2a,b). **b**, Images of purified FtsZ-647 (3 μM) and sZipA-488 (1 μM) on top of an SLB in PUREfrex2.0 background supplemented with Ficoll70 (12.5% m/v). Three typical fields of view showing different protein network morphologies are reported. Images in the FtsZ-A647 channel are shown. Scale bars represent 10 μm.



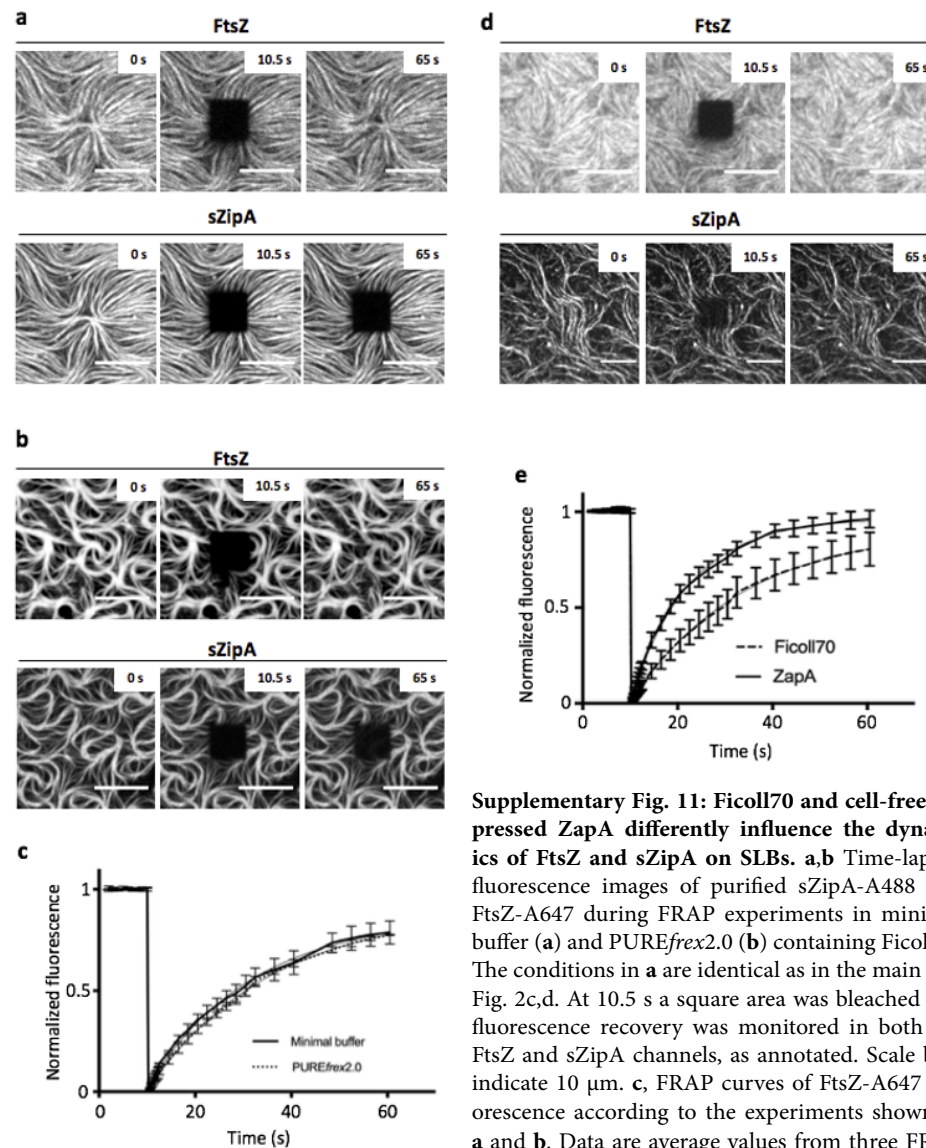
Supplementary Fig. 8: Instability and morphological heterogeneity of ZapA-mediated FtsZ polymer networks. **a**, ZapA, cell-free synthesized from the native gene sequence, promotes formation of FtsZ bundles (3 μ M of purified FtsZ-A647) recruited on an SLB pre-incubated with 1 μ M purified sZipA-A488. Four different fields of view in the FtsZ-A647 channel are shown. **b**, Time-lapsed images of the same SLB region showing disassembly of FtsZ bundles over a few seconds imaging (from left to right). Scale bars indicate 10 μ m.



Supplementary Fig. 9: Different phenotypes of sZipA-FtsZ co-filament networks in the presence of cell-free synthesized ZapA. **a**, A solution containing purified FtsZ-A647, cell-free expressed ZapA from the *zapA_{opt}* construct and additional 2 mM GTP, was incubated on top of an sZipA-A488-bound SLB. Images are from the FtsZ-A647 and sZipA-A488 channels, as annotated. **b**, Same conditions as in **a**. sZipA-FtsZ-ZapA co-filaments were abundantly found to point upwards the SLB and extend in the bulk phase. Both FtsZ-A647 and sZipA-A488 channels are displayed, as annotated. Scale bars are 10 μ m.



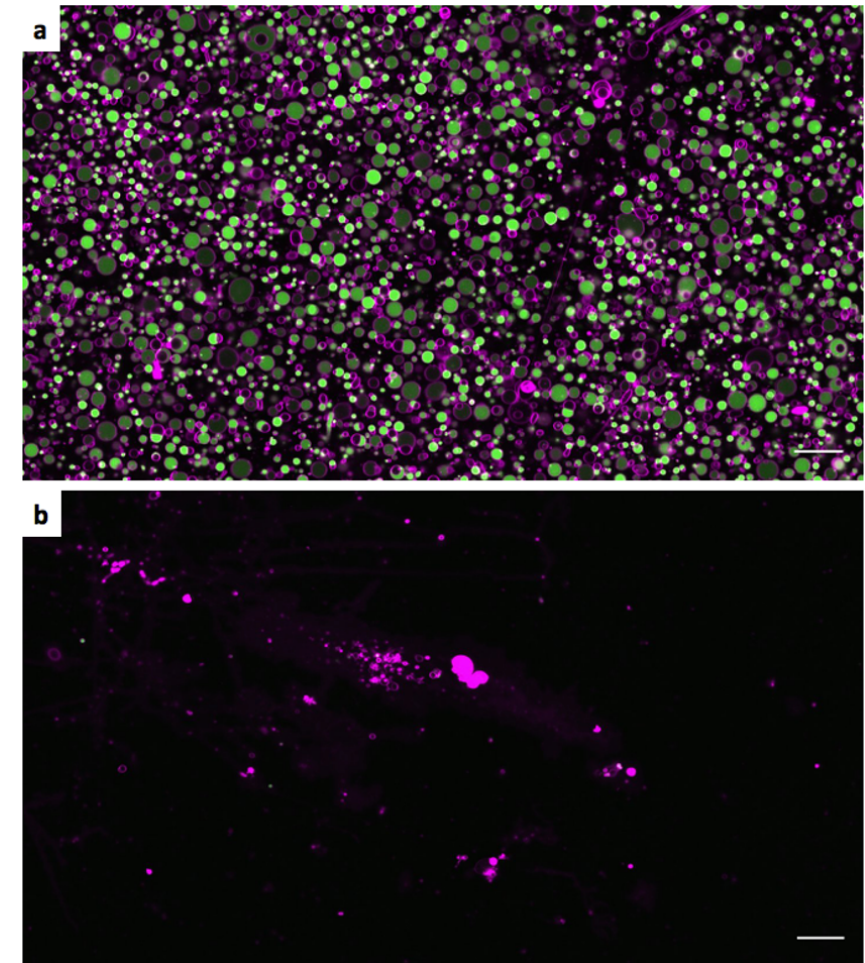
Supplementary Fig. 10: Cell-free synthesized ZapA is unable to produce membrane-bound FtsZ filaments in the absence of ZipA and FtsA. Concentration of purified FtsZ-A647 was 3 μ M. Scale bar represents 10 μ m.



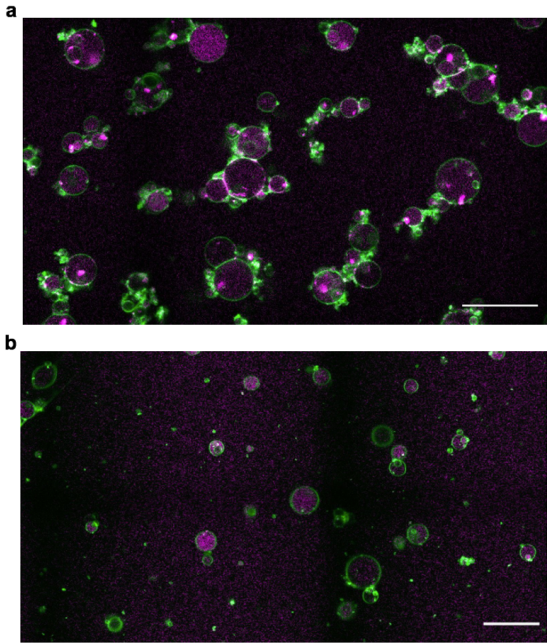
Supplementary Fig. 11: Ficoll70 and cell-free expressed ZapA differently influence the dynamics of FtsZ and sZipA on SLBs. **a,b** Time-lapsed fluorescence images of purified sZipA-A488 and FtsZ-A647 during FRAP experiments in minimal buffer (**a**) and PURE_{refx2.0} (**b**) containing Ficoll70. The conditions in **a** are identical as in the main text Fig. 2c,d. At 10.5 s a square area was bleached and fluorescence recovery was monitored in both the FtsZ and sZipA channels, as annotated. Scale bars indicate 10 μ m. **c**, FRAP curves of FtsZ-A647 fluorescence according to the experiments shown in **a** and **b**. Data are average values from three FRAP

experiments and error bars represent standard deviation values. Exponential fits are appended. No recovery of sZipA signal was observed in either buffer conditions indicating poor lateral diffusion and turnover of the membrane-bound sZipA. We found that the recovery time (or recovery half-time) of FtsZ is about 15.2 ± 1.4 s in minimal buffer and about 17.6 ± 1.3 s in PURE system background. This result indicates that the FtsZ turnover rate between the bulk and filaments is similar in the two media. **d**, Time-lapsed fluorescence images of purified sZipA-A488 and FtsZ-A647 during FRAP experiments with the cell-free expressed *zapA_{opt}* gene. The conditions are identical as in the main text Fig. 2c. At 10.5 s a square area was bleached and fluorescence recovery was monitored in both the FtsZ and sZipA channels, as annotated. Different fields of view are shown. Scale bars indicate 10 μ m. **e**, FRAP curves of FtsZ-A647 fluorescence corresponding to the experiment shown in **d**. Data are average values from

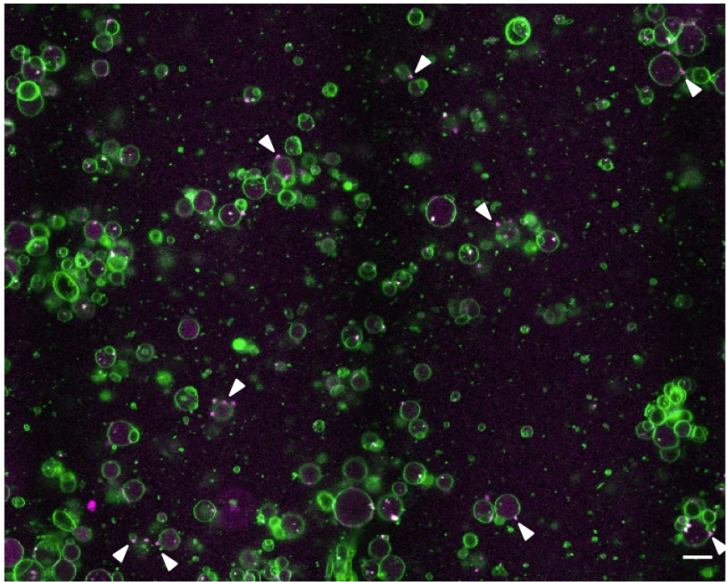
four FRAP experiments and error bars represent standard deviation values. Exponential fits are appended. FRAP experiments show that FtsZ-A647 monomers undergo twice faster exchange rate between filaments and bulk with ZapA expressed from the optimized or non-optimized construct than with Ficoll70 (~ 7.5 s vs. ~ 17 s).



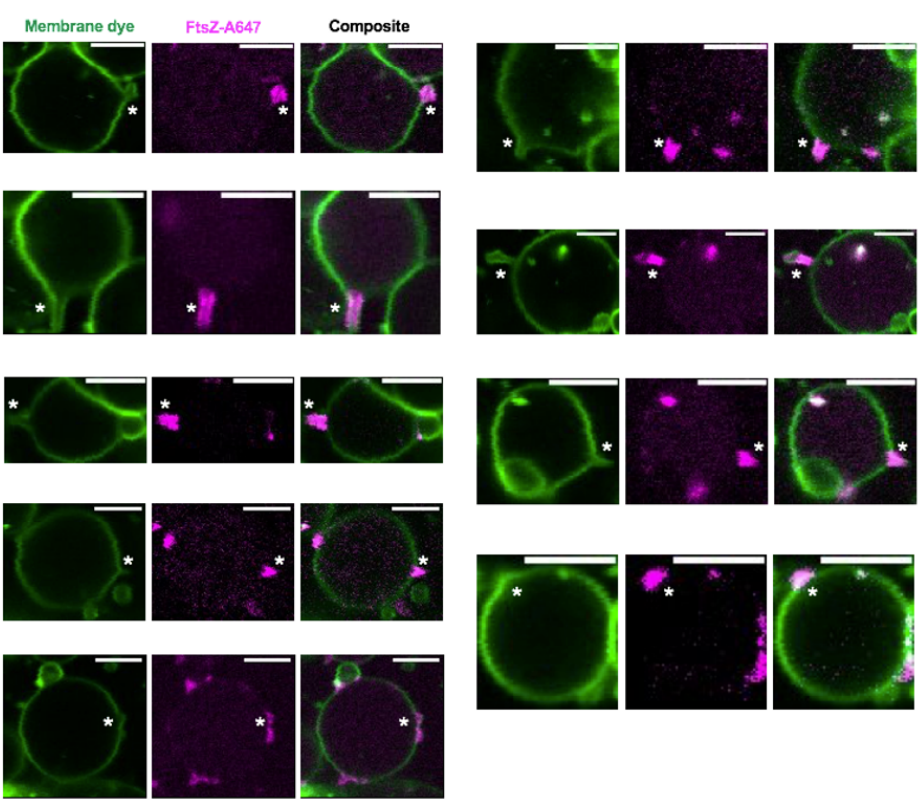
Supplementary Fig. 12: Ficoll70 impairs formation of gene-expressing liposomes. **a**, Fluorescence confocal image of liposomes expressing the *yfp* gene reporter. The same protocol was used to express cytoskeletal proteins, as shown in the main text Fig. 3 and 4. The membrane dye signal is coloured in magenta and the YFP fluorescence is colored in green. **b**, The presence of Ficoll70 in the swelling medium alters the production of liposomes. Scale bars represent 20 μ m.



Supplementary Fig. 13: Confocal fluorescence images of FtsZ-A647-containing liposomes with and without expressed FtsA. **a**, Population of liposomes containing FtsA and purified FtsZ-A647 after 6 h expression of the *ftsA_{opt}* construct. Agglutinated small liposomes can be seen around larger vesicles. **b**, Population of liposomes containing purified FtsZ-A647 but no *ftsA_{opt}* gene. The image was taken after 6 h incubation to reproduce the conditions for gene expression (**a**). The occurrence of small vesicles surrounding a big liposome is much lower than in the presence of in situ synthesized FtsA. Moreover, FtsZ-A647 is localized evenly in the lumen of vesicles. Membrane is coloured in green and FtsZ-A647 in red. Different imaging settings have been used compared to the image shown in **a**, explaining the difference in background signal in the FtsZ-A647 channel. Scale bars represent 20 μm.



Supplementary Fig. 14: Confocal fluorescence image of liposomes containing purified FtsZ-A647 and in situ expressed FtsA. Experimental conditions are identical as in the main text Fig. 3. The image was taken after ~3.5 h incubation for gene expression. Fluorescence from the membrane dye is coloured in green and FtsZ-A647 signal is in magenta. Arrowheads point to liposomes exhibiting budding spots or constriction sites. Scale bar represents 20 μm.



Supplementary Fig. 15: Confocal fluorescence images of individual liposomes containing purified FtsZ-A647 and in situ expressed FtsA. Experimental conditions are identical as in the main text Fig. 3. Fluorescence from the membrane dye is coloured in green and FtsZ-A647 signal is in magenta. The composite image is the overlay of the two channels. Asterisks indicate budding spots or constriction sites. Scale bars represent 5 μm.

Supplementary files

The Supplementary Movies and Source Data file are provided here <https://www.nature.com/articles/s42003-020-01258-9#Sec30>.

Supplementary references

1. Loose, M. & Mitchison, T. J. The bacterial cell division proteins FtsA and FtsZ self-organize into dynamic cytoskeletal patterns. *Nat. Cell Biol.* **16**, 38–46 (2014).
2. Martos, A. *et al.* Characterization of self-association and heteroassociation of bacterial cell division proteins FtsZ and ZipA in solution by composition gradient–static light scattering. *Biochemistry* **49**, 10780–10787 (2010).
3. Wang, X. & Lutkenhaus, J. The FtsZ protein of *Bacillus subtilis* is localized at the division site and has GTPase activity that is dependent upon FtsZ concentration. *Mol. Microbiol.* **9**, 435–442 (1993).
4. Sossong, T. M., Brigham-Burke, M. R., Hensley, P. & Pearce, K. H. Self-activation of guanosine triphosphatase activity by oligomerization of the bacterial cell division protein FtsZ. *Biochemistry* **38**, 14843–14850 (1999).
5. González, J. M. *et al.* Essential cell division protein FtsZ assembles into one monomer-thick ribbons under conditions resembling the crowded intracellular environment. *J. Biol. Chem.* **278**, 37664–71 (2003).
6. Martos, A. *et al.* FtsZ polymers tethered to the membrane by ZipA are susceptible to spatial regulation by Min waves. *Biophys. J.* **108**, 2371–2383 (2015).
7. Cabré, E. J. *et al.* Bacterial division proteins FtsZ and ZipA induce vesicle shrinkage and cell membrane invagination. *J. Biol. Chem.* **288**, 26625–34 (2013).
8. Furusato, T. *et al.* *De novo* synthesis of basal bacterial cell division proteins FtsZ, FtsA, and ZipA inside giant vesicles. *ACS Synth. Biol.* **7**, 953–961 (2018).
9. Rivas, G., Alfonso, C., Jiménez, M., Monterroso, B. & Zorrilla, S. Macromolecular interactions of the bacterial division FtsZ protein: from quantitative biochemistry and crowding to reconstructing minimal divisomes in the test tube. *Biophys. Rev.* **5**, 63–77 (2013).

Min waves without MinC can pattern FtsA-FtsZ filaments on model membranes

Elisa Godino, Anne Doerr, & Christophe Danelon

Although the essential proteins that drive bacterial cytokinesis have been identified and reconstituted in vitro, the precise mechanisms by which they dynamically interact to enable symmetrical division are largely unknown. In *Escherichia coli*, cell division begins with the formation of a proto-ring composed of FtsZ and its membrane-tethering proteins FtsA and ZipA. In the broadly proposed molecular scenario for ring positioning, Min waves composed of MinD and MinE distribute the FtsZ-polymerization inhibitor MinC away from mid-cell, where the Z-ring can form. Therefore, MinC is believed to be an essential element connecting the Min and FtsZ systems. Here, by using cell-free gene expression on planar lipid membranes, we demonstrate that MinDE drive the formation of dynamic, antiphase patterns of FtsZ-FtsA co-filaments even in the absence of MinC. This behavior is also observed when the proteins are compartmentalized inside microdroplets. These results suggest that Z-ring positioning may be achieved with a more minimal set of proteins than previously envisaged, providing a fresh perspective about the role of MinC. Moreover, we propose that MinDE oscillations may constitute the minimal localization mechanism of an FtsA-FtsZ constricting ring in a prospective synthetic cell.

Essentially as published: Godino, E. *et al.*, Min waves without MinC can pattern FtsA-FtsZ filaments on model membranes, *bioRxiv* (2021) DOI: 10.1101/2021.11.15.468671

Introduction

In *Escherichia coli* bacteria, a ring-forming multiprotein complex drives membrane constriction at the future division site¹. The proto-ring is composed of the three proteins FtsZ, FtsA and ZipA^{2,3}. FtsZ is a tubulin homologue with GTPase activity that can polymerize into protofilaments^{4,5}. FtsZ has no affinity for lipids and is anchored to the membrane by ZipA and the actin homologue FtsA⁶⁻⁸. This set of proteins acts as a scaffold, recruiting other factors to form a mature divisome. The Min system in *E. coli* is composed of the three proteins MinC, MinD, and MinE. Together, they provide the localization cues that restrict the assembly of the FtsZ ring to the middle of the cell, following a commonly accepted sequence of molecular events⁹. MinD is an ATPase that dimerizes and is recruited on the membrane when bound to ATP. Once at the membrane, MinD interacts with MinE, which stimulates the ATPase activity of MinD leading to the release of both proteins from the membrane. This dynamic interplay between MinD and MinE, together with the geometrical constraints of the cell, cause oscillating gradients of the two proteins at the cell poles¹⁰⁻¹³. MinC travels with the MinDE waves, where it inhibits the assembly of FtsZ protofilaments. As a result of the Min oscillations, the time-averaged concentration of the MinD-MinC complex is higher at the poles, encouraging the formation of the Z-ring to mid-cell¹⁴⁻¹⁶.

Despite numerous in vitro studies about membrane-anchored FtsZ¹⁷⁻²⁰ and Min dynamics^{16,21-23}, data about the spatiotemporal regulation of FtsA-FtsZ cytoskeletal structures by MinDEC are scarce²⁴. It is known that MinC is required for correct placement of the division site in vivo^{10,13}. On the other hand, several reports suggest that MinDE oscillations may act as a spatial regulator of membrane proteins²⁵⁻²⁷. The abundances of the membrane proteome in wild-type and Δmin *E. coli* cells were compared, revealing that Min oscillating gradients modulate protein association with the inner membrane²⁵. Moreover, MinDE dynamic patterns spatiotemporally regulate and transport peripheral membrane proteins on supported lipid bilayers (SLBs) and in microcompartments^{26,27}. These recent findings raise the question of whether the oscillating MinDE gradients could influence membrane localization of FtsA-FtsZ filaments in the absence of MinC. Interestingly, when FtsZ-YFP-MTS (a chimera of truncated FtsZ, YFP, and the membrane-targeting sequence of MinD) was combined with MinDE proteins on an SLB, static FtsZ-YFP-MTS networks were not affected by the Min surface waves²⁶. The use of a chimeric FtsZ in these in vitro assays leaves open questions, since the ability of MinDE oscillating gradients to influence the lateral distribution of FtsZ might be different with the native membrane anchor FtsA.

Herein, we set out to elucidate this question by combining MinDE(C), where '(C)' indicates the presence or absence of MinC, and FtsA-FtsZ in open and closed model membrane systems. As a medium for our cell-free assays, we use the PURE system, a minimal gene expression system reconstituted primarily from *E. coli* constituents^{28,29}. The activity of PURE-expressed FtsA and MinDEC from single-gene constructs has already been validated^{24,30}. Here, we design a DNA

template containing the *E. coli* genes *ftsA*, *minD* and *minE* concatenated in the form of three transcriptional units (tri-cistron). All proteins are expressed at physiologically relevant levels and in active states, allowing us to examine the interplay between the spatial organization of FtsA-FtsZ cytoskeletal structures and MinDE(C) membrane patterns on SLBs and within microdroplets. We find that MinDE surface waves act as a spatial regulator of FtsA-FtsZ filaments in a MinC-independent manner. The possible implications regarding bacterial cell division and implementation of a minimal FtsZ ring in synthetic cells are discussed.

Results

Cell-free co-expression of FtsA, MinD and MinE at physiological levels

As an experimental design strategy to co-reconstitute the Min and FtsZ subsystems, we created a multicistronic DNA template containing the genes of the *E. coli* proteins FtsA, MinD, and MinE (Fig. 1a). The DNA template (5 nM) was constitutively expressed in PURE_{frex}2.0 and the abundance of the three synthesized proteins was quantified by targeted liquid chromatography-coupled mass spectrometry (LC-MS)(Fig. 1a and Supplementary Fig. 1). After 3 hours of expression, the obtained concentrations were $1.5 \pm 0.1 \mu\text{M}$ for FtsA, $4.2 \pm 0.9 \mu\text{M}$ for MinD and $3.2 \pm 0.4 \mu\text{M}$ for MinE (mean \pm SD, three biological replicates) (Fig. 1b). These values give a good approximation of the total amounts of full-length proteins but may overestimate the concentrations of active proteins. Similar concentration values were reported in vivo: $\sim 0.5 \mu\text{M}$ for FtsA³¹, and an equimolar amount of MinD and MinE ranging between 1 and 3 μM ^{32,33}. Kinetics of FtsA, MinD and MinE production revealed that most of FtsA and MinD proteins were synthesized within the first 3 hours of co-expression (Fig. 1c). The apparent translation rate was calculated by fitting a phenomenological model to the experimental data yielding values of $0.018 \pm 0.002 \mu\text{M min}^{-1}$ for FtsA, $0.043 \pm 0.016 \mu\text{M min}^{-1}$ for MinD and $0.027 \pm 0.002 \mu\text{M min}^{-1}$ for MinE (mean \pm SD of fitted parameter values, three biological replicates). The expression lifespan, defined as the time point at which protein production stops, was determined for each protein: $119 \pm 28 \text{ min}$ (FtsA), $144 \pm 28 \text{ min}$ (MinD) and $250 \pm 16 \text{ min}$ (MinE). These values are consistent with those obtained from kinetic profiles of other PURE-expressed proteins^{34,35}.

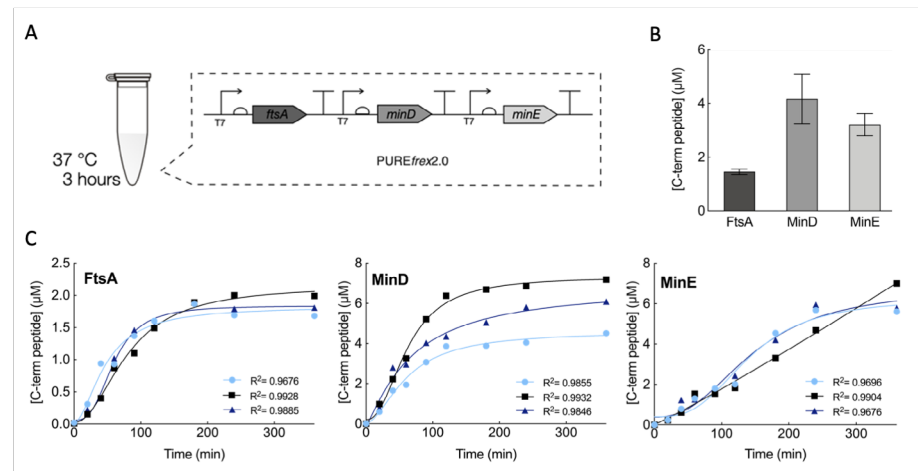


Figure 1: Quantification of cell-free expressed FtsA, MinD and MinE proteins from a single DNA construct. **a**, Each gene, *ftsA*, *minD* and *minE*, was placed under its own T7 promoter, ribosome binding site and T7 transcription terminator and was constitutively expressed with PURE_{flex}2.0 in test-tube reactions. **b**, Quantitative LC-MS analysis of FtsA, MinD and MinE protein production after 3 hours of expression at 37°C. Abundance of the most C-terminal proteolytic peptide was quantified for each protein using an internal standard (QconCAT). Data represent mean values over three biological repeats, each analyzed in three technical replicates. **c**, Concentration of FtsA, MinD and MinE (most C-terminal peptide) as a function of the expression time course (from 0 to 6 hours). Symbols represent data from three independent experiments. The solid lines are fits to a mathematical model for gene expression kinetics (Methods section).

Integration of MinDEC dynamic patterns and FtsA-FtsZ cytoskeletal structures on SLBs

We next investigated how the MinDEC and FtsA-FtsZ networks mutually interact on SLBs. The tri-cistron DNA was expressed in test-tube reactions to produce FtsA and MinDE. Purified FtsZ-A647 (FtsZ conjugated to the AlexaFluor647 fluorophore, 3 μM) and eGFP-MinC (fusion between the enhanced green fluorescent protein and MinC, 0.5 μM) were subsequently added, along with adenosine triphosphate (ATP, extra 2.5 mM) and guanosine triphosphate (GTP, extra 2 mM) (Fig. 2a). Sample was transferred onto an SLB and the membrane organization of the FtsZ- and Min-subsystems was imaged by time-lapse fluorescence microscopy. We found that the membrane area close to the center of the chamber exhibited exclusively FtsA-FtsZ filaments and ring-like structures (Fig. 2b), with cytoskeletal properties similar to that observed in the absence of Min proteins^{20,30}. In contrast, the edge of the chamber was occupied by MinDEC dynamic patterns only. In between these two regions, mixed patterns involving the two subsystems were observed (Fig. 2b). Spatial discrimination in distinct domains occurred immediately after supplying the PURE sample. We assume that molecular diffusion at the membrane is constrained by the edge of the chamber, resulting in

a higher concentration of membrane-bound MinD and MinE^{36,37} that outcompete FtsA for membrane coverage.

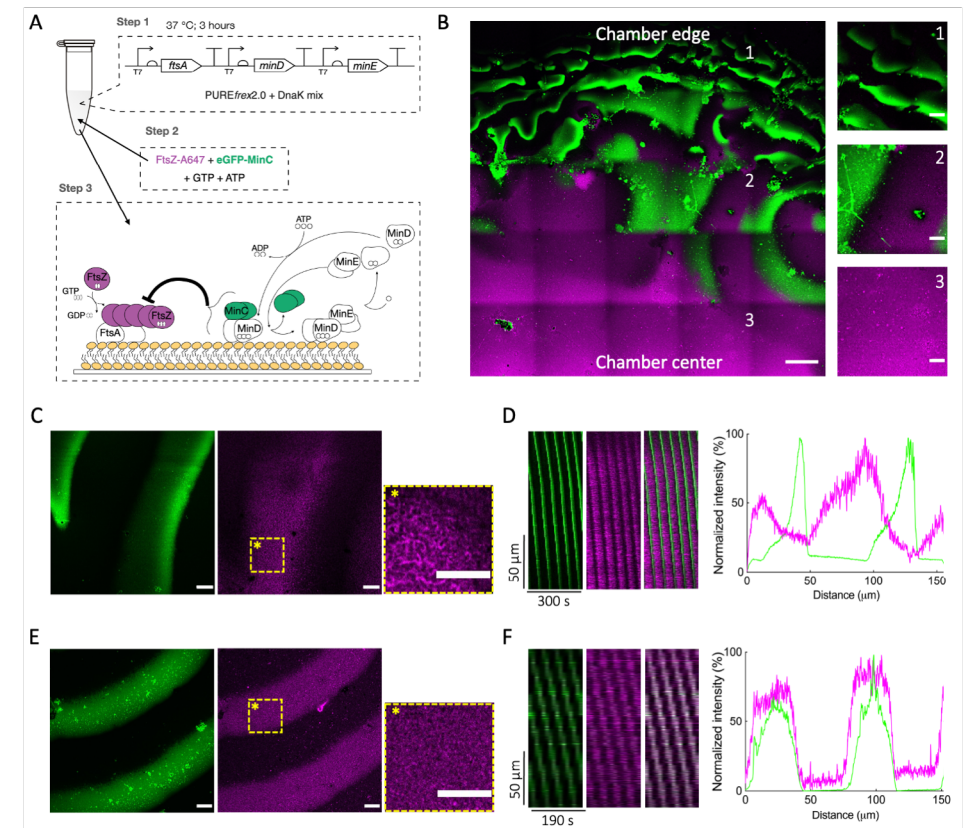


Figure 2: Integration of MinDEC surface waves with FtsA-FtsZ filament structures on supported membranes. **a**, Schematic of the experimental approach. Genes *ftsA*, *minD* and *minE* were co-expressed from the three-cistron DNA template (5 nM) in PURE system with a DnaK chaperone mix for 3 hours at 37°C. The solution was then supplemented with 2.5 mM ATP, 2.0 mM GTP, 0.5 μM eGFP-MinC and 3 μM FtsZ-A647 before transfer on top of an SLB. The cartoon depicts the main biochemical steps underlying FtsZ polymerization, its recruitment to the membrane by FtsA, and the influence of the reconstituted Min network. **b**, Mosaic of 5×5 tile scan microscope images showing large-scale organization of FtsA-FtsZ and MinDEC dynamic patterns. FtsA-FtsZ rings mostly populate the center of the chamber (3), while MinDEC oscillating gradients dominate at the edges of the chamber (1). In between these two areas (2), correlated patterns of the two subsystems can be seen. Signals from eGFP-MinC and FtsZ-A647 are in green and magenta, respectively. Composite images of overlaid channels are shown. Scale bar is 50 μm. **c**, Fluorescence microscopy images of FtsA-FtsZ and MinDEC dynamic patterns taken from the intermediate SLB area (2). A zoom-in image of the framed area in the FtsZ channel is also displayed, showing the organization of FtsA-FtsZ into curved filaments and ring-like structures. Scale bars are 10 μm. **d**, The time evolution of planar waves was analyzed and kymographs were constructed. On the right, examples of intensity profiles of MinC and FtsZ are shown. Color coding is the same as

for the microscopy images. **e**, Fluorescence microscopy images of FtsZ and MinDEC dynamic patterns when omitting FtsA. A zoom-in image of the framed area in the FtsZ channel is also displayed, showing that in the absence of FtsA, FtsZ fails to organize into cytoskeletal structures. **f**, Kymographs constructed from the time series images shown in (**e**). On the right, intensity profiles of MinC and FtsZ signals showing that FtsZ travels with the MinDEC waves in the absence of a membrane anchor.

In the areas where FtsA-FtsZ and Min proteins coexisted, FtsZ could undergo different types of dynamic behaviors shaped by Min oscillatory gradients, including planar waves, rotating spirals, and standing waves (Fig. 2b,c and Supplementary Fig. 2). Fluorescence intensity profiles showed that membrane localization of MinC and FtsZ anti-correlated (Fig. 2d, Movie S1). The intensity distribution found for the traveling wave was broader for FtsZ than MinC. Calculated wavelength of MinC planar waves in the region where the two subsystems coexisted was $113 \pm 30 \mu\text{m}$ and the wave velocity was $0.71 \pm 0.30 \mu\text{m s}^{-1}$ (mean \pm SD, from three biological replicates). Standing waves showed a characteristic oscillation time of $105 \pm 24 \text{ s}$. In the area where FtsZ signal was not detectable, the Min wavelength was $57 \pm 13 \mu\text{m}$, i.e. about half the value measured in the intermediate region. This result suggests that membrane-bound FtsA-FtsZ filaments influence the Min wave properties by increasing the wavelength (Supplementary Fig. 2b). When omitting FtsA through expression of a bi-cistronic DNA template containing only the *minD* and *minE* genes, FtsZ rings were no longer observed on the bilayer (Fig. 2e, Movie S2). Instead, FtsZ traveled in phase with MinC on the MinDE waves (Fig. 2e,f, Movie S2). The observed colocalization of the MinC and FtsZ patterns was consistent with previous results that indicated weak transient interaction between MinC and non-membrane bound FtsZ³⁸. Calculated wavelength was $59 \pm 14 \mu\text{m}$, similar to the value measured for MinDEC patterns in the area where FtsA-FtsZ were excluded. This result supports the hypothesis that the presence of FtsA-FtsZ on the membrane increases the wavelength of propagating Min waves.

Following a traditional view of the interplay between the two subsystems, the dynamic behavior of FtsZ reported in Fig. 2b-c is expected to be the result of the inhibitory interaction of traveling MinC on FtsA-bound FtsZ. However, a different interpretation would be that FtsA-FtsZ oscillatory gradients originated from the direct action of the MinDE proteins, a possible scenario that we investigated in the next section.

MinDE oscillatory gradients, without MinC, drive the formation of FtsA-FtsZ cytoskeletal patterns on SLBs

To explore the hypothesis that MinC has a dispensable function in regulating FtsA-FtsZ membrane dynamics, we repeated the experiments described above, this time replacing purified eGFP-MinC by a trace amount of purified eGFP-MinD (100 nM) as a reporter of the Min oscillations (Fig. 3a). On a large scale, FtsA-FtsZ structures were more prominent in the

center of the chamber, while Min waves preferentially populate the outer area of the chamber. Coexistence of both MinDE and FtsA-FtsZ dynamic patterns occurred in between these two regions (Fig. 3b), similarly as observed in the presence of MinC (Fig. 2b).

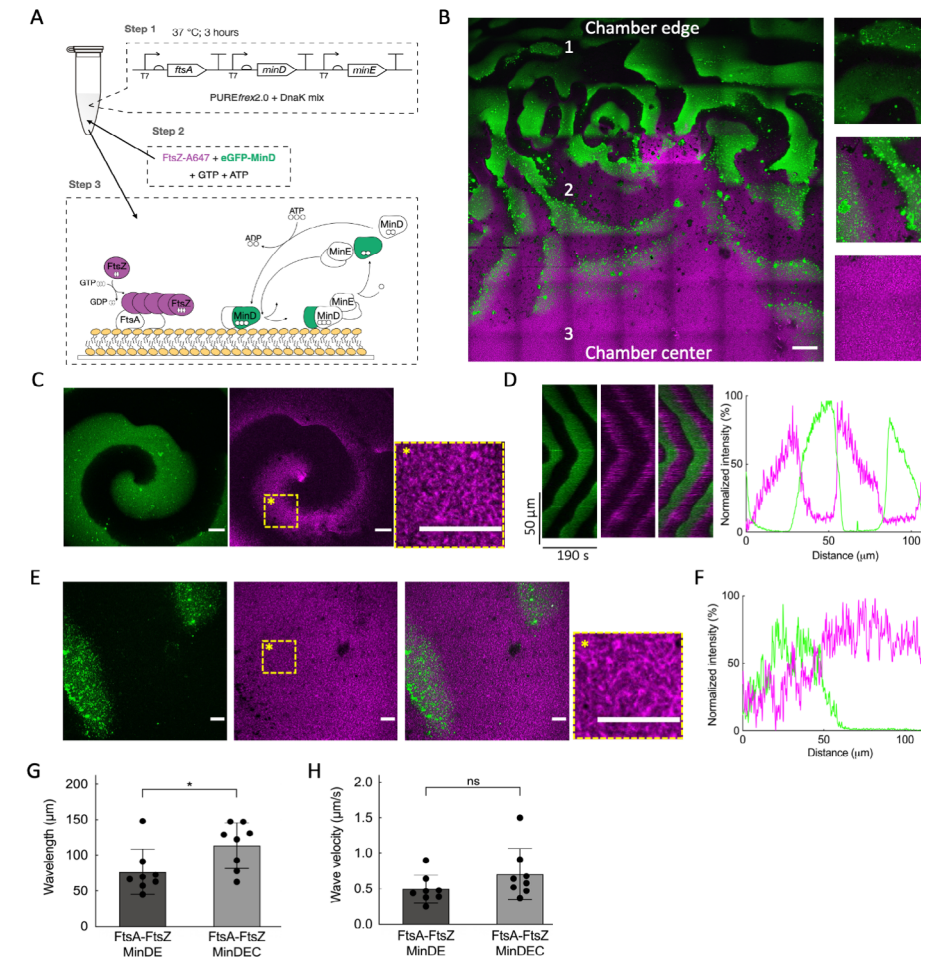


Figure 3: MinDE proteins, without MinC, regulate FtsA-FtsZ patterns on supported membrane assays. **a**, Schematic of the experimental workflow for end-point expression assays. Genes *ftsA*, *minD* and *minE* were co-expressed from a single DNA template (5 nM) in the PURE system in the presence of DnaK chaperone mix for 3 hours at 37°C. The solution was then supplemented with 2.5 mM ATP, 2.0 mM GTP, 100 nM eGFP-MinD and 3 μM FtsZ-A647 before transfer on top of an SLB. **b**, Mosaic of 7x7 tile scan microscope images showing large-scale organization of FtsA-FtsZ and MinDE dynamic patterns. FtsA-FtsZ rings mostly populate the center of the chamber (3), while MinDE oscillating gradients dominate at the edges of the chamber (1). In between these two areas (2), correlated patterns of the two subsystems can be seen. Signals from eGFP-MinD and FtsZ-A647 are in green and magenta, respectively. Composite images of overlaid channels are shown. Scale bar is 50 μm. **c**, Fluorescence mi-

croscopy images of FtsA-FtsZ and MinDE dynamic patterns taken from the intermediate SLB area (2) showing sharp propagating waves of FtsA-FtsZ and MinDE on the SLB. A zoom-in image of the framed area in the FtsZ channel is also displayed, showing the organization of FtsA-FtsZ into curved filaments and ring-like structures. Scale bar is 10 μm . **d**, The time evolution of the spiral wave in (c) was analyzed, and kymographs were constructed. On the right, examples of intensity profiles of MinD and FtsZ are shown. Color coding is the same as for microscopy images. **e**, As in (c) but low-amplitude propagating waves of FtsZ anticorrelating with MinDE patterns are shown. Scale bar is 10 μm . **f**, The time evolution of the wave was analyzed, and kymographs were constructed. On the right, examples of intensity profiles of MinD and FtsZ are shown. Color coding is the same as for microscopy images. **g,h**, Graphs reporting the calculated wavelength (g) and velocity (h) for MinDEC and MinDE waves, both in the presence of FtsA-FtsZ. Data are from three biological replicates and two to three fields of view have been analyzed per sample. Bar height represents the mean value, and the standard deviation is appended. Symbols are values for individual fields of view aggregated from three biological replicates. Values obtained for different conditions were statistically compared by performing a two-tailed Welch's *t*-test. Asterisk indicates *P* value < 0.05, while 'ns' denotes a non-significant difference with *P* value > 0.05.

Several dynamic behaviors were found in the extended area in which FtsA-FtsZ ring-like structures and MinDE coexisted. In most fields of view MinDE patterns could effectively rearrange FtsA-FtsZ filaments (Fig. 3c,d and Supplementary Fig. 3a, Movie S3 and S4). In a few cases, anticorrelated propagating waves of FtsZ and MinDE with a low amplitude were also observed (Fig. 3e,f, Movie S4). These two types of rearrangements might be the manifestation of different local concentrations of MinDE or FtsA-FtsZ on the bilayer. Also, areas with a higher concentration of FtsA and FtsZ may support formation of more stable cytoskeletal structures (longer residence time on the membrane) that are less susceptible to be redistributed by MinDE. The fact that we did not observe such dim propagating waves of FtsZ in the presence of MinC (Fig. 2b,c) can be explained by MinC's depolymerizing effect that prevents stable FtsZ bundles from forming, reduces the local concentration of FtsA-FtsZ and facilitates propagation of the MinDE diffusion barrier.

Quantifying the Min wave properties in the areas where FtsA-FtsZ ring-like structures were effectively rearranged, we calculated a wavelength for the MinD signal of $76 \pm 30 \mu\text{m}$ and wave velocity of $0.5 \pm 0.2 \mu\text{m s}^{-1}$ (mean \pm SD, from three biological replicates), while standing waves had a characteristic oscillation time of $109 \pm 36 \text{ s}$. In regions with no visible FtsZ signal, a Min wavelength of $71 \pm 22 \mu\text{m}$ was measured, with no significant differences between the center and the edge of the chamber (Supplementary Fig. 3b). In our previous work²⁴, MinDE surface waves in PURE system exhibited a wavelength of $43 \pm 7 \mu\text{m}$ and a velocity of $0.5 \pm 0.1 \mu\text{m s}^{-1}$. The data reported here show an increased wavelength of the MinDE oscillations, suggesting that FtsA-FtsZ cytoskeletal structures influence the wave properties (Supplementary Fig. 3b). Another possibility could be the difference in MinDE concentrations in the two studies ($4.2 \pm 0.9 \mu\text{M}$ and $3.2 \pm 0.4 \mu\text{M}$ in the present study vs $19 \pm 7 \mu\text{M}$ and $5 \pm 4 \mu\text{M}$ in the previous study, for MinD and MinE respectively). Moreover, we found that the wavelength increased in the presence of MinC, while the velocity remained mostly unaffected (Fig. 3g,h).

We then asked whether FtsA alone, i.e. not engaged into FtsA-FtsZ co-filaments, was also subjected to spatial reorganization by the MinDE propagating diffusion barrier. Low-amplitude anticorrelated patterning of FtsA has already been reported with purified proteins in simple buffer conditions²⁶. Here, a PURE solution containing pre-expressed FtsA, MinD and MinE was supplemented with purified FtsA conjugated to the AlexaFluor488 fluorophore (0.4 μM) for imaging (Supplementary Fig. 3c). MinDE waves were able to generate sharp FtsA dynamic patterns even in the absence of FtsZ. This finding corroborates previous observations with peripheral membrane proteins, but the modulation is noticeably more pronounced in our assay than previously reported²⁶.

We performed a series of control experiments that confirm that MinDE constitutes the minimal set of proteins to re-organize FtsA-FtsZ cytoskeletal structures on SLBs (Supplementary Fig. 3d,e). In addition, we demonstrated that in situ protein biogenesis through expression of the three-gene construct on top of the SLB supports the formation of MinDE(C) traveling waves that pattern FtsA-FtsZ co-filaments (Supplementary Fig. 4). However, the two subsystems coexist over the entire membrane surface, which contrasts with the spatial segregation of Min waves and FtsA-FtsZ filaments when pre-expressed proteins were added to the imaging chamber (Fig. 2b and Fig. 3b).

MinC is dispensable for coupling the Min waves and FtsA-FtsZ in closed compartments

We finally investigated if the findings from flat bilayer assays were also valid in a closed environment that better mimics the cellular context in terms of membrane surface-to-volume ratio and finite protein numbers. To do so, the FtsA-FtsZ and Min systems were co-reconstituted within lipid microdroplets. We first expressed the tri-cistronic DNA template in a test tube and the pre-ran PURE_{flex}2.0 solution was encapsulated inside water-in-oil droplets (Fig. 4a). The vast majority of the droplets displayed both FtsZ and Min protein signals on the inner surface (Supplementary Figs. 5a and 6a, Movie S5). Only a few droplets exhibited either Min dynamic patterns or FtsA-FtsZ networks. Time lapse imaging showed that in both samples with (Fig. 4b, Supplementary Fig. 5 and Movie S6) and without MinC (Fig. 4c, Supplementary Fig. 6 and Movie S6), dynamic concentration gradients of Min and FtsZ formed at the lipid monolayer, and that the two patterns were anticorrelated, as observed on SLBs. In most of the droplets, FtsZ and MinDE(C) assembled on opposite sides of the membrane forming two or multiple domains (Fig. 4b,c, Supplementary Figs. 5a,c and 6a,c). These patches were not static, they migrated along the droplets surface (Fig. 4b,c Movie S6). Other droplets exhibited circling patterns in which MinDE(C) and FtsZ chased one another along the droplet interface, with no visible intraluminal diffusion within the imaging plane (Fig. 4b and Movie S6). In droplets larger than 20 μm in diameter, it was possible to visualize cytoskeletal FtsZ structures forming a cortex and being re-localized by Min waves (Fig. 4d

and Supplementary Figs. 5d and 6d and Movie S7). More complex dynamic patterns were also observed in large droplets, including multiple interfacial FtsZ polarization sites rearranged by the Min dynamics (Fig. 4e and Supplementary Figs. 5 and 6), resembling the standing Min waves reported on SLBs. For the different phenotypes the antiphase localization of the two subsystems persisted in time. Parameter values for the pattern dynamics were broad, with wavelength and wave velocity respectively ranging between 42-174 μm and 0.16-0.58 $\mu\text{m s}^{-1}$ (8 droplets) with MinC, and between 24-167 μm and 0.23-0.60 $\mu\text{m s}^{-1}$ (8 droplets) without MinC. These values were consistent with those found on SLB. No significant differences due to the presence or absence of MinC could be measured.

These data confirm the functional integration of FtsA-FtsZ and Min proteins in closed compartment, further demonstrating that MinC is not essential to create dynamic FtsZ patterns in vitro when FtsA acts as the membrane anchor.

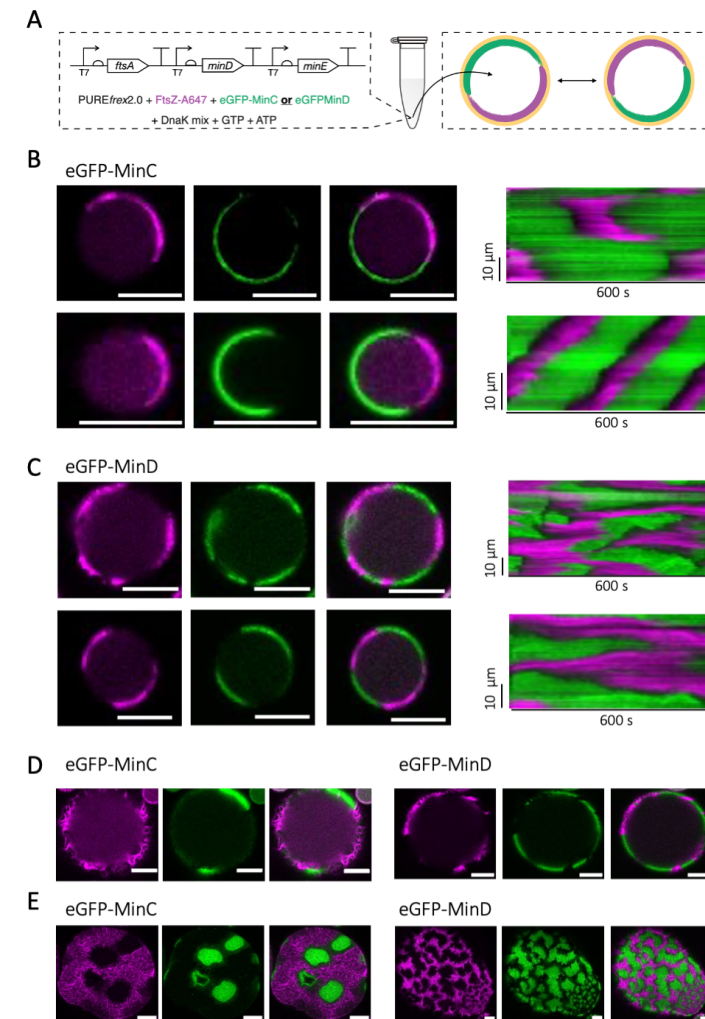


Figure 4: Functional reconstitution of MinDE(C) and FtsA-FtsZ networks in microdroplets. **a**, Schematic illustration of the droplet assays. The DNA template containing the genes *ftsA*, *minD*, and *minE* (5 nM) was expressed in a test tube in the presence of DnaK mix. The pre-ran PURE_{frex2.0} solution was encapsulated inside water-in-oil droplets, along with ATP (2.5 mM), GTP (2 mM), FtsZ-A647 (3 μM) and either purified eGFP-MinC (0.5 μM) or eGFP-MinD (100 nM). **b**, Fluorescence images (split channels and composite) of two droplets exhibiting antiphase dynamic patterns of MinDEC and FtsA-FtsZ. The corresponding kymographs are displayed. The droplet at the bottom exhibited a circling pattern yielding a characteristic kymograph. **c**, Same as in **(b)** except that eGFP-MinC was substituted with eGFP-MinD. **d**, Same as in **(b)** and **(c)** (exact condition is as specified) except that bigger droplets (diameter >20 μm) were imaged. Here, more defined cytoskeletal FtsZ structures were visible. **e**, Same as in **(b-d)** (exact condition is as specified) except that the images have been acquired closer to the dome of large droplets. Here, multiple interfacial FtsZ polarization sites rearranged by the Min dynamics were visible. Color coding: eGFP-MinC and eGFP-MinD (green), FtsZ-A647 (magenta). Scale bars are 10 μm .

Discussion

In this work we reconstituted MinDE(C) dynamics with FtsA-FtsZ cytoskeletal networks in a cell-free environment that accounts for the complex molecular content of the bacterial cytoplasm. To accomplish this, we used the PURE system to express a three-gene DNA template encoding for MinD, MinE and FtsA (Fig. 1). FtsA is an essential, widely conserved membrane anchor protein, playing a major role in Z-ring formation and downstream protein recruitment⁷. It is known that the nature of the FtsZ membrane anchor influences the dynamics of FtsZ assembly in SLB assays²⁰. Therefore, the questions of whether and how the Min system drives the spatial rearrangement of FtsA-bound FtsZ are relevant; yet, they have hitherto not been explored.

We found that membrane-bound FtsA-FtsZ filaments organize into dynamic, anti-phased, patterns driven by the MinDEC system (Fig. 2b,c and Supplementary Fig. 4a). The traditional explanation for the emergence of FtsZ oscillation gradients is that the membrane-tethered polymers reorganize as a result of the interaction with MinC(D). However, similar dynamic behaviors were observed in the absence of MinC (Fig. 3b,c and Supplementary Fig. 4b,c), demonstrating that MinDE act as a minimal spatiotemporal regulator of FtsA-anchored FtsZ filaments on SLBs. This conclusion is also valid when the two subsystems are enclosed in water-in-oil droplets (Fig. 4).

FtsZ redistribution on lipid membranes has not been documented in the absence of MinC when ZipA (soluble version) was used in place of FtsA³⁸. Dynamic patterns of ZipA-FtsZ only emerged with MinC traveling on MinDE waves. In this previous study, ZipA was not mobile³⁸, which might have compromised the rearrangement of ZipA-FtsZ cofilaments by the MinDE oscillatory gradients. When the Min system was combined with the fusion protein FtsZ-YFP-MTS on SLBs, two distinct scenarios were reported²⁶: dynamic FtsZ-YFP-MTS rings were reorganized by MinDE, while static FtsZ-YFP-MTS networks remained unaffected. In both cases, supplementing MinC stimulated formation of clear FtsZ-YFP-MTS patterns²⁶. Moreover, FtsZ-YFP-MTS and Min systems have been coupled inside droplets³⁹ or PDMS (Polydimethylsiloxane) compartments⁴⁰, showing that Min waves comprising MinC create dynamic FtsZ surface patterns^{39,40}. These earlier results involving ZipA³⁸ or FtsZ-YFP-MTS^{26,39,40} differ from the robust dynamic patterning of FtsA-FtsZ reported here in the absence of MinC, indicating that different membrane targeting proteins may respond differently to Min concentration gradients. Based on the present observations, both on open and closed membranes, we propose that MinDE oscillations alone constitute the minimal localization mechanism of the FtsA-FtsZ proto-ring. This assumption is reinforced by the recent discovery that MinDE act as a general propagating diffusion barrier exerting steric pressure that can redistribute membrane proteins in vitro^{26,27}.

In vivo, functional MinC is undoubtedly needed to prevent septum misplacement and asymmetric division, a phenotype known as minicell¹⁰. The dispensable function of MinC

in regulating FtsZ-FtsA dynamics, as reported here, suggests that MinDE oscillations play a more central role in patterning critical division components in *E. coli* than solely distributing MinC at the cell pole, where Z-ring formation is prohibited. After all, in vivo studies have shown that ZipA, as well as other early division proteins, counter-oscillate with MinC⁴¹. ZipA traveling in phase with FtsZ was interpreted as resulting from the interaction between these two proteins during filament depolymerization by MinC. However, ZipA might also be redistributed by the MinDE oscillations. FtsA and ZipA follow the FtsZ pattern in time, and the three proteins are detectable at midcell with no significant delay³¹, suggesting a tightly coordinated regulatory mechanism. The earliest phase of cytokinesis in *E. coli* includes the cytosolic assembly of short FtsZ protofilaments that bind transiently everywhere on the inner membrane and, over time, migrate and cluster at the cell's center⁴². Our results suggest that MinDE promotes the localization of short FtsA-FtsZ filaments at midcell by acting as a propagating steric hindrance on the membrane, competing with the fast detaching-binding short filaments (Fig. 5a). The high local concentration of short filaments in the middle of the cell then encourages lateral interaction, bundling and extension of filaments, and eventually proto-ring formation. It should be noted that in slow growing *E. coli* cells, condensation of membrane-bound FtsZ filaments into a ring occurs in the absence of the Min system⁴³, indicating that other mechanisms guide the ring assembly and its localization. As shown in Fig. 3e, in some instances FtsA-FtsZ structures cannot effectively be displaced by MinDE only. MinC inhibits long FtsA-FtsZ filaments by depolymerizing membrane-bound FtsZ structures, by competing with the membrane proteins for binding to FtsZ⁴⁴, and by capping growing polymers⁴⁵. By lowering the residence time of FtsA-FtsZ filaments on the membrane, MinC may assist MinDE in effectively reorganizing the FtsA-FtsZ structures (Fig. 5b). In addition, MinC could be critical in managing the pool of FtsZ that is not at the division site (up to 70% of the available FtsZ⁴⁶), i.e. by buffering the concentration of cytosolic FtsZ. The observation that FtsZ travels in phase with MinC in the absence of a membrane anchor lends support to this hypothesis (Fig. 2e). In *E. coli*, MinC overexpression impairs cytokinesis, resulting in cell filamentation⁴⁷. The inhibitory effect is caused by MinC sequestering a large pool of free FtsZ⁴⁸. This depletion process is likely enhanced by the interaction of MinC to MinD, which increases the local concentration of MinC at the membrane.

Finally, our finding will have implications toward the reconstitution of a more elementary regulatory mechanism for positioning the division site in a synthetic cell. DNA-encoded protein synthesis and compartmentalization are important design elements to building a minimal cell. Therefore, demonstrating that the FtsZ and Min subsystems can be partly expressed from a multigene DNA template, functionally integrated, and encapsulated in droplets is a step forward to establishing a synthetic division mechanism. Implementation of a coupled FtsA-FtsZ-MinDE(C) system inside deformable lipid vesicles^{24,30} might be a route to symmetrical division of artificial cells. Spatiotemporal redistribution of other bacterial

division proteins, such as ZapA, ZapB, MatP, and of lipid synthesis enzymes⁴⁹ could also be explored in the future.

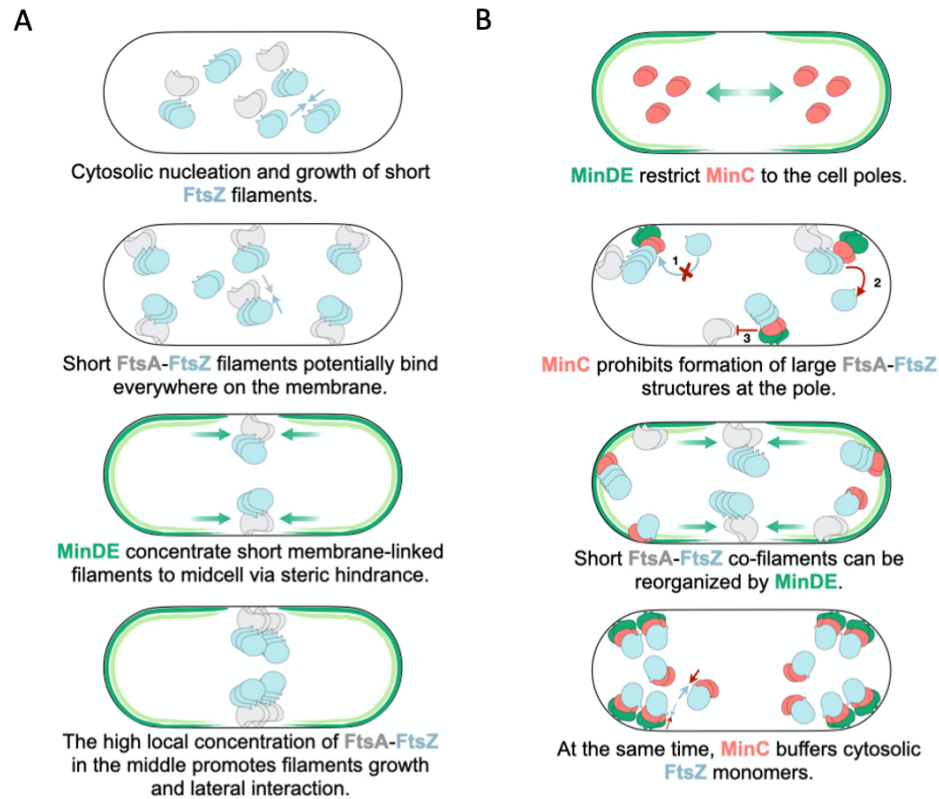


Figure 5: Model for the patterning of bacterial cytokinesis components by MinDE oscillations in *E. coli*. **a**, Short protofilaments of FtsA-FtsZ nucleate and grow in the cytosol. The short FtsZ-FtsA (and possibly ZipA-FtsZ) filaments bind at random locations along the membrane. MinDE propagating diffusion barrier concentrates the short filaments at midcell. The high local concentration of short filaments in the middle promotes lateral interaction, bundling and extension of filaments, and subsequent proto-ring formation. **b**, MinD-MinE dynamics generate a concentration maximum of MinC at the poles, where the formation of extended FtsA-FtsZ structures that could not be displaced by MinDE only is prohibited by the following processes: MinCD inhibits long FtsA-FtsZ structures by capping growing FtsZ polymers (1), by depolymerizing FtsZ structures (2), and by competing with other membrane proteins for binding to FtsZ (3). The short co-filaments have a reduced lifetime at the membrane and can more easily be outcompeted by MinDE at the division site. Furthermore, MinC is responsible for sequestering FtsZ monomers through direct interaction, keeping the cytosolic concentration of FtsZ lower than the threshold to form long filaments and bundles. The interaction between membrane-bound MinD and MinC boosts the local concentration of MinC, which might operate as a mechanism to accentuate the depletion of FtsZ subunits. Together, the processes described in A and B restrict proto-ring formation to midcell.

Methods

Purified proteins

The proteins eGFP-MinD and eGFP-MinC were purified using previously described methods²³. Protein concentrations were quantified via Bradford assay and eGFP absorbance measurements. FtsZ was dialyzed against 20 mM Hepes/HCl, pH 8.0, with 50 mM KCl, 5 mM MgCl₂, and 1 mM ethylenediaminetetraacetic acid (EDTA). The protein was initially polymerized at 30 °C using 20 mM CaCl₂ and 2 mM GTP, then the mixture was incubated at 30 °C for 15 min with a 20-fold excess of Alexa Fluor 647 (A647). This two-step process helps reduce labeling-induced alterations in FtsZ assembly. The precipitate was resuspended on ice in 50 mM Tris/HCl, pH 7.4, with 100 mM KCl, and the unbound fluorescent probe was extracted by gel filtration, as per standard protocol for column purification (Gel Wizard SV). Purified FtsZ-Alexa647 was kept in storage buffer (50 mM Tris, 500 mM KCl, 5 mM MgCl₂, and 5% glycerol) at pH 7, as previously described⁵⁰. FtsA was expressed and purified according to published protocols⁵¹. Cells were suspended in 50 mM Tris-HCl, 1 mM TCEP, 1 mM PMSE, pH 7.5, treated with 10 g/mL DNase, sonicated and centrifuged. The pellet was washed two times with 20 mM Tris-HCl, 10 mM EDTA, pH 7.5, and 1% (v/v) Triton X-100. Inclusion bodies were dissolved in 20 mM Tris-HCl, 5 M guanidine-HCl, 0.5 M NaCl, pH 7.5, loaded in a HisTrap FF column (GE Healthcare) and rinsed in 20 mM imidazole. An imidazole elution gradient (20–500 mM) was applied and the eluted fractions were kept at –80 °C. FtsA was refolded by dialysis against 50 mM Tris-HCl, 0.5 M NaCl, 5 mM MgCl₂, 0.2 mM TCEP, and 0.1 mM ADP, pH 8 at 4 °C. Buffer was replaced with 50 mM Tris-HCl, 0.5 M KCl, 5 mM MgCl₂, 0.2 mM TCEP and 0.1 mM ADP, pH 7.5. Concentration of FtsA was measured by Bradford assay. FtsA was fluorescently labeled with AlexaFluor-488 (1:10 molar ratio) for 30 min in 50 mM Hepes/HCl (pH 8.0), 100 mM KCl, and 5 mM MgCl₂.

Preparation of DNA constructs

minD, *minE* and *FtsA* genes were amplified by standard polymerase chain reaction (PCR) amplified using Phusion High-Fidelity DNA polymerase (New England Biolabs, USA) as previously reported^{24,30}. The plasmid DE was assembled via Gibson assembly (Gibson Assembly Master Mix of New England BioLabs, Inc.). The assembly was performed at equimolar concentrations of linearized plasmid MinDpUC57 and MinE DNA fragments for 1 hour at 50 °C. The primers in Table S1 were used: ChD173+504 and ChD1139+1140. Transformation of the Gibson assembly products into *E. coli* TOP10 competent cells was done by heat shock, after which cells were resuspended in 200 µL of fresh prechilled liquid lysogeny broth (LB) medium and incubated for 1 hour at 37 °C and 250 r.p.m. Then, the cultures were plated in solid LB medium with ampicillin and grew overnight at 37 °C.

Colonies were picked up and cultured in 1 mL of liquid LB medium with 100 $\mu\text{g mL}^{-1}$ of ampicillin for 16 hours at 37 °C and 250 r.p.m. Plasmid purification was performed using the PureYield™ Plasmid Miniprep System (Promega). Concentration and purity of DNA were checked on NanoDrop. Linear DNA construct was prepared by PCR using the forward and reverse primers ChD365 and ChD174, respectively, annealing to the T7 promoter and T7 terminator sequences (Supplementary Table 1).

The plasmid ADE was assembled via Gibson assembly, using equimolar concentrations of linearized plasmid FtsApUC57 and the MinDE DNA fragment, for 1 hour at 50 °C. The primers in Supplementary Table 1 were used: ChD420+1145 and ChD365+174. Transformation of the Gibson assembly products into *E. coli* TOP10 competent cells was done by heat shock, after which cells were resuspended in 200 μL of fresh prechilled liquid lysogeny broth (LB) medium and incubated for 1 hour at 37 °C and 250 r.p.m. Then, the cultures were plated in solid LB medium with ampicillin and grew overnight at 37 °C. Colonies were picked up and cultured in 1 mL of liquid LB medium with 100 $\mu\text{g mL}^{-1}$ of ampicillin for 16 hours at 37 °C and 250 r.p.m. Plasmid purification was performed using the PureYield™ Plasmid Miniprep System (Promega). Concentration and purity of DNA were checked on NanoDrop. Linear DNA construct was prepared by PCR using the forward and reverse primers ChD1187 and ChD174, respectively, annealing to the T7 promoter and T7 terminator sequences. For both linear constructs (DE and ADE) amplification products were checked on a 1% agarose gel and were further purified using Wizard SV gel (standard column protocol). Concentration and purity were measured by NanoDrop. All sequences were confirmed by sequencing. MinE-, and FtsA-coding DNA fragments (starting with a T7 promoter and ending with a T7 terminator) are sequence-optimized for codon usage, CG content, and 5' mRNA secondary structures. Sequences of the linearized constructs can be found in the Supplementary Methods.

Cell-free gene expression in bulk

Gene expression was performed using PUREfrex2.0 (GeneFrontier Corporation, Japan) and 5 nM of a linear DNA template following the supplier's recommendations. The solution was supplemented with 1 μL of DnaK Mix (GeneFrontier Corporation), which consists of purified DnaK, DnaJ, and GrpE chaperone proteins from *E. coli*. Twenty microliter reactions were run in PCR tubes for 3 hours at 37 °C. Purified proteins (FtsZ-A647, eGFP-MinC/D), ATP and/or GTP were supplied to the mixture only when specified.

QconCAT purification

A quantitative concatemer (QconCAT) protein was designed to contain two specific peptides for FtsA and MinD, one for MinE and two for ribosomal core proteins. These include the most C-terminal proteolytic peptide that we could accurately identify for each protein of interest^{24,30}. QconCAT was expressed in BL21(DE3) cells in M9 medium with $^{15}\text{NH}_4\text{Cl}$ and

ampicillin. A pre-culture was diluted 1:100 to a 50 mL expression culture. Protein expression was induced at $\text{OD}_{600} = 0.5$ with 1 mM isopropyl β -D-1-thiogalactopyranoside and cells were grown for 3 hours at 37 °C. Cells were harvested by centrifugation and the pellet was dissolved in 1 mL B-PER. 10 μL of 10 mg mL^{-1} lysozyme and 10 μL of DNaseI (ThermoScientific, 1 U μL^{-1}) were added and the sample was incubated for 10 min at room temperature. The lysate was centrifuged for 20 min at 16,000 $\times g$ and the pellet resuspended in 2 mL of a 1:10 dilution of B-PER in MilliQ water. The sample was twice again centrifuged, and the pellet was resuspended in 2 mL 1:10 diluted B-PER and centrifuged again. The pellet was resuspended in 600 μL of 10 mM Tris-HCl pH 8.0, 6 M guanidinium chloride and incubated at room temperature for 30 min. After spinning down the insolubilized protein fraction the supernatant was loaded onto an equilibrated mini NiNTA spin column (Qiagen) and the flow-through was reloaded twice to maximize protein binding. The column was washed twice with 600 μL of 10 mM Tris-HCl pH 6.3, 8 M urea and the QconCAT was eluted with 3 \times 200 μL of 10 mM Tris-HCl pH 4.5, 8 M urea, 400 mM imidazole. The eluate was dialyzed overnight and for additional 4 hours against 10 mM Tris-HCl pH 8.0, 100 mM KCl with a 10-kDa cutoff slide-a-lyzer cassette (ThermoScientific).

Trypsin digest

Per LC-MS injection, 1.5 μL of PURE system reaction was mixed with 3 μL of 100 mM Tris-HCl pH 8.0, 0.3 μL of 20 mM CaCl_2 , and 0.8 μL MilliQ water. Samples were incubated at 90 °C for 10 min to stop the reaction. Then, 0.6 μL of QconCAT (0.3 mg mL^{-1}) was added, the sample was incubated again at 90 °C for 10 min and after cooling to room temperature, 1 μL 250 mM fresh iodoacetamide was added and the sample incubated for 30 min at room temperature in the dark. Then 0.3 μL of 1 mg mL^{-1} trypsin (trypsin-ultra, MS-grade, New England Biolabs) was added and samples were incubated at 37 °C overnight. After addition of 0.7 μL 10% trifluoroacetic acid, samples were centrifuged in a table-top centrifuge (5415 R, Eppendorf) for 10 min at maximum speed. The supernatant was transferred to a glass vial with small-volume insert for LC-MS/MS analysis.

LC-MS/MS analysis

LC-MS/MS analysis was performed on a 6460 Triple Quad LCMS system (Agilent Technologies, USA) using Skyline software⁵². Per run 7 μL of sample was injected to an ACQUITY UPLC® Peptide CSH™ C18 Column (Waters Corporation, USA). The peptides were separated in a gradient of buffer A (25 mM formic acid in MilliQ water) and buffer B (50 mM formic acid in acetonitrile) at a flow rate of 500 μL per minute and at a column temperature of 40 °C. The column was equilibrated with 98% buffer A. After injection, the gradient was changed linearly over 20 min to 70% buffer A, over the next 4 min to 60% buffer A, and over the next 30 s to 20% buffer A. This ratio was held for another 30 s and the column was finally flushed with

98% buffer A to equilibrate for the next run. Selected peptides were measured by multiple reaction monitoring. For both FtsA and MinD, two peptides were analyzed, one for MinE. Two peptides from ribosomal proteins were also measured as a control. The peak area ratio of unlabeled peptides (^{14}N , expressed or PURE component) and ^{15}N -labeled QconCAT peptides was calculated for the ribosomal core proteins (average value over the two peptides) and for the proteins of interest. The concentration of the selected peptides for the proteins of interest was then deduced knowing the concentration of ribosomal core proteins in PURE system. Data processing was performed using a script written in Mathematica (Wolfram Research, version 11.3).

Phenomenological fitting of FtsA, MinD and MinE production kinetics

FtsA, MinD, and MinE most C-terminal peptide concentrations were fit using a phenomenological model to estimate apparent kinetic parameters: final yield, production rate, and translation lifetime. The following sigmoid equation was used⁵³:

$$y = k' + k \frac{t^n}{t^n + K^n} \quad (\text{Eq. 1})$$

where t is the time in minutes, y the peptide concentration at a given time point, and k' , k , K , and n are fit parameters. Using this expression, the final yield corresponds to k and the plateau time, or expression lifespan, is expressed as:

$$T_{\text{plateau}} = \frac{2K}{n} + K \quad (\text{Eq. 2})$$

The apparent translation rate, which is defined as the steepness at time $t = K$, is:

$$v_{\text{translation}} = \frac{kn}{4K} \quad (\text{Eq. 3})$$

The kinetics from three independent experiments were fit, and the extracted parameter values are reported as the average and standard deviation.

Fabrication and cleaning of the imaging chamber

Home-made imaging glass chambers were used in all the assays²⁴. Three microscopy glass slides were bonded together using NOA 61 glue (Norland Products). Holes were drilled across the three-slide layer, with diameters of 2.5 mm. A 150- μm thick coverslip (Menzel-Gläser) was attached on one side of the slide with NOA 61 to form the bottom of the chamber. Chambers were cleaned by 10-min washing steps in a bath sonicator (Sonorex Digitec, Bandelin) using the following solutions: chloroform and methanol (volume 1:1), 2% Hellmanex, 1 M KOH, 100% ethanol, and MilliQ water. In addition, after a couple of experiments the glass chambers were subjected to acid Piranha treatment.

Lipids

1,2-dioleoyl-sn-glycero-3-phosphocholine (DOPC), 1,2-dioleoyl-sn-glycero-3-phosphoglycerol (DOPG) and 1',3'-bis[1,2-dioleoyl-sn-glycero-3-phospho]-glycerol (18:1 CL) were purchased from Avanti Polar Lipids as chloroform solutions.

Preparation of small unilamellar vesicles

Small unilamellar vesicles (SUVs) were used as precursors for SLB production. DOPC (4 μmol) and DOPG (1 μmol) lipids dissolved in chloroform were mixed in a glass vial. A lipid film was formed on the vial wall by solvent evaporation under a moderate flow of argon and desiccated for 30 min at room temperature. The lipid film was resuspended with 400 μL of SLB buffer (50 mM Tris, 300 mM KCl, 5 mM MgCl_2 , pH 7.5) and the solution was vortexed for a few minutes. The final lipid concentration was 1.25 mg mL^{-1} . A two-step extrusion (each of eleven passages) was performed utilizing an Avanti mini extruder (Avanti Polar Lipids) with 250 μL Hamilton syringes, filters (drain disc 10 mm diameter, Whatman), and a polycarbonate membrane with pore size 0.2 μm (step 1) or 0.03 μm (step 2) (Nuclepore track-etched membrane, Whatman).

Formation of SLBs

The imaging chamber was treated with oxygen plasma (Harrick Plasma basic plasma cleaner) for 30 min to activate the glass surface. Immediately after, an SUV solution was added to the sample reservoir at a final lipid concentration of 0.94 mg mL^{-1} together with 3 mM CaCl_2 . The chamber was sealed with a 20 \times 20 mm coverslip by using a double-sided adhesive silicone sheet (Life Technologies). After sample incubation at 37°C for 30 min, the chamber was carefully opened and the SLB was rinsed six times with SLB buffer.

Activity assays on supported membranes

The constructs *ftsA-minD-minE* and *minD-minE* were expressed with PUREfrex2.0 in test tubes as described above and the solution was supplemented with the following compounds: 2 mM GTP, 2.5 mM ATP, 3 μM purified FtsZ-A647, and either 0.5 μM eGFP-MinC or 100 nM purified eGFP-MinD as specified in the text (all final concentrations) in a total volume of 20 μL . The sample was added on top of an SLB, and the imaging chamber was sealed with a 20 \times 20 mm coverslip by using a double-sided adhesive silicone sheet. For assays involving in situ expression, a 20 μL PUREfrex2.0 mixture containing one of the two DNA constructs was supplemented with 2 mM GTP, 2.5 mM ATP, 3 μM purified FtsZ-A647, and either 0.5 μM eGFP-MinC or 100 nM purified eGFP-MinD as specified in the text (all final concentrations), and the solution was directly incubated on top of an SLB. 0.4 μM purified FtsA-A488 was used only when specified in the main text. The chamber was closed as indicated above, and the sample was immediately imaged with a time lapse fluorescence microscope for up to

5.5 hours at 37°C. Numerous fields of view were acquired at various time points during the expression period.

Droplet preparation

15 mol% 18:1 CL and 85 mol% DOPC in chloroform were mixed in a glass vial. A lipid film was deposited on the wall of the vial upon solvent evaporation through a gentle flow of nitrogen and was further desiccated for 30 min at room temperature. The lipid film was resuspended with mineral oil (Sigma Aldrich, St. Louis, MO) to a final concentration of 2.5 mg mL⁻¹ and the solution was vortexed for a few minutes. The inner solution consisted of a pre-ran PURE system solution supplemented with DnaK, 2 mM GTP, 2.5 mM ATP, 3 µM purified FtsZ-A647, and either 0.5 µM eGFP-MinC or 100 nM purified eGFP-MinD as indicated in the text. Five microliter of inner solution was added to 30 µL of the oil/lipid mixture. The droplet-oil mixture was pipetted on a coverslip and imaged with a fluorescence confocal microscope.

Confocal microscopy

Droplets and SLBs were imaged using a Nikon A1R Laser scanning confocal microscope with an SR Apo TIRF 100× oil-immersion objective. FtsZ-A647 and eGFP-MinC/D were excited using the 640-nm and 488-nm laser lines, respectively, and suitable emission filters were used. For image acquisition, the software NIS (Nikon) was utilized, with identical settings for all samples. Throughout imaging, samples were kept on a temperature-controlled stage (Tokai Hit INU) that was held at 37 °C.

Image analysis

Fiji⁵⁴ or MatLab version R2020b were used for image analysis. Fiji's profile plots tool was used to generate fluorescence intensity profiles. The tool displays a two-dimensional graph of pixel intensities along a line drawn in the direction of the moving wave. The wavelength and velocity of the dynamic patterns on SLBs were determined by producing a kymograph parallel to the direction of the traveling wave. Lines were identified using a linear Hough transform after binarization of the kymograph using Sobel edge detection. The slope of the lines equates to the wave velocity, while the distance between the lines corresponds to the wavelength. The frequency of oscillations of a standing wave was determined by computing the autocorrelation function over time for each pixel and identifying the first peak of the function.

References

1. E. Bi, J. Lutkenhaus, FtsZ ring structure associated with division in *Escherichia coli*. *Nature* **354**, 161–164 (1991).
2. C. A. Hale, P. A. de Boer, Recruitment of ZipA to the septal ring of *Escherichia coli* is dependent on FtsZ and independent of FtsA. *J. Bacteriol.* **181**, 167–76 (1999).
3. X. Ma, D. W. Ehrhardt, W. Margolin, Colocalization of cell division proteins FtsZ and FtsA to cytoskeletal structures in living *Escherichia coli* cells by using green fluorescent protein. *Proc. Natl. Acad. Sci.* **93**, 12998–13003 (1996).
4. P. de Boer, R. Crossley, L. Rothfield, The essential bacterial cell-division protein FtsZ is a GTPase. *Nature* **359**, 254–256 (1992).
5. A. Mukherjee, J. Lutkenhaus, Guanine nucleotide-dependent assembly of FtsZ into filaments. *J. Bacteriol.* **176**, 2754–8 (1994).
6. S. Pichoff, J. Lutkenhaus, Unique and overlapping roles for ZipA and FtsA in septal ring assembly in *Escherichia coli*. *EMBO J.* **21**, 685–93 (2002).
7. S. Pichoff, J. Lutkenhaus, Tethering the Z ring to the membrane through a conserved membrane targeting sequence in FtsA. *Mol. Microbiol.* **55**, 1722–1734 (2005).
8. C. A. Hale, P. A. de Boer, Direct binding of FtsZ to ZipA, an essential component of the septal ring structure that mediates cell division in *E. coli*. *Cell* **88**, 175–85 (1997).
9. V. W. Rowlett, W. Margolin, The Min system and other nucleoid-independent regulators of Z ring positioning. *Front. Microbiol.* **6**, 478 (2015).
10. P. A. J. De Boer, R. E. Crossley, L. I. Rothfield, A division inhibitor and a topological specificity factor coded for by the minicell locus determine proper placement of the division septum in *E. Coli*. *Cell* **56**, 641–649 (1989).
11. Z. Hu, A. Mukherjee, S. Pichoff, J. Lutkenhaus, The MinC component of the division site selection system in *Escherichia coli* interacts with FtsZ to prevent polymerization. *Proc. Natl. Acad. Sci. U. S. A.* **96**, 14819–24 (1999).
12. Z. Hu, C. Saez, J. Lutkenhaus, Recruitment of MinC, an inhibitor of Z-ring formation, to the membrane in *Escherichia coli*: role of MinD and MinE. *J. Bacteriol.* **185**, 196–203 (2003).
13. D. M. Raskin, P. A. de Boer, MinDE-dependent pole-to-pole oscillation of division inhibitor MinC in *Escherichia coli*. *J. Bacteriol.* **181**, 6419–24 (1999).
14. C. A. Hale, H. Meinhardt, P. A. de Boer, Dynamic localization cycle of the cell division regulator MinE in *Escherichia coli*. *EMBO J.* **20**, 1563–72 (2001).
15. K. Kruse, A dynamic model for determining the middle of *Escherichia coli*. *Biophys. J.* **82**, 618–27 (2002).
16. D. M. Raskin, P. A. de Boer, Rapid pole-to-pole oscillation of a protein required for directing division to the middle of *Escherichia coli*. *Proc. Natl. Acad. Sci. U. S. A.* **96**, 4971–6 (1999).
17. D. A. Ramirez-Diaz, *et al.*, Treadmilling analysis reveals new insights into dynamic FtsZ ring architecture. *PLOS Biol.* **16**, e2004845 (2018).
18. M. Krupka, *et al.*, *Escherichia coli* FtsA forms lipid-bound minirings that antagonize lateral interactions between FtsZ protofilaments. *Nat. Commun.* **8**, 15957 (2017).
19. M. Krupka, M. Sobrinos-Sanguino, M. Jiménez, G. Rivas, W. Margolin, *Escherichia coli* ZipA organizes FtsZ polymers into dynamic ring-like protofilament structures. *MBio* **9**, e01008-18 (2018).
20. M. Loose, T. J. Mitchison, The bacterial cell division proteins FtsA and FtsZ self-organize into dynamic cytoskeletal patterns. *Nat. Cell Biol.* **16**, 38–46 (2014).
21. Z. Hu, J. Lutkenhaus, Topological regulation of cell division in *E. coli*. Spatiotemporal oscillation of MinD requires stimulation of its ATPase by MinE and phospholipid. *Mol. Cell* **7**, 1337–43 (2001).
22. M. Loose, E. Fischer-Friedrich, J. Ries, K. Kruse, P. Schwill, Spatial regulators for bacterial cell division self-organize into surface waves in vitro. *Science* **320**, 789–792 (2008).
23. M. Loose, E. Fischer-Friedrich, C. Herold, K. Kruse, P. Schwill, Min protein patterns emerge from rapid rebinding and membrane interaction of MinE. *Nat. Struct. Mol. Biol.* **18**, 577–583 (2011).
24. E. Godino, *et al.*, De novo synthesized Min proteins drive oscillatory liposome deformation and regulate FtsA-FtsZ cytoskeletal patterns. *Nat. Commun.* **10**, 4969 (2019).
25. H. L. Lee, *et al.*, Quantitative proteomics analysis reveals the Min system of *Escherichia coli* modulates reversible protein association with the inner membrane. *Mol. Cell. Proteomics* **15**, 1572–1583 (2016).
26. B. Ramm, *et al.*, The MinDE system is a generic spatial cue for membrane protein distribution in vitro. *Nat. Commun.* **9**, 3942

(2018).

27. Y. L. Shih, *et al.*, Active transport of membrane components by self-organization of the Min proteins. *Biophys. J.* **116**, 1469–1482 (2019).

28. Y. Shimizu, *et al.*, Cell-free translation reconstituted with purified components. *Nat. Biotechnol.* **19**, 751–755 (2001).

29. Y. Shimizu, T. Kanamori, T. Ueda, Protein synthesis by pure translation systems. *Methods* **36**, 299–304 (2005).

30. E. Godino, *et al.*, Cell-free biogenesis of bacterial division proto-rings that can constrict liposomes. *Commun. Biol.* **3** (2020).

31. S. Rueda, M. Vicente, J. Mingorance, Concentration and assembly of the division ring proteins FtsZ, FtsA, and ZipA during the *Escherichia coli* cell cycle. *J. Bacteriol.* **185**, 3344–51 (2003).

32. P. A. de Boer, R. E. Crossley, A. R. Hand, L. I. Rothfield, The MinD protein is a membrane ATPase required for the correct placement of the *Escherichia coli* division site. *EMBO J.* **10**, 4371–80 (1991).

33. Y. L. Shih, X. Fu, G. F. King, T. Le, L. Rothfield, Division site placement in *E. coli*: Mutations that prevent formation of the MinE ring lead to loss of the normal midcell arrest of growth of polar MinD membrane domains. *EMBO J.* **21**, 3347–3357 (2002).

34. A. Doerr, *et al.*, Modelling cell-free RNA and protein synthesis with minimal systems. *Phys. Biol.* **16**, 025001 (2019).

35. A. Doerr, D. Föschepoth, A. C. Forster, C. Danelon, In vitro synthesis of 32 translation-factor proteins from a single template reveals impaired ribosomal processivity. *Sci. Rep.* **11**, 1898 (2021).

36. J. Schweizer, *et al.*, Geometry sensing by self-organized protein patterns. *Proc. Natl. Acad. Sci. U. S. A.* **109**, 15283–15288 (2012).

37. L. Wettmann, M. Bonny, K. Kruse, Effects of geometry and topography on Min-protein dynamics. *PLoS One* **13**, e0203050 (2018).

38. A. Martos, *et al.*, FtsZ Polymers tethered to the membrane by ZipA are susceptible to spatial regulation by min waves. *Biophys. J.* **108**, 2371–2383 (2015).

39. K. Zieske, G. Chwastek, P. Schwill, Protein patterns and oscillations on lipid monolayers and in microdroplets. *Angew. Chemie Int. Ed.* **55**, 13455–13459 (2016).

40. K. Zieske, P. Schwill, Reconstitution of self-organizing protein gradients as spatial cues in cell-free systems. *Elife* **3** (2014).

41. P. Bisicchia, S. Arumugam, P. Schwill, D. Sherratt, MinC, MinD, and MinE drive counter-oscillation of early-cell-division proteins prior to *Escherichia coli* septum formation. *MBio* **4** (2013).

42. B. E. Walker, J. Männik, J. Männik, Transient membrane-linked FtsZ assemblies precede Z-ring formation in *Escherichia coli*. *Curr. Biol.* **30**, 499–508.e6 (2020).

43. M. W. Bailey, P. Bisicchia, B. T. Warren, D. J. Sherratt, J. Männik, Evidence for divisome localization mechanisms independent of the Min system and SlmA in *Escherichia coli*. *PLOS Genet.* **10**, e1004504 (2014).

44. B. Shen, J. Lutkenhaus, The conserved C-terminal tail of FtsZ is required for the septal localization and division inhibitory activity of MinC(C)/MinD. *Mol. Microbiol.* **72**, 410–424 (2009).

45. S. Arumugam, Z. Petrašek, P. Schwill, MinCDE exploits the dynamic nature of FtsZ filaments for its spatial regulation. *Proc. Natl. Acad. Sci. U. S. A.* **111**, E1192–200 (2014).

46. D. E. Anderson, F. J. Gueiros-Filho, H. P. Erickson, Assembly dynamics of FtsZ rings in *Bacillus subtilis* and *Escherichia coli* and effects of FtsZ-regulating proteins. *J. Bacteriol.* **186**, 5775–5781 (2004).

47. P. A. J. De Boer, R. E. Crossley, L. I. Rothfield, Roles of MinC and MinD in the site-specific septation block mediated by the MinCDE system of *Escherichia coli*. *J. Bacteriol.* **174**, 63–70 (1992).

48. K. T. Park, A. Dajkovic, M. Wissel, S. Du, J. Lutkenhaus, MinC and FtsZ mutant analysis provides insight into MinC/MinD-mediated Z ring disassembly. *J. Biol. Chem.* **293**, 5834–5846 (2018).

49. D. Blanken, D. Föschepoth, A. C. Serrão, C. Danelon, Genetically controlled membrane synthesis in liposomes. *Nat. Commun.* **11** (2020).

50. J. M. González, *et al.*, Essential cell division protein FtsZ assembles into one monomer-thick ribbons under conditions resembling the crowded intracellular environment. *J. Biol. Chem.* **278**, 37664–71 (2003).

51. A. Martos, *et al.*, Isolation, characterization and lipid-binding properties of the recalcitrant FtsA division protein from *Escherichia coli*. *PLoSone* **7**, e39829. (2012)

52. B. MacLean, *et al.*, Skyline: An open source document editor for creating and analyzing targeted proteomics experiments. *Bioinformatics* (2010).

53. J. Ang, E. Harris, B. J. Hussey, R. Kil, D. R. McMillen, Tuning response curves for synthetic biology. *ACS Synth. Biol.* **2**, 547–567 (2013).

54. C. T. Rueden, *et al.*, ImageJ2: ImageJ for the next generation of scientific image data. *BMC Bioinformatics* (2017).

Supplementary Information

DNA sequence of the *minD-minE* construct

TAATACGACTCACTATAGGGGAATTGTGAGCGGATAACAATTCCCCTCTAGAAATAATTTTGTTTAACTTTAAGAAG-GAGATATACATATGGCACGCATTATTGTTGTTACTTCGGGCAAAGGGGGTGTGGTAAGACAACCTCCAGCGCGGC-CATCGCCACTGGTTTGGCCCAGAAGGGAAAGAAAAGTGTCTGATAGATTTTGATATCGGCCTGCGTAATCTCGACCT-GATTATGGGTTGTGAACGCCGGTTCGTTACGATTCGTCAACGTCATTCAGGGCGATGCAACGCTAAATCAGGCGT-TAATTAAGATAAGCGTACTGAAAATCTCTATATTCTGCCGGCATCGCAAACACGCGATAAAGATGCCCTCACCCGT-GAAGGGGTCGCCAAAGTTCTTGATGATCTGAAAGCGATGGATTTTGAATTTATCGTTTGTGACTCCCCGGCAGG-GATTGAAACCGGTGCGTTAATGGCACTCTATTTTGCAGACGAAGCCATTATTACCACCAACCCGGAAGTCTCCTCAG-TACGCGACTCTGACCGTATTTAGGCATTCTGGCGTCGAAATCACGCCGCGCAGAAAATGGCGAAGAGCCTATTAAG-GAGCACCTGCTGTTAACGCGCTATAACCCAGGCCGCGTAAGCAGAGGTGACATGCTGAGCATGGAAGATGTGCTG-GAGATCCTGCGCATCAAACGTCGCGGTGATCCCAGAGGATCAATCAGTATTGCGCGCTCTAACCCAGGTGAACCG-GTCATTCTCGACATTAACGCCGATGCGGGTAAAGCCTACGAGATACCGTAGAACGCTGTTGGGAGAAGAAGCTCCT-TTCCGCTTCATTGAAGAAGAGAAGAAAGGCTTCCTCAAACGCTTGTTCGGAGGATAAGGATCCGGCTGCTAA-CAAAGCCCCGAAAGGAGCTGAGTTGGCTGCTGCCACCGCTGAGCAATAACTAGCATAACCCCTTGGGGCTCTAAACG-GGTCTTGAGGGGTTTTTTGATTGGGTATCGGATCCCGGGCCGTCGACTGCAGAGGCCTGCATGCAAGCTTGG-CGTAATCATGGTCATAGCTGTTTCCTGTGTGTAATACGACTCACTATAGGGGAATTGTGAGCGGATAACAAT-TCCCCTCTAGAAATAATTTTGTTTAACTTTAAGAAGGAGATATACATATGCGCTGCTGGATTCTTTCTGAGCCGTAA-GAAAAACACCGCGAACATCGCGAAAGAGCGCTCGCAATCATTGTTGCGGAGCGTCGTCGTAGCGATGCGGAACCG-CACTACCTGCCGACGTGCGTAAAGATATCCTGGAAGTGATTTGCAAGTATGTTCAAATTGACCCGGAGATGGTGAC-CGTTTCAGCTGGAACAAAAGGACGGTGATATCAGCATTCTGGAGCTGAACGTTACCTGCGGAAAGCGGAGGAACT-GAAGTAAGGATCCGGCTGCTAACAAAGCCCCGAAAGGAGCTGAGTTGGCTGCTGCCACCGCTGAGCAATAACTAG-CATAACCCCTTGGGGCTCTAAACGGGTCTTGAGGGGTTTTTTG

DNA sequence of the *ftsA-minD-minE* construct

TAATACGACTCACTATAGGGGAATTGTGAGCGGATAACAATTCCCCTCTAGAAATAATTTTGTTTAACTTTAAGAAG-GAGATATACATATGGCACGCATTATTGTTGTTACTTCGGGCAAAGGGGGTGTGGTAAGACAACCTCCAGCGCGGC-CATCGCCACTGGTTTGGCCCAGAAGGGAAAGAAAAGTGTCTGATAGATTTTGATATCGGCCTGCGTAATCTCGACCT-GATTATGGGTTGTGAACGCCGGTTCGTTACGATTCGTCAACGTCATTCAGGGCGATGCAACGCTAAATCAGGCGT-TAATTAAGATAAGCGTACTGAAAATCTCTATATTCTGCCGGCATCGCAAACACGCGATAAAGATGCCCTCACCCGT-GAAGGGGTCGCCAAAGTTCTTGATGATCTGAAAGCGATGGATTTTGAATTTATCGTTTGTGACTCCCCGGCAGG-GATTGAAACCGGTGCGTTAATGGCACTCTATTTTGCAGACGAAGCCATTATTACCACCAACCCGGAAGTCTCCTCAG-TACGCGACTCTGACCGTATTTAGGCATTCTGGCGTCGAAATCACGCCGCGCAGAAAATGGCGAAGAGCCTATTAAG-GAGCACCTGCTGTTAACGCGCTATAACCCAGGCCGCGTAAGCAGAGGTGACATGCTGAGCATGGAAGATGTGCTG-GAGATCCTGCGCATCAAACGTCGCGGTGATCCCAGAGGATCAATCAGTATTGCGCGCTCTAACCCAGGTGAACCG-GTCATTCTCGACATTAACGCCGATGCGGGTAAAGCCTACGAGATACCGTAGAACGCTGTTGGGAGAAGAAGCTCCT-TTCCGCTTCATTGAAGAAGAGAAGAAAGGCTTCCTCAAACGCTTGTTCGGAGGATAAGGATCCGCTGCTAA-CAAAGCCCCGAAAGGAGCTGAGTTGGCTGCTGCCACCGCTGAGCAATAACTAGCATAACCCCTTGGGGCTCTAAACG-GGTCTTGAGGGGTTTTTTGATTGGGTATCGGATCCCGGGCCGTCGACTGCAGAGGCCTGCATGCAAGCTTGG-CGTAATCATGGTCATAGCTGTTTCCTGTGTGTAATACGACTCACTATAGGGGAATTGTGAGCGGATAACAAT-TCCCCTCTAGAAATAATTTTGTTTAACTTTAAGAAGGAGATATACATATGCGCTGCTGGATTCTTTCTGAGCCGTAA-GAAAAACACCGCGAACATCGCGAAAGAGCGCTCGCAATCATTGTTGCGGAGCGTCGTCGTAGCGATGCGGAACCG-CACTACCTGCCGACGTGCGTAAAGATATCCTGGAAGTGATTTGCAAGTATGTTCAAATTGACCCGGAGATGGTGAC-

CGTTCAGCTGGAACAAAAGGACGGTGATATCAGCATTTCTGGAGCTGAACGTTACCCCTGCCGGAAGCGGAGGAACT-
GAAGTAAGGATCCGGCTGCTAACAAAGCCGAAAGGAAGCTGAGTTGGCTGCTGCCACCGCTGAGCAATAACTAG-
CATAACCCCTTGGGGCCTCTAAACGGGTCTTGAGGGGTTTTTTT

Table S1. List of primers used in this study.

Name	Sequence (5' to 3')
173 ChD	CACACAGGAAACAGCTATGAC
174 ChD	GAGTCAGTGAGCGAGGAAG
365 ChD	CAGTCACGACGTTGTAAACGAC
420 ChD	GGAGAGGCGGTTTGCCTAT
504 ChD	CTGCCCCGCTTTCCAGTCGGGAAA
1139 ChD	CATGGTCATAGCTGTTTCTGTGTGTAATACGACTCACTATAGG
1140 ChD	GGTTTCCCGACTGGAAAGCGGGCAGCAAAAAACCCCTCAAGACCCG
1145 ChD	CCGTCGTTTTACAACGTCGTGACTGGCGTTGGCCGATTCATTAATGC
1187 ChD	GGCGATTAAAGTTGGGTAACG

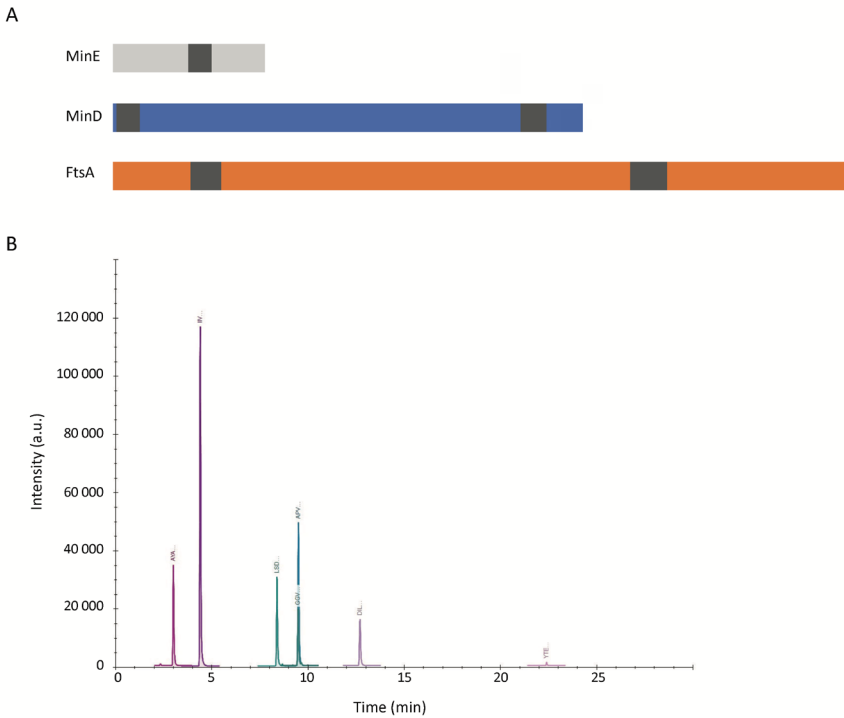
Table S2. Transitions of the MS/MS measurements for the proteolytic peptides of the indicated proteins. Accelerator voltage was kept constant at 4 eV.

Protein	Compound name	Precursor ion (m/z)	Product ion (m/z)	Collision energy (eV)	Ion name
MinD	AYADTVR	462.725	690.342	15.3	y6
MinD	AYADTVR	462.725	619.305	15.3	y5
MinD	AYADTVR	462.725	304.162	15.3	y2
MinD	AYADTVR	462.725	235.108	15.3	b2
MinD	AYADTVR	462.725	306.145	15.3	b3
MinD	AYADTVR	462.725	621.288	15.3	b6
QconCAT	AYADTVR	468.208	699.315	15.3	y6
QconCAT	AYADTVR	468.208	627.281	15.3	y5
QconCAT	AYADTVR	468.208	309.147	15.3	y2
QconCAT	AYADTVR	468.208	237.102	15.3	b2
QconCAT	AYADTVR	468.208	309.136	15.3	b3
QconCAT	AYADTVR	468.208	627.270	15.3	b6
FtsA	YTELLNLVNEEILQLQEK	1095.089	1243.653	34.9	y10
FtsA	YTELLNLVNEEILQLQEK	1095.089	871.525	34.9	y7
FtsA	YTELLNLVNEEILQLQEK	1095.089	758.441	34.9	y6
FtsA	YTELLNLVNEEILQLQEK	1095.089	645.357	34.9	y5
FtsA	YTELLNLVNEEILQLQEK	1095.089	517.298	34.9	y4
FtsA	YTELLNLVNEEILQLQEK	1095.089	847.456	34.9	b7
QconCAT	YTELLNLVNEEILQLQEK	1106.555	1257.611	34.9	y10
QconCAT	YTELLNLVNEEILQLQEK	1106.555	881.495	34.9	y7
QconCAT	YTELLNLVNEEILQLQEK	1106.555	767.414	34.9	y6
QconCAT	YTELLNLVNEEILQLQEK	1106.555	653.333	34.9	y5
QconCAT	YTELLNLVNEEILQLQEK	1106.555	523.280	34.9	y4
QconCAT	YTELLNLVNEEILQLQEK	1106.555	855.432	34.9	b7
MinE	DILEVIC[+57]K	495.270	874.507	15.6	y7
MinE	DILEVIC[+57]K	495.270	761.423	15.6	y6
MinE	DILEVIC[+57]K	495.270	648.339	15.6	y5

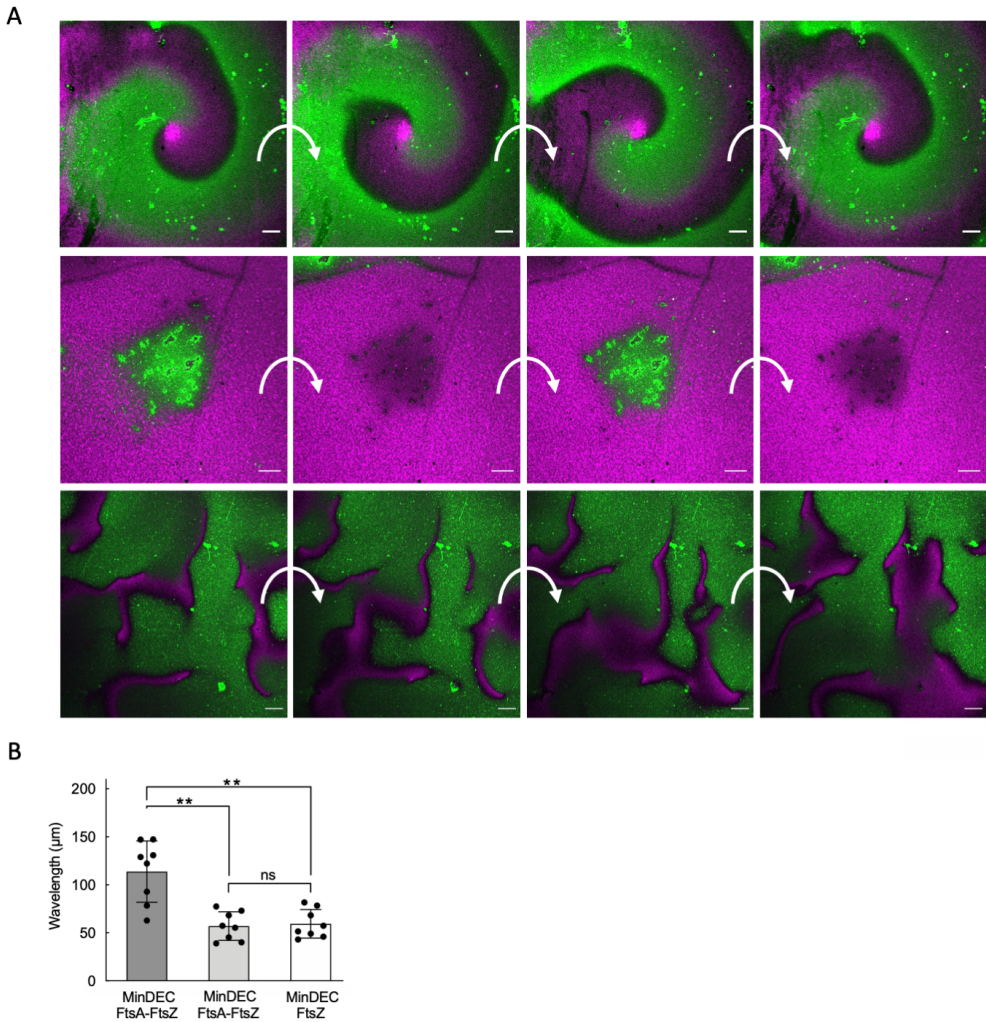
MinE	DILEVIC[+57]K	495.270	471.245	15.6	b4
MinE	DILEVIC[+57]K	495.270	570.313	15.6	b5
MinE	DILEVIC[+57]K	495.270	683.397	15.6	b6
QconCAT	DILEVIC[+57]K	499.757	882.483	15.6	y7
QconCAT	DILEVIC[+57]K	499.757	768.402	15.6	y6
QconCAT	DILEVIC[+57]K	499.757	654.321	15.6	y5
QconCAT	DILEVIC[+57]K	499.757	475.233	15.6	b4
QconCAT	DILEVIC[+57]K	499.757	575.299	15.6	b5
QconCAT	DILEVIC[+57]K	499.757	689.380	15.6	b6
FtsA	GGVNDLESVVK	558.798	903.478	18.3	y8
FtsA	GGVNDLESVVK	558.798	789.435	18.3	y7
FtsA	GGVNDLESVVK	558.798	674.408	18.3	y6
FtsA	GGVNDLESVVK	558.798	561.324	18.3	y5
FtsA	GGVNDLESVVK	558.798	432.282	18.3	y4
FtsA	GGVNDLESVVK	558.798	214.119	18.3	b3
QconCAT	GGVNDLESVVK	565.279	913.449	18.3	y8
QconCAT	GGVNDLESVVK	565.279	797.412	18.3	y7
QconCAT	GGVNDLESVVK	565.279	681.388	18.3	y6
QconCAT	GGVNDLESVVK	565.279	567.306	18.3	y5
QconCAT	GGVNDLESVVK	565.279	437.267	18.3	y4
QconCAT	GGVNDLESVVK	565.279	217.110	18.3	b3
MinD	IIVVTSGK	408.763	703.435	13.7	y7
MinD	IIVVTSGK	408.763	590.351	13.7	y6
MinD	IIVVTSGK	408.763	491.282	13.7	y5
QconCAT	IIVVTSGK	413.250	711.411	13.7	y7
QconCAT	IIVVTSGK	413.250	597.330	13.7	y6
QconCAT	IIVVTSGK	413.250	497.265	13.7	y5
QconCAT	IIVVTSGK	413.250	429.300	13.7	b4
QconCAT	IIVVTSGK	413.250	531.345	13.7	b5
Ribosomal protein S4	LSDYGVQLR	525.783	850.442	17.3	y7
Ribosomal protein S4	LSDYGVQLR	525.783	735.415	17.3	y6
Ribosomal protein S4	LSDYGVQLR	525.783	572.351	17.3	y5
Ribosomal protein S4	LSDYGVQLR	525.783	635.304	17.3	b6
QconCAT	LSDYGVQLR	532.263	949.438	17.3	y8
QconCAT	LSDYGVQLR	532.263	861.409	17.3	y7
QconCAT	LSDYGVQLR	532.263	745.385	17.3	y6
QconCAT	LSDYGVQLR	532.263	581.325	17.3	y5
QconCAT	LSDYGVQLR	532.263	541.220	17.3	b5
QconCAT	LSDYGVQLR	532.263	641.286	17.3	b6
Ribosomal protein L6	APVVVPAGVDVK	575.845	883.525	18.9	y9
Ribosomal protein L6	APVVVPAGVDVK	575.845	784.456	18.9	y8
Ribosomal protein L6	APVVVPAGVDVK	575.845	685.388	18.9	y7

Ribosomal protein L6	APVVVPAGVDVK	575.845	268.166	18.9	b3
Ribosomal protein L6	APVVVPAGVDVK	575.845	367.234	18.9	b4
Ribosomal protein L6	APVVVPAGVDVK	575.845	466.302	18.9	b5
QconCAT	APVVVPAGVDVK	582.326	893.495	18.9	y9
QconCAT	APVVVPAGVDVK	582.326	793.430	18.9	y8
QconCAT	APVVVPAGVDVK	582.326	693.364	18.9	y7
QconCAT	APVVVPAGVDVK	582.326	271.157	18.9	b3
QconCAT	APVVVPAGVDVK	582.326	371.222	18.9	b4
QconCAT	APVVVPAGVDVK	582.326	471.288	18.9	b5

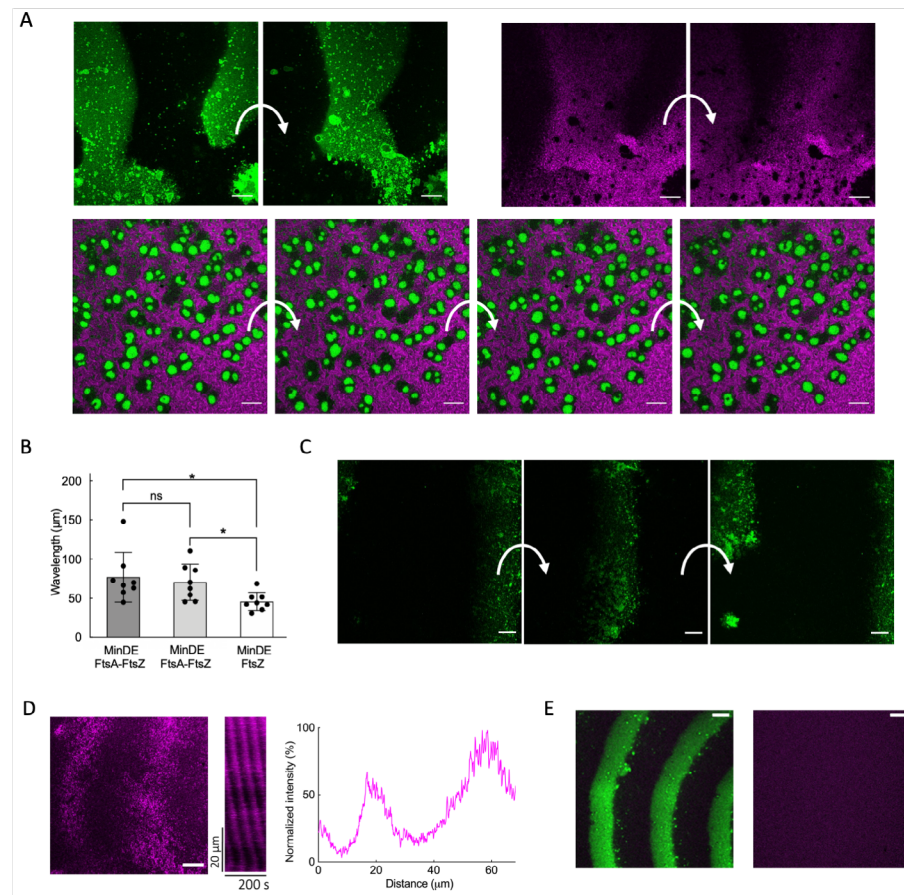
Supplementary figures



Supplementary Fig. 1: Quantitative LC-MS analysis of cell-free synthesized FtsA, MinD and MinE in bulk reactions. **a**, Cartoon depicting the position of the analyzed specific proteolytic peptides (dark grey domains) along the primary sequence of FtsA, MinD and MinE, from N-term (left) to C-term (right). **b**, LC-MS chromatogram of the investigated peptides. From left to right: AYADTVER (MinD); IIVVTSGK (MinD); LSDYGVQLR (ribosomal protein S4); GGVNDLESVVK (FtsA); APVVVPAGVDVK (ribosomal protein L6); DILEVICK (MinE); YTELLNLVNEEILQLQEK (FtsA). The two peptides for ribosomal proteins were used for quality control.

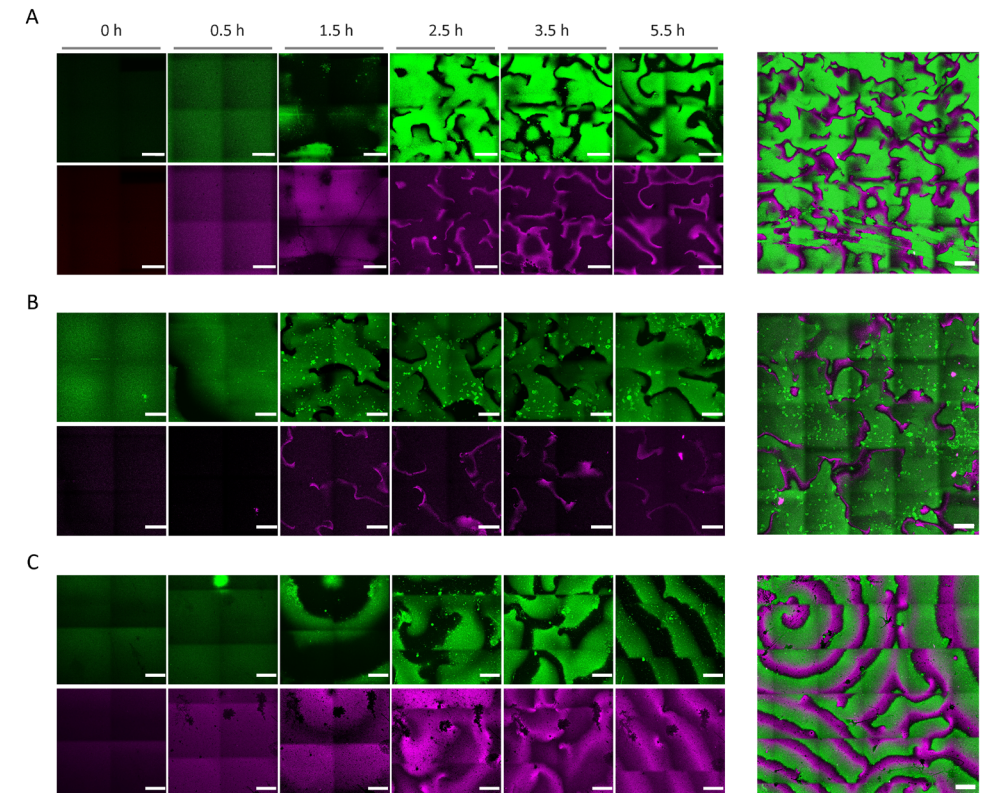


Supplementary Fig. 2: MinDEC patterns and FtsA-FtsZ structures in supported membrane assays. **a**, Composite fluorescence microscopy images of FtsA-FtsZ and MinDEC dynamic patterns on an SLB. Different patterns including spirals (top), standing (middle) and random (bottom) are shown. Arrows indicate time lapse between images. Experimental conditions and color coding are the same as in main text Fig. 2b,c. Scale bars are 10 μm. **b**, Calculated wavelengths for MinDEC waves in areas where FtsA-FtsZ co-existed (dark grey), were excluded (light grey), and without expressed FtsA (white). Data are from three biological repeats and two to three fields of view have been analyzed per sample. Bar height represents the mean value and the error bar corresponds to the standard deviation. Symbols are values for individual fields of view aggregated from three biological replicates. Values obtained for different conditions were statistically compared by performing a two-tailed Welch's *t*-test. Asterisks indicate *P* value < 0.01, while 'ns' denotes a non-significant difference with *P* value > 0.05.



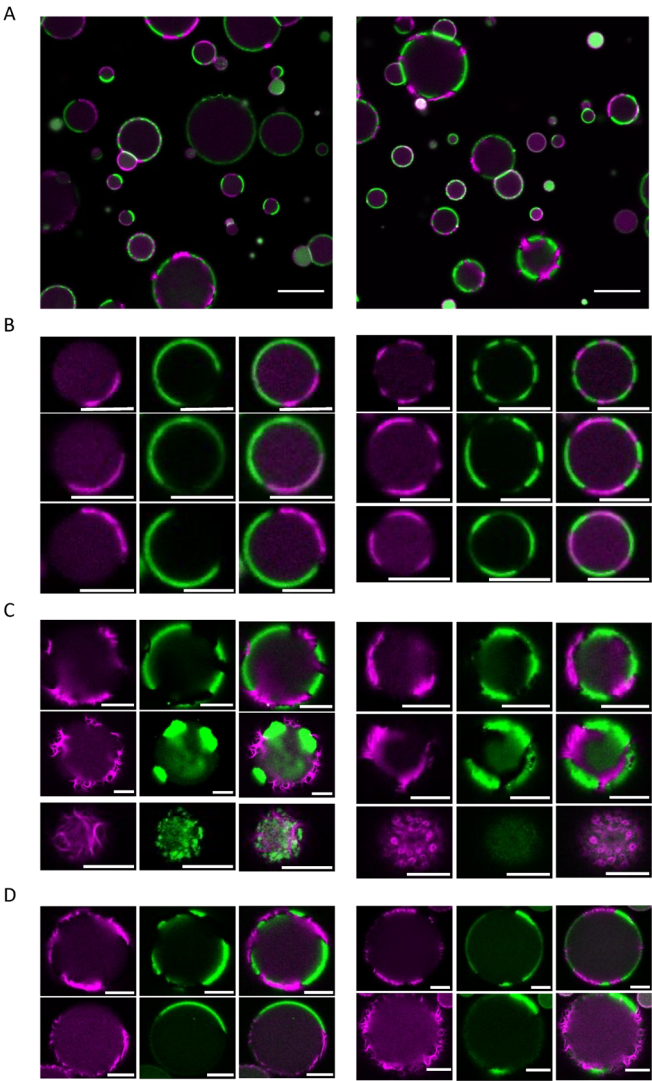
Supplementary Fig. 3: Self-organized MinDE proteins, without MinC, can effectively rearrange FtsA-FtsZ filaments on supported membranes. **a**, Fluorescence microscopy images showing that MinDE dynamic patterns rearrange the FtsA-FtsZ ring networks on an SLB. Examples of planar (top, split channels) and standing (bottom, merged channels) waves are shown. Arrows indicate time lapse between images. Experimental conditions and color coding are the same as in main text Fig. 3. Scale bars are 10 μm. **b**, Calculated wavelengths for MinDE waves in areas where FtsA-FtsZ co-existed (dark grey), were excluded (light grey), and without expressed FtsA (white). Data are from three biological repeats and two to three fields of view have been analyzed per sample. Bar height represents the mean value and the error bar corresponds to the standard deviation. Symbols are values for individual fields of view aggregated from three biological replicates. Values obtained for different conditions were statistically compared by performing a two-tailed Welch's *t*-test. Asterisks indicate *P* value < 0.05, while 'ns' denotes a non-significant difference with *P* value > 0.05. **c**, Fluorescence microscopy images of FtsA (0.4 μM FtsA-A488, green signal) dynamic patterns driven by MinDE on an SLB. Sharp propagating waves of FtsA are visible. Arrows indicate time lapse between images. **d**, Fluorescence microscopy image of FtsA-FtsZ dynamic patterns on an SLB. Purified MinD reporter was omitted to rule out effects from a possible contamination with MinC. The corresponding kymograph is displayed, as well as the intensity profile of FtsZ signal along the direction of wave propagation. **e**, Fluorescence microscopy images of FtsZ and

MinDE dynamic patterns without expressed FtsA and purified eGFP-MinD (100 nM). In this condition, FtsZ is not recruited to the membrane (right image). Color coding: eGFP-MinD (green), FtsZ-A647 (magenta). Scale bars are 10 μm.

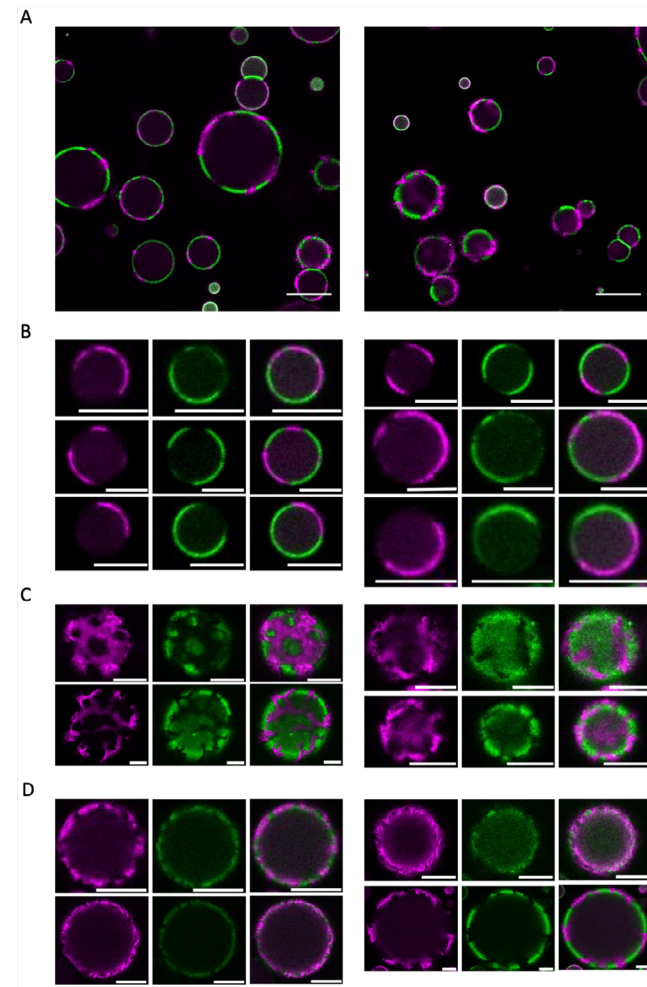


Supplementary Fig. 4: Dynamic patterning of MinDE(C) and FtsA-FtsZ during in situ co-expression of FtsA, MinD and MinE. Samples were monitored up to 5.5 hours to study pattern creation and temporal evolution. **a**, Two-by-two tile scan microscope images showing medium-scale organization of FtsA-FtsZ and MinDE(C) dynamic patterns at different time points. A mosaic image of 5×5 fields of view acquired after 3.5 hours of expression reveals large-scale, uniformly distributed waves of FtsA-FtsZ and MinDE(C). Signals from eGFP-MinC and FtsZ-A647 are in green and magenta, respectively. The two channels were overlaid to compose the large mosaic image. Scale bars are 20 μm and 50 μm for the 2×2 and 5×5 tile scans, respectively. **b**, Same as in A except that eGFP-MinC was replaced by a trace amount of purified eGFP-MinD (green). **c**, Same as in B but in this sample the protein network self-organized into spirals and planar waves. Dynamic FtsA-FtsZ patterns anti-correlating with the traveling MinDE(C) waves formed uniformly across the chamber. The coexistence of the two subsystems over the entire membrane surface contrasts with the spatial segregation of Min waves and FtsA-FtsZ filaments when pre-expressed proteins were added to the imaging chamber (main text Fig. 2b and Fig. 3b). This different behavior may be attributed to protein-specific expression kinetics, which influences the coupling of the two subsystems at large length scales. For instance, MinE production being slow (main text Fig. 1c) enables MinD and FtsA to bind homogeneously all over the available membrane within the first hour until MinE concentration rises, triggering wave formation. Furthermore, in situ protein biogenesis may occur

in close proximity to the lipid bilayer due to the intrinsic ability of ribosomes to bind to membranes, which potentially results in a different local concentration of FtsA and MinD comparing-with pre-expressed proteins. In the assays conducted without MinC, eGFP-MinD was recruited to the membrane at the start of the reaction (b and c). After ~30 min, extensive dynamic patterns of MinDE appeared, followed by FtsZ surface waves that became more pronounced as more FtsA was synthesized. After 1 to 1.5 hours of gene expression, the anticorrelated concentration gradients of membrane-bound FtsA-FtsZ and MinDE became well defined. Here too, MinDE self-organized into crisper traveling waves as protein synthesis was progressing. In the presence of eGFP-MinC, rings of FtsA-FtsZ filaments formed after 1 hour of gene expression, concomitant to the emergence of MinDEC patterns that began in sporadic areas as standing waves (a). In the course of protein production, MinDEC self-organized into sharper traveling waves that colonized the whole chamber, causing stronger patterning of membrane-recruited FtsZ (a). Together, these results demonstrate that in situ cell-free gene expression can be exploited for timing protein-protein and protein-membrane interactions, which modulates the large-scale organization of the coupled Min-FtsA-FtsZ system.



Supplementary Fig. 5: Reconstitution of MinDEC and FtsA-FtsZ subsystems in water-in-oil droplets. Composite fluorescence microscopy images of droplet populations and a library of single droplet images with reconstituted MinDEC patterns and FtsA-FtsZ subsystems are shown. **a**, Composite image of droplet population. Experimental conditions were as described in main text Fig. 4b. **b**, Fluorescence images of droplets exhibiting antiphase dynamic patterns of MinDEC and FtsA-FtsZ. Experimental conditions were as described in main text Fig. 4b. **c**, Same as in (a), but images were acquired closer to the dome of the droplets. Multiple interfacial FtsZ polarization sites rearranged by the Min dynamics are visible. Experimental conditions were as described in main text Fig. 4b. **d**, Same as in (b-c), except that bigger droplets (diameter >20 μm) were imaged. Here, FtsZ cytoskeletal structures are clearly resolved. (**a-d**) Experimental conditions were as described in main text Fig. 4b. Color coding: eGFP-MinC (green), FtsZ-A647 (magenta). Scale bars are 10 μm.



Supplementary Fig. 6: Reconstitution of MinDE and FtsA-FtsZ subsystems in water-in-oil droplets. Composite fluorescence microscopy images of droplet populations and a library of single droplet images with reconstituted MinDE patterns and FtsA-FtsZ subsystems are shown. **a**, Composite image of droplet population. Experimental conditions were as described in main text Fig. 4c. **b**, Fluorescence images of droplets exhibiting antiphase dynamic patterns of MinDE and FtsA-FtsZ. Experimental conditions were as described in main text Fig. 4c. **c**, Same as in (**a**), but images were acquired closer to the dome of the droplets. Multiple interfacial FtsZ polarization sites rearranged by the Min dynamics are visible. Experimental conditions were as described in main text Fig. 4c. **d**, Same as in (**b-c**), except that bigger droplets (diameter $>20\ \mu\text{m}$) were imaged. Here, FtsZ cytoskeletal structures are clearly resolved. Experimental conditions were as described in main text Fig. 4c. (**a-d**) Color coding: eGFP-MinD (green), FtsZ-A647 (magenta). Scale bars are $10\ \mu\text{m}$.

Supplementary files

The Supplementary Movies and Source Data file are provided here <https://www.biorxiv.org/content/10.1101/2021.11.15.468671v1.supplementary-material>.

FtsA-FtsZ in liposomes: constricting necks and budding vesicles, yet a step away from division

Elisa Godino & Christophe Danelon

Building upon our experiments showing FtsA-FtsZ contractile rings in liposomes, we decided to further characterize these phenotypes, provide statistics over the observed features, and explore conditions that may lead to division. Wild-type FtsA or the gain-of-function mutant FtsA* were cell-free expressed with FtsZ inside liposome compartments. A large number of liposomes with extended membrane necks and budding vesicles were tracked over time and thoroughly characterized. We found that FtsA induced relatively short necks and bigger vesicles, whereas FtsA* formed longer tubular necks with small, clustered vesicles. In both cases, the two-protein system failed to generate visible division events, even when increasing the osmolarity outside liposomes. Possible routes to attempt division directed by in situ synthesized FtsA-FtsZ are discussed.

Introduction

Cytokinesis is a prerequisite for self-reproduction in all living systems. Thus, incorporating a division strategy into the rational design of a synthetic cell is crucial¹. To accomplish compartmental self-replication, we can strive to imitate cellular life, where with a few exceptions, division is coordinated by an enzymatic machinery². In most scenarios, a constricting ring forms at midcell and causes the cell to split³. With its limited number of well-characterized components, the *Escherichia coli* divisome has undeniably been at the heart of numerous efforts to achieve controllable liposome division^{4–11}. The cell-free reconstruction of the ring-forming FtsZ^{12,13} and its membrane anchoring proteins FtsA and ZipA¹⁴ has significantly contributed to our understanding of the division's intricate functioning and dynamics.

In 2008, Osawa and colleagues showed data suggesting that Z-rings could generate constriction forces within tubular liposomes in the absence of motor proteins⁴. In their work, FtsZ-mts (FtsZ with a membrane targeting sequence fused to the C terminus) caused membrane invagination, though never achieving full constriction. The authors then proposed that the mechanism that generates the driving force was dependent on the conformational change of FtsZ from straight to curved filaments. Later in 2013, Osawa et al., reported Z-ring-driven membrane constriction to the point of septation⁶. According to the authors, FtsA*, a gain of function mutants of FtsA, was required to achieve complete scission, as such observation was not made in their previous work with FtsZ-mts. These findings implied that the membrane protein is involved in Z-ring organization⁶.

Soon after, Szwedziak et al., using FtsZ and FtsA from *Thermotoga maritima*, showed cryoEM images of continuous filament rings surrounding the liposome membrane and effectively generating constriction sites⁸. The authors proposed an alternative mechanism for constriction, attributing the sliding and shortening of overlapping FtsZ filaments as the force generator⁸.

Ramirez Diaz and colleagues proposed that FtsZ filaments do not only have a single curvature orientation¹⁵, and that the innate twisting helical structure drives the previously described liposome deformations. In a subsequent work, the same group pulled soft lipid tubes from liposomes¹¹. The lipid tubes were actively altered into helical spring-like structures by the FtsZ filaments. The study established that FtsZ-YFP-mts treadmill triggers membrane deformations of deflated liposomes via torsional stress, which is reliant on GTP hydrolysis¹¹.

In 2020, using cell-free gene expression, we reconstituted FtsA-FtsZ rings inside liposomes, which resulted in membrane necks with budding vesicles¹⁰. As we recognized the potential of this gene-encoded division module toward self-reproduction, we felt the need to investigate a larger set of membrane remodeling events, as well as to monitor dynamic behaviors. Our experimental design and image analysis were guided by the question

whether division occurs or not. Specifically: Is the combination of the membrane proteins FtsA and FtsZ sufficient to drive liposome division? Is the FtsA gain-of-function mutant required for full septation? Could a hypertonic environment aid fission of the FtsZ-constricted membrane neck?

To answer these questions, FtsA or FtsA* were de novo synthesized inside liposomes with FtsZ. For each membrane protein, over 50 liposomes exhibiting a clear membrane neck and/or budding vesicles were imaged over time. Division was not observed for any of the studied conditions. Interestingly, we found that expression of either of the two FtsA versions produced different liposome phenotypes. FtsA led to short necks and bigger vesicles, while FtsA* drove the formation of long tubular protrusion, often leading to thin extended necks with smaller, clustered, vesicles. Moreover, our results indicate that FtsZ-mediated lipid extrusion via torsional stress is the main driver of membrane neck formation and vesicle budding. Finally, we discussed experimental approaches to assist FtsA-FtsZ with external mechanisms and achieve liposome division.

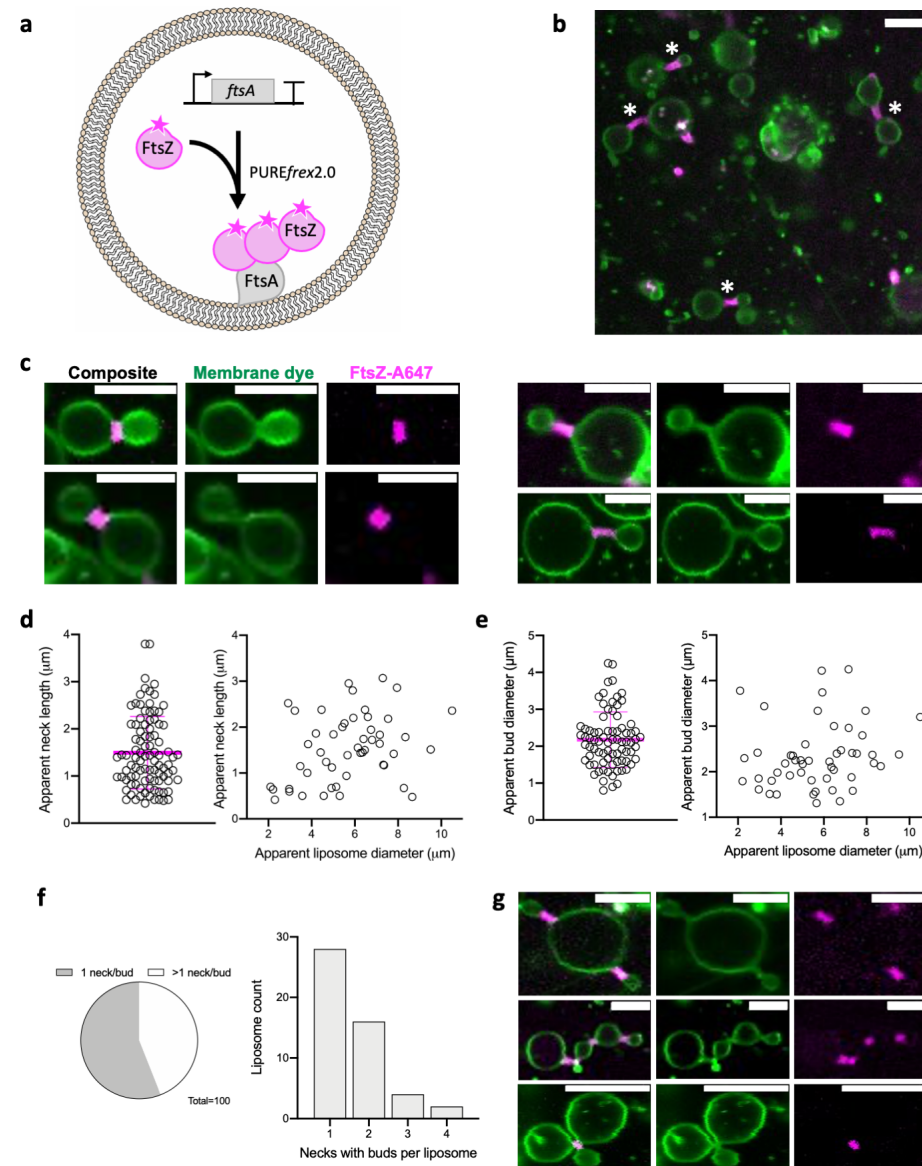
Results

We began by reconstituting the FtsA-FtsZ cytoskeletal networks as we have done previously¹⁰, with some minor protocol modifications to maximize the formation of necks and budding vesicles (Method section). Cell-free gene expression was performed after supplementing adenosine triphosphate, guanosine triphosphate, a highly purified chaperone mix, a protein-based RNase inhibitor, and FtsZ-A647 (Fig. 1a). As expected, most of the liposomes exhibited FtsZ-A647 on the inner surface of the membrane, where membrane remodeling was also visible (Fig. 1b). Several forms of membrane deformation and protrusion were generated by the recruited FtsZ. The optimized protocol resulted in an increase in the occurrence of budding vesicles connected to the parental liposome via a membrane neck colocalizing with FtsZ (Fig. 1b, Supplementary Fig. 1a).

FtsZ membrane recruitment was detectable within 1.5 hour of expression, while liposome shape deformation was seen after 2-3 hours. The budding neck generally spans over a few microns and forms a tubular structure coated with FtsZ (Fig. 1c). The apparent length of the FtsZ-coated neck is $1.5 \pm 0.8 \mu\text{m}$ (three biological replicates, over 50 membrane protrusions analyzed). No correlation was found between the size of the parental liposome and the length of the neck (Fig. 1d). The tethered vesicles have an apparent (and most likely underestimated) diameter of $2.2 \pm 0.8 \mu\text{m}$ (three biological replicates, over 50 buds analyzed) (Fig. 1e).

We observed that multiple necks with blebs can develop from a single mother liposome (Fig. 1f,g), representing about 44% of the total number of constricted liposomes. Up to four necks with attached vesicles may be derived from a mother liposome and liposomes can be linked by several necks either in a row or via a branching point (Fig. 1g).

We repeated the assays several times with various lipid compositions (DOPG-DOPC and DOPG-DOPC-DOPE-CL), batches of lipids, DNA templates, PURE system, and purified FtsZ, confirming our results. Therefore, we conclude that our protocol is robust and highly reproducible in generating liposome constriction via FtsZ-FtsA.



eling events driven by FtsA-FtsZ. Asterisks highlight FtsA-FtsZ-coated membrane necks and budding vesicles. **c**, Confocal fluorescence images of single constricted liposomes. The membrane neck can be shorter than 1 μ m (left) or longer (right). **d**, The extension of the membrane neck has been analyzed. The neck was measured at its best focus. One image for each parental liposome was taken close to the equatorial plane to determine the apparent diameter. No correlation was observed between the parental liposome size and neck extension. Fifty parental liposomes have been analyzed, each dot corresponds to one measurement. The magenta line represents the mean value with its relative standard deviation. **e**, The apparent bud size has been analyzed. The apparent diameter of the bud and of the parental liposome close to their equatorial plane was measured. Fifty parental liposomes have been analyzed. The magenta line represents the mean value with its relative standard deviation. **f**, Analysis of the distribution of necks with blebs. 44% of the parental liposomes feature more than one neck. The number of necks ranges from 1 to 4. Considering the fast dynamics of these lipid structures, more of them might be hidden outside the focal plane, therefore these values are likely underestimated. Fifty parental liposomes have been analyzed. **g**, Confocal fluorescence images showing that multiple necks with attached vesicles may form from one single parental liposome (top), and that several liposomes can be linked by necks in a row (middle) or that multiple buds might be connected via one branching point (bottom). The membrane dye is displayed in green and FtsZ-A647 is in magenta. The composite image is the overlay of the two channels. Scale bars 5 μ m.

We then decided to track constricted liposomes over time to determine whether division might occur either by closure of the neck or detachment of the bud. We examined over 50 liposomes with varying numbers of necks and blebs. Images were collected every 10 seconds for a duration spanning from a few minutes to 40 minutes (Fig. 2a). The duration of the recording was chosen as a function of the degree of the motions of the imaged structures and our ability to maintain them in focus. None of the liposomes underwent visible division during recording. As a result, we can confidently state that FtsA-FtsZ is capable of constricting liposomes but does not drive division events in the condition studied. Some tiny blebs, less than 1 μ m in diameter, may have been expelled from the parental liposome, but these events were rare and ambiguous, in part because of the difficulties of recording over multiple focus planes. The release of small buds might explain the buildup of small vesicles observed six hours after gene expression¹⁰, but we have no direct experimental evidences.

Monitoring the liposomes overtime allowed us to observe the dynamical behaviors of the necks and buds. We found that the neck structures were quite dynamic and appeared to slide along the liposome membrane. These dynamic behaviors are consistent with torsional stress and lipid extrusion directed by the FtsZ within the neck. We also observed a few instances, where opposite membrane sites were constricting, presumably as a result of the condensation of the FtsZ structure (Fig. 2b, Supplementary Fig. 1b).

Figure 1: Characterization of FtsA-FtsZ contractile rings in liposomes. **a**, Schematic illustration of the liposome reconstitution assay. The *ftsA* gene was expressed within phospholipid vesicles in the presence of 3 μ M purified FtsZ-A647. **b**, Confocal fluorescence image showing liposomes with membrane remod-

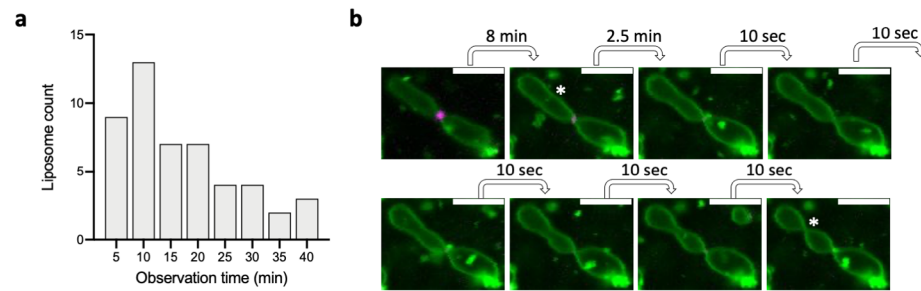


Figure 2: a, Overtime analysis of constricted liposomes. The graph reports the number of liposomes with necks and blebs that were observed over a certain time span (from a few minutes to 40 minutes). Images were recorded at the confocal microscope every 10 s, the duration of the recording depended on the dynamics of the liposome structures. None of the studied liposomes underwent division during the observation period. **b**, Series of confocal fluorescence images showing a liposome constricting in the course of time. The asterisk indicates the constriction site. The corresponding FtsZ-A647 fluorescent signal is not visible since the membrane remodeling started 8 minutes after the start of imaging and the fluorophore is therefore already bleached. The time between consecutive images is indicated. The membrane dye is in green and FtsZ-A647 is in magenta. The composite image is the overlay of the two channels. Scale bars 5 μ m.

To better visualize the extent of membrane modification and the possible presence of released vesicles, we next chose to investigate the deformation process by supplying the division players from the outside of the liposomes. We prepared liposomes using the standard swelling solution depleted from the *ftsA* DNA construct and purified FtsZ. Those were supplemented in the external solution after the liposomes were transferred in the imaging chamber, and DNAase was omitted (Fig. 3a). After 1 hour, we observed that FtsZ was recruited on the outside of the liposomes and was drilling concave deformations into the vesicle membrane (Supplementary Fig. 2a,b). Multiple distinct inward tubular membrane structures coated with FtsZ were detected as gene expression continued (Fig. 3b,c,d). The tubular deformation, which resembles the previously described necks, spanned several microns. FtsZ-coated membrane tubulations appeared to develop irrespective of liposome size, and numerous invagination buds or tubes were observed (Fig. 3b). Membrane tubulation frequently led to at least one terminal bud, as also reported with in-liposome expression. Some of the associated vesicles can be several microns in diameter (Fig. 3c). In some vesicles with diameter > 5 μ m, densely packed invaginated membrane structures with branching points can accumulate (Fig. 3d). The fact that FtsA-FtsZ clusters at a constriction neck can split, resulting in multiple necks separated by blebbing vesicle, is a relatively common phenomenon when the proteins were present inside the liposomes (Fig. 1g and Fig 3e from chapter 2) may explain this observation. We carefully examined the numerous inner vesicles over time and along Z-stacks to assess if they were tethered to the parental liposome. This was indeed the case and we concluded that none of the inward membrane protrusions matured into division events. This sort of

membrane shape transformations is compatible with the extrusion of lipid material by screw-like forces prompted by FtsZ filaments, imposing torsional stress on the membrane, as recently described¹¹. Overall, by monitoring several constricted liposomes overtime, exposing division proteins inside or outside, we gather that tubular membrane extrusion is the most prevalent mechanism for FtsZ to promote the development of membrane necks with budding vesicles.

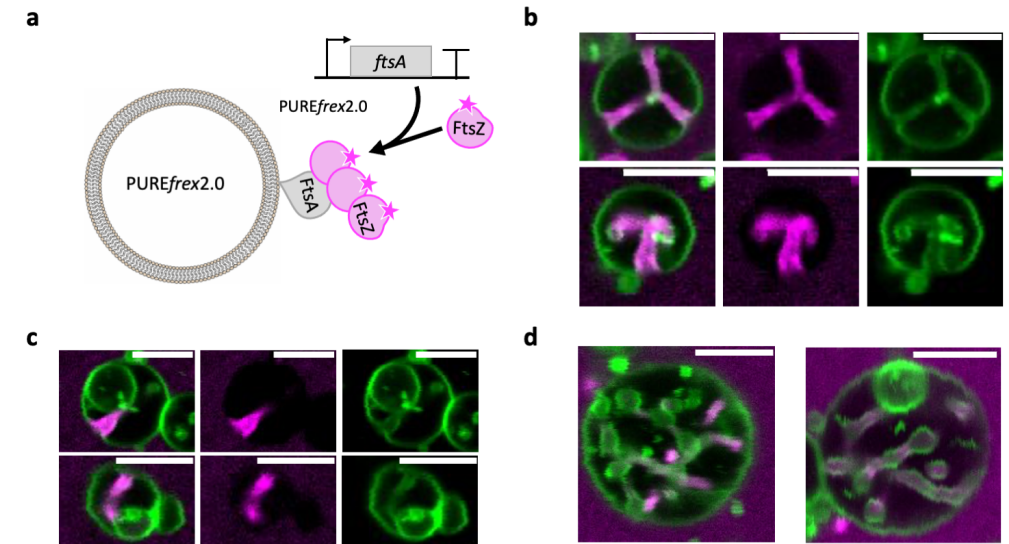


Figure 3: Characterization of FtsA-FtsZ contractile rings provided from the liposomes outside. **a**, Schematic illustration of the inside-out liposome reconstitution assays. The *ftsA* DNA template and 3 μ M purified FtsZ-A647 were supplemented in the outer liposome solution. FtsA-FtsZ structures could only form on the membrane outside the liposomes. **b**, Confocal fluorescence images of liposomes exhibiting numerous inward tubulations coated with FtsZ. **c**, Confocal fluorescence images of liposomes displaying inward tubulations with large tethered vesicles. **d**, Images of large liposomes loaded with large amounts of invaginated membrane structures pinched off by visible FtsZ clusters. The membrane dye is in green and FtsZ-A647 is in magenta. The composite image is the overlay of the two channels. Scale bars 5 μ m.

After determining that membrane constriction and neck formation constituted a highly reproducible phenotype and that division events did not occur, we decided to investigate if an osmolarity change could promote splitting. Osmotically deflated liposomes are particularly prone to membrane remodeling in the presence of division players¹⁶. To increase the external osmosis, we added 100 mM sucrose to the outer solution of liposomes containing FtsA and FtsZ. Surprisingly, just a few liposomes seemed to have an increase in the number of FtsZ-coated membrane necks and buds (Supplementary Fig. 3a). Instead, most of the liposomes went through a “reversing” deformation process and relaxed back into a spherical shape (Fig. 4a,b). More specifically, after osmotic deflation, liposomes with a stable constriction site and budding vesicle started to wobble, which destabilized the FtsZ-coated neck, this was followed by drastic membrane remodeling, and subsequent rearrangement into a spherical

shape. No daughter vesicles were released during the process.

When a greater concentration of sucrose (200 mM) was applied to the liposomes, the sample lost in quality and the remaining liposomes showed numerous elongated membrane protrusions with several constriction sites (Supplementary Fig. 3b). Overall, the addition of sucrose proved to not be a viable route toward FtsZ-based liposome division.

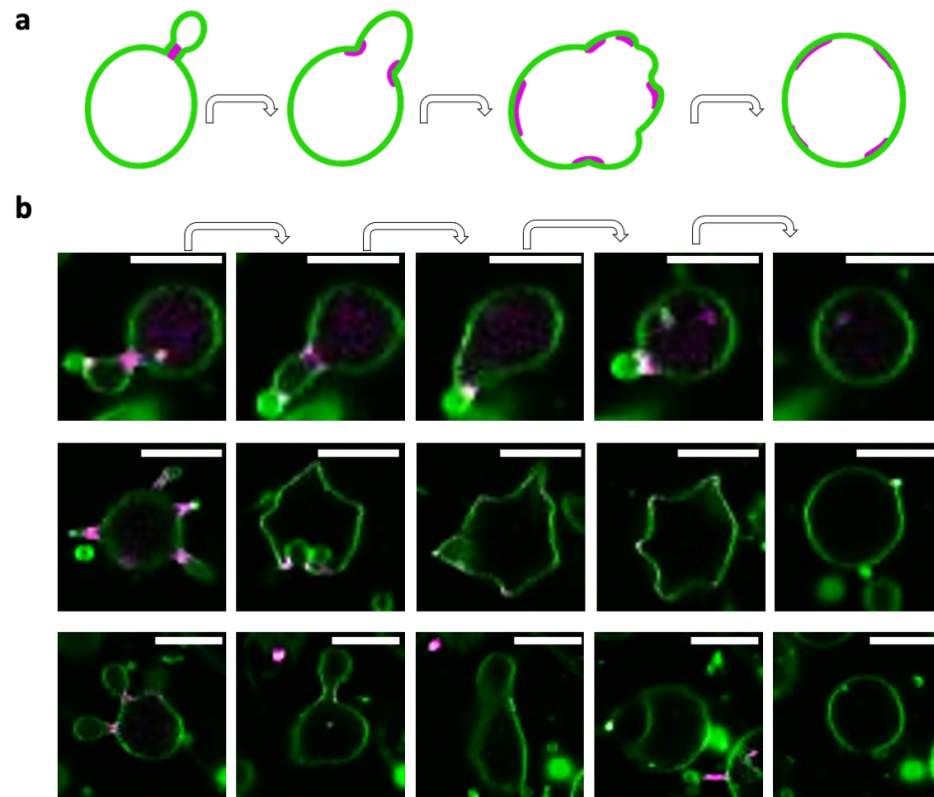


Figure 4: Liposome constriction and osmolarity change. **a**, Schematic illustration of liposome shape transformation upon addition of sucrose. **b**, Examples of three liposomes containing cell-free expressed FtsA and purified FtsZ-A647, and supplemented with sucrose (100 mM). Upon osmotic shock the membrane neck containing FtsZ was destabilized, followed by an extensive membrane remodeling during which liposomes incorporated the excess of the neck and buds to assume a spherical shape. The arrows indicate a time sequence. The images are overlay of the membrane dye signal (green) and the FtsZ-A647 signal (magenta). Scale bars 5 μm .

We then asked if the lack of division events was related to the fact that we employed the wild-type *E. coli* FtsA instead of FtsA*, an FtsA gain-of-function mutant with a single amino acid mutation in R286W¹⁸, as in Osawa et al.⁶, where complete septation was claimed by the authors. Therefore, we opted to cell-free express FtsA* inside liposomes and reconstruct FtsA*-FtsZ

cytoskeletal structures following the same protocol as with FtsA (Fig. 5a). Likewise, ATP (2 mM), GTP (2 mM), DnaK mix, SUPERase, and FtsZ-A647 (3 mM) were added to the cell-free gene expression mixture, which was used to prepare DOPC-DOPG liposomes via natural swelling.

De novo synthesized FtsA* successfully recruited FtsZ to the membrane as shown by the colocalization of the FtsZ-A647 and membrane dye signals (Fig. 5b,c,d). Membrane recruitment of FtsZ in the form of patches was visible within 1.5 h of expression and major liposome-remodeling events were observed after 2 h. From first look already, the FtsA*-FtsZ-induced liposome deformations were different than with FtsA. The majority of the liposomes exhibited long and narrow outward membrane protrusions, completely coated with FtsZ (Fig. 5b). The tubular protrusions were rather long, spanning over several microns (Fig. 5c), with an estimated mean \pm standard deviation value of the length of $3.2 \pm 1.5 \mu\text{m}$ (three biological replicates, over 50 membrane protrusions analyzed). No correlation was observed between parental liposome size and neck extension. The necks generated with the wildtype FtsA and FtsZ were about twofold shorter. Because the outward deformations were very dynamic in both the z-plane and along the membrane, imaging them was difficult, especially over time. The outer part of the long membrane tubes can bifurcate into two or three branches (Fig. 5d). In some cases, tiny vesicles were linked to the parental liposome through the long protrusions. The small buds had a size of $1.1 \pm 0.6 \mu\text{m}$ (mean \pm standard deviation across three biological replicates for a total of 40 buds) and were typically clustered (Fig. 5e,f). No events of bud detachment were observed. However, it is important to note that imaging the same buds, even over a short time span, was not really feasible due to their distance from the mother liposome, their restricted size, and their extreme dynamics.

Other membrane remodeling morphologies, such as patches, small outward membrane deformations or short protrusions were also observed but their occurrence was low. The canonical phenotype observed with FtsA, i.e. large (diameter $>2 \mu\text{m}$) vesicles tethered to the parental liposome through a membrane neck, was rarely detected with FtsA* (Supplementary Fig. 4a). Our results suggest that FtsA* is not a good candidate for synthetic cell division. The tiny size of the budding vesicles creates an extreme asymmetric, imbalanced division process, which is incompatible with a second generation of synthetic cells.

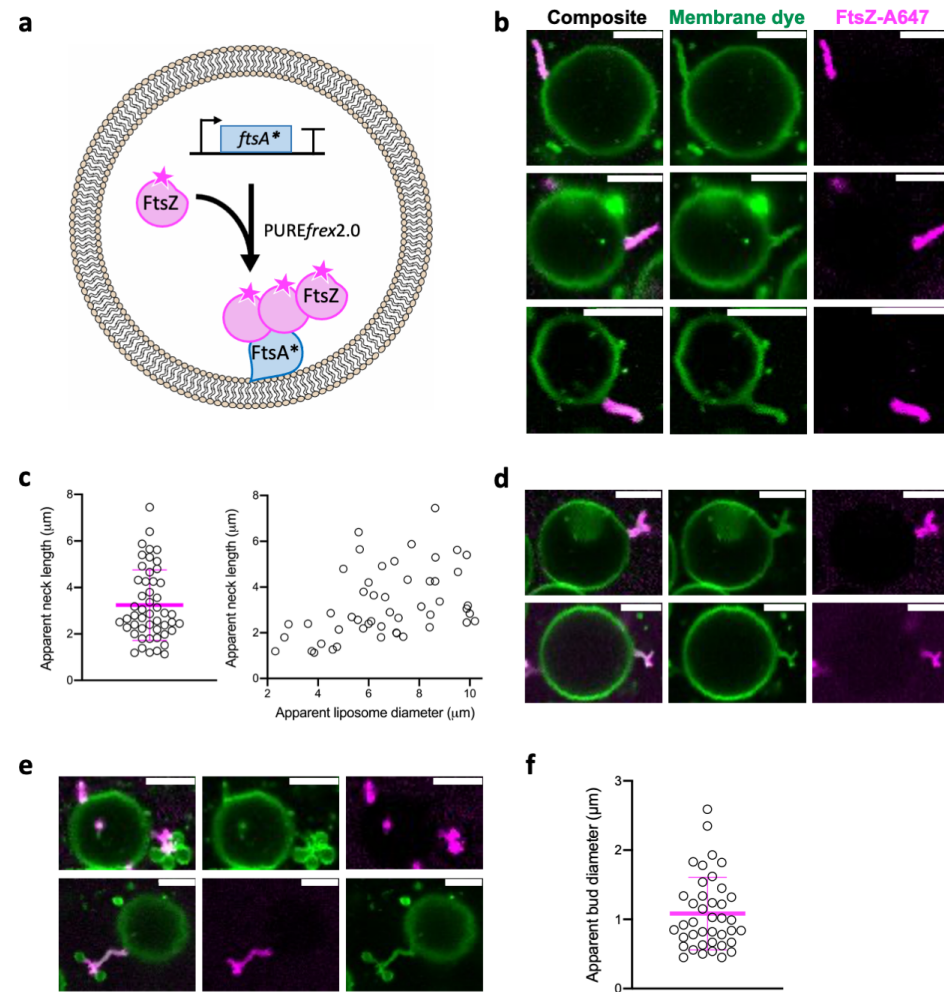


Figure 5: Replacing FtsA with FtsA* and characterization within liposomes. **a**, Schematic illustration of the FtsA*-FtsZ liposome experiments. The *ftsA** DNA template was expressed within phospholipid vesicles in the presence of 3 μ M purified FtsZ-A647 as previously described with the wild-type gene. **b**, Confocal fluorescence images of liposomes exhibiting long and narrow outward membrane protrusions, completely coated with FtsZ. **c**, The extension of the membrane neck has been quantified as described in Fig. 1. Fifty parental liposomes have been analyzed. The magenta line represents the mean value with its relative standard deviation. **d**, Confocal fluorescence images showing that long tubulated membranes can bifurcate into two or three branches. **e**, The extremity of the neck can bear a cluster of small vesicles. **f**, The apparent bud size has been analyzed as described in Fig. 1. The magenta line represents the mean value with its relative standard deviation. The membrane dye is in green and FtsZ-A647 is in magenta. The composite image is the overlay of the two channels. Scale bars 5 μ m.

Discussion

In this study, we improved our methodology to produce gene-expressing vesicles, thus increasing the frequency of FtsA-FtsZ-induced liposome constriction events, which allowed us to perform a quantitative analysis over the different morphologies observed. Expression and membrane interaction of FtsA-FtsZ filaments from the outside of liposomes helped us reconstruct the sequence of events yielding neck formation and vesicle budding (Fig. 3b): First, concave membrane depressions were formed, followed by deep invagination, which resulted in the extrusion of membrane tubules. The inward deformations are comparable to those observed when purified FtsZ-YFP-mts was bound to the outside of liposomes⁵. FtsZ protofilaments generating a bending force on the membrane was suggested as a preliminary process causing concave depressions⁴. According to a more recent study, the inward membrane protrusions are caused by a corkscrew-like FtsZ helix with multiple curvature directions¹⁵. A follow-up study revealed that membrane tubulation is induced by torsional stress caused by an intrinsic twist along the FtsZ filament, and that GTPase activity increases this torsional stress¹¹. Interestingly, we also noticed a less common deformation mechanism in which the membrane is pinched off, resulting in neck formation (Fig. 2b). This observation is more consistent with another proposed model in which FtsZ filaments wrapped around the liposome membrane slide, pulling the opposing membrane regions together⁸. We propose that in vitro liposome constriction sites may be caused by different types of mechanisms, with torsional stress being the dominant one.

Combining with data obtained using the gain-of-function mutant FtsA*, our results indicate that expressed FtsA*/FtsA and FtsZ robustly form ring-like structures within liposomes, which leads to consistent liposome constriction in the form of more-or-less elongated necks, but fails to trigger division events. Therefore, an FtsA-FtsZ-based minimal mechanism is unlikely to drive synthetic cell division on its own. The reported example of septum closure to the point of division appears today very questionable⁶. Altogether, the recent findings indicate that ring assembly and membrane extrusion or deformation are insufficient for liposome division.

The reconstruction of Z-rings in vitro, as described in this research and many others, provides compelling evidence for FtsZ force generation via a variety of suggested processes^{5,8,11,15,19–21}. However, there has been considerable disagreement regarding the role of FtsZ in cell constriction over the years, particularly since it was reported that FtsZ is not the rate-limiting factor for bacterial cytokinesis²². Excluding the resistance provided by the cell wall, *E. coli* exhibits a turgor pressure of approximately 0.3 MPa²³ (corresponding to a needed force of 50 nN)²⁴. The force produced by FtsZ is believed to be in the range of pN^{19,25}, which is therefore insufficient to promote cell division. It was recently proposed that, in *E. coli*, it might not be necessary to resolve turgor pressure because the periplasm and cytoplasm may have about the same turgor²⁶. This hypothesis led to a scenario in which FtsZ drives inward deformations

in vivo, pulling from the inside, in combination with an excess of membrane that helps in reducing the force necessary for membrane constriction²⁵. Further in vitro studies involving membrane proteins and other division players, as well as active membrane synthesis enzymes, may be beneficial to decipher the role of FtsZ in cellular division.

In synthetic cell research, cell-free expressed FtsA and FtsZ is an excellent place to start and serves as a scaffold to integrate extra elements which, together, will form a division machinery. The reproducible membrane necks with tethered vesicles generated here offer a reliable platform. Furthermore, the division machinery is guided by an internal genome, which is a critical aspect for establishing autonomous synthetic cells. A gene-driven approach not only preserves autonomy, but it also allows for genotype-phenotype investigations and for the laboratory evolution of the division module. To create an all-gene FtsZ proto-ring capable of dividing liposomes, we should further investigate the extraordinary capacity of live cells to divide and complement natural processes with an engineering framework. As a first step, we envisage integrating FtsA and FtsZ with the ring-positioning MinDE system. It has been demonstrated that Min oscillations cause substantial membrane remodeling^{27,28}. It is likely that the resulting changes in mechanical properties, in combination with the forces exerted by FtsZ, might promote the fission event.

Another aspect to consider, especially when combining the two systems, is that division may be easier to reproduce in an elongated liposome with aspect ratios similar to rod-like bacteria, not only because the systems operate in an elongated morphology, but also because division necessitates an increase in the area-to-volume ratio²⁹, something that an elongated shape would provide. Elongation is often the initial stage towards binary fission, followed by membrane invagination. A similar two-step approach could be used for the synthetic cell. Reconstituting the entire elongosome complex as found in *E. coli* may not be the ideal option for a minimal system³⁰⁻³². In attempting to elongate the liposomes, the use of thermal expansion^{33,34}, electric fields^{35,36}, or cell-free expressed bacterial tubulin³⁷ would be recommended.

Other techniques to overcome the energy barrier for fission are available. One option is the alteration of the osmotic pressure to produce the desired final volume for the daughter liposomes. It is known that the type of osmotic agent used can be crucial in the advancement of liposome deformation. In the present work, we have observed the effects of increasing the outer osmolarity by supplementing sucrose. We saw reverse liposome deformation, which likely means that the substantial membrane remodeling caused by the hypertonic environment destabilized the necks and the liposome relaxed into a spherical shape (Fig. 3 B). It should be noted that at concentrations such as the ones used here, sucrose can bind to the membrane¹⁷, increasing the mean surface area per lipid and, hence the vesicle surface-to-volume ratio. Sucrose binding might cause significant fluctuations of the expanded membrane, which creates forces in the opposite direction than those exerted by FtsZ. Shape transformation due to changes in the outer liposome osmotic pressure should be investigated further, both

by increasing and decreasing it. The use of different analytes and approaches for osmolarity reduction outside of pre-constricted liposomes, could be used in the future to disassemble FtsZ-necks and promote division. Monovalent anions and cations, divalent cations, and monosaccharides, the latter of which have been shown to bind less to the membrane¹⁷, should be taken into consideration.

Membrane expansion is another option that can be accomplished through either gene-guided lipid synthesis within liposomes^{38,39} or the incorporation of lipids from the external environment. Lipid synthesis currently yields no more than 10% compartment growth, but the establishment of robust membrane areal growth has recently become an active research³⁹. Although fatty acid micelles have been used to achieve lipid incorporation^{40,41}, fusion of liposomes with small unilamellar vesicles supplemented in the external environment is appealing and could be aided using synthetic membrane binding DNA nanostructures⁴².

Using composite membranes with varying lipid shapes and chain lengths may be considered to alter liposome morphology and membrane tension⁴³⁻⁴⁶. Furthermore, the surface of the liposome could be asymmetrically modified to increase the line tension and spontaneous curvature. A relevant example in this direction is the usage of the photosensitizer Chlorin e6, which causes local lipid peroxidation upon illumination over a time scale of minutes⁴⁷. Lastly, mechanical perturbations, such as gentle shear forces or sonication, may also elicit division events at the membrane neck of constricted liposomes (e.g. with FtsA-FtsZ), a scenario that may have been important in the development of early life before full genetic control⁴⁸. External adjustments to aid compartment division appears to be a step away from autonomy, but it is not. First, the genes encoded inside the synthetic cell govern the timing and course of division and drive the neck and bleb development. Then, the synthetic cell's response to one or more external stimuli triggers the final abscission. The combination of gene-expressed FtsA-FtsZ with the proposed external processes will result in a functional quasi-autonomous division mechanism that can be incorporated in a minimal synthetic cell cycle.

Methods

DNA constructs

The *ftsA* construct (starting with a T7 promoter and ending with the T7 terminator) was sequence-optimized for codon usage, GC content and 5' mRNA secondary structures, and was inserted in pUC57 plasmid, (GeneScript). *E. coli* TOP10 competent cells were transformed with the plasmid by heat shock. Plasmid purification was performed using the PureYield™ Plasmid Miniprep System (column method, Promega). Plasmid concentration and purity were checked on a Nanodrop.

The *ftsA**(FtsA_R286W) template was constructed using site-directed mutagenesis PCR on plasmid pUC57 *ftsA*_opt with primers 1279 ChD + 1280 ChD (Supplementary Table 1). PCR product was checked on a 1% agarose gel stained with SYBR safe, imaged with a ChemiDoc™ Imaging System (BioRad Laboratories), and purified with the Wizard SV Gel kit (Promega). The purified DNA was incubated with DpnI (New England BioLabs®, Inc.) to remove residual plasmid and the linear DNA was purified again with Wizard SV Gel kit. DNA concentration and purity were measured using a ND-1000 UV-Vis Spectrophotometer (Nanodrop Technologies). *E. coli* DH5α competent cells were transformed by heat shock. Cells were centrifuged, resuspended in 50 µL of fresh prechilled liquid lysogeny broth (LB) medium and incubated for 1 h at 37°C and 250 rpm. The cultures were plated on solid LB medium with ampicillin and grew overnight at 37°C. Plasmid purification was performed using the PureYield™ Plasmid Miniprep System (column method, Promega). Plasmid concentration and purity were checked on a Nanodrop. The DNA was sequence analyzed.

Linear templates for PURE system reactions were prepared by PCR using the plasmids as substrates with primers 709 ChD and 757 ChD (Supplementary Table 1). Amplification products were checked on a 1% agarose gel and were purified using the Wizard SV Gel kit. DNA concentration and purity were measured using a ND-1000 UV-Vis Spectrophotometer (Nanodrop Technologies). The sequences of the linearized constructs can be found in the Supplementary Methods.

Purified protein

Labeled purified FtsZ was prepared as previously described⁴⁹. More information are reported in the method section of chapter 3.

Cell-free gene expression

PURE^{frex}2.0 (GeneFrontier Corporation, Japan) was utilized following storing and handling instructions provided by the supplier. Linear DNA templates were used in gene expression assays (20 µL volume) at a final concentration of 5 nM, along with 1 µL of DnaK Mix (GeneFrontier Corporation) and SUPERase•In™ RNase Inhibitor (0.75 U/µL final, Invitrogen).

The reaction was also supplemented with 2 mM GTP, 2 mM ATP, 3 µM FtsZ-A647 and then used for lipid film swelling. Gene expression was performed at 37°C for a minimum of 3 hours unless differently specified.

Preparation of the imaging chambers

Home-made glass chambers were utilized as described in chapter 3 with no modifications.

Lipids

1,2-dioleoyl-sn-glycero-3-phosphocholine (DOPC), 1,2-dioleoyl-sn-glycero-3-phosphoglycerol (DOPG), and 1,2-distearoyl-sn-glycero-3-phosphoethanolamine-N-[biotinyl(polyethylene glycol)-2000 (DSPE-PEG-biotin), were from Avanti Polar Lipids. Texas Red 1,2-dihexadecanoyl-sn-glycero-3-phosphoethanolamine (DHPE-TexasRed) was from Invitrogen.

Production of lipid-coated beads

Glass beads were coated with the following lipids: DOPC (75 mol%), DOPG (25 mol%), DSPE-PEG-biotin (1 mass%) and DHPE-TexasRed (0.5 mass%) for a total mass of 5 mg, according to published protocol (Chapter 2 and 3). Lipids dissolved in chloroform were combined in a round-bottomed glass flask. Methanol containing 100 mM rhamnose (Sigma Aldrich) was added in a chloroform-to-methanol volume ratio of 2.5:1. 1.5 g of 212–300 µm glass beads (acid washed, Sigma Aldrich) were added to the lipid-rhamnose solution. Chloroform was depleted by rotary evaporation at 200 mbar for 2 hours at room temperature, and then overnight desiccation. The lipid-coated beads were kept under argon at –20 °C.

Production and immobilization of gene-expressing liposomes

A PURE^{frex}2.0 reaction mixture was assembled as described above. Either *ftsA*_{opt} or FtsA* DNA constructs were added at a final concentration of 5 nM. The 20 µL expression solution was supplemented with: 1 µL of DnaK Mix, and 0.75 U/µL SUPERase 2 mM GTP, 2 mM ATP, and a fresh batch FtsZ-A647 (of 3 µM). SUPERase was supplemented as a modification of the previous protocol and was shown to be helpful, as the quantity of liposomes with FtsA-FtsZ structures rose substantially. About 20 mg of lipid-coated beads was added to the solution and liposomes were formed by natural swelling of the lipid film for 45 min while tumbling at 4 °C in the cold room, protected from light. This was a protocol adjustment we included to optimize time management and lipid beads tumbling. Four freeze-thaw cycles were then applied by dipping the sample in liquid nitrogen and thawing on ice. The sample reservoir of the imaging chamber was functionalized as described in the method section of chapter 3. About 7 µL of the liposome solution was carefully pipetted (with a cut tip) into the imaging chamber and supplemented with RQ1 DNase (0.07 U µL⁻¹) to preclude gene expression outside

liposomes. For the assays of gene expression outside liposomes about 7 μ L of the liposome solution was carefully pipetted (with a cut tip) into the imaging chamber and supplemented the FtsA construct as well as 3 μ M FtsZ-A647. RQ1 DNase was omitted. In all the assays the chamber was sealed by sticking a 20 \times 20 mm coverslip with a double-sided adhesive silicone sheet. Expression was performed directly on the confocal microscope at 37 °C for 3–6 h. In the experiment assessing hypertonic conditions, 100 mM or 200 mM of sucrose were carefully pipetted in the imaging chamber after 3 h of gene expression.

Confocal microscopy

Liposomes were imaged using a Nikon A1R Laser scanning confocal microscope coupled with an SR Apo TIRF 100 oil immersion objective. To scan the membrane dye (Texas Red) and FtsZ-A647, the 561 nm and 640 nm laser lines were employed in conjunction with adequate emission filters. Imaging was performed utilizing the NIS (Nikon) program, with identical settings throughout all experiments. While acquiring the images, samples were kept at 37 °C in a temperature-controlled stage.

Image analysis

Fiji⁵⁰ was used for image analysis. A line was drawn to determine the apparent length of the necks and the liposomes diameters.

Statistics and reproducibility

All the experiments discussed in this report were replicated, and identical findings were achieved. Microscope images reported in the main text are representative images of the analyzed samples across at least three independent biological replicates.

References

- Schwille, P. Division in synthetic cells. *Emerg. Top. Life Sci.* **3**, 551–558 (2019).
- Kretschmer, S., Ganzinger, K. A., Franquelim, H. G. & Schwille, P. Synthetic cell division via membrane-transforming molecular assemblies. *BMC Biol.* **2019** *171* **17**, 1–10 (2019).
- Balasubramanian, M. K., Srinivasan, R., Huang, Y. & Ng, K. H. Comparing contractile apparatus-driven cytokinesis mechanisms across kingdoms. *Cytoskeleton* **69**, 942–956 (2012).
- Osawa, M., Anderson, D. E. & Erickson, H. P. Reconstitution of contractile FtsZ rings in liposomes. *Science*. **320**, 792–794 (2008).
- Osawa, M., Anderson, D. E. & Erickson, H. P. Curved FtsZ protofilaments generate bending forces on liposome membranes. *EMBO J.* **28**, 3476–84 (2009).
- Osawa, M. & Erickson, H. P. Liposome division by a simple bacterial division machinery. *Proc. Natl. Acad. Sci. U. S. A.* **110**, 11000–4 (2013).
- Cabré, E. J. *et al.* Bacterial division proteins FtsZ and ZipA induce vesicle shrinkage and cell membrane invagination. *J. Biol. Chem.* **288**, 26625–34 (2013).
- Szwedziak, P., Wang, Q., Bharat, T. A. M., Tsim, M. & Löwe, J. Architecture of the ring formed by the tubulin homologue FtsZ in bacterial cell division. *Elife* **3**, e04601 (2014).
- Furusato, T. *et al.* De novo synthesis of basal bacterial cell division proteins FtsZ, FtsA, and ZipA inside giant vesicles. *ACS Synth. Biol.* **7**, 953–961 (2018).
- Godino, E. *et al.* Cell-free biogenesis of bacterial division proto-rings that can constrict liposomes. *Commun. Biol.* **3**, (2020).
- Ramirez-Diaz, D. A. *et al.* FtsZ induces membrane deformations via torsional stress upon GTP hydrolysis. *Nat. Commun.* **2021** *121* **12**, 1–11 (2021).
- de Boer, P., Crossley, R. & Rothfield, L. The essential bacterial cell-division protein FtsZ is a GTPase. *Nature* **359**, 254–256 (1992).
- Mukherjee, A. & Lutkenhaus, J. Guanine nucleotide-dependent assembly of FtsZ into filaments. *J. Bacteriol.* **176**, 2754–8 (1994).
- Pichoff, S. & Lutkenhaus, J. Unique and overlapping roles for ZipA and FtsA in septal ring assembly in *Escherichia coli*. *EMBO J.* **21**, 685–93 (2002).
- Ramirez-Diaz, D. A. *et al.* Treadmilling analysis reveals new insights into dynamic FtsZ ring architecture. *PLOS Biol.* **16**, e2004845 (2018).
- Ganzinger, K. A. *et al.* FtsZ reorganization facilitates deformation of giant vesicles in microfluidic traps. *Angew. Chemie Int. Ed.* **59**, 21372–21376 (2020).
- Andersen, H. D., Wang, C., Arleth, L., Peters, G. H. & Westh, P. Reconciliation of opposing views on membrane–sugar interactions. *Proc. Natl. Acad. Sci. U. S. A.* **108**, 1874 (2011).
- Geissler, B., Elraheb, D. & Margolin, W. A gain-of-function mutation in *ftsA* bypasses the requirement for the essential cell division gene *zipA* in *Escherichia coli*. *Proc. Natl. Acad. Sci.* **100**, 4197–4202 (2003).
- G, L., BR, D., TM, D., D, W. & SX, S. Condensation of FtsZ filaments can drive bacterial cell division. *Proc. Natl. Acad. Sci. U. S. A.* **106**, 121–126 (2009).
- Erickson, H. P., Taylor, D. W., Taylor, K. A. & Bramhill, D. Bacterial cell division protein FtsZ assembles into protofilament sheets and minirings, structural homologs of tubulin polymers. *Proc. Natl. Acad. Sci. U. S. A.* **93**, 519–523 (1996).
- Lu, C., Reedy, M. & Erickson, H. P. Straight and curved conformations of FtsZ are regulated by GTP hydrolysis. *J. Bacteriol.* **182**, 164–170 (2000).
- Coltharp, C., Buss, J., Plumer, T. M. & Xiao, J. Defining the rate-limiting processes of bacterial cytokinesis. *Proc. Natl. Acad. Sci.* **113**, E1044–E1053 (2016).
- Deng, Y., Sun, M. & Shaevitz, J. W. Direct measurement of cell wall stress stiffening and turgor pressure in live bacterial cells. *Phys. Rev. Lett.* **107**, 158101 (2011).
- Xiao, J. & Goley, E. D. Redefining the roles of the FtsZ-ring in bacterial cytokinesis. *Curr. Opin. Microbiol.* **34**, 90 (2016).
- Osawa, M. & Erickson, H. P. Turgor pressure and possible constriction mechanisms in bacterial division. *Front. Microbiol.* **0**, 111 (2018).

26. HP, E. How bacterial cell division might cheat turgor pressure - a unified mechanism of septal division in Gram-positive and Gram-negative bacteria. *Bioessays* **39**, (2017).

27. Litschel, T., Ramm, B., Maas, R., Heymann, M. & Schwille, P. Beating vesicles: encapsulated protein oscillations cause dynamic membrane deformations. *Angew. Chemie Int. Ed.* **57**, 16286–16290 (2018).

28. Godino, E. *et al.* De novo synthesized Min proteins drive oscillatory liposome deformation and regulate FtsA-FtsZ cytoskeletal patterns. *Nat. Commun.* **10**, 4969 (2019).

29. Döbereiner, H. G., Käs, J., Noppl, D., Sprenger, I. & Sackmann, E. Budding and fission of vesicles. *Biophys. J.* **65**, 1396–403 (1993).

30. Den Blaauwen, T., de Pedro, M. A., Nguyen-Distèche, M. & Ayala, J. A. Morphogenesis of rod-shaped sacculi. *FEMS Microbiol. Rev.* **32**, 321–344 (2008).

31. Szwedziak, P. & Löwe, J. Do the divisome and elongasome share a common evolutionary past? *Curr. Opin. Microbiol.* **16**, 745–751 (2013).

32. Ploeg, R. van der *et al.* Colocalization and interaction between elongasome and divisome during a preparative cell division phase in *Escherichia coli*. *Mol. Microbiol.* **87**, 1074–1087 (2013).

33. Chapman, D. Phase transitions and fluidity characteristics of lipids and cell membranes. *Q. Rev. Biophys.* **8**, 185–235 (1975).

34. Jimbo, T., Sakuma, Y., Urakami, N., Zihlerl, P. & Imai, M. Role of inverse-cone-shape lipids in temperature-controlled self-reproduction of binary vesicles. *Biophys. J.* **110**, 1551 (2016).

35. Dimova, R. *et al.* Giant vesicles in electric fields. *Soft Matter* **3**,817 (2007)

36. Salipante, P. F. & Vlahovska, P. M. Vesicle deformation in DC electric pulses. *Soft Matter* **10**, 3386–3393 (2014).

37. Kattan, J., Doerr, A., Dogterom, M. & Danelon, C. Shaping liposomes by cell-free expressed bacterial microtubules. *ACS Synth. Biol.* **10** (2021),

38. Scott, A. *et al.* Cell-free phospholipid biosynthesis by gene-encoded enzymes reconstituted in liposomes. *PLoS One* **11**, e0163058 (2016).

39. Blanken, D., Foschepoth, D., Serrão, A. C. & Danelon, C. Genetically controlled membrane synthesis in liposomes. *Nat. Commun.* **11**, (2020).

40. Rasi, S., Mavelli, F. & Luisi, P. L. Matrix effect in oleate micelles-vesicles transformation. *Orig. life Evol. Biosph.* **2004** *341* **34**, 215–224 (2004).

41. MM, H., SM, F. & JW, S. Experimental models of primitive cellular compartments: encapsulation, growth, and division. *Science*. **302**, 618–622 (2003).

42. PMG, L. *et al.* A DNA-programmed liposome fusion cascade. *Angew. Chem. Int. Ed. Engl.* **56**, 13228–13231 (2017).

43. Traïkia, M., Warschawski, D. E., Lambert, O., Rigaud, J. L. & Devaux, P. F. Asymmetrical Membranes and Surface Tension. *Biophys. J.* **83**, 1443–1454 (2002).

44. Tomoki Tanaka, Ryoko Sano, Yuko Yamashita, and & Masahito Yamazaki. Shape changes and vesicle fission of giant unilamellar vesicles of liquid-ordered phase membrane induced by lysophosphatidylcholine. *Langmuir* **20**, 9526–9534 (2004).

45. and, Y. I. & Masahito Yamazaki. Vesicle fission of giant unilamellar vesicles of liquid-ordered-phase membranes induced by amphiphiles with a single long hydrocarbon chain. *Langmuir* **23**, 720–728 (2006).

46. Andes-Koback, M. & Keating, C. D. Complete budding and asymmetric division of primitive model cells to produce daughter vesicles with different interior and membrane compositions. *J. Am. Chem. Soc.* **133**, 9545–9555 (2011).

47. Dreher, Y., Jahnke, K., Schröter, M. & Göpfrich, K. Light-triggered cargo loading and division of dna-containing giant unilamellar lipid vesicles. *Nano Lett.* **21**, 5952–5957 (2021).

48. Hentrich, C. & Szostak, J. W. Controlled growth of filamentous fatty acid vesicles under flow. *Langmuir* **30**, 14916 (2014).

49. González, J. M. *et al.* Essential cell division protein FtsZ assembles into one monomer-thick ribbons under conditions resembling the crowded intracellular environment. *J. Biol. Chem.* **278**, 37664–71 (2003).

50. Rueden, C. T. *et al.* ImageJ2: ImageJ for the next generation of scientific image data. *BMC Bioinformatics* (2017) doi:10.1186/s12859-017-1934-z.

Supplementary Information

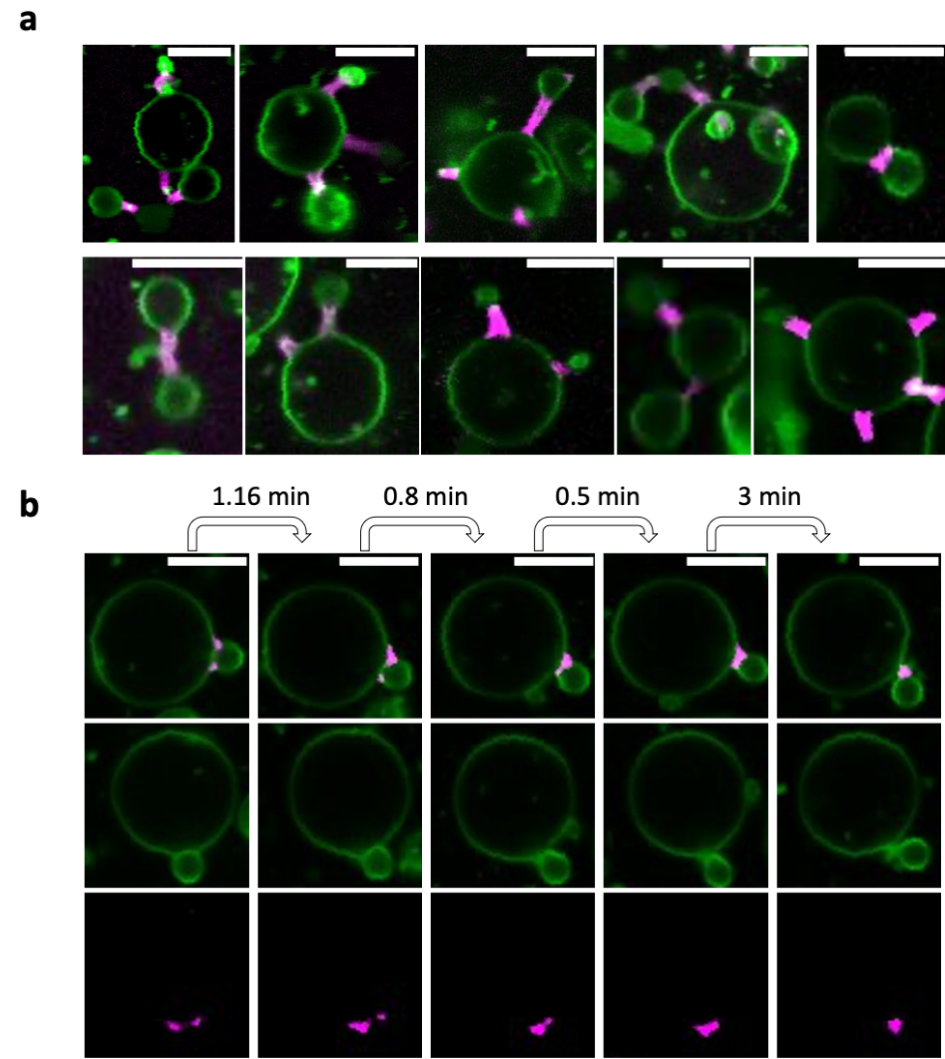
DNA sequence of the *ftsA*^{*} construct

TAATACGACTCACTATAGGGGAATTGTGAGCGGATAACAATTCCCCTCTAGAAATAATTTTGTTTAACTTTAAGAAG-GAGATATACATATGATCAAGGCGACCGACCGTAAGCTGGTTGTGGGCCTGGAGATTGGCACCGCGAAGGTTGCGG-CGCTGGTTGGCGAGGTTCTGCGCGATGGTATGGTTAACATTATCGGCGTTGGTAGCTGCCCGAGCCGTGGCATGGA-CAAAGGTGGTGTGAACGACCTGGAAGCGTGGTTAAGTGCCTGCAGCTGCGATTGACCAGGCGGAGCTGATGGCG-GACTGCCAAATCAGCAGCGTTTACCTGGCGCTGAGCGGCAAGCACATCAGCTGCCAAAACGAGATTGGTATGGTGC-CGATTAGCGAAGAGGAAGTTACCCAGGAAGATGTGGAGAACGTGGTTCACACCGCGAAAAGCGTTCGTGTGCGTGAT-GAACACCGTGTGCTGCACGTTATCCCAGCAAGAATACGCGATCGATTACCAGGAAGGTATCAAAAACCGGTTGGTCT-GAGCGGTGTTTCGTATGCAGGCGAAAAGTGCACCTGATTACCTGCCACAACGATATGGCGAAGAACATTGTGAAAGCG-GTTGAACGTTGCGGTCTGAAGGTTGACCAGCTGATCTTCGCGGGTCTGGCGAGCAGCTACAGCGTTCTGACCGAA-GATGAGCGTGAACGTTGGTGTTCGCTGTGGATATCGGCGGTGGCACGATGGATATCGCGGTGTATACCGGTGGCG-CGCTGCGTCACACCAAAGTGATTCCGTATCGGGTAACGTGGTTACCAGCGACATCGCGTACGCGTTTGGCACCCCGC-CGAGCGATGCGGAGGCGATCAAAGTGCCTCACGGTTGCGCGCTGGGTAGCATTGTGGGTAAAGATGAGAGCGTG-GAAGTTCGAGCGTTGGTGGCCGTCGCCCGCTAGCCTGCAACGTGAGACCGTGGCGGAAGTTATCGAGCCGCGT-TACACCGAACTGCTGAACCTGGTGAACGAAGAGATCCTGCAACTGCAAGAGAACTGCGTCAGCAAGGTGTTAAG-CACCACCTGGCGGCGGGCATTGTTCTGACCGGCGGTGCGGCGCAGATCGAAGTCTGGCGCGCTGCGCGCAACGT-GTTTTCCACACCCAAGTTCGTATCGGTGCGCCGCTGAACATCACCGGTCTGACCGATTACGCGCAAGAGCCGTACTAT-AGCACCGCGGTTGGTCTGCTGCACCTATGGCAAAGAGAGCCACCTGAACGGCGAGGCGGAAGTGGAGAAGCGTGT-GACCGCGAGCGTTGGTAGCTGGATTAAGCGTCTGAATAGCTGGCTGCGTAAGGAGTTCTAAGGATCCGGCTGCTAA-CAAAGCCGAAAGGAAGCTGAGTTGGCTGCTGCCACCGCTGAGCAATAACTAGCATAACCCCTTGGGGCCTCTAAACG-GGCTTTGAGGGGTTTTTTG

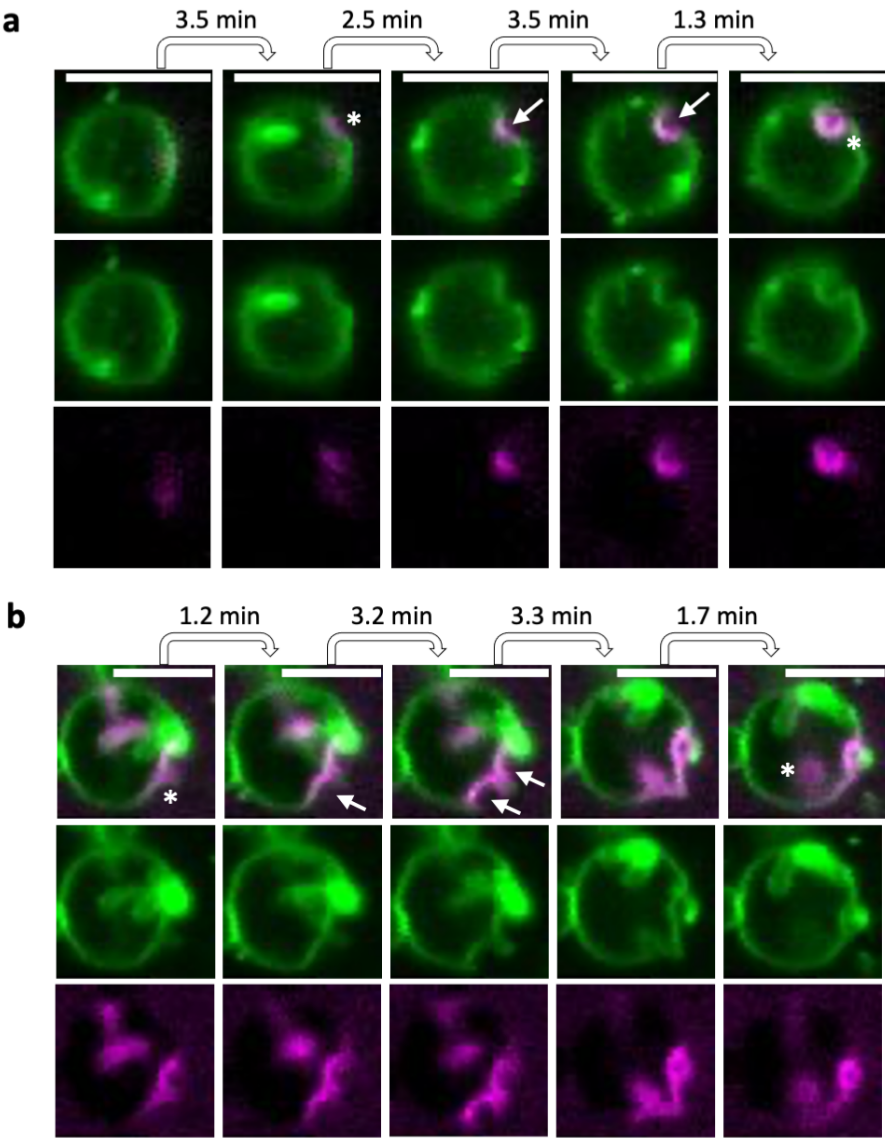
Table S1. List of primers used in this study.

Name	Sequence (5' 3')	Comment
709 ChD	CAAAAAACCCCTCAAGACCCGTTTAGAGG	Anneals to T7 terminator
757 ChD	TAATACGACTCACTATAGGG	Anneals to T7 promoter
1279 ChD	CCGTGGAGCCTGCAACGTCAGACCCTGG	FW mutagenesis primer ftsA_R286W
1280 ChD	AGGCTCCACGGCGACGGCCACCAACGCTC	RV mutagenesis primer ftsA_R286W

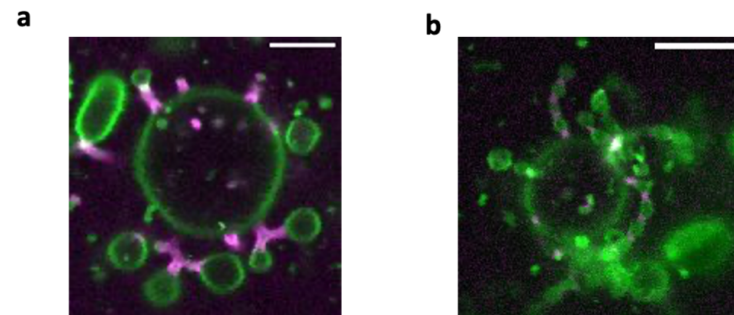
Supplementary figures



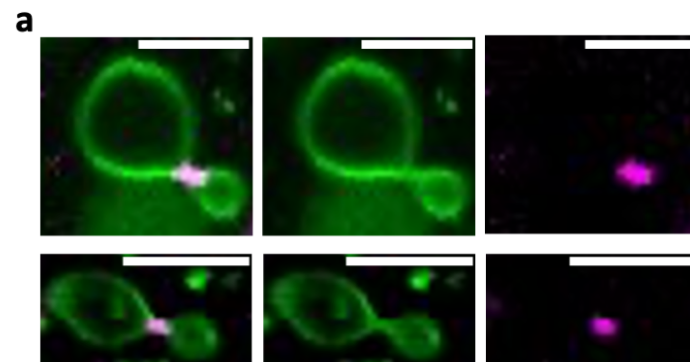
Supplementary Fig. 1: a, Confocal fluorescence images of liposomes exhibiting different morphologies of membrane necks and budding vesicles driven by FtsA-FtsZ. The *ftsA* DNA template was expressed within phospholipid vesicles in the presence of 3 μ M purified FtsZ-A647. The length of the necks can vary, multiple necks with attached vesicles may form from one single parental liposome, and multiple buds can be connected via branching. **b,** Time series of confocal fluorescence images showing a liposome in which opposing membrane regions fuse as a result of the condensation of FtsZ polymers. The time interval between consecutive images is indicated. The membrane dye is in green and FtsZ-A647 is in magenta. The composite image is the overlay of the two channels. Scale bars 5 μ m.



Supplementary Fig. 2: a,b, Time-lapse fluorescence images of two independent liposomes showing FtsZ clusters recruited on the outside of the liposome drilling into the liposome membrane. The time interval between consecutive images is indicated. The membrane dye is in green and FtsZ-A647 is in magenta. The composite image is the overlay of the two channels. Scale bars 5 μ m.



Supplementary Fig. 3: **a**, Confocal fluorescence image of a liposome exhibiting an increase in the number of FtsZ-driven membrane necks and buds upon addition of 100 mM sucrose. **b**, Confocal fluorescence image of a liposome with numerous elongated membrane protrusions and several constriction sites. External sucrose concentration was 200 mM. The sample quality was compromised. The images are overlay of the membrane dye (green) and FtsZ-A647 (magenta) channels. Scale bars 5 μ m.



Supplementary Fig. 4: Confocal fluorescence images of two liposomes where the *ftsA** DNA construct was expressed in the presence of 3 μ M purified FtsZ-A647. The liposomes show large vesicles (relative to the size observed in most liposomes) tethered to the parental liposome through a membrane neck, resembling the canonical phenotype with FtsA. The membrane dye is in green and FtsZ-A647 is in magenta. The composite image is the overlay of the two channels. Scale bars 5 μ m.

Imaging flow cytometry for high-throughput phenotypic characterization of synthetic cells

Elisa Godino, Ana Restrepo Sierra, Christophe Danelon

Liposomes have sparked a widespread interest in different research fields, such as synthetic biology, membrane biophysics, and pharmaceutical applications. For instance, the encapsulation of purified proteins or of a minimal gene expression machinery within liposomes has provided a scaffold to build synthetic cells from the bottom-up. Gathering quantitative data about the 'phenotypes' of liposomes, such as protein organization, membrane localization, and vesicle morphology, is important to assess the reconstitution efficiency and compare different liposome production methods. Yet, this practically represents a challenging task because the traditional methods, flow cytometry and fluorescence microscopy, suffer from either one-dimension features or low-throughput, respectively. Herein, we introduce imaging flow cytometry (IFC) as a high-throughput liposome screening technology that integrates the benefits of fluorescence imaging and flow cytometry. Imaging flow cytometry offers multicolor image data for every recorded event, enabling a deeper morpho-biochemical analysis of individual liposomes within a diverse population. Moreover, the collected images can be subjected to multi-parameter analyses to yield a set of quantitative features that best describe the liposomes' properties. In this study, we examined several cell-like behaviors in large populations of gene-expressing liposomes. We established IFC as a new synthetic biology tool for high-content imaging of heterogeneous populations of liposomes harboring complex features relying on proteins and nucleic acids. The ability to acquire large datasets is matched by an urgent need for the analysis of heterogeneous liposome mixtures. We believe that IFC can accelerate both fundamental and applied liposome research.

Introduction

Liposomes are valuable membrane model systems to study a wide range of cellular mechanisms^{1,2}. These lipid vesicles, constituted by an adaptable lipid bilayer, sparked considerable attention by closely resembling the cell membrane, while being highly biocompatible, robust, non-immunogenic, and simple to manufacture^{1,3}. Liposomes are classified by their size as small unilamellar vesicles (SUVs, diameter ranging from 0.02 μm to 0.1 μm), large unilamellar vesicles (LUVs, from 0.1 μm to 1 μm), and giant unilamellar vesicles (GUVs, with a diameter $>1 \mu\text{m}$)⁴. Liposomes have found a broad range of applications as nanoreactors⁵, drug delivery vehicles^{6,7}, diagnostic instruments^{6,8}, food matrices⁹, biosensors¹⁰, and fundamental research tools^{11,12}. Thanks to their multiple properties, GUVs have also emerged as synthetic cell membrane models^{13,14}.

As the characteristics of the liposome populations can vary substantially depending on employed lipids and production techniques, measuring GUVs qualities and morphological features in a consistent manner is critical. Moreover, having robust technologies and data analysis pipelines to better analyze in-liposome biochemistry and membrane processes is a must. A combination of methodologies is frequently required to obtain statistically relevant and information-rich datasets. Fluorescence microscopy is a powerful technique for studying phenotypic traits within GUVs at high spatial and temporal resolution. However, due to the limited throughput of image acquisition, it is currently difficult to convert microscopy-collected information into a large dataset that can accurately represent a population^{15,16}. For instance, in a typical imaging chamber, only a few thousands of gene expressing liposomes may be observed¹⁷. Attempts have been made to circumvent the low throughput limits of microscopy. One example is the implementation of microarray-based assays that combine microfluidics and fluorescence microscopy^{18,19}. However, the use of these tools is still restricted by the liposome generation technique, liposome sizes, the necessity of immobilizing liposomes, the limited case scenarios that can be explored, and the difficulties associated with analyzing large collections of liposome images. The latter is a recurring issue in microscopy. Despite the use of image-processing programs and ad hoc statistical algorithms, acquired images cannot be easily translated into quantitative data, resulting in a difficult, time-consuming, and possibly subjective data interpretation¹⁶.

Flow cytometry has proven to be an excellent approach for high-throughput GUVs analysis. This technology can utilize liposome suspension as an input to collect light scattering and fluorescence data from each individual liposome^{20,21}. Flow cytometry has been used to analyze a wide range of GUVs structural and dynamical properties. These include: size and lamellarity^{22–24}, protein-membrane interaction²⁵, gene expression¹⁷, and a variety of other phenotypes that can be described by the presence, absence, or change of a fluorescence signal. Nonetheless, flow cytometry still relies on a one-dimensional fluorescence signal, which severely limits the spectrum of properties that can be investigated (protein localization, in-

liposome protein interactions, among others)^{20,21}. Therefore, a methodology that can gather accurate morphological and functional information from single vesicles at high speed from large populations is needed.

Imaging flow cytometry (IFC) is a technology that combines the advantages of fluorescence microscopy with the high-throughput capabilities of flow cytometry²⁶ (Fig. 1a). The capacity to use a vesicle suspension as sample, plus the possibility to capture separate images for each single detected object are two of the great benefits of IFC over fluorescence microscopy. Moreover, when compared to flow cytometry, IFC identifies the collected objects by their real images and allows multidimensional image-based identification of more complex phenotypes. Finally, the ability to store data in the form of images lowers the risk of errors like recording false positive events. ImageStream, a commercially available IFC, comes with a dedicated image processing software called IDEAS that has an easy-to-use interface to recognize, count, and run statistical analyses on thousands of events. The program provides visual validation of any individual image. This is a powerful tool for having an instant idea of the chosen analysis pipeline(s) such that any adjustments can be done promptly. Imaging flow cytometry has quickly gained popularity in a variety of cell biology-related disciplines involving the identification and quantification of rare cellular phenotypes within heterogeneous populations²⁷. Imaging flow cytometry has for example been used to examine apoptosis depending on alteration of nuclear morphology and structure^{28,29}, cell cycle progression according to chromatin condensation^{30,31}, protein and molecule translocation and/or co-localization in different cellular compartments^{32–34}, and cytoskeleton structures³⁵. As analogous phenomena must be investigated while building liposome-based synthetic cells, we believe that IFC has great potential to overcome the existing bottlenecks in studying large populations of cell-like GUVs, in particular of gene-expressing vesicles^{36–40}.

In this work we used the commercial ImageStream to investigate different cell-like phenotypes from thousands of gene-expressing liposomes. Particularly, we decided to characterize essential biological modules, largely investigated by the synthetic cell community^{41–43}. These included transcription-translation^{17,44–46}, DNA self-replication^{38,47}, de novo cytoskeleton formation^{48–50} and membrane binding of bacterial division proteins³⁹ (Fig. 1b). We report the optimal conditions for collecting and analyzing these complex liposome datasets and demonstrate that IFC can efficiently be used to interrogate GUVs displaying a variety of phenotypes at high throughput. Furthermore, we provide a comprehensive description of our image analysis pipelines with IDEAS. This includes liposome identification, selection of unilamellar vesicles, and characterization of membrane and intraluminal properties. These analysis templates can be applied for the assessment of any other liposome population generated with different methodologies and exhibiting diverse phenotypes.

We believe that IFC can pave the road for synthetic cell research. Moreover, applying IFC for liposome screening will also allow us to assess liposome quality and provide an accurate,

statistically relevant, comparison between different liposome production techniques. This could be useful not only for fundamental research but also for a wide range of liposome-based therapeutics within the pharmaceutical and biomedical fields.

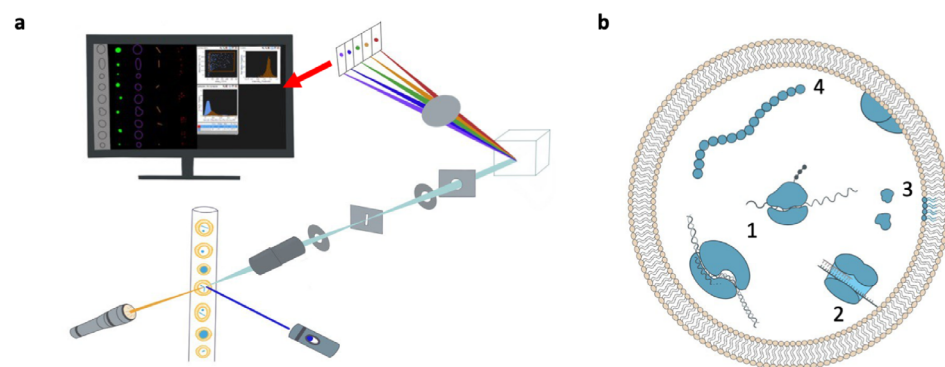


Figure 1: Introducing IFC to characterize gene expressing synthetic cells. **a**, Schematic representation of the primary components of the ImageStream. Giant vesicles are hydrodynamically focused into a core stream and orthogonally illuminated. The fluorescent, transmitted, and scattered light emitted by the liposomes is captured by the imaging objective and separated into multi-spectral bands via the optical decomposition components. Light is finally projected on a charge-coupled detector (CCD). While recording, digital pictures are displayed on the computer and stored for analysis. Adapted from²⁸. **b**, Illustration of a liposome-based synthetic cell displaying relevant biological processes. The PURE (Protein Synthesis Using Recombinant Elements) system and DNA are encapsulated into phospholipid vesicles to re-construct cellular functions, such as transcription-translation (1), DNA replication (2), phospholipid biosynthesis (3), and the formation of cytoskeletal structures (4).

Results

Data analysis and liposome identification

For each sample, we collected around a million events, which we examined in batch mode by opening 100'000 recorded items at a time. The raw file not only contained liposomes, but also excessively small vesicles, aggregates of all sizes and shapes, lipid debris, and left-over speed beads (beads employed to monitor sample flow and ensure focus and core tracking). Therefore, the first stage in the analysis should be finding a gating strategy that would include all relevant giant liposomes and exclude any other objects. To achieve this, we started by determining an appropriate mask, i.e. the area of an image that will be used for further processing. Although the software includes pre-loaded masks, it is possible to create a customized mask by adjusting the channel and scalar values to better determine the section of the image that will be used for each feature computation. As we are interested in investigating each liposome as a whole, we

decided to re-adjust the default IDEAS mask to better encompass both lumen and membrane (Fig. 2a). A multistep approach was used to identify liposomes, by discarding all non-focus events and non-liposome objects. The first step comprised a comparative analysis over the *area* and *aspect ratio* features (Fig. 2b). As the pixels are rendered into square micrometers (μm^2), the *area* is given as the microns squared within the utilized mask. We determined that any object having a surface area less than $40 \mu\text{m}^2$ is too small to be detected with sufficient resolution. The *aspect ratio* corresponds to the ratio between the minor axis and the major axis of each object and specifies how round an item is. The *aspect ratio* of circular objects equals 1 while oblong structures have significantly lower values. Thus, all objects with an aspect ratio of less than 0.4 were excluded (Fig. 2c). To further optimize the selection of liposomes only, we devised an additional three-step screening method and a selection for in-focus events. Extra steps can be added to the liposome identification pipeline when needed, depending on the liposome quality and/or the study requirements. The initial step in the screening process was to compare the *intensity* of the membrane signal vs the *area* of the mask (Fig. 2d). Debris and left over out-of-focus objects were deleted as events with small areas and low intensity. Objects with small *area* and high membrane *intensity* were discarded as aggregates. Then, we used the *gradient RMS* feature to only select in-focus liposomes (Fig. 2e). The *gradient RMS* feature assesses the sharpness of an image by identifying large variations in pixel values. We determined that all events with a *gradient RMS* less than 18 were out-of-focus (Fig. 2e,f). The second step included a selection for higher *H-homogeneity* values (Fig. 2g), followed by a third step based on the *H-Correlation mean* and *standard deviation* (Fig. 2h). These *H features* establish a set of texture features that describe the spatial relationships between the pixel values within the mask. Low *H-homogeneity*, as well as an elevated *H-Correlation mean* value combined with a low standard deviation, pointed to aggregates. An alternative option to identify liposomes in the absence of a membrane signal is to use the brightfield channel and to apply an analysis pipeline similar to the one described above (Supplementary Fig. 1). However, it is important to mention that when using the brightfield channel it is more difficult to distinguish similar structures; to be more precise, a stricter gating needs to be applied with the drawback that some 'good' liposomes may be discarded. Ideally, the gating via the brightfield channel can be facilitated if the liposomes contain a fluorescent signal within their lumen.

We confirmed the accuracy of our liposome-selection pipeline by visually inspecting individual events of the final population. Note that visual inspection was carried out consistently throughout the analysis for choosing the best screening features as well as to confirm each of the resulting populations at every step of the analysis. We concluded that with our proposed data analysis strategy, a clean liposome population has been carefully identified (Fig. 2i). The detected liposomes can now be subjected to more advanced morphological and/or biochemical analyses.

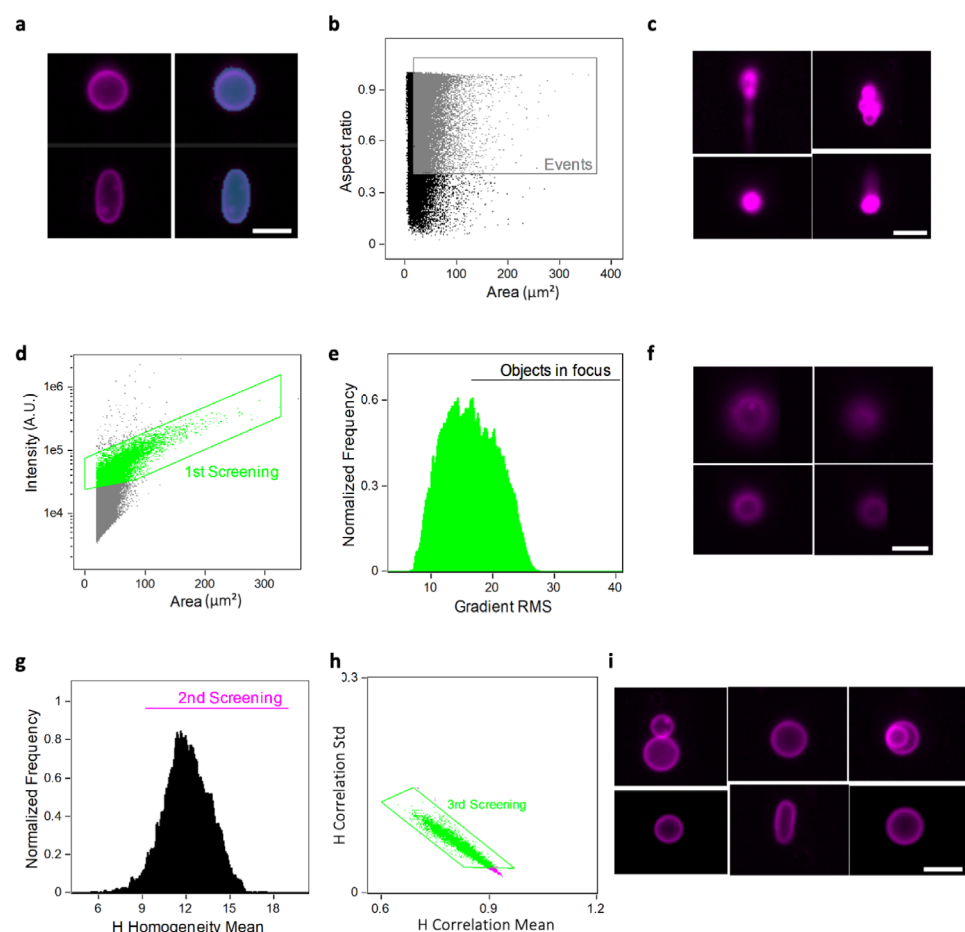


Figure 2: Sequential pipeline for liposome gating with IFC. The displayed images are representative for the whole sample. Scatterplots are from 100'000 recorded items, as we analyzed 1 million events by opening them in sequential batch mode. **a**, Images captured with ImageStream showing two liposomes (left) with their respective mask (right). The mask specifies the area to be used during the analysis and it was customized to select for the whole liposome. **b**, Comparative analysis over the *area* and *aspect ratio* features. Object having a surface area higher than $40 \mu\text{m}^2$ and an aspect ratio higher than 0.4 were gated as relevant events (Gated in grey). **c**, Images of some aggregates with different sizes and shapes that we eliminated via this first analysis step. **d**, 1/3 step to optimize the selection of a population consisting exclusively of liposome. Comparison of the *intensity* of the membrane signal vs the *area* of the mask (Gated in green). **e**, Selection for in-focus events, based on the *gradient RMS* feature. The events having a *gradient RMS* higher than 18 were selected as in focus and kept into the analysis. **f**, Images captured with ImageStream showing potential liposomes excluded from the analysis because they were classified as out-of-focus. **g**, 2/3 step to optimize the selection of a population consisting exclusively of liposome. Selection for higher *H-homogeneity* values (Gated in magenta). **h**, 3/3 step to optimize the selection of a population consisting exclusively of liposome. Comparative analysis of the *H-Correlation mean* and *standard deviation*. The selected objects (Gated in green) correspond to the final liposome population,

which is clean from all undesired events. **i**, Images of some of the liposomes within the final gate. Liposomes have different morphologies. For all the images, the magenta color represents the membrane signal. Scale bar is $7 \mu\text{m}$.

Determination of morphological features

Investigating liposome morphological features, such as size, shape, lamellarity and homogeneity is essential for understanding the inner working processes and quantifying the differences between GUVs' production protocols¹⁶. The functionality of encapsulated material can also be strongly influenced by the liposome morphology, and vice versa.

PURE system-containing liposomes made by the natural swelling process are polydisperse¹⁷. They are also not limited to a spherical shape. Microscopy has revealed elongated liposomes, aggregates of numerous vesicles, and multilamellar morphologies. We decided to examine liposome properties produced with this method, while also providing a generic template for analyzing the morphological features of liposomes generated using different approaches.

By displaying the *diameter* distribution, we found that, despite some clear heterogeneity, the majority of the liposomes (91%) had a *diameter* smaller than $10 \mu\text{m}$ (Fig.3a). We then looked at the liposome morphology. For this, we examined the *circularity* feature to quantify any deviation from a spherical form (Fig. 3b,c). The *circularity* feature determines how much the analyzed mask deviates from a circle. It is calculated by dividing the average distance between the object's edge and its center by the variance of such a distance. As a result, the more an object is circular, the smaller the variance and thus the higher the circularity value.

Intravesicular membrane features such as multi-layered and inner vesicles should also be identified. To determine multilamellar and multivesicular liposomes within the spherical liposome population we used the IDEAS tool called "*feature finder wizard*". The tool assists the user in identifying the optimal feature that best describe a particular phenotypic trait. To employ the *wizard*, one needs to select individual event images for each of the phenotypes of interest to gather a dataset of at least 25 images. With the fed datasets, the software then suggests the best features to better differentiate between the populations. We selected two populations of liposome with the morphological trait to be separated, namely unilamellar vs multilamellar, and performed the automated analysis. The end result was a graph that compared *compactness* and *Max Pixel* features (Fig. 3d,e,f). *Compactness* measures the degree to which an object is packed together. The higher the value, the more condensed the object. The *Max Pixel* feature is the largest value obtained from the background subtracted pixels from the input mask.

Finally, we sought to investigate the non-spherical liposomes. These events can be classified in rod-shaped (Fig. 3g) and doublets (two liposomes attached together) (Fig. 3h). For identifying each population, we utilized the *feature finder wizard*. The outcome of the analysis was a scatter plot between the texture features: *H-entropy std* and *H-correlation std* (Fig. 3i). As useful as this *wizard* analysis was in distinguishing between the two populations, we would like to

point out that it is not entirely precise. In fact, when using such feature, we identified both false positives and false negatives while many liposomes were left unclassified. We believe that the power of machine learning, as supplied by an upgraded version of the IDEAS program, could be an added benefit in these instances. With the current strategies, we managed to find that 45% of the 62'408 liposomes examined were spherical, with 42% being multilamellar or multivesicular (Fig. 3j). The 55% of non-spherical liposomes can be split into 15% elongated and 69% doublets (Fig. 3k).

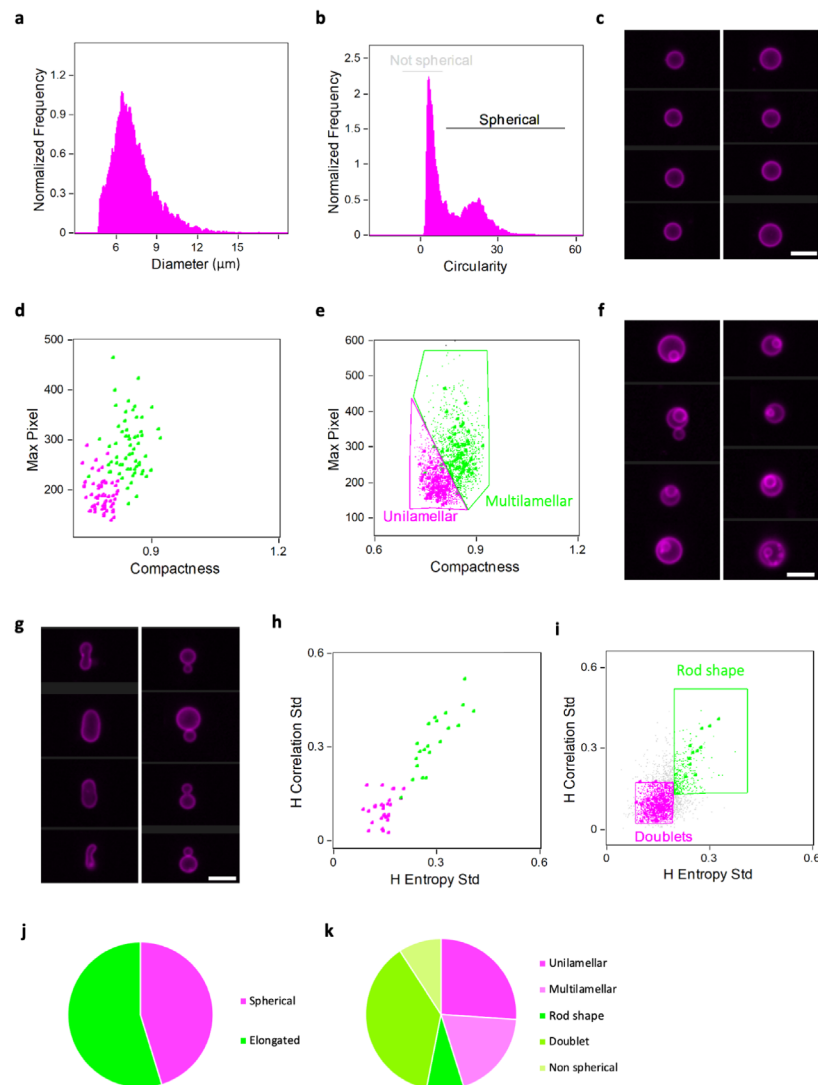


Figure 3: Characterization of liposome morphological features. **a**, Liposome size distribution was determined using the *diameter* feature. **b**, Shape was examined via the *circularity* feature. Objects with

high circularity value were gated as spherical liposomes (Gated in black). **c**, Images of liposomes from the gated population of spherical objects. **d**, Output from the *feature finder wizard* tool performed to distinguish liposomes having intravesicular membrane features. Comparison of the *compactness* and *circularity* features. **e**, Graph reporting the analysis (*compactness* vs *circularity*) performed on all the data point of the spherical population. Multilamellar/multivesicular liposome are gated in green and unilamellar in magenta. **f**, Representative images of the gated multilamellar/multivesicular liposomes. **g**, Images showing two different phenotypes present in the non-spherical liposomes gated in (b) (grey). On the left what we identify as rod-shaped liposome; on the right the doublets which correspond to two liposomes attached together. **h**, Output from the *feature finder wizard* tool performed for identifying the two non-spherical populations illustrated in (g). The *wizard* tool resulted in a comparison of *H entropy std* and *H correlation std*. **i**, Graph reporting the analysis (*H entropy std* and *H correlation std*) applied to the whole non-spherical liposome population. Rod-shaped liposomes are gated in green, doublets in magenta. **j,k**, graphical representation of the statistics obtained from morphological analysis performed on a set of over 70'000 liposomes from one independent sample. For all the images, the magenta color represents the membrane signal. Scale bar is 7 μm.

Identification biological processes within liposomes

So far, we have seen the power of IFC in acquiring images and identifying liposomes, as well as in extracting structural and morphological properties. Next, we applied these analytical capabilities to investigate a suite of biological mechanisms occurring within the lumen, at the membrane, or both. In all cases, the processes were directed by DNA and gene expression was supported by the PURE system^{51,52}, an in vitro transcription-translation technology well suited for the construction of a synthetic cell.

YFP expression as a transcription-translation readout

For analyzing a simple one-gene expression phenotype, we prepared liposomes containing PURE_{frex2.0} and a linear DNA construct encoding the fluorescent reporter protein YFP¹⁷. The expression of YFP was promoted by incubating the liposome suspension for 16 hours at 37 °C. The sample was then run into the ImageStream. The membrane signal was used to identify liposomes using the analysis pipeline explained before, and the YFP fluorescence was used as the gene-expressing phenotypic read-out. To identify the liposomes expressing YFP, we first generated a fitting mask and then plotted the *intensity* associated to the 488-nm channel (Fig. 4a). After applying an intensity threshold above which liposomes were classified as expressing, we discovered that approximately 60% of liposomes showed YFP expression. By plotting the *area* of the liposomes (measured in the membrane channel as previously explained) and the *intensity* of the YFP, we found substantial liposome-to-liposome heterogeneity with no clear relationship between YFP expression and liposome size (Fig. 4b). Liposomes of similar sizes exhibit YFP intensity that may vary a lot. Compositional heterogeneity in terms of the number of encapsulated DNA molecules and PURE system components may explain differences in the levels of gene expression. We then compared the sizes of the expressing and non-expressing liposomes (Fig. 4c) and found no significant difference between the two populations.

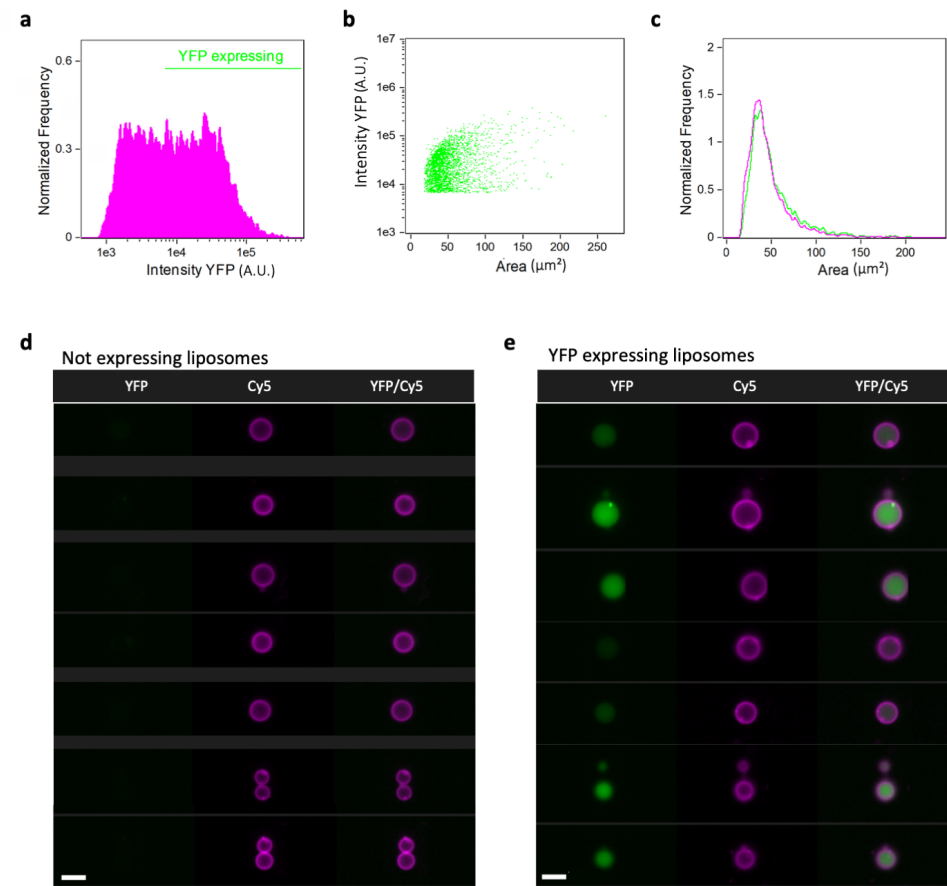


Figure 4: Gating of YFP-expressing liposomes. **a**, Liposomes which expressed YFP were gated via *intensity* feature calculated in the YFP channel (Gated in green). **b**, Scatter plot of the liposomes *area* vs the *intensity* of the YFP. No correlation between YFP expression and liposome size is observed. **c**, Comparison of the liposome size distribution between YFP expressing liposomes (green) and non-expressing liposomes (magenta). **d,e** Representative images of the non-expressing liposomes (**d**) and the YFP expressing liposomes (**e**). For all the images, liposome membrane is in magenta, while YFP is in green. Scale bar is 7 μm . The analysis was performed on a set of over 70'000 liposomes from one biological sample.

In-liposome transcription-translation and replication

We also exploited the ImageStream to investigate IVTTR (in-vitro transcription-translation and replication) inside liposomes³⁸. A linear ori-flanked DNA fragment, encoding for the essential Phi29 replication proteins DNAP and TP, was encapsulated into liposomes, together with the replication auxiliary proteins P5 and P6³⁸. The expressed DNAP and TP can replicate their own template, leading to an increased DNA concentration inside the liposomes, which can be spotted using a DNA intercalating dye³⁸ such as dsGreen. In-liposome DNA replication yields three main phenotypic traits: (1) empty liposomes that do not contain enough DNA to result in dsGreen signal (Fig. 5d), (2) liposomes that are homogeneously filled with dsGreen signal in the lumen (Fig. 5e), and (3) liposomes in which the dsGreen accumulates in the form of an internal bright spot (replication blob) (Fig. 5f). Phenotypes (2) and (3) are indicative of successful DNA amplification.

For investigating the presence of all three phenotypes, we prepared a DNA-replication liposome suspension as reported in the methods section and ran it into the ImageStream. To identify the liposome population with a successful DNA amplification, we first computed the dsGreen *intensity* of each of the collected liposome events (Fig. 5a). After applying a background intensity threshold, we found that 36% of liposomes were active for DNA replication. Then, for distinguishing phenotypes (2) and (3), we screened several IDEAS features and found that *std Dev* and *H-Homogeneity mean* offered the best combination to discriminate the phenotypes with high accuracy (Fig. 5b). In more detail, the *Std Dev* feature describes the general distribution of pixel intensities by computing the standard deviation of the pixel intensity values in the defined mask. A greater *Std Dev* value implies that the object being analysed has a higher texture. Liposome with high *Std Dev* and low *H-Homogeneity mean* are the ones displaying a bright replication blob. Thanks to the large number of analysed images, we discovered that the liposomes having a replication blob had a smaller area when compared to the ones having a homogeneous dsGreen lumen signal (Fig. 5c). Amongst the liposomes that were positive for DNA replication, 66% correspond to phenotype (2), and 34% to phenotype (3) (Fig. 5g).

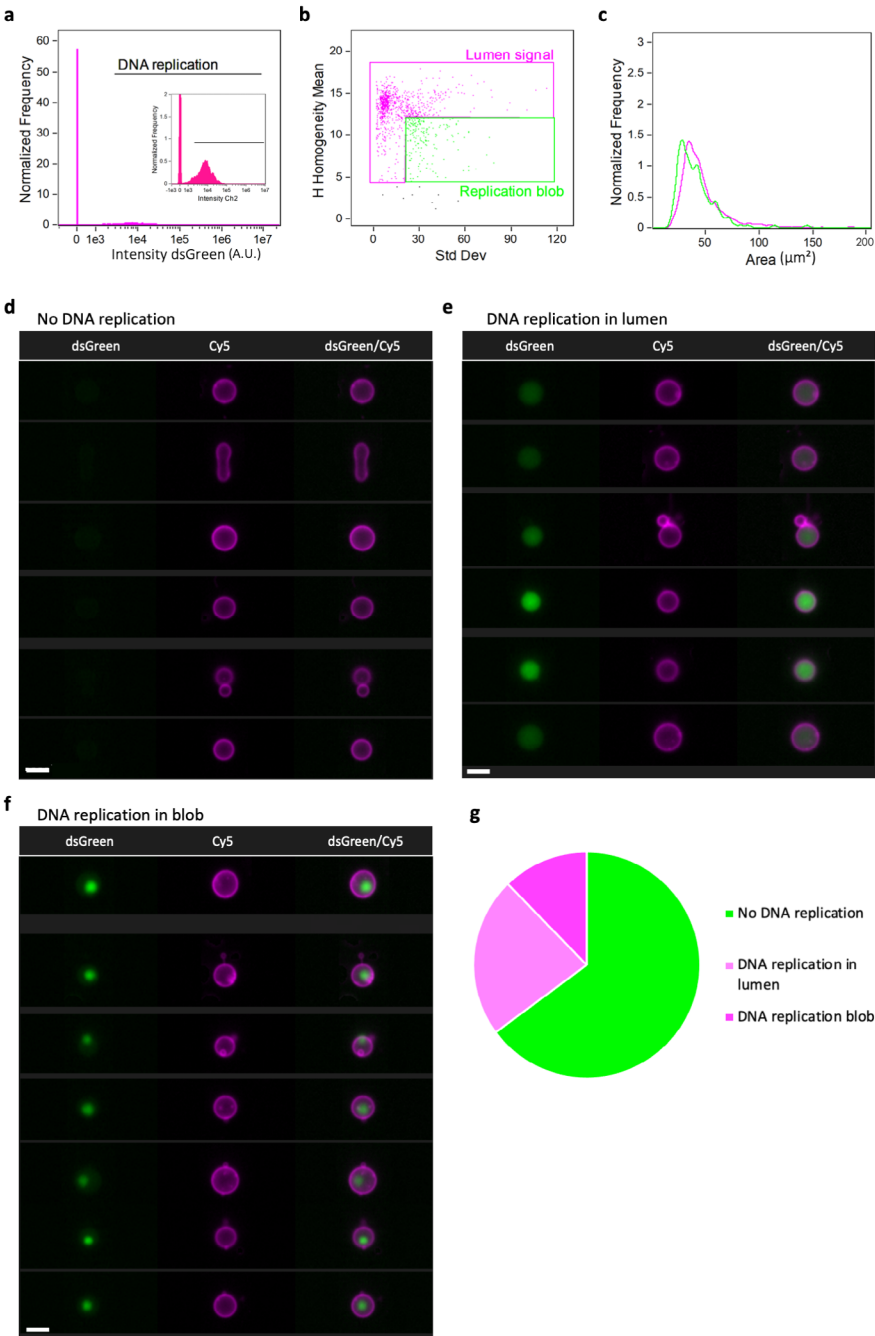


Figure 5: Gating of liposomes exhibiting DNA self-replication. **a**, Gating of liposomes with successful DNA replication as indicated by the presence of dsGreen via the *intensity* feature (Gated black). The plot

contains a zoom-in version of the scatter plot to better show the population selected. **b**, Identification of replication blobs was performed via *std Dev* and *H Homogeneity mean* features. In magenta, the liposomes classified as showing dsGreen signal homogeneously distributed within the lumen. In green, the liposomes classified as containing a DNA replication blob. **c**, Comparison of the liposome size distribution between the two types of DNA-replicating liposomes: magenta (even dsGreen) and green (clustered dsGreen). The liposomes having a replication blob show a smaller area. **d,e,f** Representative images of empty liposomes that do not show DNA replication (**d**), liposomes that show increased DNA amounts with even dsGreen signal in the lumen (**e**), and liposomes that show increase DNA amounts with clustered dsGreen signal (**f**). **g**, Graphical representation of the statistics obtained from the analysis performed on a set of over 60'000 liposomes from one biological sample. For all the images, membrane signal is in magenta, while dsGreen is in green. Scale bar is 7 μm .

Intraluminal cytoskeletal structures with expressed bacterial tubulin

Bacterial microtubules are filaments composed of polymerized BtubA and BtubB observed in *Prostheco bacter* cells^{53,54}. Previous studies demonstrated that BtubA/B can be functionally produced from DNA templates using the PURE system⁴⁸. When compartmentalized inside liposomes, de novo generated BtubA/B tubulins, together with a mix of DnaK chaperone and 100 nM of Atto488-labeled purified BtubA/B (A488-BtubA/B), self-organized into cytoskeletal structures of various morphologies⁴⁸. Liposomes were incubated at 37 °C for about 2.5 hours to promote gene expression before being run through ImageStream. Liposomes with no expression showed uniform fluorescence in their lumen (due to the encapsulated A488-BtubA/B) (Fig. 6c), while those with effectively expressed tubulin proteins showed filaments within the lumen (Fig. 6d).

The membrane signal was used to select liposomes following our previously described pipeline, while the lumen A488- BtubA/B fluorescence signal was employed to identify microtubules. We discarded from the analysis all the vesicles that did not show enough *intensity* in the A488-probe channel (Fig. 6a). Then, a wide range of textural features were explored individually and in combination to distinguish the liposomes with cytoskeletal structures. The *Std Dev* function proved to be the most adequate one for detecting inner inhomogeneity, and, when combined with the *contrast* feature produced the best outcome (Fig. 6b). The *contrast* feature assesses an image's sharpness by identifying big variations in pixel values in the image. Higher *Std Dev* and high *contrast* images corresponded to BtubA/B-expressing liposomes containing cytoskeletal structures. These accounted for around 4% of the total number of liposomes.

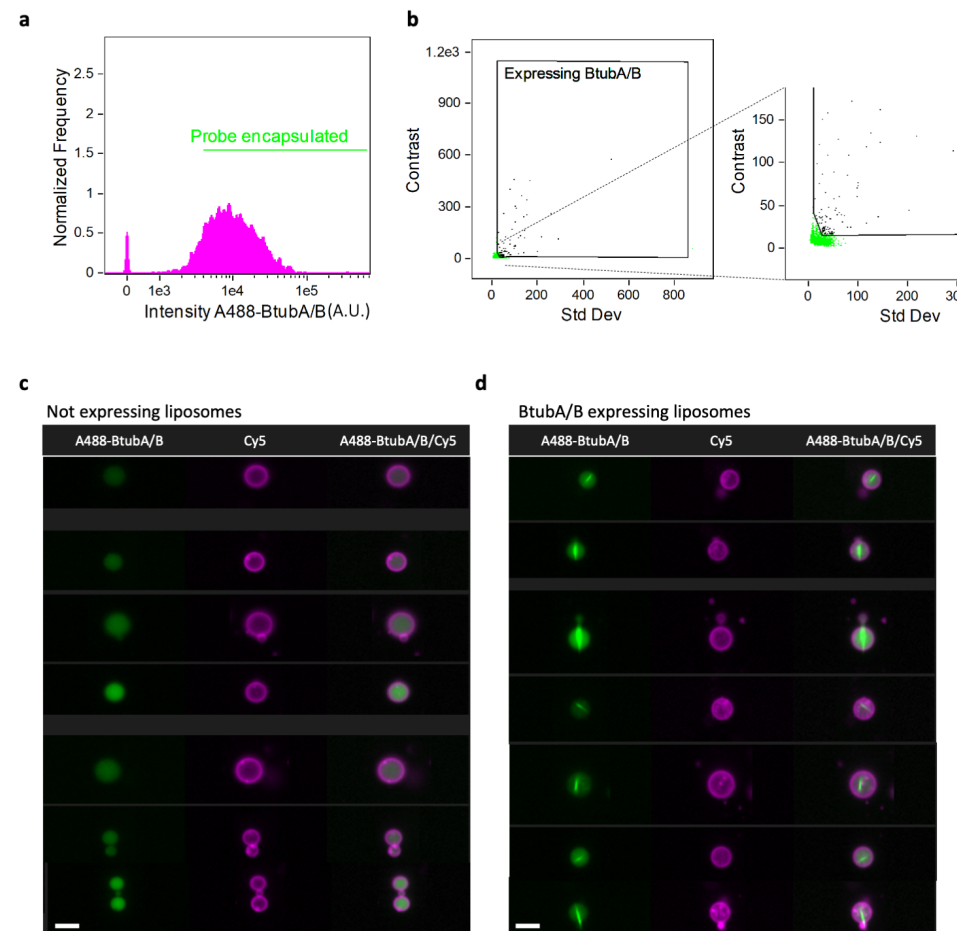


Figure 6: Gating of liposomes with expressed bacterial tubulin organized into cytoskeletal structures. **a**, Gating of liposomes encapsulating A488-BtubA/B as found with the *intensity* feature (Gated green). **b**, Liposomes with cytoskeletal structures were identified by plotting the *Std Dev* with the *contrast* feature (Gated black). A zoom-in image is shown on the side to better visualize the two populations and the applied gating. **c,d**, Representative images of the non-expressing liposomes (**c**) and the BtubA/B-expressing liposomes showing cytoskeletal structures formed within the lumen (**d**). For all the images, membrane signal is in magenta, while A488-BtubA/B is in green. Scale bar is 7 μ m. The analysis was performed on a set of over 35'000 liposomes from one biological sample.

Binding of expressed Min proteins to the membrane

The Min system, which comprises three proteins MinC, MinD, and MinE, is primarily responsible for the spatial organization of the division site in *E. coli*⁵⁵. The Min proteins self-organize at the cytoplasmic membrane's inner surface and oscillate between the two cell poles in a dynamic manner. MinD and MinE drive the oscillations, while MinC travels on the waves through interacting with MinD⁵⁶. We wanted to explore the potential of IFC in detecting protein binding to the membrane. To do this, the membrane protein MinD was cell-free synthesized inside liposomes, and eGFP-MinC was used as a fluorescent reporter³⁹. As MinE was omitted, no oscillations were expected. Once MinD is expressed, it adheres to the membrane, recruiting eGFP-MinC (Fig. 7c). MinC is exclusively found in the lumen when MinD is not expressed (Fig. 7d). Liposomes containing the DNA templates for MinD, purified eGFP-MinC and DnaK were produced, incubated for 3 hours at 37 °C, and then run on ImageStream³⁹. The membrane signal was used to identify liposomes, again following the protocol described above, and the localization of the eGFP-MinC fluorescence in the lumen or/and on the membrane was used to assess the activity of expressed MinD. Because the overall liposome quality in this sample was low due to the many vesicles showing inner lipid aggregates, we had to include an additional image processing step to ensure a precise liposome selection. We used the *H-Correlation* and *H-Contrast standard deviations*, to analyze the images texture on the membrane channel, local intensity variations correspond to the presence of lipid aggregations (Fig. 7a). To identify the liposomes having an eGFP-MinC signal on the membrane (corresponding to the liposomes expressing MinD), we used the *bright detail similarity R3* feature (Fig. 7b). The *bright detail similarity R3* feature compares the bright image detail of two images and can be used to measure signal co-localization. The feature computes the log-transformed Pearson's correlation coefficient of small bright region (3 pixels radius) inside the mask provided for the two input images. Here, the membrane and the eGFP-MinC images and mask were chosen as input. Events with a similarity greater than 3 were regarded as correlated and the corresponding liposomes were classified as MinD-expressing. Liposomes expressing MinD accounted for approximately 54% of the total population.

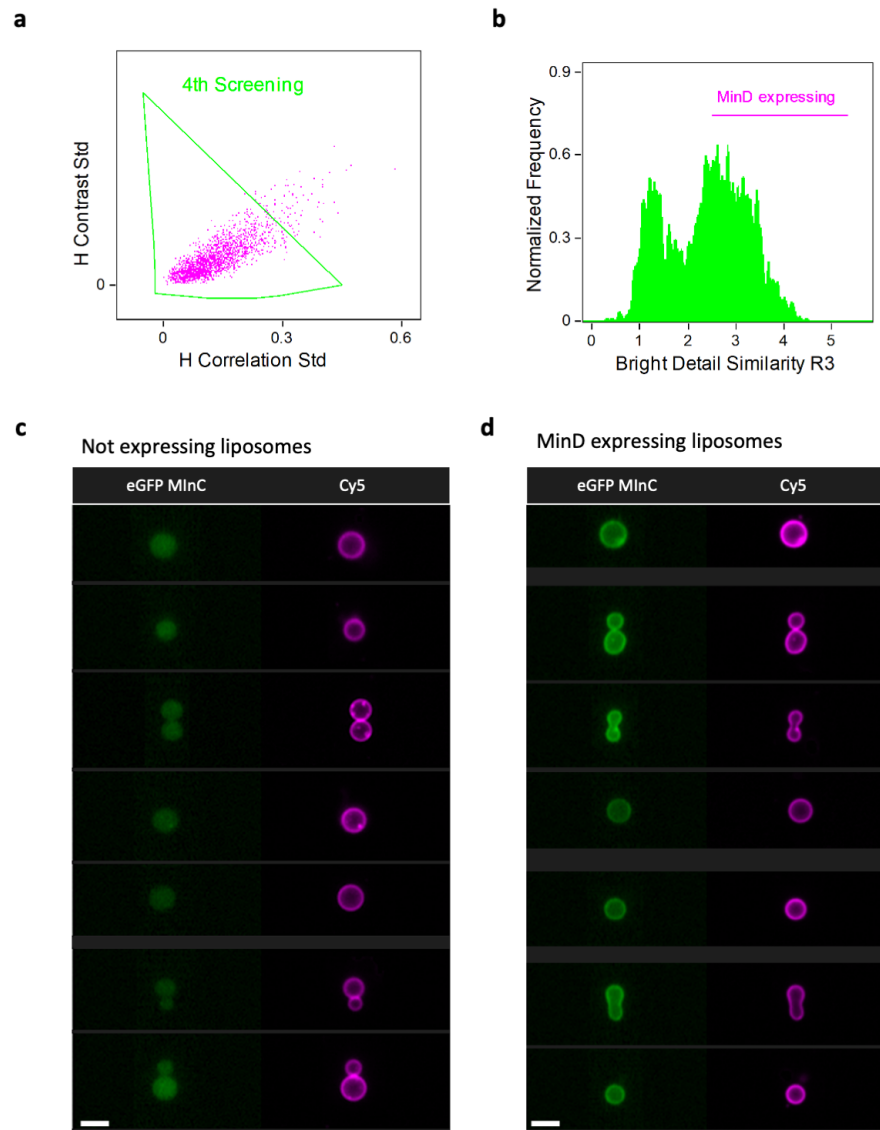


Figure 7: Gating of liposomes expressing the membrane-binding protein MinD. **a**, Additional image processing for the identification of a higher quality liposome population. The extra step included plotting the *H-Correlation* and the *H-Contrast standard* deviations features. Gated events are in green. **b**, Liposomes showing eGFP-MinC signal on the membrane, corresponding to the ones that have successful MinD expression, were gated via the *bright detail similarity R3* feature (Gate in magenta). **c,d**, Representative images of liposomes not expressing or expressing MinD at a concentration that is not sufficient to recruit MinC on the membrane (c) and of MinD-expressing liposomes showing eGFP-MinC recruitment on the membrane (d). For all the images, membrane signal is in magenta, while eGFP-MinC is in green. Scale bar is 7 μ m. The analysis was performed on a set of 40'000 liposomes from one biological sample.

Discussion

Here, we introduced IFC as a novel and high-throughput approach for detecting, phenotyping and quantifying individual cell-sized liposomes. IFC provides image-based validation of the recorded objects and allows for true differentiation between small particles, multilamellar vesicles, multivesicular structures, and aggregates (Fig. 2). Moreover, we could distinguish between elongated objects, such as rod-shape liposomes and doublets (Fig. 3).

Populations of genetically identical liposomes display heterogeneity due to significant differences in expression levels. Having a diversified population of gene-expressing liposomes can be beneficial. Indeed, a wider combinatorial space of morphological variables can be examined within one sample, increasing the possibility of finding liposomes having desirable phenotypes. Along with the differences in gene expression level, the diversity of traits to be co-reconstituted increases the variety of sophisticated details to be analyzed. We have shown that the IFC technology is able to identify subtle internal features such as DNA bright spots (Fig. 5) and cytoskeletal structures (Fig. 6) in the lumen of liposomes with an inner fluorescence background. IFC is also useful to acquire high-quality images of phenomena that occur in the proximity of the membrane, such as membrane protein interactions (Fig. 7). By detecting multidimensional features at high throughput, IFC ensures that the information regarding liposome subpopulations is not ignored, helping to deal with the heterogeneity of cell-free expressing synthetic cells.

Our standardized data analysis pipeline can be used to correctly identify phenotypes of interest and to compare samples with no selection bias. The software IDEAS provides over 200 features to assess and analyze the collected images covering a wide range of liposome phenotypic characterizations.

We demonstrated that IFC technology can be used to screen a high-throughput number of liposomes. Throughout the study we gathered about 1 million events per investigated condition. After analyzing all the collected events we found that about 6% were liposomes (60'000 liposomes on average, considering all samples used in the study). This dataset was acquired by running about 0.5 μ L of liposome solution of a 8 μ L sample volume. The number of identified liposomes may vary according to the production methods. Practical adjustments, independent of liposome preparation, can be made to increase the number of collected liposomes. First, during the acquisition, gating can be applied to exclude small debris and aggregates. This gating could be performed via a comparative analysis over the *area* and *aspect ratio* features as shown in Fig. 2b, thus making sure that the 1 million collected events are more representative of an interesting population. The only difference with our reported data would be that the first filtering step is performed during acquisition instead of during analysis. An additional gating could also be performed during acquisition based on focus as shown in Fig. 2e. Performing strict gating during the acquisition will help increasing the number of relevant events. However, one important remark is that during acquisition the user can not

adjust the channel masks. Therefore, to be more precise with the final liposome selection, we suggest performing again the steps during the analysis. Lastly, the number of liposomes in the gated population can be further increased by scaling up the volume of the analyzed sample. The method is unquestionably high-throughput and can be quickly scaled up to ultra-high-throughput liposome detection. The number of events gathered is not a burden for IFC, neither with the data analysis of such big and complex data sets. Data analysis pipelines can easily be saved as templates for the analysis of multiple data batches (from 1K to 100K events). Data processing is then rapid and not excessively computationally demanding.

Other than what presented here, we believe that IFC can be exploited for an even more vast set of analyses; in our proof of concept, we only employed two detection channels (488 nm and 642 nm). However, the system also collects signals for brightfield and scattered lights. The brightfield could be implemented to identify liposomes in the absence of a membrane dye (Supplementary Fig. 1). Furthermore, the collection of instrument parts includes lasers with other wavelengths (375 nm, 405 nm, 561 nm and 592 nm are also available), which can be useful for the analysis of even more complex phenotypic traits simultaneously.

The image-based interrogation of morphological characteristics of large liposome populations can be extremely beneficial when building synthetic cell compartments. Liposome production can vary in yield, relative size and physical properties. Accurate protocol optimization is typically constrained by the several input parameters that must be screened in order to acquire statistically relevant data. The use of IFC could alleviate this screening barrier, as also shown in a recent study that applied the instrument to optimize liposome production via water-in-oil emulsion transfer methods⁵⁷. As the instrument can screen liposomes prepared from various techniques, such as natural swelling, cDICE, eDICE, and emulsion droplets, IFC could also be used to compare liposomes manufacturing protocols. This would assist with making informed decisions about the experimental settings to use in different in vitro reconstitution challenges, hence aiding liposome engineering.

Finally, the capabilities of IFC could go beyond image-based screening. In the future, an added cell sorting module will enable collection of liposomes exhibiting specific properties for further analytical investigations. Recently, a new powerful technology developed by Goda et al.^{58,59}, enabled the image-activated sorting of cells and small organisms (IACS). Leveraging image-activated liposome sorting will be revolutionary to investigate compartmentalized in vitro evolution of proteins, genetic and metabolic networks, and, ultimately, system's level functionality of the synthetic cells⁶⁰.

Methods

Purified proteins

eGFP-MinC was purified according to published protocols^{39,61}. Protein concentration was determined by Bradford assay and by measuring eGFP absorbance.

BtubAB was purified and labelled as previously described except that C41(DE3) cells were used for expression instead of BL21(DE3)^{48,62}. Concentration of purified bacterial tubulin was determined from absorbance.

DNA constructs

All DNA constructs are linear products of PCR reactions starting from a parental plasmid. Concentration and purity of DNA were checked on NanoDrop. Sequences of the unpublished linear constructs used as templates in PURE system reactions can be found in the Supplementary Methods.

Constructs containing the *minD*, *btubA* or *btubB* gene were assembled as previously reported^{39,48}. Forward and reverse primers ChD709 and ChD757, respectively, annealing to the T7 promoter and T7 terminator sequences were used for PCR.

The *YFP* and *DNAP-TP* expressing plasmids were sub-cloned into ori-containing vectors via Gibson Assembly. All the plasmids were cloned into *E. coli* Top10 chemically competent cells. Individual clones were screened and confirmed by Sanger sequencing at Macrogen-Europe B.V. Sequence-verified plasmids were extracted from outgrown cells in LB/ampicillin (50 g/ml) using the PURE Yield Plasmid Miniprep kit (Promega). Linear fragments were obtained from PCR amplification using Phusion High-Fidelity DNA Polymerase (NEB) with the forward and reverse primers ChD491 and ChD492, respectively. The amplified PCR fragments were purified using QIAquick PCR purification kit (Qiagen). For the purification of DNAP-TP expressing fragments, RNeasy MinElute Cleanup columns (Qiagen) were utilized instead of DNA columns provided with the kit. The general QIAquick manufacturer protocol was modified by having a longer pre-elution buffer drying step (at least 4 minutes at 10,000 g with open columns), and a longer column incubation step (at least 5 minutes) with ultrapure water (20-30 l of Merck Milli-Q water) prior to the final DNA elution. The purified DNA was quantified by Nanodrop 2000c spectrophotometer (Isogen Life Science) and further analyzed for size and purity with DNA gel electrophoresis. Purified DNA fragments were stored at -20°C.

Lipids

DOPC, DOPE, DOPG, 1,3'-bis[1,2-dioleoyl-sn-glycero-3-phospho]-glycerol (18:1 CL), and 1,2-distearoyl-sn-glycero-3-phosphoethanolamine-N-[biotinyl(polyethylene glycol)-2000] (DSPE-PEG-biotin) and DHPE-Cy5 were from Avanti Polar Lipids.

Preparation of lipid-coated beads

A lipid mixture with the following composition was prepared: DOPC (50 mol%), DOPE (36 mol%), DOPG (12 mol%), 18:1 CL (2 mol%), DSPE-PEG-biotin (1 mass%), and DHPE-Cy5 (0.5 mass%) for a total mass of 2 mg. Lipids dissolved in chloroform were mixed in a round-bottom glass flask. Methanol containing 100 mM rhamnose was added to the lipid solution with a chloroform-to-methanol volume ratio of 2.5:1. Then, 1.5 g of 212–300 μm glass beads (acid washed, Sigma Aldrich) was poured to the lipid-rhamnose solution, and the organic solvent was removed by rotary evaporation at 200 mbar for 2 hours at room temperature, followed by overnight desiccation. Lipid-coated beads were stored under argon at -20°C until use.

Production of gene expressing liposomes

A 20 μL PUREfrex2.0 reaction mixture was assembled in a 1.5 mL Eppendorf tube. The composition for each swelling solution is as followed:

- YFP: PUREfrex2.0, 4 nM of YFP and MilliQ water to reach a final volume.
- DNA replication: PUREfrex2.0, 20 mM ammonium sulfate, 300 μM dNTPs, 750 $\mu\text{g mL}^{-1}$ purified p5 protein, 210 $\mu\text{g mL}^{-1}$ purified p6 protein, 1.2 units μL^{-1} of Superase-In RNase inhibitor (Ambion), and 4 nM of template DNAP and TP DNA constructs.
- Bacterial tubulin: PUREfrex2.0, 1 μL DnaK mix (GeneFrontier Corporation), 100 nM Atto488-BtubA/B, 3.75 nM of *btubA* and 2.5 nM of *btubB* DNA constructs⁴⁸.
- Min system: PUREfrex2.0, 1 μL DnaK mix, 2.5 mM ATP, 0.5 μM purified eGFP-MinC, 5 nM of *minD* template³⁹.

About 10 mg of lipid-coated beads was transferred to the swelling solution and liposomes were formed by natural swelling of the lipid film. For uniform liposome swelling, the 1.5 ml Eppendorf tube containing the reaction mixtures were gently rotated on an automatic tube rotator (VWR) at 4°C along its axis for 30 minutes. The samples were then subjected to four freeze/thaw cycles in liquid nitrogen/ice. Using a cut pipette tip, 10 μL of glass bead-free liposome suspension was transferred to a PCR tube, where it was mixed with 1 μL of DNase I (0.07 U μL^{-1}) (Thermo Scientific). The PCR tubes with the liposome suspension were incubated in a ThermalCycler (C1000 Touch, Biorad) at 30°C (for DNA replication) or 37°C (for all the other conditions over a period ranging from 3 to 16 hours, as specified in the main text). The suspensions were finally diluted and, when necessary, stained prior to the imaging flow cytometry run as described below.

Sample preparation for imaging flow cytometry

A liposome suspension of 1 μL was diluted in 100 μL of homemade PURE buffer (20 mM HEPES-KOH pH 7.6, 180 mM potassium glutamate, 14 mM magnesium acetate). To remove any remaining glass beads from the liposome swelling, the liposome dilution was gently

filtered through a cell-strainer cap (35 μm nylon) from 5 mL round bottom polystyrene test tubes (Falcon). When needed, additional liposome staining was performed according to the nature of the sample: for DNA replication DNA staining was performed with dsGreen (Lumiprobe) dye at a 1:100.000 dilution. The final mixture was incubated for 30-60 minutes at room temperature to equilibrate the binding.

Collection and analysis of IFC data

All samples were analyzed with the Amnis ImageStream^x Mk II and INSPIRE acquisition software (201.1.0.724) (Luminex). The following laser power settings were used:

Morphology analysis, 150 for 488 nm / 50 for 642 nm / 3 for 785 nm,

YFP, 40 for 488 nm / 50 for 642 nm / 3 for 785 nm,

DNA replication, 15 for 488 nm / 50 for 642 nm / 3 for 785 nm,

Bacterial tubulin, 120 for 488 nm / 40 for 642 nm

Min system, 200 for 488 nm / 50 for 642 nm / 3 for 785 nm.

A 60X magnification objective was used, focus was set to automatic mode, and fluidics were set to low speed and high sensitivity. One million events were collected for each of sample, which corresponds to an estimated volume of 40 to 50 μL of the diluted liposome suspension. All data were analyzed with IDEAS6.2 analysis software (Luminex).

References

1. Walde, P., Cosentino, K., Engel, H. & Stano, P. Giant vesicles: preparations and applications. *Chembiochem* **11**, 848–865 (2010).
2. Pick, H., Alves, A. C. & Vogel, H. Single-vesicle assays using liposomes and cell-derived vesicles: from modeling complex membrane processes to synthetic biology and biomedical applications. *Chem. Rev.* **118**, 8598–8654 (2018).
3. Fernandez-Trillo, F., Grover, L. M., Stephenson-Brown, A., Harrison, P. & Mendes, P. M. Vesicles in nature and the laboratory: elucidation of their biological properties and synthesis of increasingly complex synthetic vesicles. *Angew. Chemie Int. Ed.* **56**, 3142–3160 (2017).
4. Rideau, E., Dimova, R., Schwille, P., Wurm, F. R. & Landfester, K. Liposomes and polymersomes: a comparative review towards cell mimicking. *Chem. Soc. Rev.* **47**, 8572–8610 (2018).
5. Bain, J. & Staniland, S. S. Bioinspired nanoreactors for the biomineralisation of metallic-based nanoparticles for nanomedicine. *Phys. Chem. Chem. Phys.* **17**, 15508–15521 (2015).
6. Daraee, H., Etemadi, A., Kouhi, M., Alimirzalu, S. & Akbarzadeh, A. Application of liposomes in medicine and drug delivery. *Artif Cells Nanomed Biotechnol.* **44**, 381–391 (2016).
7. Al-Jamal, W. T. & Kostarelos, K. Liposomes: from a clinically established drug delivery system to a nanoparticle platform for theranostic nanomedicine. *Acc. Chem. Res.* **44**, 1094–1104 (2011).
8. György, B., Hung, M. E., Breakefield, X. O. & Leonard, J. N. Therapeutic applications of extracellular vesicles: clinical promise and open questions. *Annu. Rev. Pharmacol. Toxicol.* **55**, 439–464 (2015).
9. Liu, W. *et al.* Research progress on liposomes: Application in food, digestion behavior and absorption mechanism. *Trends Food Sci. Technol.* **104**, 177–189 (2020).
10. Bally, M. *et al.* Liposome and lipid bilayer arrays towards biosensing applications. *Small* **6**, 2481–2497 (2010).
11. Chan, Y. H. M. & Boxer, S. G. Model membrane systems and their applications. *Curr. Opin. Chem. Biol.* **11**, 581–587 (2007).
12. Lagny, T. J. & Bassereau, P. Bioinspired membrane-based systems for a physical approach of cell organization and dynamics: usefulness and limitations. *Interface Focus* **5**, (2015).
13. Caschera, F. & Noireaux, V. Integration of biological parts toward the synthesis of a minimal cell. *Curr. Opin. Chem. Biol.* **22**, 85–91 (2014).
14. Blain, J. C. & Szostak, J. W. Progress toward synthetic cells. *Annu. Rev. Biochem.* **83**, 615–640 (2014).
15. Bibi, S. *et al.* Microscopy imaging of liposomes: From coverslips to environmental SEM. *Int. J. Pharm.* **417**, 138–150 (2011).
16. Robson, A. L. *et al.* Advantages and limitations of current imaging techniques for characterizing liposome morphology. *Front. Pharmacol.* **9**, 80 (2018).
17. Blanken, D., van Nies, P. & Danelon, C. Quantitative imaging of gene-expressing liposomes reveals rare favorable phenotypes. *Phys. Biol.* **16**, 045002 (2019).
18. Saliba, A. E. *et al.* A quantitative liposome microarray to systematically characterize protein-lipid interactions. *Nat. Methods* **2013** **11**, 47–50 (2013).
19. Christensen, S. M. & Stamou, D. Vesicle arrays as model-membranes and biochemical reactor systems. *Biomimetic Membranes for Sensor and Separation Applications* 87–112 (2011).
20. Chen, C., Zhu, S., Huang, T., Wang, S. & Yan, X. Analytical techniques for single-liposome characterization. *Anal. Methods* **5**, 2150–2157 (2013).
21. Kanásová, M. & Nesměrák, K. Systematic review of liposomes' characterization methods. *Monatshfte für Chemie - Chem. Mon.* **148**, 1581–1593 (2017).
22. Sunami, T., Shimada, K., Tsuji, G. & Fujii, S. Flow cytometric analysis to evaluate morphological changes in giant liposomes as observed in electrofusion experiments. *Langmuir* **34**, 88–96 (2018).
23. Vorauer-Uhl, K., Wagner, A., Borth, N. & Kättinger, H. Determination of liposome size distribution by flow cytometry. *Cytometry* **39** (2), 166–71 (2000).
24. Nishimura, K. *et al.* Population analysis of structural properties of giant liposomes by flow cytometry. *Langmuir* **25**, 10439–10443 (2009).
25. Temmerman, K. & Nickel, W. A novel flow cytometric assay to quantify interactions between proteins and membrane lipids. *J. Lipid Res.* **50**, 1245 (2009).
26. Basiji, D. A., Ortyń, W. E., Liang, L., Venkatachalam, V. & Morrissey, P. Cellular image analysis and imaging by flow cytometry. *Clin. Lab. Med.* **27**, 653 (2007).
27. Zuba-Surma, E. K. & Ratajczak, M. Z. Analytical capabilities of the imagerstream cytometer. *Methods Cell Biol.* **102**, 207–230 (2011).
28. George, T. C. *et al.* Distinguishing modes of cell death using the ImageStream multispectral imaging flow cytometer. *Cytometry. A* **59**, 237–245 (2004).
29. Khuda, S. E., Loo, W. M., Janz, S., Ness, B. Van & Erickson, L. D. Deregulation of c-myc confers distinct survival requirements for memory b cells, plasma cells, and their progenitors. *J. Immunol.* **181**, 7537 (2008).
30. Gillard, G. O. & Farr, A. G. Features of medullary thymic epithelium implicate postnatal development in maintaining epithelial heterogeneity and tissue-restricted antigen expression. *J. Immunol.* **176**, 5815–5824 (2006).
31. Blasi, T. *et al.* Label-free cell cycle analysis for high-throughput imaging flow cytometry. *Nat. Commun.* **2016** **7**, 1–9 (2016).
32. Fanning, S. L. *et al.* Receptor cross-linking on human plasmacytoid dendritic cells leads to the regulation of IFN- α production. *J. Immunol.* **177**, 5829–5839 (2006).
33. George, T. C. *et al.* Quantitative measurement of nuclear translocation events using similarity analysis of multispectral cellular images obtained in flow. *J. Immunol. Methods* **311**, 117–129 (2006).
34. Beum, P. V. *et al.* Quantitative analysis of protein co-localization on B cells opsonized with rituximab and complement using the ImageStream multispectral imaging flow cytometer. *J. Immunol. Methods* **317**, 90–99 (2006).
35. Konstantinidis, D. G. *et al.* Signaling and cytoskeletal requirements in erythroblast enucleation. *Blood* **119**, 6118–6127 (2012).
36. Nomura, S. I. M. *et al.* Gene expression within cell-sized lipid vesicles. *ChemBioChem* **4**, 1172–1175 (2003).
37. Noireaux, V. & Libchaber, A. A vesicle bioreactor as a step toward an artificial cell assembly. *Proc. Natl. Acad. Sci. U. S. A.* **101**, 17669–17674 (2004).
38. van Nies, P. *et al.* Self-replication of DNA by its encoded proteins in liposome-based synthetic cells. *Nat. Commun.* **9**, 1583 (2018).
39. Godino, E. *et al.* De novo synthesized Min proteins drive oscillatory liposome deformation and regulate FtsA-FtsZ cytoskeletal patterns. *Nat. Commun.* **10**, 4969 (2019).
40. Blanken, D., Foschepoth, D., Serrão, A. C. & Danelon, C. Genetically controlled membrane synthesis in liposomes. *Nat. Commun.* **11**, (2020).
41. Noireaux, V., Maeda, Y. T. & Libchaber, A. Development of an artificial cell, from self-organization to computation and self-reproduction. *Proc. Natl. Acad. Sci.* **108**, 3473–3480 (2011).
42. Forster, A. C. & Church, G. M. Towards synthesis of a minimal cell. *Mol. Syst. Biol.* **2**, 45 (2006).
43. Murtas, G. Artificial assembly of a minimal cell. *Molecular BioSystems* vol. 5 1292–1297 (2009).
44. Nourian, Z., Roelofsen, W. & Danelon, C. Triggered gene expression in fed-vesicle microreactors with a multifunctional membrane. *Angew. Chemie Int. Ed.* **51**, 3114–3118 (2012).
45. Nourian, Z. & Danelon, C. Linking genotype and phenotype in protein synthesizing liposomes with external supply of resources. *ACS Synth. Biol.* **2**, 186–193 (2013).
46. van Nies, P. *et al.* Unbiased tracking of the progression of mRNA and protein synthesis in bulk and in liposome-confined reactions. *ChemBioChem* **14**, 1963–1966 (2013).
47. Libicher, K., Hornberger, R., Heymann, M. & Mutschler, H. In vitro self-replication and multicistronic expression of large synthetic genomes. *Nat. Commun.* **11**, 1–8 (2020).
48. Kattan, J., Doerr, A., Dogterom, M. & Danelon, C. Shaping liposomes by cell-free expressed bacterial microtubules. *ACS Synth. Biol.* **10**, 2447–2455 (2021).
49. Godino, E. *et al.* Cell-free biogenesis of bacterial division proto-rings that can constrict liposomes. *Commun. Biol.* **3**, (2020).
50. Furusato, T. *et al.* De novo synthesis of basal bacterial cell division proteins FtsZ, FtsA, and ZipA inside giant vesicles. *ACS Synth. Biol.* **7**, 953–961 (2018).
51. Shimizu, Y. *et al.* Cell-free translation reconstituted with purified components. *Nat. Biotechnol.* **19**, 751–755 (2001).
52. Shimizu, Y., Kanamori, T. & Ueda, T. Protein synthesis by pure translation systems. *Methods* **36**, 299–304 (2005).
53. Rosati, G., Verni, F. & Lenzi, P. 'Epixenosomes': Peculiar epibionts of the ciliate Euplotidium itoi: The formation of the extrusive apparatus and the ejecting mechanism. *Eur. J. Protistol.* **29**, 238–245 (1993).
54. Petroni, G., Spring, S., Schleifer, K. H., Verni, F. & Rosati, G. Defensive extrusive ectosymbionts of Euplotidium (Ciliophora)

that contain microtubule-like structures are bacteria related to Verrucomicrobia. *Proc. Natl. Acad. Sci. U. S. A.* **97**, 1813–1817 (2000).

55. Rowlett, V. W. & Margolin, W. The Min system and other nucleoid-independent regulators of Z ring positioning. *Front. Microbiol.* **6**, 478 (2015).

56. Rowlett, V. W. & Margolin, W. The bacterial Min system. *Curr. Biol.* **23**, R553–R556 (2013).

57. Matsushita-Ishiodori, Y., Hanczyc, M. M., Wang, A., Szostak, J. W. & Yomo, T. Using imaging flow cytometry to quantify and optimize giant vesicle production by water-in-oil emulsion transfer methods. *Langmuir* **35**, 2375–2382 (2019).

58. Nitta, N. *et al.* Intelligent image-activated cell sorting. *Cell* **175**, 266–276.e13 (2018).

59. Isozaki, A. *et al.* Intelligent image-activated cell sorting 2.0. *Lab Chip* **20**, 2263–2273 (2020).

60. Abil, Z. & Danelon, C. Roadmap to building a cell: an evolutionary approach. *Front. Bioeng. Biotechnol.* **8**, 927 (2020).

61. Loose, M., Fischer-Friedrich, E., Herold, C., Kruse, K. & Schwille, P. Min protein patterns emerge from rapid rebinding and membrane interaction of MinE. *Nat. Struct. Mol. Biol.* **18**, 577–583 (2011).

62. Diaz-Celis, C. *et al.* Bacterial tubulins a and b exhibit polarized growth, mixed-polarity bundling, and destabilization by gtp hydrolysis. *J. Bacteriol.* **199**, (2017).

Supplementary Information

Sequence of YFP (5’→3’, complete linear construct)

AAAGTAAGCCCCACCCTCACATGATACCATTCCTAATATCGACATAATCCGTCGATCCTCGGCATACCATGAT-CAGGGAGGGAAACTACTACTTAATATATCAATCTATAGACCTACTAGATAGGTTTGTCAATGAACAACATAAAACGA-CACAGAATCCCACGTTTTAGCGCTTCGTCTGTGTCGCATGTGAAATTAATACGACTCACTATAGGGAGACCACAACG-GTTTTCCCTCTAGAAATAATTTTGTTAACCTTAAGAAGGAGATATACATATGCGGGGTTCTCATCATCATCATCAT-CATGGTATGGCTAGCATGACTGGTGGACAGCAAATGGGTGCGGATCTGTACGACGATGACGATAAGGATCCGATG-GTTAGCAAAGGCGAAGAACTGTTTACGGGCGTGGTGCCGATTCTGGTGGAACCTGGACGGCGACGTGAACGGTCA-CAAATTCAGCGTTTTCGGGCGAAGGTGAAGGCGATGCGACCTATGGTAAACTGACGCTGAAATTTATTTGCAACCAC-CGGTAAACTGCCGGTGCCGTGGCCGACCCTGGTTACCACGTTTGGTTATGGCCTGCAGTGTTTCGCGCGCTACCCG-GATCATATGAAACAACACGACTTTTTCAAATCTGCCATGCCGGAAGGTTATGTGCAGGAACGTACGATTTTCTTTAAAGATGACGGCAACTACAAAACCCGCGCAGAAAGTCAAATTTGAAGGTGATACGCTGGTGAAACCGTATTGAACTGAAA-GGCATCGATTTCAAAGAAGACGGTAATATCCTGGGCCATAAACTGGAATACAACCTACAACCTCCCACAACGTTTA-CATCATGGCAGATAAAACAGAAAAACGGTATCAAAGTCAACTTCAAAATCCGCCATAACATCGAAGATGGCTCAGTG-CAACTGGCTGACCACTACCAGCAAAACACCCCGATCGGTGATGGCCCGGTTCTGCTGCCGGACAATCATTATCTGAGC-TACCAGTCTGCACTGAGTAAAGATCCGAACGAAAAACGTGACCACATGGTCCTGCTGGAATTTGTGACGGCGGCT-GGTATTACGCTGGGCATGGATGAACTGTATAAATGAAAGCTTCCCGGGAAAGTATATATGAGTAAAGATATCGACG-CAACTGAATGAAATGGTGAAGGACGGGTCCAGGTGTGGCTGCTTCGGCAGTGCAGCTTGTTGAGTAGAGTGT-GAGCTCCGTAACTAGTCGCGTCGATATCCCCGGGCTAGCATAACCCCTTGGGGCCTCTAAACGGGTCTTGAGGGGT-TTTTTGCCTCCTATGATTGGTTGTCTTATTACCTTACTTCTATTATAGTATAACATGTTAAACGATAGTTTGTCTACCCT-TTTCGACAAATTGATGATAATAAATAGTATAGGTATATAGTCGTGATTAGTTGTTAGATTCTTGTCGAAGATAGTCGGT-CAATGGGGAAATGGTGTATGTTGTCGCTGTACCCTACTTT

Sequence of DNAP-TP (5’→3’, complete linear construct)

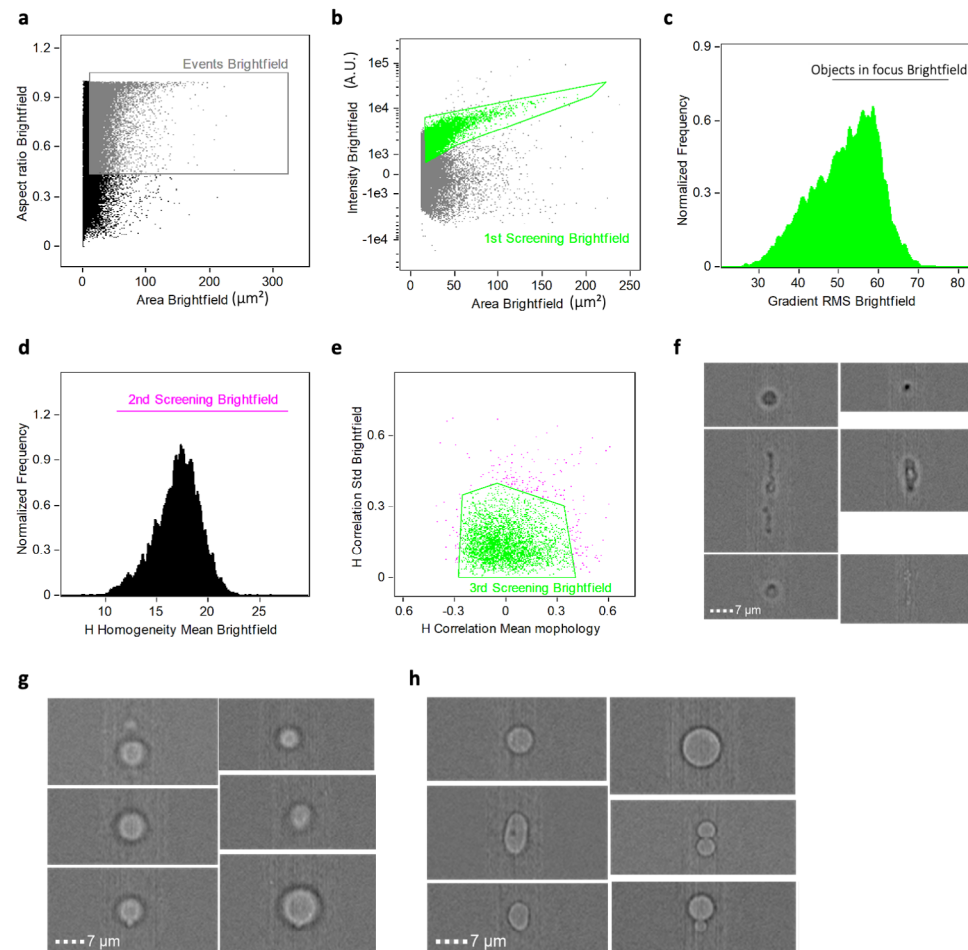
AAAGTAAGCCCCACCCTCACATGATACCATTCCTAATATCGACATAATCCGTCGATCCTCGGCATACCATGAT-CAGGGAGGGAAACTACTACTTAATATATCAATCTATAGACCTACTAGATAGGTTTGTCAATGAACAACATAAAACGA-CACAGAATCCCACGTTTTAGCGCTTCGTCTGTGTCGCATGTGAaATTAATACGACTCACTATAGGGAGACCA-CAACGGTTTTCCCTCTAGAAATAATTTTGTTAACCTTAAGAAGGAGATATACATATGCCGCGTAAAAATGTACAGCTG-CGATTTTGAAACGACGACGAAAGTTGAAGATTGCCGTGTCTGGGCCTATGGTTATATGAACATCGAAGACCAT-TCAGAATATAAAATTGGCAACTCGCTGGATGAATTTATGGCGTGGGTGCTGAAAGTTCAGGCCGACCTGTACTTCCA-CAATCTGAAATTTGATGGTGCGTTCAATTATCAACTGGCTGGAACGTAATGGCTTTAAATGGAGCGCGATGGTCTGC-GCAACACCTATAATACGATTATCTCTCGTATGGCCAATGGTATATGATTGATATCTGCCTGGGCTACAAAGGTAAACG-

CAAAATTCATACCGTGATCTATGACAGCCTGAAAAAACTGCCGTTTCCGGTGAAGAAAATTGCGAAAGATTTCAAACT-GACCGTCCTGAAAGGGCGATATTGACTATCACAAAGAACGTCCGGTTGGTTACAAAATCACGCCGGAAAGATATGCG-TACATTA AAAACGATATCCAGATTATCGCAGAAGCTCTGCTGATTCAGTTTAAACAAGGCCTGGATCGCATGACCGC-CGGCAGTGACTCCCTGAAAGGTTTCAAAGATATCATCACACGAAAAAATTTAAGAAAGTGTTCCCGACCCTGAGCCT-GGGTCTGGATAAAGAAGTTCGTTATGCATACCGCGGCGGTTTACGTGGCTGAACGACCGTTTCAAAGAAAAA-GAAATTGGCGAGGGTATGGTCTTTGATGTGAATAGTCTGTATCCGGCTCAGATGTACTCCCGCCTGCTGCCGTAT-GGCGAACCGATCGTTTTTCGAGGGTAAATATGTCTGGGATGAAGACTACCCGCTGCATATTCAGCACATCCGTTGT-GAATTTGAACTGAAAGAAGGTATATTCGACCATTCAAATCAAACGTAGCCGCTTCTATAAGGGTAACGAATACCT-GAAAAGCTCTGGCGGTGAAATCGCAGACCTGTGGCTGAGTAACGTGATCTGGAAGTATGAAAGAACATTACGATCT-GTACAACGTTGAATACATCTCCGGCCTGAAATTTAAAGCCACCACGGGTCTGTTTAAAGATTTCAATTGACAAATG-GACCTACATCAAAACCACGTCTGAAGGTGCAATCAAACAGCTGGCTAAACTGATGCTGAACAGCCTGTATGGCAAT-TTGATCTAATCCGGATGTTACCGGTAAAGTCCCGTACCTGAAAGAAAATGGCGCTCTGGGTTTTTCGCCCTGGGCGAA-GAAGAAACCAAAGATCCCGGTGTATACGCCGATGGGTGTTTTTCATTACCGCGTGGGCACGTTACACCACCATCACCGC-CGCACAAGCGTGCTATGACCCGATTATCTACTGTGATACCGACTCAATTCATCTGACCGGCACGGAATCCCGGATGT-GATTAAAGATATCGTTGACCCGAAAAAACTGGGTATTGGGCACACGAATCGACCTTTAAACGTGCTAAATACCTG-CGCCAGAAAACGTACATCCAAGACATCTACATGAAAGAAGTCGATGGCAAACCTGGTGGAAGGTTACCCGGATGAC-TATACCGACATTAATTTTCGGTGAAATGCGCCGGCATGACCGATAAAATTAAGAAAGAAGTGACGTTTCGAAAAT-TTCAAAGTGGGTTTCAGTCGCAAAATGAAACCGAAACCGGTCCAAGTTCGGGCGGCGTTGTGCTGGTTCGAT-GACACCTTCACGATCAATAAGAATTGTACTAGAGTATCTGTTAGTTTTTTTCTACTAGAGTACTAGAGTATCTGT-TAGTTTTTTTTCATCGGATCCCGGGCCCGTCGACTGCTAATACGACTCACTATAGGGCCCTCTGGAGACACCAGAG-GGTTTACATGTTTTATTGTTTAACTTTAAGAAGGAGATATACTAATGGCACGCAGCCCGCGCATCCGCATCAAAGA-TAACGACAAAGCCGAATACGCCCCGCTGGTGAAAAATACGAAAGCTAAATCGCACGTACCAAGAAAAAATATGG-CGTGGATCTGACGGCTGAAATTGACATCCCGGATCTGGACTCATTTGAAACCCGCGCGCAGTTCAATAAATGAAAA-GAACAAGCTAGCTCTTTTACGAACCGTGCGAATATGCGCTATCAGTTCGAGAAAAACGCCCTACGGTGTGGTTG-CATCGAAAGCTAAAATTGCGGAAATCGAACGTAAACCCAAAGAAAGTTCAACGCCTGGTCGATGAAAAAATCAAAGC-CATGAAAGACAAAAGAATATTACGCAGGCGGTAAACCGCAGGGCACGATTGAACAACGTATCGCCATGACCTCAC-CGGCACATGTGACGGGTATCAACCGTCCGCACGATTTTGACTTCAGTAAAGTTTCGCAGTTACTCCCGTCTGCG-CACCCCTGGAAGAATCCATGGAATGCGCACGGATCCGCAGTATTACGAAAAAGAAAATGATTTCAGCTGCAACTGAAT-TTTATCAAAAGCGTCGAAGGCTCATTTAACTCGTTTCGATGCGGCCGACGAACTGATTGAAGAACTGAAGAAAATTC-CGCCGGATGACTTTTATGAACTGTTCTGCGTATTAGCGAAATCTCTTTGAAGAATTCGATTCTGAAGGCAACAC-CGTCGAAAAATGTGGAGGGTAACGTTTACAAAATCTGTGCTATCTGGAACAATATCGTCGTGGTGATTTTGATCT-GTCGCTGAAAAGGCTTCTAATAGCATAACCCCTTGGGGCCTCTAAACGGGTCTTGAGGGGTTTTTGCCTCCTATGATTG-GTTGTCTTATTACCTTACTTCTATTATAGTATAACATGTTAAACGATAGTTTGTCTACCCTTTTCGACAAATTGATGA-TAATAAATAGTATAGGTATATAGTCGTGATTAGTTGTTAGATTCTTGTCGAAGATAGTCGGTCAATGGGGAAATGGTG-TATGTTGTCGCTGTACCCTACTTT

Supplementary Table 1: List of primers used in this study.

Name	Sequence (5’ 3’)
ChD491	AAAGTAAGCCCCACCCTCACATG
ChD492	AAAGTAGGGTACAGCGACAACATACAC
ChD709	CAAAAAACCCCTCAAGACCCGTTTAGAGG
ChD757	TAATACGACTCACTATAGGG

Supplementary figures



Supplementary Fig. 1: Liposome gating in the absence of a membrane dye. The brightfield channel was used to identify liposome that did not have a membrane signal. The pipeline is similar to the one reported in figure 2. A mask fitting the area to be used during the analysis in brightfield channel was created. Identifying liposomes via the brightfield channel is a valid strategy. However, it is more difficult to distinguish between certain similar phenotypes resulting in stricter gating and the loss of some good liposomes. We always recommend visual inspections of all gated populations. Lumen signal can help distinguish for finer details. **A**, Comparative analysis over the area and aspect ratio features. Object having a surface area higher than $30 \mu\text{m}^2$ and aspect ratio higher than 0.4 were gated as relevant events (grey gate). **B**, 1/3 step to optimize the selection of a population consisting exclusively of liposome. Comparison of the intensity of the brightfield signal vs the area of the mask (green gate). **C**, 1/3 Selection for in-focus events, based on the RMS feature. The events having a *gradient RMS* higher than 45 were selected as in focus and kept into the analysis (black gate). **D**, 2/3 step to optimize the selection of a population consisting exclusively of liposome. Selection for higher *H-homogeneity* values (magenta

gate). **E**, 3/3 step to optimize the selection of a population exclusively consisting of liposome. Comparative analysis of the *H-Correlation* mean and standard deviation. The selected objects (green gate) correspond to the final liposome population, which is cleared from all undesired events. **F**, Images of some aggregates with different sizes and shapes that we eliminated via this first analysis step. **G**, Images captured with ImageStream showing potential liposomes excluded from the analysis because out of focus. **H**, Images of some of the liposomes within the final gate. Liposomes have different morphologies. For all the images captured with the ImageStream the brightfield channel is shown. Scale bar is $7 \mu\text{m}$. The analysis in the Brightfield channel was performed as an example on a small set of 8'000 liposomes from one independent sample.

FtsZ and Min systems: concluding remarks and future perspectives

Elisa Godino & Christophe Danelon

The combination of the Min system and FtsA-FtsZ rings into liposomes is one of the research paths we have explored, which proved to be challenging and that we did not have enough time to investigate in full. This objective stuck with us due to its scientific relevance and its central role in completing the circle of our in vitro reconstitution journey. This is why, in this final chapter, we discuss possible strategies aimed at establishing a functional integration of the Min and FtsZ systems in liposomes to constrict the membrane and eventually split the mother vesicle into two equal-sized daughter vesicles. We start by discussing the possible implementation of cell-free expressed FtsZ as a key component of liposome division. Next, we examine various parameters to be fine-tuned to enhance transcription-translation and facilitate the integration of the two systems in liposomes. We then argue that the implementation of temporal control over the expression of the different genes is necessary for timing the self-organization events underlying division. Finally, we discuss how in vitro evolution can complement rational design to aid in the expression of a dividing machinery.

Can FtsZ still play a role in the gene-directed division of liposomes?

The primary goal of reconstructing a synthetic cell is to push the frontiers of biological engineering, with the possible added value that we will better understand the molecular and cellular processes along the way¹⁻³. Many different molecules can be used to carry out biological tasks, regardless of whether their functionality is consistent with what occurs in the original organism(s) from which these molecules are derived. FtsZ has long been recognized as the main player in the bacterial cytokinesis mechanism⁴. This positioned FtsZ at the center of several in vitro studies aimed at elucidating its involvement during cell constriction and division⁵⁻¹¹. However, there has been significant disagreement over the years regarding whether FtsZ is the major source of membrane constriction, especially since it was shown that cell wall synthesis, not FtsZ as previously assumed, is the rate-limiting component for constriction¹². While evidence seems to suggest that FtsZ is not the major driver of cell division in vivo, the protein has been found to deform and constrict liposome membranes^{9-11,13-17}. As per the in vitro results, researching into an FtsZ-based synthetic cell division machinery might be a viable route. FtsZ-driven liposome division, if successful, would be an engineering achievement with no indication of in vivo significance. As of now, there is no robust, unambiguous documentation about FtsZ-mediated liposome division. Mindful of the potential of FtsZ, while embracing the freedom of exploiting a non-physiological mechanism for synthetic cell division, we mentioned in the discussion part of Chapter 5 several external factors that might assist FtsZ in completing the division process. We suggested achieving synthetic cell division by integrating biological and physical processes. We suggested to increase the area-to-volume ratio via thermal expansion^{18,19}, electric fields^{20,21} or alteration of the osmotic pressure²², to change membrane expansion through the incorporation of SUVs²³⁻²⁵ as well as to tune membrane lipid composition²⁶⁻²⁹ and to exert perturbation via shear forces, pore integration or ligand interaction³⁰. The proposed strategy yields a 'semi-autonomous' division mechanism, whereby genetic control is combined with external physical processes. Such an approach will likely be compatible with the other modules of the synthetic cell maintaining the flow of information from DNA to protein. However, in the long run, the objective is clearly to achieve autonomous self-replication.

Perhaps FtsZ from other species (e.g. mycoplasma and *C. crescentus*) may have distinct properties that would be more suitable than the *E. coli* one for dividing liposomes. A phylogenetic study of FtsZ revealed highly diverse FtsZ sequences, which might represent a plethora of Z-ring-associated protein variations that could help regulate the Z-ring to a functional state³¹. In addition, other proteins and factors³², such as FtsN and Zap, should be further investigated to see whether they aid in completing liposome division. A logic step to follow-up on the work described in this dissertation is the in-liposome implementation of a working gene-expressed FtsA-FtsZ-Min system, not only because of their physiological interconnection but also because Min oscillations can cause substantial membrane

remodeling^{33,34}. It is likely that the resulting changes in mechanical properties, in combination with the forces exerted by FtsZ, might promote the fission event. Recurring challenges when co-expressing multiple genes inside liposomes consist in the limiting PURE system performance³⁵ and in the coordination of the biochemical networks to combine modules. In the next paragraphs, we would like to describe our vision on how to fill this gap, providing a strategy that includes both the rational (when possible) implementation of genetic control and in vitro evolution as an engineering tool.

The current status in integration of MinDE and FtsA-FtsZ within liposomes

At the time I am writing these lines, the functional combination of the Min system with FtsA and FtsZ in liposomes has not been achieved yet, neither starting from the genes nor from solely purified proteins. We attempted to reach such a milestone during the last few months, with only moderate success. We were seeking for liposomes with Min oscillatory patterns in the presence of FtsZ recruited on the membrane. In an ideal scenario, FtsZ would still be able to constrict the liposomes and respond to the Min dynamics, for example by oscillating, getting destabilized or re-localized.

We considered different experimental conditions. First, the genes for FtsA, MinD and MinE were expressed either from three separate constructs, or from a tri-cistronic DNA (droplet assays in Chapter 4), in the presence of cell-free expressed MinC and/or FtsZ. Besides, we increased the concentration of ATP and changed the ratios of purified proteins and/or chaperones. The best results we obtained was a couple of small (< 5 µm in diameter) and extremely rare liposomes with both FtsZ-A647 and MinD-A488 (traces of purified protein) localized on the membrane in the form of static patches (Fig. 1a,b). Most of the liposomes in the sample had MinD recruited on the membrane, with only a few exhibiting oscillations. FtsZ membrane recruitment was an extremely rare phenotype and never resulted in constriction, indicating a problem with FtsA.

Overall, recruitment of both systems on the membrane was so uncommon that we did not consider the integration successful. Nevertheless, this approach did help us establish a first goal toward the integration of the two systems since we first need to get both FtsZ and Min proteins to co-exist on the membrane. As cytoskeletal patterns of FtsZ and FtsA spatially regulated by cell-free expressed MinDE(C) were observed on supported lipid bilayers and within droplets (Chapter 4), we know that the proteins are functional and can effectively operate together (Chapter 4). We hypothesize that proper functioning of the combined systems in liposomes may be achieved by strictly regulating expression levels of the different division proteins. To do so, we propose to design a new DNA construct using a synergetic method that combines rational design with in vitro evolution.

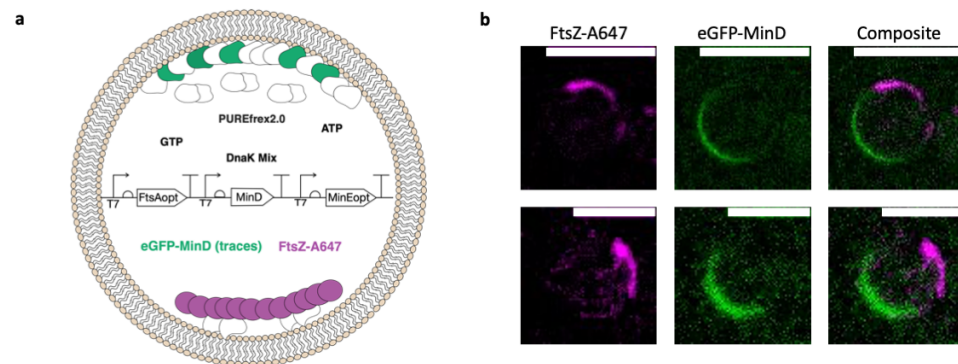


Figure 1: Attempting the reconstitution of MinDE(C) and FtsA-FtsZ networks in liposomes. **a**, Schematic illustration of the liposome assays. The DNA template containing the genes *ftsA*, *minD*, and *minE* (10 nM) was expressed within phospholipid vesicles in the presence of DnaK mix, ATP (2.5 mM), GTP (2 mM), purified FtsZ-A647 (3 μM) and purified eGFP-MinD (100 nM). **b**, Confocal fluorescence images (split channels and composite) of two liposomes exhibiting antiphase MinDE and FtsA-FtsZ on the membrane. This phenotype was extremely rare. eGFP-MinD (green), FtsZ-A647 (magenta). Scale bars are 5 μm.

Control over gene expression to improve systems integration

Balancing the effective concentration of proteins is essential for in vivo cell division. Small differences in the amounts of key cell division players can have a significant impact on cell proliferation^{36,37}. Throughout the cell cycle, a complex collection of regulatory elements, comprising growth rate-mediated signaling, antisense RNAs, and effector proteins, guarantees that adequate amounts of division proteins are produced at a specific time³⁸. As a result, to minimize the negative effects of unbalanced protein expression in liposomes, the concentration of division proteins must be tuned. Control over cell-free expression levels could for instance be achieved by modulating the strength of transcription and translation of the individual genes (Fig. 2).

In PURE system, transcription is mediated by the T7 RNA polymerase, a phage DNA-dependent RNA polymerase that is highly selective for T7 promoter^{39,40}. The T7 promoter is a conserved bacteriophage DNA sequence that spans over 17 to +6 nucleotides from the transcription initiation site⁴¹. The T7 promoter has been extensively studied, and several promoter variants with dramatically increased/decreased transcription yields in vitro have been found^{42–44}. A collection of T7 transcriptional promoters was previously characterized in PURE system by monitoring the fluorescence signal using a Spinach aptamer⁴². Changing the strength of promoters resulted in a consistent distribution of transcriptional levels. Unfortunately, the same correlation was not reflected in the amounts of synthesized proteins, indicating that the tight degree of transcriptional control was lost during the translation

step⁴². More recently, almost 8000 T7 promoter variants were tested in *E. coli*⁴³. In order to investigate whether some of those sequences could be used to tune protein levels in PURE system reactions, four T7 promoter variants with relative transcriptional activity ranging from 1% to 100% were studied. Interestingly, results showed that the protein abundance mirrored the strength of the T7 promoter variant employed⁴³.

Testing promoters beyond T7 could be another way to further widen the transcriptional regulation toolbox in PURE system. This can be accomplished by introducing alternative RNA polymerases, with affinity to specific and unique promoters, in the cell-free reactions. RNA polymerases that were proven to work in PURE system include the bacteriophage T3 RNA polymerase and the SP6 RNA polymerase that have a remarkable specificity for their respective promoter sequences. An alternative to the restricted pool of bacteriophages transcription elements, can be provided by the large, well-characterized, and highly modular repertoire of *E. coli* promoter/operators. However, the use of bacterial promoters is limited given the low transcription rate of *Escherichia coli* RNA polymerases, which is about 8 times slower than the T7 RNA polymerase present in the PURE system⁴⁵. Adding two transcription elongation factors, GreA and GreB, to the PURE system reaction, on the other hand, enhanced *E. coli* RNA polymerase transcription rates by approximately five folds⁴⁶.

When developing multi-gene synthetic constructs, terminator sequences should also be introduced to avoid transcriptional read-through⁴⁷. A terminator is a sequence added after the gene STOP codon to regulate transcription termination. Terminators for bacteriophage T7 RNA polymerase are classified into two categories: class I and class II⁴⁸. The class I terminator is derived from the T7 bacteriophage genome, which has a single T7 RNAP terminator known as T7-T phi⁴¹. This terminator site encodes an RNA sequence capable of forming a stable stem-loop hairpin structure, and it is followed by a U run. The T7-T phi terminator is inherently inefficient since the bacteriophage relies on a certain level of read-through for the expression of downstream genes⁴¹. The class II terminator was discovered in the cloned human preproparathyroid hormone (PTH) gene⁴⁹. This terminator lacks visible structure in the RNA but has a conserved sequence (ATCTGTT) followed by U runs that cause the T7 RNA polymerase to stall⁵⁰. The vesicular stomatitis virus (vsv) carries a Class II terminator which is just 18 bp long (TATCTGTTAGTTTTTTC). Because of its small size and efficacy, this terminator has been frequently employed in vitro^{51,52}. Concatenating multiple vsv terminators in tandem increases termination efficiency. Therefore, consecutive sequences might be employed to regulate complex multiple gene constructs⁵³.

Gene expression can likewise be modulated by altering the translation process, in particular by acting on the ribosome binding site (RBS). The RBS is located in the 5' untranslated region at the upstream of the start codon, and, as the name implies, it recruits ribosomes at the start of translation. The RBS is made up of a consensus sequence, known as the Shine-Dalgarno sequence, and a spacer between the consensus sequence and the starting codon⁵⁴.

Because of its central role in translation, the RBS has a significant influence on protein translation levels^{55,56}. In contrast to the T7 promoter, changing the RBS has a major impact on protein synthesis in PURE system, yet the expression levels do not follow a predictable pattern. Although RBS of varying activities can be programmed, the downstream coding sequence significantly influences the translation rate⁵⁷.

Another aspect that can affect translation is the location of the genes inside the operon, as well as their orientation. It is known that gene location has no effect on mRNA synthesis in PURE system, but the amount of synthesized protein from the first (most upstream) gene is systematically higher⁴². Codon optimization and sequence optimization are also tools that can be used to up/down regulate expression levels. The MinE and FtsA genes will most likely continue to be sequence optimized for averaged codon usage in *E. coli* genes, GC content, and avoidance of 5' RNA secondary structure.

Moreover, fine-tuning the reaction mixture (e.g., concentration of genes, RNA polymerases, ribosomes, enzyme mix, tRNAs, initiation and elongation factors, nutrient mix, and chaperones) and conditions, such as temperature and time, is key to improve the PURE system performance. Lowering the temperature during gene expression, for example, may be helpful in reducing the synthesis of aggregation-prone peptides⁵⁸ and in slowing down the T7 RNA polymerases. The latter effect has been shown to improve transcription–translation coupling in a cell lysate⁵⁹, although not in PURE system³⁵.

Exploring all the involved variables will require several rounds of design, build, and test cycles. Because the complexity of the system to be optimized is quite enormous, it may rapidly become prohibitive to test all the variables with a brute force approach (Fig. 2).

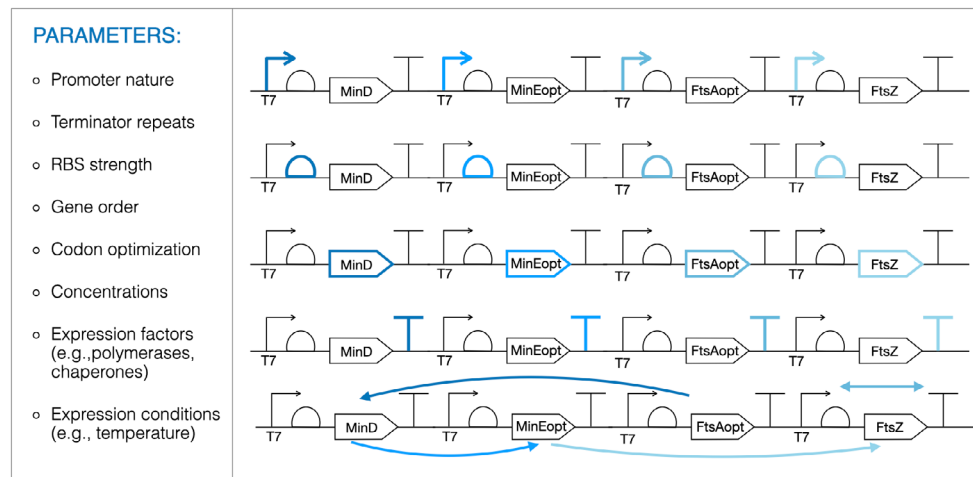


Figure 2: Control over protein expression levels can be addressed by fine-tuning a plethora of parameters. Among the variables to modulate there is transcription (choice of promoter strength and promoter origin, use of different polymerases, selection of terminator and introduction of terminator re-

peats), translation (choice of RBS strength and synergy with the gene, gene location and orientation), the composition of the reaction solution, as well as the expression conditions. The number of parameters involved is so large that it is almost impossible to systematically test them all in various combinations.

Triggering the division event in time

In addition to the fine-tuning of the protein concentration, temporal control over the expression of the different genes may facilitate the integration and coordination of the FtsZ and Min systems. In vivo, the precise timing of protein interactions is essential to orchestrate the many division events. Example of temporal control at the genetic level is the observation that transcriptional activity of *ftsZ* rises during the cell cycle, with an increase in FtsZ production correlating with the appearance of the Z-ring^{60–62}. Engineering temporal control as a generic regulatory mechanism will allow us to trigger the initiation of the division process and to coordinate it with other functions, such as DNA replication and lipid synthesis.

Dynamic behaviors, e.g. oscillations and hierarchical assembly of molecular complexes, can be achieved by designing genetic circuits, such as transcriptional delay and feedback loops^{63–66}. Nowadays, libraries of well-characterized genetic parts are available, making it easier to design sophisticated synthetic gene networks^{67,68}. Early examples of synthetic circuits reconstituted in cell-free systems include DNA switches and feedforward circuits⁶⁹, transcriptional activation and repression cascades with various polymerases and repressors⁷⁰, and the encapsulation of genetic networks and cascades in liposomes⁷¹.

In this section, we will discuss one conceivable scenario for genetic control over the co-expression of the Min system and an FtsZ-based minimal divisome (Fig. 3). This case study is based on a fixed-sized liposome and the assumption that the expression of each gene follows a simple sigmoidal curve (Chapter 2 and 4 Fig. 1). All the needed genetic elements will be placed on a single piece of DNA to avoid fluctuations in expression dynamics due to differences in the relative amounts of the individual genes in liposomes. In the simplest scenario, MinD, MinE and FtsA can be constitutively expressed. The regulatory elements and the coding sequences employed will still be tuned. Delaying FtsZ expression would ensure that the Min waves have enough time to form and that there is sufficient FtsA on the membrane. More in general, events like DNA replication and lipid synthesis should occur prior to division. One option is to simply delay the transcription of the *ftsZ* gene, as it occurs in vivo, for instance by using a two-cassette gene network in which an SP6 RNA polymerase is produced and drives the expression of FtsZ, which is under control of an SP6 promoter. Alternatively, FtsZ expression can be triggered by an external stimulus, allowing the division process to begin only when intended. This could be realized by using an inducible promoter^{65,72–74} or by introducing a riboswitch^{75–77}. Therefore, division will occur only when the signal molecule is delivered to the liposomes.

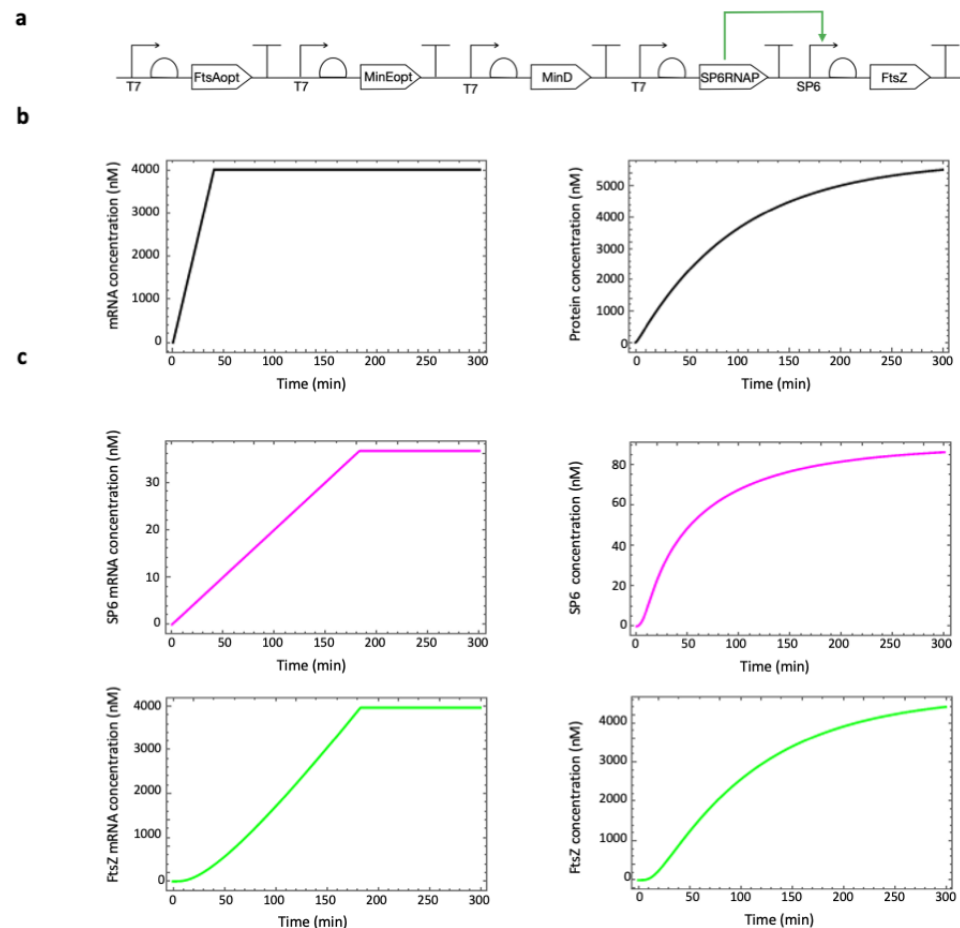


Figure 3: Introducing temporal regulation over FtsZ expression. **a**, Illustration of a possible polycistronic construct for expressing the Min and FtsZ systems. To achieve FtsZ-delayed expression, a gene network is designed that first generates the SP6 RNA polymerase, which then drives the expression of FtsZ via the SP6 promoter. **b** and **c**, Gene expression dynamics simulations for gene expression **b**, simulation of independent, not delayed gene expression **c**, simulation of an independent gene expression (that emulates the expression of the SP6 polymerases) in the presence of a second gene whose expression is delayed because of its dependence on the expression product of the previous gene (emulate FtsZ delayed expression). We can observe the predicted gene expression dynamics (mRNA and protein concentrations as a function of time) over the course of 6 hours. As expected, FtsZ transcription and translation are delayed compared to a situation in which gene expression is independent from the expression of another gene. The simulation was implemented in Mathematica 10.2.0.0. and was carried out using a mathematical model developed as a simplified version of a previously published work from our laboratory. The equations as written in Mathematica, as well as the parameters used, are presented in the Supplementary Informations.

As we have seen in Chapter 4, MinC seems not to be essential and is therefore omitted in a first implementation of the genetic network. If one decides to introduce the *minC* gene, it will be important to keep its expression level low because a high concentration of MinC inhibits the oscillatory behavior of MinDE. One possibility is to express the codon optimized *minC* gene as part of a negative feedback loop, for instance by introducing a lacO site upstream *minC* and expressing *lacI* from the same operon. The lacI protein will dimerize and bind to its lacO site, repressing its own transcription and that of MinC. This means that the production of MinC will first increase and then be repressed, thus avoiding excessive amounts of MinC overtime.

Although we do not foresee a necessity to reduce the lifespan of mRNA and protein to improve time resolution, it is worth noting that in vivo, where complexity is considerably greater than in our minimal system, cell division is regulated by proteases that identify and degrade specific substrates. ClpXP, a member of the AAA+ protease family, reduces the concentration of FtsZ within the Z-ring in *E. coli*^{78,79}. Other cell division proteins, such as MinD, have been recognized as ClpXP substrates⁸⁰. Even though it degrades FtsZ⁷⁸ and destabilizes MinCD copolymers in vitro⁸¹, ClpXP is not required for cell division⁸². Implementation of targeted protein degradation has been demonstrated in cell lysates⁸³ and in PURE system⁸⁴.

In vitro evolution as a tool to achieve systems integration

As we have just seen in the previous paragraphs, adjusting the expression level of the proteins of interest involves finetuning various components including DNA elements, proteins, and experimental conditions. We propose leveraging the potential of in vitro evolution as a complementary engineering method to help in the screening of the various parameters⁸⁵. Life evolves via spontaneous mutations and selection of the fittest organisms throughout a long-standing course of self-reproduction. Directed in vitro evolution consists in the generation of a mutant library and in the screening and selection of the optimal variants for a targeted property^{86,87}.

Because we were unable to observe the coexistence of the Min system and FtsA-FtsZ on the membrane in our liposome studies, we believe that this should be the first challenge to tackle. To obtain membrane recruitment of the two systems, we propose to co-evolve a construct including MinD, MinE, FtsA, and in the presence of trace levels of purified fluorescent MinD and FtsZ as readout. If co-expressed MinD and FtsA are both at functional levels, we should be able to see both of their interacting fluorescent proteins on the membrane.

The creation of a library is a key stage in accomplishing directed evolution since the size, nature, and quality of the genetic library all have a significant influence on the outcome⁸⁸. A library can be designed by modifying sequences, gene order and orientation, and operon occupancy. The coding sequence can be targeted for mutagenesis to enhance the protein of interest (e.g., solubility, stability, activity, specificity, and interactions), while the regulatory

sequences (T7 promoter, RBS, T7 terminator, and G10 leader sequence) can be targeted to optimize expression levels, metabolic fluxes, and synergies⁸⁹. Knowing that all the proteins in the two systems can in principle operate together (Chapter 4), we suspect that the loss of activity within liposomes is caused by alterations in expression levels or impairment in the metabolic network. Therefore, we propose to investigate protein expression optimization by focusing on regulatory sequences, as well as gene ordering and orientation. We suggest exploring the usage of T7 promoters with different strengths. There is no need to build a library for this regulatory sequence, but rather to carefully select a few promoters with different relative strengths (ranging from low to high) from the current available library⁴³, and to be able to scan throughout the range of transcriptional activity. Among the other regulatory sequences, the rational design of the ribosome binding site (RBS) should receive special attention. As previously mentioned, because of its central role in translation, the RBS has a significant influence on protein translation levels. The Shine-Dalgarno sequence is conserved and will not be targeted, but the spacer sequence and length are known to influence translation efficiency and should be aimed specifically⁹⁰. Because the effectiveness of the RBS might vary depending on the downstream coding sequence⁹¹, the creation of a specific library will be required.

Once ready, the library will be encapsulated and expressed inside liposomes that serve as the cell-like evolutionary unit (Fig. 4). Designing experiments to have no more than a single DNA molecule per liposome (typically using <50 pM bulk DNA concentrations), on average, will ensure the linkage between genotype (DNA) and phenotype (recruitment of MinC and FtsZ). However, the presence of one DNA molecule per liposome may result in low or insufficient protein expression. If the problem arises, we recommend to encode the Phi29 DNA replication machinery inside the liposomes⁹². The stochastic partitioning of the many reactants during liposome formation brings functional heterogeneity⁹³ and, therefore, only a few liposomes will exhibit membrane co-localization. Employing vast DNA libraries will result in a diverse population of liposomes, each of which may be considered an individual experiment.

Liposome selection should be realized with high-throughput imaging-based screening methods. A new enabling technology holding great potential for liposome selection is intelligent image-activated cell sorting (IACS)^{94,95}, which combines microfluidics, high-throughput microscopy, real-time intelligent image computation, decision making, and cell sorting. The selected liposomes will be disrupted in order to retrieve their DNA, which will then be amplified and re-encapsulated in a subsequent round of the evolution cycle. Rounds of genetic diversification combined with selection of those liposomes exhibiting a desirable phenotype, will enrich the population with liposomes having better-integrated Min-FtsZ systems. The DNA variants that led to the desired phenotype will be sequenced and reverse-engineered to understand the molecular mechanisms conferring an optimized integration.

In this section, we outlined one of the conceivable scenarios that might be explored to co-

evolve the two systems for improved combination. Of course, once the proteins are located on the membrane (selection criteria), there is no assurance that oscillations will occur or that FtsZ will form a stable ring and constrict the liposomes. New methods will have to be developed to interrogate temporal behaviors and sort liposomes according to dynamic properties. This semi-rational approach will provide crucial information for successful module integration in general and synthetic cell building.

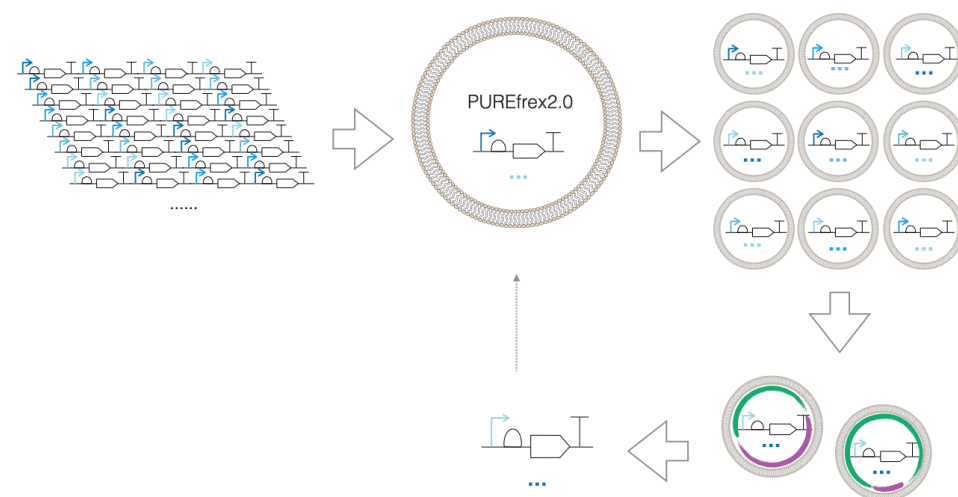


Figure 4: Overview of the in vitro evolution cycle to integrate Min and FtsZ functions. A library of regulatory elements is established; the picture represents a library in which various promoters are used, but RBS can also be mutagenized. The library and PURE system are encapsulated within liposomes together with traces of fluorescently labeled FtsZ and MinD. No more than one DNA copy, on average, is entrapped to ensure genotype-phenotype coupling. Upon gene expression only a few liposomes will have FtsZ and MinD recruited on the membrane. IACS will be used to identify and sort these liposomes. The DNA will be extracted from the selected liposomes, amplified, and re-encapsulated in new liposomes.

Concluding remarks

Overall, the findings in this dissertation indicate that the essential molecular architecture of a minimal division apparatus can be recreated in liposomes starting from DNA. We showed that liposome membrane remodeling can be genetically regulated in PURE system via two distinct biological mechanisms: periodic elongation of liposomes via Min protein oscillations, and membrane constriction and neck formation via FtsA-FtsZ rings. We then found that MinC is not required for the spatiotemporal regulation of FtsA-FtsZ filaments, thereby reducing the number of factors needed for synthetic cell division. Realizing actual liposome fission via the *E. coli* division components remains a big challenge. Nonetheless, we believe that further engineering of a gene-encoded FtsZ-based machinery will eventually lead to controlled division. Many creative efforts to assist liposome scission may be envisioned through internal (more autonomous) or external (semi-autonomous) adjustments to the system. The final working mechanisms may be different than the in vivo cell division processes, but it will represent a significant milestone towards building a synthetic cell.

Of course, there will be challenges along the way. Understanding the biophysical phenomena that induce liposome shape alterations should be prioritized. When contemplating an *E. coli* based division mechanism, module integration will most likely need a rod shape. As we will be working to provide genetic control over liposome division, we must acknowledge the current limitations in expressing multiple genes in PURE system. It will become urgent to discover solutions to enhance its expression levels, lifetime, and robustness.

References

- Noireaux, V., Maeda, Y. T. & Libchaber, A. Development of an artificial cell, from self-organization to computation and self-reproduction. *Proc. Natl. Acad. Sci.* **108**, 3473–3480 (2011).
- Forster, A. C. & Church, G. M. Towards synthesis of a minimal cell. *Molecular Systems Biology*. **2**, 45 (2006).
- Murtas, G. Artificial assembly of a minimal cell. *Molecular BioSystems*. **5**, 1292–1297 (2009).
- Rico, A. I., Krupka, M. & Vicente, M. In the beginning, *Escherichia coli* assembled the proto-ring: an initial phase of division. *J. Biol. Chem.* **288**, 20830–20836 (2013).
- Mukherjee, A. & Lutkenhaus, J. Analysis of FtsZ assembly by light scattering and determination of the role of divalent metal cations. *J. Bacteriol.* **181**, 823–832 (1999).
- Loose, M. & Mitchison, T. J. The bacterial cell division proteins FtsA and FtsZ self-organize into dynamic cytoskeletal patterns. *Nat. Cell Biol.* **16**, 38–46 (2014).
- Mateos-Gil, P. *et al.* FtsZ polymers bound to lipid bilayers through ZipA form dynamic two dimensional networks. *Biochim. Biophys. Acta - Biomembr.* **1818**, 806–813 (2012).
- Ramirez-Diaz, D. A. *et al.* Treadmilling analysis reveals new insights into dynamic FtsZ ring architecture. *PLOS Biol.* **16**, e2004845 (2018).
- Osawa, M., Anderson, D. E. & Erickson, H. P. Reconstitution of contractile FtsZ rings in liposomes. *Science*. **320**, 792–794 (2008).
- Cabré, E. J. *et al.* Bacterial division proteins FtsZ and ZipA induce vesicle shrinkage and cell membrane invagination. *J. Biol. Chem.* **288**, 26625–34 (2013).
- Osawa, M. & Erickson, H. P. Liposome division by a simple bacterial division machinery. *Proc. Natl. Acad. Sci. U. S. A.* **110**, 11000–4 (2013).
- Coltharp, C., Buss, J., Plumer, T. M. & Xiao, J. Defining the rate-limiting processes of bacterial cytokinesis. *Proc. Natl. Acad. Sci.* **113**, E1044–E1053 (2016).
- Osawa, M., Anderson, D. E. & Erickson, H. P. Curved FtsZ protofilaments generate bending forces on liposome membranes. *EMBO J.* **28**, 3476–84 (2009).
- Szwedziak, P., Wang, Q., Bharat, T. A. M., Tsim, M. & Löwe, J. Architecture of the ring formed by the tubulin homologue FtsZ in bacterial cell division. *Elife* **3**, e04601 (2014).
- Furusato, T. *et al.* De Novo Synthesis of Basal Bacterial Cell Division Proteins FtsZ, FtsA, and ZipA Inside Giant Vesicles. *ACS Synth. Biol.* **7**, 953–961 (2018).
- Godino, E. *et al.* Cell-free biogenesis of bacterial division proto-rings that can constrict liposomes. *Commun. Biol.* **3**, (2020).
- Ramirez-Diaz, D. A. *et al.* FtsZ induces membrane deformations via torsional stress upon GTP hydrolysis. *Nat. Commun.* **2021 121** **12**, 1–11 (2021).
- Chapman, D. Phase transitions and fluidity characteristics of lipids and cell membranes. *Q. Rev. Biophys.* **8**, 185–235 (1975).
- Jimbo, T., Sakuma, Y., Urakami, N., Ziherl, P. & Imai, M. Role of inverse-cone-shape lipids in temperature-controlled self-reproduction of binary vesicles. *Biophys. J.* **110**, 1551 (2016).
- Dimova, R. *et al.* Giant vesicles in electric field. *Soft Matter*. **3**, 817–827 (2007).
- Salipante, P. F. & Vlahovska, P. M. Vesicle deformation in DC electric pulses. *Soft Matter* **10**, 3386–3393 (2014).
- Ganzinger, K. A. *et al.* FtsZ reorganization facilitates deformation of giant vesicles in microfluidic traps. *Angew. Chemie Int. Ed.* **59**, 21372–21376 (2020).
- Rasi, S., Mavelli, F. & Luisi, P. L. Matrix effect in oleate micelles-vesicles transformation. *Orig. life Evol. Biosph.* **2004 341** **34**, 215–224 (2004).
- Hanczyk, M. M., Fujikawa, S. M. & Szostak, J. W. Experimental models of primitive cellular compartments: encapsulation, growth, and division. *Science* **302**, 618–622 (2003).
- PMG, L. *et al.* A DNA-programmed liposome fusion cascade. *Angew. Chem. Int. Ed. Engl.* **56**, 13228–13231 (2017).
- Traikia, M., Warschawski, D. E., Lambert, O., Rigaud, J. L. & Devaux, P. F. Asymmetrical membranes and surface tension. *Biophys. J.* **83**, 1443–1454 (2002).
- Tomoki Tanaka, Ryoko Sano, Yuko Yamashita, and Masahito Yamazaki. Shape changes and vesicle fission of giant unilamellar vesicles of liquid-ordered phase membrane induced by lysophosphatidylcholine. *Langmuir* **20**, 9526–9534 (2004).

28. and, Y. I. & Masahito Yamazaki. Vesicle fission of giant unilamellar vesicles of liquid-ordered-phase membranes induced by amphiphiles with a single long hydrocarbon chain. *Langmuir* **23**, 720–728 (2006).
29. Andes-Koback, M. & Keating, C. D. Complete budding and asymmetric division of primitive model cells to produce daughter vesicles with different interior and membrane compositions. *J. Am. Chem. Soc.* **133**, 9545–9555 (2011).
30. Dreher, Y., Jahnke, K., Schröter, M. & Göpfrich, K. Light-triggered cargo loading and division of DNA-containing giant unilamellar lipid vesicles. *Nano Lett.* **21**, 5952–5957 (2021).
31. Pal, A., Saha, B. K. & Saha, J. Comparative in silico analysis of *ftsZ* gene from different bacteria reveals the preference for core set of codons in coding sequence structuring and secondary structural elements determination. *PLoS One* **14**, (2019).
32. Baranova, N. *et al.* Diffusion and capture permits dynamic coupling between treadmilling FtsZ filaments and cell division proteins. *Nat. Microbiol.* **2020** 53 5, 407–417 (2020).
33. Litschel, T., Ramm, B., Maas, R., Heymann, M. & Schwille, P. Beating vesicles: encapsulated protein oscillations cause dynamic membrane deformations. *Angew. Chemie Int. Ed.* **57**, 16286–16290 (2018).
34. Godino, E. *et al.* De novo synthesized Min proteins drive oscillatory liposome deformation and regulate FtsA-FtsZ cytoskeletal patterns. *Nat. Commun.* **10**, 4969 (2019).
35. Doerr, A. *et al.* Modelling cell-free RNA and protein synthesis with minimal systems. *Phys. Biol.* **16**, 025001 (2019).
36. Dai, K. & Lutkenhaus, J. The proper ratio of FtsZ to FtsA is required for cell division to occur in *Escherichia coli*. *J. Bacteriol.* **174**, 6145 (1992).
37. Dewar, S. J., Begg, K. J. & Donachie, W. D. Inhibition of cell division initiation by an imbalance in the ratio of FtsA to FtsZ. *J. Bacteriol.* **174**, 6314 (1992).
38. Dewar, S. J. & Dorazi, R. Control of division gene expression in *Escherichia coli*. *FEMS Microbiol. Lett.* **187**, 1–7 (2000).
39. Shimizu, Y. *et al.* Cell-free translation reconstituted with purified components. *Nat. Biotechnol.* **19**, 751–755 (2001).
40. Shimizu, Y., Kanamori, T. & Ueda, T. Protein synthesis by pure translation systems. *Methods* **36**, 299–304 (2005).
41. Dunn, J. J., Studier, F. W. & Gottesman, M. Complete nucleotide sequence of bacteriophage T7 DNA and the locations of T7 genetic elements. *J. Mol. Biol.* **166**, 477–535 (1983).
42. Chizzolini, F., Forlin, M., Cecchi, D. & Mansy, S. S. Gene position more strongly influences cell-free protein expression from operons than t7 transcriptional promoter strength. *ACS Synth. Biol.* **3**, 363–371 (2014).
43. Komura, R., Aoki, W., Motone, K., Satomura, A. & Ueda, M. High-throughput evaluation of T7 promoter variants using biased randomization and DNA barcoding. *PLoS One* **13**, e0196905 (2018).
44. Conrad, T., Plumbom, I., Alcobendas, M., Vidal, R. & Sauer, S. Maximizing transcription of nucleic acids with efficient T7 promoters. *Commun. Biol.* **2020** 31 3, 1–8 (2020).
45. Makarova, O. V., Makarov, E. M., Sousat, R. & Dreyfus, M. Transcribing of *Escherichia coli* genes with mutant T7 RNA polymerases: Stability of lacZ mRNA inversely correlates with polymerase speed. **92**, 12250–12254 (1995).
46. Maddalena, L. L. *et al.* GreA and GreB enhance expression of *Escherichia coli* RNA polymerase promoters in a reconstituted transcription-translation system. *ACS Synth. Biol.* **5**, 929–935 (2016).
47. Chen, Y. J. *et al.* Characterization of 582 natural and synthetic terminators and quantification of their design constraints. *Nat. Methods* **10**, 659–664 (2013).
48. Macdonald, L. E., Durbin, R. K., Dunn, J. J. & McAllister, W. T. Characterization of two types of termination signal for bacteriophage T7 RNA polymerase. *J. Mol. Biol.* **238**, 145–158 (1994).
49. Mead, D. A., Szczesna-Skorupa, E. & Kemper, B. Single-stranded DNA 'blue' T7 promoter plasmids: a versatile tandem promoter system for cloning and protein engineering. *Protein Eng.* **1**, 67–74 (1986).
50. Lyakhov, D. L. *et al.* Pausing and termination by bacteriophage T7 RNA polymerase. *J. Mol. Biol.* **280**, 201–213 (1998).
51. Du, L., Gao, R. & Forster, A. C. Engineering multigene expression in vitro and in vivo with small terminators for T7 RNA polymerase. *Biotechnol. Bioeng.* **104**, 1189–1196 (2009).
52. Du, L., Villarreal, S., & Forster, A. C. Multigene expression in vivo: supremacy of large versus small terminators for T7 RNA polymerase. *Biotechnol. Bioeng.* **109**, 1043–1050 (2012).
53. Forster, A. C. & Church, G. M. Synthetic biology projects in vitro. *Genome Res.* **17**, 1–6 (2007).
54. Ringquist, S. *et al.* Translation initiation in *Escherichia coli*: sequences within the ribosome-binding site. *Mol. Microbiol.* **6**, 1219–1229 (1992).
55. Zelcbuch, L. *et al.* Spanning high-dimensional expression space using ribosome-binding site combinatorics. *Nucleic Acids Res.* **41**, (2013).
56. Mutalik V. K. *et al.* Quantitative estimation of activity and quality for collections of functional genetic elements. *Nat. Methods* **10**, 347–353 (2013).
57. Chizzolini, F. *et al.* Cell-free translation is more variable than transcription. *ACS Synth. Biol.* **6**, 638–647 (2017).
58. Niwa, T. *et al.* Bimodal protein solubility distribution revealed by an aggregation analysis of the entire ensemble of *Escherichia coli* proteins. *Proc. Natl. Acad. Sci. U. S. A.* **106**, 4201–4206 (2009).
59. Iskakova, M. B., Szaflarski, W., Dreyfus, M., Remme, J., & Nierhaus, K. H. Troubleshooting coupled in vitro transcription-translation system derived from *Escherichia coli* cells: synthesis of high-yield fully active proteins. *Nucleic Acids Res.* **34**, (2006).
60. Yi, Q. M., Rockenbach, S., Ward, J. E. Jr & Lutkenhaus, J. Structure and expression of the cell division genes *ftsQ*, *ftsA* and *ftsZ*. *J. Mol. Biol.* **184**, 399–412 (1985).
61. Dewar, S. J., Kagan-Zur, V., Begg, K. J. & Donachie, W. D. Transcriptional regulation of cell division genes in *Escherichia coli*. *Mol. Microbiol.* **3**, 1371–1377 (1989).
62. Männik, J., Walker, B. E. & Männik, J. Cell cycle-dependent regulation of FtsZ in *Escherichia coli* in slow growth conditions. *Mol. Microbiol.* **110**, 1030–1044 (2018).
63. Noireaux, V., Bar-Ziv, R. & Libchaber, A. Principles of cell-free genetic circuit assembly. *Proc. Natl. Acad. Sci.* **100**, 12672–12677 (2003).
64. Shin, J. & Noireaux, V. An *E. coli* cell-free expression toolbox: application to synthetic gene circuits and artificial cells. *ACS Synth. Biol.* **1**, 29–41 (2012).
65. Niederholtmeyer, H., Stepanoëa, È. & Maerkl, S. J. Implementation of cell-free biological networks at steady state. *Proc. Natl. Acad. Sci. U. S. A.* **110**, 15985–15990 (2013).
66. Takahashi, M. K. *et al.* Characterizing and prototyping genetic networks with cell-free transcription-translation reactions. *Methods* **86**, 60–72 (2015).
67. Canton, B., Labno, A. & Endy D. Refinement and standardization of synthetic biological parts and devices. *Nat. Biotechnol.* **26**, 787–793 (2008).
68. Shetty, R. P., Endy, D., Knight, T. F. & Jr. Engineering BioBrick vectors from BioBrick parts. *J. Biol. Eng.* **2**, 5 (2008).
69. Kim, J., White, K. S. & Winfree, E. Construction of an in vitro bistable circuit from synthetic transcriptional switches. *Mol. Syst. Biol.* **2**, 68 (2006).
70. Noireaux, V., Bar-Ziv, R. & Libchaber, A. Principles of cell-free genetic circuit assembly. *Proc. Natl. Acad. Sci. U. S. A.* **100**, 12672–12677 (2003).
71. Ishikawa, K., Sato, K., Shima, Y., Urabe, I. & Yomo, T. Expression of a cascading genetic network within liposomes. *FEBS Lett.* **576**, 387–390 (2004).
72. Karig, D. K., Iyer, S., Simpson, M. L. & Doktycz, M. J. Expression optimization and synthetic gene networks in cell-free systems. *Nucleic Acids Res.* **40**, 3763–3774 (2012).
73. Niederholtmeyer, H., Xu, L. & Maerkl, S. J. Real-Time mRNA Measurement during an in vitro transcription and translation reaction using binary probes. *ACS Synth. Biol.* **2**, 411–417 (2012).
74. Kobori, S., Ichihashi, N., Kazuta, Y. & Yomo, T. A controllable gene expression system in liposomes that includes a positive feedback loop. *Mol. Biosyst.* **9**, 1282–1285 (2013).
75. Martini, L. & Mansy, S. S. Cell-like systems with riboswitch controlled gene expression. *Chem. Commun.* **47**, 10734–10736 (2011).
76. Tabuchi, T. & Yokobayashi, Y. Cell-free riboswitches. *RSC Chem. Biol.* **2**, 1430–1440 (2021).
77. Chushak, Y. *et al.* Characterization of synthetic riboswitch in cell-free protein expression systems. *RNA Biol.* **18**, (2021)
78. Camberg, J. L., Hoskins, J. R. & Wickner, S. ClpXP protease degrades the cytoskeletal protein, FtsZ, and modulates FtsZ polymer dynamics. *Proc. Natl. Acad. Sci.* **106**, 10614–10619 (2009).
79. Viola, M. G., LaBreck, C. J., Conti, J. & Camberg, J. L. Proteolysis-dependent remodeling of the tubulin homolog FtsZ at the division septum in *Escherichia coli*. *PLoS One* **12**, e0170505 (2017).
80. Flynn, J. M., Neher, S. B., Kim, Y. I., Sauer, R. T. & Baker, T. A. Proteomic discovery of cellular substrates of the ClpXP protease reveals five classes of ClpX-recognition signals. *Mol. Cell* **11**, 671–683 (2003).
81. LaBreck, C. J. *et al.* Degradation of MinD oscillator complexes by *Escherichia coli* ClpXP. *J. Biol. Chem.* **296**, (2021).

82. Gottesman, S., Clark, W. P., De Crecy-Lagard, V. & Maurizi, M. R. ClpX, an alternative subunit for the ATP-dependent Clp protease of *Escherichia coli*. Sequence and in vivo activities. *J. Biol. Chem.* **268**, 22618–22626 (1993).
83. Karzbrun, E., Shin, J., Bar-Ziv, R. H. & Noireaux, V. Coarse-grained dynamics of protein synthesis in a cell-free system. *Phys. Rev. Lett.* **106**, 048104 (2011).
84. Nourian, Z. Towards the assembly of a minimal oscillator. (2015). doi:10.4233/uuid:a8c308e8-3f03-48ba-b6e4-2ce017dae778.
85. Abil, Z. & Danelon, C. Roadmap to building a cell: an evolutionary approach. *Front. Bioeng. Biotechnol.* **8**, 927 (2020).
86. Briones, C. Evolution, In Vitro. *Encycl. Astrobiol.* 1–3 (2014)
87. Nishikawa, T., Sunami, T., Matsuura, T., & Yomo T. Directed evolution of proteins through in vitro protein synthesis in liposomes. *J. Nucleic Acids* **2012**, (2012).
88. Bratulic, S. & Badran, A. H. Modern methods for laboratory diversification of biomolecules. *Curr. Opin. Chem. Biol.* **41**, 50 (2017).
89. Levo, M., & Segal, E. In pursuit of design principles of regulatory sequences. *Nat. Rev. Genet.* **15**, 453–468 (2014).
90. Vellano, R. L. & Rabinowitz, J. C. The influence of ribosome-binding-site elements on translational efficiency in *Bacillus subtilis* and *Escherichia coli* in vivo. *Mol. Microbiol.* **6**, 1105–1114 (1992).
91. Salis, H. M., Mirsky, E. A., & Voigt, C. A. Automated design of synthetic ribosome binding sites to control protein expression. *Nat. Biotechnol.* **27**, 946–950 (2009).
92. van Nies, P. *et al.* Self-replication of DNA by its encoded proteins in liposome-based synthetic cells. *Nat. Commun.* **9**, 1583 (2018).
93. Blanken, D., van Nies, P. & Danelon, C. Quantitative imaging of gene-expressing liposomes reveals rare favorable phenotypes. *Phys. Biol.* **16**, 045002 (2019).
94. Nitta, N. *et al.* Intelligent image-activated cell sorting. *Cell* **175**, 266–276.e13 (2018).
95. Isozaki, A. *et al.* Intelligent image-activated cell sorting 2.0. *Lab Chip* **20**, 2263–2273 (2020).

Supplementary Information

Equations and parameters used in the gene expressions simulation model implemented in Mathematica 10.2.0.0.

Expression with no delay:

$$\begin{aligned}
 D[\text{ktl}[t], t] &= -\text{kinact} \times \text{ktl}[t] \\
 D[\text{NTP}[t], t] &= -\text{ktr} \times \text{cDNA} \times \frac{\text{NTP}[t]}{\text{NTP}[t] + 20} \times 250 \\
 D[\text{mRNA}[t], t] &= \text{ktr} \times \text{cDNA} \times \frac{\text{NTP}[t]}{\text{NTP}[t] + 20} - \text{kinactmRNA} \times \text{mRNA}[t] \\
 D[\text{protein}[t], t] &= \text{ktl}[t] \times \frac{\text{mRNA}[t]}{\text{Km} + \text{mRNA}[t]}
 \end{aligned}$$

Initial concentrations: mRNA[0]=0, protein[0]=0, ktl[0]=60, NTP[0]=1000000

Parameter used: ktr→20, kinact→0.01, kinactmRNA→0, Km→60, cDNA→2

Expression with delay:

$$\begin{aligned}
 D[\text{ktl}[t], t] &= -\text{kinact} \times \text{ktl}[t] \\
 D[\text{NTP}[t], t] &= -\left(\text{ktr} \times \text{cDNA} \times \frac{\text{NTP}[t]}{\text{NTP}[t] + 20} \times \text{ktr2} \times \text{cDNA} \times \frac{\text{NTP}[t]}{\text{NTP}[t] + 20} \times \frac{\text{mSP6}[t]}{\text{mSP6}[t] + \text{KmSP6}} \right) \times 250 \\
 D[\text{mSP6}[t], t] &= \text{ktr} \times \text{cDNA} \times \frac{\text{NTP}[t]}{\text{NTP}[t] + 20} - \text{kinactmRNA} \times \text{mSP6}[t] \\
 D[\text{mFtsZ}[t], t] &= \text{ktr2} \times \text{cDNA} \times \frac{\text{NTP}[t]}{\text{NTP}[t] + 20} \times \frac{\text{SP6}[t]}{\text{SP6}[t] + \text{KmSP6}} - \text{kinactmRNA} \times \text{mFtsZ}[t] \\
 D[\text{SP6}[t], t] &= \text{ktl}[t] \times \frac{\text{mSP6}[t]}{\text{Km} + \text{mSP6}[t] + \text{mFtsZ}[t]} \\
 D[\text{FtsZ}[t], t] &= \text{ktl}[t] \times \frac{\text{mFtsZ}[t]}{\text{Km} + \text{mSP6}[t] + \text{mFtsZ}[t]}
 \end{aligned}$$

Initial concentrations: mSP6[0]=0, mftsZ[0]=0, SP6[0]=0, FtsZ[0]=0, ktl[0]=60, NTP[0]=1000000

Parameter used: ktr→20, ktr2→20, KmSP6→200, kinact → 0.01, kinactmRNA → 0, Km → 60, cDNA×SP6 → 0.01, cDNA×FtsZ → 2

In this simplified model we assumed Michaelis–Menten (MM) kinetics for all reactions.

Michaelis-Menten kinetics was first used to model the rate of transcription from a promoter as a function of nucleotides. The limiting NTP's Km was set to a low level (in this case 20 nM), this allows for the typical mRNA curve, which begins linearly and then suddenly ceases when the NTPs are consumed. ktr is the transcription rate constant, cDNA is the concentration of coding DNA (which is

set at constant), $k_{\text{inactmRNA}}$ accounts for mRNA inactivation overtime (this mRNA cannot be used for translation), and $\text{mRNA}[t]$ is the concentration of the mRNA being transcribed. In the scenario 'expression with delay', we adjusted transcription to be a function of nucleotides and of the SP6 RNAP concentration that is changing over time as the SP6 RNAP gets expressed.

Translation was also modeled with MM kinetics; the translation rate can be described as a function of the concentrations of mRNA with a time-dependent maximum translation rate (exponential decay). k_{tl} is the translation rate constant, k_{inact} reflects some inactivation mechanisms that occurs over time and results in the inactivation of the translation machinery. In the scenario 'expression with delay' translation of multiple proteins (FtsZ and SP6 RNAP) take place, there the model accounts for the fact that distinct mRNAs compete with one another for the translation machinery.

No phenomenological fitting was performed; all parameters were set to values resulting in plausible outputs. The model was only intended to explore reasonable scenarios.

Summary

The Christophe Danelon lab is involved in the long-term effort to construct an autonomous minimal cell using a bottom-up approach. Our goal is to achieve self-maintenance, self-reproduction, and evolution of a liposome compartment containing a minimal genome and a cell-free gene expression system. Self-reproduction requires splitting of the mother compartment into two daughter cells. The project described in this dissertation is part of the group's attempts to create a minimal division unit for the synthetic cell. The development of a gene-driven, controllable, content-preserving liposome division strategy is an ongoing challenging task. Here, we reconstituted some of the organizational mechanisms for division of *Escherichia coli* in a cell-free system. In *E. coli*, cytokinesis is mediated by a multiprotein complex that forms a contractile ring-like structure at the division site. The ring is composed of the cytosolic filament-forming protein FtsZ, as well as its membrane anchoring proteins FtsA and ZipA. The Min system assists in the ring localization at mid-cell by oscillating from pole to pole. Using liposomes as a synthetic compartment and PURE system for cell-free gene expression, we reconstituted membrane-bound cytoskeletal structures and oscillating gradients of Min proteins for liposome constriction and dynamic organization of FtsZ filaments.

In the introductory chapter, we present the notion of a minimal cell and the design strategy that has been applied throughout this project. The key proteins of *E. coli* division are then described, as well as the current state of their in vitro reconstitution.

In the first experimental chapter we set the goal of recreating oscillatory patterns from de novo synthesized Min system. First, we showed that cell-free synthesis of the *minC*, *minD*, and *minE* genes yields full-length proteins. Then, we successfully reconstituted surface waves on supported lipid bilayers (SLBs) using cell-free expressed MinDE proteins. We found that: (1) the ATP concentration in PURE system reactions needs to be increased, (2) DnaK chaperon mix must be supplied, and (3) the *minE* gene must be codon optimized for functional expression in PURE system. Co-synthesized MinD and MinE proteins placed on top of an SLB developed into planar, standing, and spiral waves. After obtaining a robust protocol for producing an active MinDE system on planar membranes, we showed that Min proteins expressed within cell-sized liposomes exhibited distinct dynamic patterns: pulsing, pole-to-pole, and circular oscillations. Interestingly, oscillatory MinDE redistribution within liposomes promotes reversible large-scale membrane deformations. Lastly, we performed a preliminary investigation on the integration of Min and FtsZ systems on SLBs.

The cell-free biogenesis of FtsZ proto-rings was the subject of the second chapter. We started by demonstrating that PURE-expressed FtsA can recruit FtsZ to the membrane, resulting in extensive networks of ring-like structures on SLBs. FtsZ polymerization and membrane

binding were also studied in the presence of purified ZipA, revealing that bundle formation requires a molecular environment that promotes lateral interactions, which can be provided through Ficoll70, an artificial crowding agent, or cell-free expressed ZapA, a native FtsZ crosslinker protein. Furthermore, we found that proto-rings of FtsA-anchored FtsZ filaments generated in liposomes constricted the membrane, yielding budding vesicles attached to the parental liposome by a neck. When including ZapA, we obtained stiffer FtsZ cytoskeletal structures that did not stimulate/elicited/encourage liposome deformation.

Following the separate expression and reconstitution of the Min and FtsA-FtsZ protein systems, we aimed to integrate them and explore how they mutually interact in space and time. We created a tri-cistronic DNA template containing the *ftsA*, *minD*, and *minE* genes. On SLBs, we observed dynamic FtsA-FtsZ patterns anti-phased with the Min surface waves. The FtsZ-depolymerization property of MinC is usually invoked to explain such a phenomenon. However, we demonstrated that MinDE can promote antiphase patterns of FtsZ-FtsA without MinC, both on planar membranes and in water-in-oil droplets. These findings indicate that Z-ring placement might be accomplished with a reduced set of proteins, offering a new viewpoint on the physiological functions of MinC and MinDE oscillations, which we discussed in Chapter 4.

Building on our finding that FtsA-anchored FtsZ filaments form membrane necks and budding vesicles in liposomes, we sought to examine this phenotype in more details and obtain quantitative insights. Therefore, in Chapter 5, we refined our protocol for generating gene-expressing liposomes, boosting the occurrence of FtsA-FtsZ-induced liposome constriction events. We synthesized either the wild-type FtsA or FtsA* (a gain of function mutant) inside liposomes containing purified FtsZ. Expression of FtsA produced short necks ($1.5 \pm 0.8 \mu\text{m}$) with large budding vesicles attached, whereas FtsA* generated long tubular membranes ($3.2 \pm 1.5 \mu\text{m}$) with clustered vesicles. The movies acquired by time lapse microscopy indicated that, for both FtsA versions, the formation of ring-like cytoskeletal structures causes persistent liposome constriction, but does not induce division. Yet, we think that an engineered gene-based division machinery relying on FtsZ is an attractive route toward division of a synthetic cell. We proposed several physical mechanisms that could aid in this process.

In Chapter 6, we presented imaging flow cytometry (IFC) as a synthetic biology tool for studying diverse cell-like properties among large populations of heterogeneous gene-expressing liposomes. IFC combines the strengths of fluorescence microscopy and flow cytometry, enabling high-throughput imaging of individual liposomes and quantitative multidimensional analysis of their features. We demonstrated that IFC allows for (i) the differentiation between small particles, multilamellar/multivesicular liposomes, and aggregates, (ii) the identification of spherical and elongated liposomes as singlets or doublets, and (iii) the recognition of relevant phenotypes for synthetic cell construction, such as DNA replication blobs, cytoskeletal protein filaments, and membrane-protein interactions.

Our last chapter begins with the question that we raised at the start of our journey: can FtsZ play a role in gene-directed liposome division? We here discuss the challenges and possible solutions for dividing a synthetic cell using FtsZ as a major element. The functional integration of the FtsZ and Min modules is considered in the light of three complementary strategies: fine-tuning transcription-translation to improve protein levels, using temporal control over gene expression to coordinate division assembly, and applying directed in vitro evolution to optimize protein activities.

Overall, the findings within this work show that the key players of *E. coli* division can be functionally reconstituted in vitro starting from genes. We were able to remodel liposome membranes via de novo synthesized proteins, discovered new properties of the FtsZ and Min protein systems, and provided novel methodologies for studying the interactions between genetic and non-genetic processes involved in cytokinesis.

Samenvatting

Het Christophe Danelon lab is betrokken bij het langetermijnproject om een autonome minimale cel te bouwen via een *bottom-up* aanpak. Ons doel is om het zelf-onderhoud, de zelf-reproductie en de evolutie van een compartiment, een liposoom dat een minimaal genoom en machinerie voor celvrije genexpressie bevat, te realiseren. Voor zelf-reproductie dient het moedercompartiment in twee dochtercellen gedeeld te worden. Het project beschreven in deze dissertatie maakt deel uit van de pogingen van de groep om een minimale delingsmachinerie te creëren voor de synthetische cel. Het ontwikkelen van een strategie om liposomen te delen op een door genen aangestuurde, controleerbare wijze waarbij de inhoud van het liposoom behouden blijft is een voortdurende uitdaging. In dit werk beschrijven we de reconstitutie in een celvrij systeem van enkele organiserende mechanismen voor deling van de bacterie *Escherichia coli*. In *E. coli* wordt de cytokinese gedreven door een complex van meerdere eiwitten dat een samentrekkende, ringachtige structuur vormt op de plek van deling. Deze ring bestaat uit FtsZ, een eiwit dat voorkomt in het cytosol en filamenten kan vormen, en FtsA en ZipA, eiwitten die zich in het membraan kunnen verankeren. Het Min-systeem draagt bij aan de lokalisatie van de ring in het midden van de cel door van pool tot pool te oscilleren. Door liposomen te gebruiken als synthetisch compartiment en het PURE-systeem voor celvrije genexpressie hebben we membraangebonden structuren van het cytoskelet en oscillerende gradiënten van Min-eiwitten gereconstitueerd voor de constrictie van liposomen en de dynamische organisatie van FtsZ-filamenten.

In het inleidende hoofdstuk presenteren we het idee van de minimale cel en de ontwerpstrategie die gedurende dit hele project gebruikt is. Vervolgens worden de belangrijkste eiwitten voor deling in *E. coli* beschreven, alsmede de huidige status van hun reconstitutie in vitro.

In het eerste experimentele hoofdstuk hebben we ons ten doel gesteld de oscillerende patronen van het Min-systeem te recreëren via de novo synthese. We lieten eerst zien dat de celvrije synthese van de *minC*-, *minD*- en *minE*-genen resulteert in eiwitten van volledige lengte. Vervolgens reconstitueerden we op succesvolle wijze door middel van celvrij tot expressie gebrachte MinDE-eiwitten oppervlaktegolven op een ondersteunde laag van lipiden (*supported lipid bilayer*, SLB). We vonden dat: (1) de concentratie van ATP in het PURE-systeem verhoogt dient te worden, (2) DnaK chaperone-mix toegevoegd moet worden en (3) de codons van het *MinE*-gen geoptimaliseerd moeten worden voor functionele expressie in het PURE-systeem. Tezamen gesynthetiseerde MinD- en MinE-eiwitten ontwikkelden zich tot vlakke, staande en spiraalvormige golven na plaatsing bovenop een SLB. Na het verkrijgen van een robuust protocol voor de productie van een actief MinDE-systeem op vlakke membranen demonstreerden we dat Min-eiwitten verschillende patronen lieten zien wanneer tot expressie gebracht in liposomen het formaat van een cel, namelijk pulserende

oscillaties, pool-tot-pool oscillaties en circulaire oscillaties. Interessant is de observatie dat de oscillerende herverdeling van MinDE binnen liposomen omkeerbare, grootschalige membraanformaties stimuleert. Ten slotte hebben we een preliminair onderzoek naar de integratie van de Min- en FtsZ-systemen op SLB's gedaan.

De celvrije biogenese van FtsZ-ringen was het onderwerp van het tweede hoofdstuk. We begonnen door aan te tonen dat FtsA, tot expressie gebracht in het PURE-systeem, FtsZ kan rekruteren naar het membraan, wat resulteert in uitgebreide netwerken van ringachtige structuren op SLB's. De polymerisatie en membraanbinding van FtsZ zijn ook bestudeerd in de aanwezigheid van gezuiverd ZipA. Uit deze experimenten bleek dat voor het vormen van bundels moleculaire omstandigheden nodig zijn die laterale interacties stimuleren. Deze omstandigheden kunnen gerealiseerd worden door middel van Ficoll70, een kunstmatige *crowding agent*, of celvrije tot expressie gebracht ZapA, een in de natuur voorkomend *crosslinker*-eiwit van FtsZ. Bovendien vonden we dat ringen van door FtsA verankerde FtsZ-filamenten, wanneer deze worden gegenereerd in liposomen, het membraan samentrokken, wat resulteerde in uitstulpende blaasjes die via een nek met het ouderlijke liposoom verbonden zijn. Als we ZapA toevoegden kregen we stijvere FtsZ-structuren die niet in staat waren het liposoom te vervormen.

Na het gescheiden tot expressie brengen en reconstitueren van de Min- en FtsA-FtsZ-eiwitsystemen stelden we ons te doel deze te integreren en hun onderlinge interacties in ruimte en tijd te verkennen. We creëerden een tri-cistronisch DNA dat de *ftsA*-, *minD*- en *minE*-genen bevat. Op SLB's observeerden we dynamische FtsA-FtsZ-patronen in tegenfase met de oppervlaktegolven van de Min-eiwitten. Het vermogen van MinC om FtsZ te depolymeriseren wordt meestal aangewend om dit fenomeen te verklaren. We lieten echter zien dat MinDE de tegenfasepatronen van FtsZ-FtsA kan doen ontstaan zonder MinC, zowel op vlakke membranen als in water-in-olie-druppels. Deze vindingen geven aan dat de plaatsing van de Z-ring bereikt zou kunnen worden met een gereduceerde set eiwitten, wat een nieuw gezichtspunt biedt op de fysiologische functies van MinC- en MinDE-oscillaties, die we hebben besproken in Hoofdstuk 4.

Voortbordurend op de bevinding dat door FtsA verankerde FtsZ-filamenten in liposomen membraannekken en uitstulpende blaasjes vormen wilden we dit fenotype in meer detail bestuderen en kwantitatieve inzichten verkrijgen. Daartoe verfijnden we in Hoofdstuk 5 ons protocol voor het genereren van liposomen waarin genen tot expressie kunnen worden gebracht, waarmee we zorgden dat liposoomconstrictie geïnduceerd door FtsA-FtsZ vaker voorkwam. We synthetiseerden ofwel wildtype FtsA of FtsA* (een mutant met verbeterde functionaliteit) binnen in liposomen die gepurificeerd FtsZ bevatten. De expressie van FtsA produceerde korte nekken ($1.5 \pm 0.8 \mu\text{m}$) met daaraan grote uitstulpende blaasjes. Daarentegen genereerde FtsA* lange buisvormige membranen ($3.2 \pm 1.5 \mu\text{m}$) met geclusterde blaasjes. Filmpjes gemaakt met time-lapse microscopie gaven aan dat, voor beide versies van

FtsA, het vormen van de ringachtige cytoskeletstructuur aanhoudende liposoomconstrictie veroorzaakt maar niet leidt tot deling. Toch denken wij dat een delingsmachinerie ontworpen op basis van FtsZ en gebaseerd op genen een aantrekkelijke route tot de deling van een synthetische cel is. We stelden meerdere fysische mechanismen voor die dit proces zouden kunnen ondersteunen.

In Hoofdstuk 6 presenteerden we *imaging flow cytometry* (IFC) als een gereedschap voor synthetische biologie om verscheidene celachtige eigenschappen te bestuderen in grote groepen heterogene liposomen waarin genen tot expressie gebracht worden. IFC combineert de sterke punten van fluorescentiemicroscopie en flowcytometrie en maakt het mogelijk om op hoge snelheid vele individuele liposomen in beeld te brengen en hun eigenschappen op kwantitatieve en multidimensionale wijze te analyseren. We lieten zien dat het met IFC mogelijk is (i) onderscheid te maken tussen kleine deeltjes, liposomen met meervoudige membranen of compartimenten en geaggregeerde membraanstructuren, (ii) onderscheid te maken tussen enkelvoudige en dubbele bolvormige en uitgerekte liposomen en (iii) relevante fenotypes te herkennen voor het bouwen van een synthetische cel zoals partikels die het resultaat zijn van DNA-replicatie, eiwitfilamenten van het cytoskelet en interacties tussen eiwitten en het membraan.

Ons laatste hoofdstuk begint met de vraag die we aan het begin van onze reis stelden: kan FtsZ een rol spelen in door genen gestuurde liposoomdeling? Hier bespreken we de uitdagingen en mogelijke oplossingen voor het delen van een synthetische cel met FtsZ als een belangrijk element. De functionele integratie van de FtsZ- en Min-modules wordt beschouwd aan de hand van drie complementaire strategieën: het nauwkeurig afstemmen van transcriptie en translatie om de hoeveelheid eiwitten te verbeteren, het controleren van genexpressie in de tijd om het samenkomen van de delingsmachinerie te coördineren en het toepassen van gestuurde in vitro-evolutie om de activiteit van eiwitten te optimaliseren.

De bevindingen in dit werk laten zien dat de belangrijkste spelers in de deling van *E. coli* op functionele wijze gereconstitueerd kunnen worden met genen als startpunt. We zijn erin geslaagd liposoommembranen te vervormen door middel van de novo gesynthetiseerde eiwitten, we hebben nieuwe eigenschappen van de FtsZ- en Min-eiwitsystemen ontdekt en we hebben nieuwe methodes ontwikkeld voor de studie van interacties tussen genetische en niet-genetische processen betrokken bij cytokinese.

Acknowledgments

First and foremost, I want to thank my supervisor, Dr. **Christophe Danelon**. Without his encouragement and assistance throughout the process, this book would not have been finalized. **Christophe** you truly are the ideal supervisor, mentor, and teacher. In the last four years you gave me the freedom to explore my research while providing me with guidance and support. You have always been available, ready to offer advice and encouragement with a perfect blend of insight and humor. I really appreciate the fact that you can listen and value my opinion. I will never forget all the time you have invested into shaping me into a better scientist, often focusing at improving my weak skills. I am grateful for all your countless lessons, for all the ‘Elisa take your time’ and ‘Let the data speak for itself’. Your wisdom and vast experience have impacted me throughout my academic career and daily life. Thank you for establishing a harmonic, safe, and fun lab that is an absolute pleasure to work in. I am delighted you gave me the chance to stay longer and enjoy some more fun.

I would like to express my gratitude to the rest of my thesis committee: Dr. **Marie-Eve Aubin-Tam**, Prof. dr. **Gijsje Koenderink**, Prof. dr. **Rivas Caballero Germán**, dr. **Jérôme Bonnet**, dr. **Kristina Ganzinger**, dr. **Dora Tang**, and Prof. dr. **Marileen Dogterom**. For their insightful feedback and suggestions on this dissertation. In particular, I would like to thank **Marie-Eve** for her encouragement and annual check-ins during my PhD, **Germán** for always being a source of knowledge and a valuable aid to our lab, as well as **Kristina Ganzinger** and **Gijsje Koenderink** for allowing me to participate in their excellent work on cDICE optimization.

I would not have been able to undertake a PhD without the solid knowledge and excitement that I received from key mentors. **Cristina** I still fondly think of my time as an undergraduate student in your class. The sparkle in your eyes when discussing synthetic biology projects was the reason why I decided to pursue a career in this research field. Thank you for enabling me to enter the iGEM universe, for inspiring me with your enthusiasm, which I still carry to this day, and for genuinely helping me even when you did not have to.

I will be forever grateful to my former research advisor, Prof. dr. **Sheref Mansy**; back then, I wasn't very talkative and confident, but I observed a lot and ended up taking many notes on the lessons learned through your supervision. Working in your group had a significant impact on molding my research method and criticizing my findings; it stimulated me, taught me dedication, and prepared me to embark on a PhD journey. Thank you also for supporting all my following application; in each position that I have landed, I have done my best to reflect the values that I have learned from you. Prof. Dr. **Stephen Blacklow**, thank you for enabling me to join your group and for presenting me with one of the most memorable experiences

of my undergraduate time. **Annarita**, the heart of our Armenise-Harvard summer school, a huge thank you to you; I respect your commitment to us even though you had millions of other things to do, and I treasure every knowledge and tip you have offered us.

Next, I want to acknowledge my lab mates for all the insightful discussions and for all the fun we have had over the past four years. **Ana**, you brought a breath of fresh air to our lab since day one. You are so kind, friendly, joyful, smart, and dedicated to science, it is a pleasure to work with you. I'm glad we had to mentor an iGEM team together, to share the supervision of a student and to work together on a shared project. I had a great time, and yeah, maybe it is time for me to apologize for the countless work-related texts I sent you on weekends and late night. **Duco**, thank you for passing on all your liposome expertise to me, for always being helpful, and for listening to me whenever I interrupted the office silence with a "can I ask you a stupid question?" Thank you for all the fun, especially at the foosball table (let's face it, we formed a great team!). **Anne**, thank you for your great contribution to my PhD, not just for your scientific inputs that were essential to my research, but mostly for being a role model to me. I sincerely admire your knowledge, work ethic, and endless enthusiasm, and I'm at a loss for words to express how much I have learned from you. Cheers to our time in the lab together, and even to the Par project, which turned out to be a major headache! **David**, my bench, and desk neighbor. Thank you for the innumerable laughs, your endless kindness, and for all the time we spent together in the lab working and dancing around. **Ilja**, thanks for keeping the lab running smoothly, for always being of tremendous help, and for being an incredible source of lab expertise that you are always ready to share. **Celine** and **Andrea**, I am glad that you two joined our lab and I am sure that with your enthusiasm you will go far. **Jonas**, thank you for welcoming me to the lab and introducing me to the FtsZ world. **Zhanar**, you are a strong woman and a bright scientist. Thank you for immediately becoming a reference for our lab. **Johannes**, thank you for your support and your sense of humor that lighted the office and lunches. **Wouter** thank you for checking in, and for teaching me precious things about self-listening and acceptance. I also want to thank all the students that have passed by in the lab during these four years, you have all been a pleasure to have around and you positively contributed to the fun (and work!) of the Danelon lab. I must thank the amazing students that I had the pleasure to work with **Jard**, **Clara**, **Gianfranco** and **Anna**. Every single one of you has been pivotal to my growth as a scientist and as a mentor, I am sure the future will hold amazing things for you.

Science is a collaborative effort, frequently crossing disciplines and stretching beyond the confines of a single lab and, during my PhD, I was fortunate to work with many other colleagues, whom I would like to thank here.

Jeremie thanks for sharing part of your enormous microscopy knowledge with me; you have

taught me a lot. I appreciate your availability, interest in our work, and patience with my tricky samples. **Fede**, **Lennard** and **Lory** thank you for letting me take part to your valuable work. **Fede**, I am grateful for all the time we spent together (in the lab, at the microscope, at the foosball table, in Sweden and outside work); I only wish we could have started collaborating sooner! **Reza** and **Eli** I am delighted that someone is taking over a project that was dear to me, thank you for allowing me to remain involved, and I hope you will get the best out of it. **Mercedes** thank you for your help with the purified divisome proteins. I also had the pleasure to supervise the TUDelft iGEM team, alongside **Timon**, **Christophe**, **Essie**, **Charlotte**, **Britte**, **Martin**, **David**, and **Ana**. Thank you for showing me how to be a better supervisor, for sharing your knowledge and wisdom, and, most importantly, for all the fun time together. Overall, I want to thank **everyone at BN** for working hard to make our department an efficient, inspiring, and dynamic environment to perform science. Finally, I want to thank the **BaSyC** consortium for allowing me to conduct my research and to be a part of a great network.

The day of graduation will always be in my heart, but so will the realization that I had the exceptional fortune to make true friends throughout the years. **Alberto**, thank you for always being there for me and for sharing experiences, both positive and negative, throughout these hectic university years. I promise that we will continue our regular coffee updates in the future, regardless of where we will be. I am glad I have met two lifelong friends in you and **Mireia**. I am also extremely grateful to **Marzia** and **Daniel**, who have become like a second family in the Netherlands. Thank you for all the fun, food and adventures.

Mamma e papà, grazie per essere sempre dalla mia parte, e per prendervi cura di me anche da lontano. Grazie per avermi fornito tutti gli strumenti necessari per costruire quello che sono oggi. **Simone**, il mio fratellino ormai non più così piccolo, grazie per essere la colla che tiene unita la nostra famiglia. È incredibile in qual misura tu sia cresciuto in questi anni. Sono grata che tu abbia trovato la tua passione e ti auguro di continuare a costruire ciò che ti rende felice. A tutta la mia **famiglia**, nonna Ida, zie/i, e cugini grazie per aver sempre trovato del tempo da passare con me ogni volta che torno a casa per qualche brevissimo periodo, mi fate sentire amata e quei momenti per me valgono moltissimo. **Lidia** e **Mauro**, grazie per avermi accolta nella vostra famiglia con un sorriso e per farmi sentire a casa ogni volta che siamo da voi.

To my husband, **Thomas**, it is because of your encouragement, love and support that I have reached this milestone today. Thank you for sharing your enthusiasm for science and your curiosity with me, for reviewing a large chunk of this book, for inspiring me to do my best and for challenging me to go beyond my limits. I am grateful to have you standing by my side.

Curriculum Vitae

Elisa Godino

07.03.1993	Born in Cles, Italy.
2007 – 2012	Diploma Agro-industrial expert Istituto Agrario di San Michele all'Adige, IT
2012 – 2015	Bachelor in Biomolecular Sciences University of Trento, Trento, IT
2015	Member UNITN 2015 iGEM team
2015 – 2017	Master in Cellular and Molecular Biotechnology University of Trento, Trento, IT
2016	Structural biology internship Harvard Medical School, Boston, US
2017	Biochemistry internship Center for Integrative Biology Trento, IT
2018 – 2021	Ph.D. bionanoscience Delft University of Technology, Delft, NL Promotor Dr. Christophe Danelon.

List of publications

Godino E., & Danelon C.; FtsA-FtsZ in liposomes: constricting necks and budding vesicles, yet a step away from division. In preparation, invited contribution.

Godino E.*, Restrepo Sierra A.* , & Danelon C.; Imaging flow cytometry for high-throughput phenotypic characterization of synthetic cells. In preparation.

Godino E., Doerr A., & Danelon C.; Min waves without MinC can pattern FtsA-FtsZ filaments on model membranes. *bioRxiv* 2021.11.15.468671 (2021). Under revision.

Van de Cauter L.* , Fanalista F.* , van Buren L.* , De Franceschi N., **Godino E.**, Bouw S., Danelon C., Dekker C., Koenderink G. H., & Ganzinger K.A.; Optimized cDICE for Efficient Reconstitution of Biological Systems in Giant Unilamellar Vesicles. *ACS Synth. Biol.* **10**, 1690–1702 (2021).

Godino E., López J.N., Zarguit I., Doerr A., Jimenez M., Rivas G., & Danelon C.; Cell-free biogenesis of bacterial division proto-rings that can constrict liposomes. *Commun. Biol.* **3**, (2020).

Godino E., López J.N., Foschepoth D., Cleij C., Doerr A., Castellà C.F., & Danelon C.; De novo synthesized Min proteins drive oscillatory liposome deformation and regulate FtsA-FtsZ cytoskeletal patterns. *Nat. Commun.* **10**, 4969 (2019).

Bonfio C., **Godino E.**, Corsini M., Fabrizi de Biani F., Guella G., & Mansy S. S.; Prebiotic iron–sulfur peptide catalysts generate a pH gradient across model membranes of late protocells. *Nat. Catal.* **1**, 616–623 (2018).

Beal, J. *et al.*; Reproducibility of fluorescent expression from engineered biological constructs in E. coli. *PLoS One* **11**, (2016).

* denotes equal contribution.

